

Controlled Positioning of Semiconductor  
Nanowires Using Transfer Printing Techniques

PhD Thesis

Dimitars Jevtics

Institute of Photonics  
Department of Physics  
University of Strathclyde  
Glasgow  
United Kingdom

May 19, 2022



This thesis is the result of the author's original research. It has been composed by the author and has not been previously submitted for examination which has led to the award of a degree.

The copyright of this thesis belongs to the author under the terms of the United Kingdom Copyright Acts as qualified by University of Strathclyde Regulation 3.50. Due acknowledgement must always be made of the use of any material contained in, or derived from, this thesis.

Dimitris Jevtic

May 19, 2022

# Abstract

The aim of this thesis work is to develop and investigate a deterministic integration approach based on the transfer-printing protocols for the integration of semiconductor nanowire devices onto non-native surfaces and into nanophotonic systems. The developed technique goes beyond the state of the art to demonstrate a semiconductor pick-and-place capability permitting successful and accurate operation at the nanoscale. In the first part of this thesis work, the controllable capture and release of target semiconductor nanowires onto host surfaces (e.g. *Au*, *SiO<sub>2</sub>*, *Si*, polymer) is presented; also arrays and patterns were created using selected nanowires as building blocks. Furthermore, a nanowire alignment method was developed allowing to control the position of single devices with high accuracy levels in the order of 200 nm. These developed protocols were used to assemble laterally aligned nanowire pairs with separations between individual elements as low as 1  $\mu\text{m}$ .

The developed transfer-printing technique was used for the assembly of photonic circuitry using nanowire lasers as the building blocks. Not only this was demonstrated in planar surfaces, but also on layered structures and in three dimensions, with a vertical separation in the order of few hundreds of nanometers. The unique laser properties of semiconductor nanowires were studied in large populations pre- and post-printing to understand the inter-wire performance variation and the effects from the transfer-printing

process. The majority of this thesis work was done using semiconductor nanowires fabricated in bulk (InP) or in core/shell (GaAs/AlGaAs) structures. The flexibility of the developed printing method however, is applicable to nanowires beyond those presented in this thesis. Finally, we have investigated possibilities of using laterally aligned nanowire pairs for the next generation of photonic devices. For systems with reduced separation ( $< 1 \mu\text{m}$ ): a numerical model describing the high-frequency dynamics of evanescently-coupled nanowire lasers pairs was investigated. For the separation where no significant coupling was found ( $> 1 \mu\text{m}$ ): a dual-colour lasing emission system with coarse and fine separations between the individual wavelengths was shown.

A significant part of this thesis work was focused on developing pick-and-place methods that allow integration of single nanowire devices and addressing challenges associated with this process. Thus, the aspiration behind this project was to develop a key-enabling technique that allows to capture a selected nanowire device and integrate it onto a target surface, with a positioning accuracy that is in the order of nanoscale dimensions of the device. The thesis work is concluded with the future directions of this project and shows preliminary results on the large-scale integration of nanowire devices and pick-and-place of quantum-dot clusters.

# Acknowledgments

I would like to express my sincere gratitude towards all the people who have helped me in this endeavor. Without their guidance, expertise, and encouragement, I would not have made headway in the project.

I would like to extend my gratitude to Antonio Hurtado and Martin D. Dawson, my project supervisors, for the fantastic opportunity of joining the institute and working on such an amazing project. This thesis work could not be completed without the effort and cooperation of Antonio Hurtado, who deserves all of the credit.

I would like to thank the senior staff at the institute including Michael J. Strain, Benoit Guilhabert, Nicolas Laurand, Vasili Savitski, Ian Watson and Keith Mathieson.

I would also like to thank my PhD colleagues, Marius Jankauskas, John McPhillimy, Paul Hill, Riccardo Casula and Jack Smith for their endless support and amazing time at the institute.

I am extremely grateful to Sharon Kelly and Lorraine Annand for their assistance and help throughout my time at the institute. To the rest of colleagues at the institute – thank you for the amazing time, it was truly a pleasure meeting you all. I would also like to thank our collaborators at the University of Manchester, the University of Cambridge, the University of Oxford and the Australian National University.

Last but not least, gratitude goes to all my friends, my family, my wife.

*To my wife and family...*

# Contents

<b>1</b>	<b>Introduction</b>	<b>1</b>
1.1	Motivation . . . . .	2
1.2	Deterministic Transfer-Printing (TP) Technique . . . . .	6
1.2.1	TP for Optoelectronic Device Fabrication . . . . .	7
1.2.2	Reversible Adhesion . . . . .	10
1.3	Semiconductor Nanowire (NW) Lasers . . . . .	15
1.3.1	Historical Perspective . . . . .	16
1.3.2	Growth Techniques for the Fabrication of NW Lasers . . . . .	18
1.3.3	Lasing Emission in Semiconductor NWs . . . . .	21
1.3.4	Fabry-Perot (FP) Cavities . . . . .	24
1.4	Thesis Outline . . . . .	30
<b>2</b>	<b>Transfer-Printing of Semiconductor Nanowires</b>	<b>33</b>
2.1	Concept and Motivation . . . . .	34
2.2	Methods . . . . .	36
2.2.1	Modified Dip-Pen Nanolithography . . . . .	37
2.2.2	Previous TP Works with Optoelectronic Structures . . . . .	40
2.3	Polymer $\mu$ -stamps for TP of NW Devices . . . . .	42

2.3.1	Procedures for the Capture/Release of NW Lasers . . . . .	42
2.3.2	Design and Fabrication of Polymer $\mu$ -Stamps . . . . .	45
2.4	Heterogeneous Integration of NW Devices . . . . .	49
2.4.1	Integration of NW Lasers into Diverse Substrates . . . . .	49
2.4.2	Fabrication of Spatial Patterns with NW lasers . . . . .	54
2.4.3	Sub- $\mu$ m Alignment of NW Devices . . . . .	57
2.5	Conclusion . . . . .	67
<b>3</b>	<b>Characterisation of NW Laser Systems</b>	<b>69</b>
3.1	Micro-Photoluminescence ( $\mu$ -PL) Setup . . . . .	69
3.1.1	Optical Excitation of NW Lasers . . . . .	74
3.1.2	Spectral Analysis and Imaging of NW Lasers' Emission . . . . .	78
3.1.3	Measurement Techniques . . . . .	81
3.2	Scanning Electron Microscope (SEM) . . . . .	84
<b>4</b>	<b>Nanophotonic Integrated Systems with Transfer-Printed Semiconductor Nanowires</b>	<b>87</b>
4.1	Integration of NW Lasers into Waveguide (WG) Systems . . . . .	88
4.1.1	Coupling Configuration Between NW Lasers and WGs . . . . .	93
4.1.2	Nanophotonic Circuits with Integrated NW Lasers . . . . .	99
4.1.3	Mechanically Flexible Systems with Integrated NW Lasers . . . . .	103
4.2	Integration of Semiconductor NW Lasers with Plasmonic Nanoantennas	107
4.2.1	TP of InP Nanowires into Cat's Eye (CE) Antenna Cavities . . . . .	109
4.2.2	Reduced Lasing Threshold and Vertical Emission in NW-CE Antenna Lasers . . . . .	111
4.3	3D Integration of NWs onto Bow-Tie Antennas for THz Sensing . . . . .	115

4.3.1	Multi-stage Fabrication of a 3D-cross NW Network . . . . .	116
4.4	Conclusion and Summary . . . . .	120
<b>5</b>	<b>Complex Hybrid Systems with NW Lasers</b>	<b>122</b>
5.1	Numerical Study of Coupled NW Laser Systems . . . . .	124
5.1.1	Design and Implementation of Coupled NW Lasers Systems . . .	125
5.1.2	Rate Equation Model . . . . .	126
5.1.3	Finite Difference Eigenmode Model . . . . .	127
5.1.4	Simulation of Evanescently Coupled NW Laser Pairs . . . . .	130
5.2	Binning of NW Lasers and ‘Champions’ Selection . . . . .	141
5.2.1	Characterisation, Binning and TP of NW Lasers . . . . .	142
5.2.2	Analysis of Target NW Devices . . . . .	147
5.2.3	Comparison between Printed and Non-Printed Devices . . . . .	151
5.3	Towards Fabricating Coupled-NW Laser Systems . . . . .	154
5.3.1	Wavelength Division Multiplexing (WDM) using NW Lasers . .	156
5.4	Conclusion and Summary . . . . .	162
<b>6</b>	<b>Conclusion and Future Work</b>	<b>164</b>
6.1	Conclusion . . . . .	165
6.2	Future Work . . . . .	171
6.2.1	Towards Large-Area and Parallel NW Printing . . . . .	171
6.2.2	Transfer-Printing of Perovskite Quantum-Dots (QDs) onto Non- Native Surfaces . . . . .	175
	<b>Bibliography</b>	<b>179</b>

# Chapter 1

## Introduction

This chapter discusses the motivations and aspirations behind this PhD project. The core aim of this work was to develop a deterministic and accurate transfer-printing (TP) technique for the heterogeneous integration of semiconductor nanowire (NW) devices into non-native substrates. Non-native substrates are defined as material platforms on which the devices were not grown. Thus, the first section of this chapter is focused on explaining the high potentials that such technique has for the implementation of novel hybrid (nano-)photonic systems that combined in a single platform nanoscale devices built from different material systems; hence permitting to circumvent limits in device fabrication imposed by material growth. In this first section of the chapter, we will also introduce state-of-the-art results in the emerging field of integrated (nano-)photonics, to put our work into context.

The second section of this Chapter will introduce the TP technique for the heterogeneous integration of photonic devices. Here, the motivation behind the development of this technique is discussed, and a historic perspective is provided showing how this integration method has evolved in recent years. Importantly, in this section the underlying physical mechanisms behind the deterministic pick-and-place mechanism of the

TP technique are introduced. We also explain why the reversible adhesion processes, in which this technique relies for operation, enable the assembly of novel hybrid optoelectronic devices. It is worth mentioning that although the introduction of the TP technique is provided in Chapter 1, the required specific tools, protocols, and methods are reported in Chapter 2, as the latter will describe our first experimental results on the TP of NW devices in a wide variety of receiving surfaces.

The third section of Chapter 1 starts with the discussion of the development of semiconductor NW lasers and their growth mechanisms. Additionally, this section will provide a brief historical perspective describing the developments which lead to the discovery of lasing emission in NW devices, (firstly demonstrated in Zinc Oxide, *ZnO*, NWs). Then, the background physics of semiconductor NWs will be presented discussing essential device properties for the successful achievement of stimulated light emission.

The last section of this chapter will provide an outline of this thesis briefly discussing the structure and themes discussed in each individual chapter of this dissertation.

## 1.1 Motivation

It goes without saying that the invention of lasers is considered one of humanity's greatest achievements of the 20<sup>th</sup> century. This became possible due to the energy quanta discovery by M. Planck, published in his works between December 1900 and January 1901 [1] that described the black-body radiation; and the concept of stimulated emission, proposed by A. Einstein in 1917 in his paper 'On the Quantum Theory of Radiation' [2]. Nearly 40 years later, in 1955, the first Maser (microwave amplification by stimulated emission of radiation) was built by C. H. Townes and his colleagues

using ammonia ( $NH_3$ ) molecules and achieving stimulated emission at the frequency at 23.87 GHz [3]. C. H. Townes along with N. G. Basov and A. M. Prochoroff were awarded the 1964 Nobel Prize in Physics for their theoretical work leading to the development of the maser [4]. Following the early developments in masers during the 1950s, a race began to demonstrate the first laser (light amplification by stimulated emission of radiation), which culminated in 1960, when T. H. Maiman reported the first ever laser in his work ‘Stimulated Optical Radiation in Ruby’ [5]. In his paper, T. H. Maiman described a process which enabled the achievement of stimulated light emission using a synthetic ruby crystal (as the gain medium) and helical xenon lamp (as the excitation source), and demonstrated lasing emission at the wavelength of 694.3 nm [5]. Following Maiman’s demonstration, key scientific advances followed promptly, including the development of the first semiconductor laser by R. N. Hall in 1962. Hall’s laser was made of Gallium Arsenide ( $GaAs$ ) and emitted in the near-infrared (NIR) at the wavelength of  $\sim 850$  nm [6]. Ever since, the fields of laser physics and photonics in general have thrived – more complex laser designs and systems have been continuously developed with enhanced material properties and geometries. In parallel, R. P. Feynman’s famous lecture ‘There’s Plenty of Room at the Bottom: An Invitation to Enter a New Field of Physics’ in 1959, sparked at the time tremendous interest in the scientific community and is considered the moment the importance of nanotechnology was recognized due to the high potential of creating novel ultra-small devices at nanoscale.

Whilst the first ultraviolet (UV) laser was demonstrated back in 1966 using  $ZnO$  material; the nanoscale counterpart was reported in 2001 by P. Yang’s Group in their work ‘Room-Temperature Ultraviolet Nanowire Nanolasers’ [7]. The reported NW lasers were only 20 – 150 nm in diameter with a length up to 10  $\mu\text{m}$  and lasing modes

at the wavelength range between 370 – 400 nm [7]. The ultra-small dimensions of these quasi-1D devices offered low-threshold lasing emission ( $\sim 40 \text{ kW/cm}^{-2}$ ) and room-temperature operation. Importantly, this remarkable work demonstrated the possibility of fabricating coherent light sources at the nanoscale with the NWs themselves forming Fabry-Perot (FP) cavities permitting light confinement and the achievement of stimulated light emission.

The rapid development of lasers, since their first demonstration in 1960 until today, has paved the way towards the manufacturing of a variety of ultra-precise systems which are ubiquitous nowadays in our society and with applications across all domains ranging from security to medicine, manufacturing, communications, etc. [8–10]. Laser systems not only have transformed our day-to-day life, but have also enabled important scientific breakthroughs – from astronomy to chemistry [11] – and in the last 60 years, lasers have been amongst the most used toolsets in Nobel Prize awarded works [11]. For instance, a laser interferometer setup was at the core of the recent discovery of gravitational waves by the LIGO observatory [12].

In parallel, in the last two decades great advances have been produced in the field of (nano-)fabrication, permitting the precise design and fabrication of a multiplicity of nanoscale devices and systems across disciplines [13,14]. In particular, (nano-)photonics is nowadays recognised as a leading scientific field due to the wide applications it offers across a variety of domains, such as security, quantum technology, artificial intelligence, biology, to name but a few [15]. However, the use of many novel and promising nanophotonic devices, including the key-enabling semiconductor NW lasers that will be studied in this thesis, is mainly restricted to research Lab environments. In particular, the transition of semiconductor NW lasers to industry settings is still largely

limited by the difficulties associated with their integration into bespoke devices and systems and their excitation. Regarding the latter, a research work by C. M. Lieber's group reported lasing emission in a semiconductor NW under electrical excitation [16]. This offered a very important step towards the practical development of semiconductor NW laser devices able to reach commercial products. However, it is still difficult to replicate those results [17], given the important fabrication challenges associated with the formation of high-quality electrical contacts in the NWs (through which the excitation is achieved) permitting to achieve lasing emission in electrically-injected NWs. Nonetheless, this is a fast moving research area at present with significant amount of groups, investment and research projects aimed at achieving room-temperature lasing emission in NW laser by means of electrical excitation [16, 18, 19].

Selective and precise integration of NW devices onto non-native surfaces and systems is another fundamental key technological challenge. This needs to be tackled to ensure the development of industry-informed NW-based systems targeting functional applications and with prospects of reaching the market. To date, various methods of positioning NWs have already been explored; however, the reported techniques showed limited performance and transfer yields when integrating single target NWs - this is discussed in Chapter 2 in greater detail. In this PhD project, we have developed a key-enabling system for the heterogeneous integration at the nanoscale of semiconductor NW lasers using deterministic TP methods. Herein, we demonstrate the accurate and controllable pick-and-place of individual and 'bundled' semiconductor NW devices by means of TP techniques. We also report novel methodologies enabling the systematic fabrication of a wide range of nanophotonic systems using semiconductor NWs as building blocks, including the development of 1D/2D arrays and bespoke struc-

tures built with NW lasers in a variety of substrates (see Chapter 2). The integration technique developed during this PhD project enables controlled removal of NW lasers from their growth substrates and positioning them at desired locations in target receiving surfaces with sub- $\mu\text{m}$  precision. This alignment accuracy opens new exciting routes of key-enabling applications as demonstrated throughout this thesis work, and which we expect to expand in the future. Furthermore, the TP technique allows engineering (nano-)photonic systems, by permitting the assembly of NW lasers and other nanoscale components with other pre-fabricated photonic components on-chip; hence enabling the achievement of coupling effects and other interactions needed for practical systems fabrication. Several (nano-)photonic systems fabricated by means of TP techniques to integrate NW devices at their core will be presented in Chapters 4 and 5. Finally, in this work we have also extended the capabilities of our developed TP tool to demonstrate pick-and-place of other nanoscale elements (in addition to NW devices). Specifically, we demonstrate the ability to integrate ultrasmall quantum-dot (QD) clusters onto target host surfaces. This thesis work describes the techniques and tools used for NW assembly as well as demonstrates the practical application of the systems and photonic circuitry, enabled by this technique.

## 1.2 Deterministic Transfer-Printing (TP) Technique

This section introduces the TP technique. We discuss the motivation behind the use of this technique as a method for nanoscale device heterogeneous integration, the underlying physics principles and the processes followed to develop the technique. TP is a deterministic pick-and-place technique, which allows transferring target objects ('inks') from their native substrates ('donor') onto host surfaces ('receiver') without

inflicting damage or modifying them. The technique also allows utilizing various target components and assembling those into systems thus permitting to circumvent material growth limitations in device fabrication [20]. The TP process is achieved using bespoke polymeric micrometric-scale stamps ( $\mu$ -stamps) that permit capturing the target inks and releasing them in the receiver. As it was mentioned at the beginning of this thesis, the device integration processes by means of TP can be achieved with high-positioning accuracy using either individual [21,22] or multiple devices at once [22] (see Chapter 2 for discussion). Moreover, by stacking devices on top of each other, TP makes possible to assemble structures vertically or creating devices with 3 degrees of freedom [23].

The polymeric  $\mu$ -stamps used for device integration in the TP technique are typically made of a polydimethylsiloxane (PDMS) material: a polymeric organo-silicon compound that is optically transparent (at visible light wavelengths) and has viscoelastic properties [24,25]. Typically,  $\mu$ -stamps are designed with specific shapes conforming to those of the devices ('inks') that are to be transfer-printed to achieve better surface contact, and therefore help achieving higher pick-up and release yield. TP relies for operation on the principle of reversible adhesion. The latter, along other important physical effects behind the TP technique, are discussed in detail in subsequent sections.

### **1.2.1 TP for Optoelectronic Device Fabrication**

The ability to precisely manipulate and control the adhesion force between two objects or surfaces offers great promise for the assembly of systems enabling a myriad of novel devices comprised of components from distinct material systems and permitting their integration with prefabricated structures. At times in history, the inspiration for scientific breakthroughs directly comes from biology: a prime example is the 'Gecko Tape'

– demonstrated in 2003 by the 2010 Physics Nobel Prize laureates A. K. Geim and K. S. Novoselov and their colleagues. In their work ‘Microfabricated adhesive mimicking gecko foot-hair’ [26], they presented a  $1 \text{ cm}^2$  polyimide array with fibrillar structures imitating those found on a gecko (*Gekko gecko*) foot, see Figs. 1.1(a-b). These tiny hairs were estimated to individually produce a force  $\sim 10^{-7} \text{ N}$  [26] and when combined in a single sample resulting in adhesion force of  $10 \text{ Ncm}^{-2}$  (due to van der Waals (VdW) and/or capillary forces) [26]. The dimensions of the fabricated devices in [26] were: height  $2 \mu\text{m}$ , pitch  $1.6 \mu\text{m}$  and diameter of  $500 \text{ nm}$ . These easily allowed to overcome the weight of a toy ( $\sim 40 \text{ g}$ ) attached to horizontal glass plane, as shown in Fig. 1.1(c). Interestingly, the same forces governing the adhesion mechanisms in the gecko’s foot are used in soft lithography – a technique introduced in 1998 by Y. Xia and G. Whitesides [27]. Soft lithography techniques utilize elastomeric stamps for embossing, printing, and moulding of nanoscale devices (for example, quantum dots) from a wide variety of materials [27]. This technique was created as an alternative method to photolithography [27], for the development of small structures and features on non-native surfaces. Importantly, unlike photolithography, soft-lithography does not require the use of complex device fabrication facilities and provides comparable repeatability whilst remaining an inexpensive technique. Soft-lithography is nowadays widely used for integrating large clusters, replicating features, and fabricating patterns on curved features, see [28–30] for selected works. However, these ‘printing’ fabrication techniques were not used to their full potential. As a result, J. A. Rogers and his group suggested the possibility to capitalise on the reversible adhesion mechanisms and developed its own deterministic printing method [20]. The method developed by Rogers et al. [20] demonstrated that, under adequate conditions, a stamp-printing technique

is capable to controllably capture selected devices or structures from their growth substrate and subsequently release them onto non-native surfaces with high yield. Shortly after their technique demonstration, J. A. Rogers' group provided proof-of-principle results on the fabrication of a wide variety of hybrid devices/systems enabled by the controllable transfer-printing included the integration of membranes, nanorods, bendable electronics and material-based patterns, just to name a few [20]. Rogers and the co-workers also worked extensively on the heterogeneous integration of microscale light emitting diodes ( $\mu$ -LEDs), a research that transited into a commercial application for their derived printing technique [20]. Rogers' developed technique came to be known as TP, although it is also referred at times as micro-transfer printing and nano-transfer-printing.

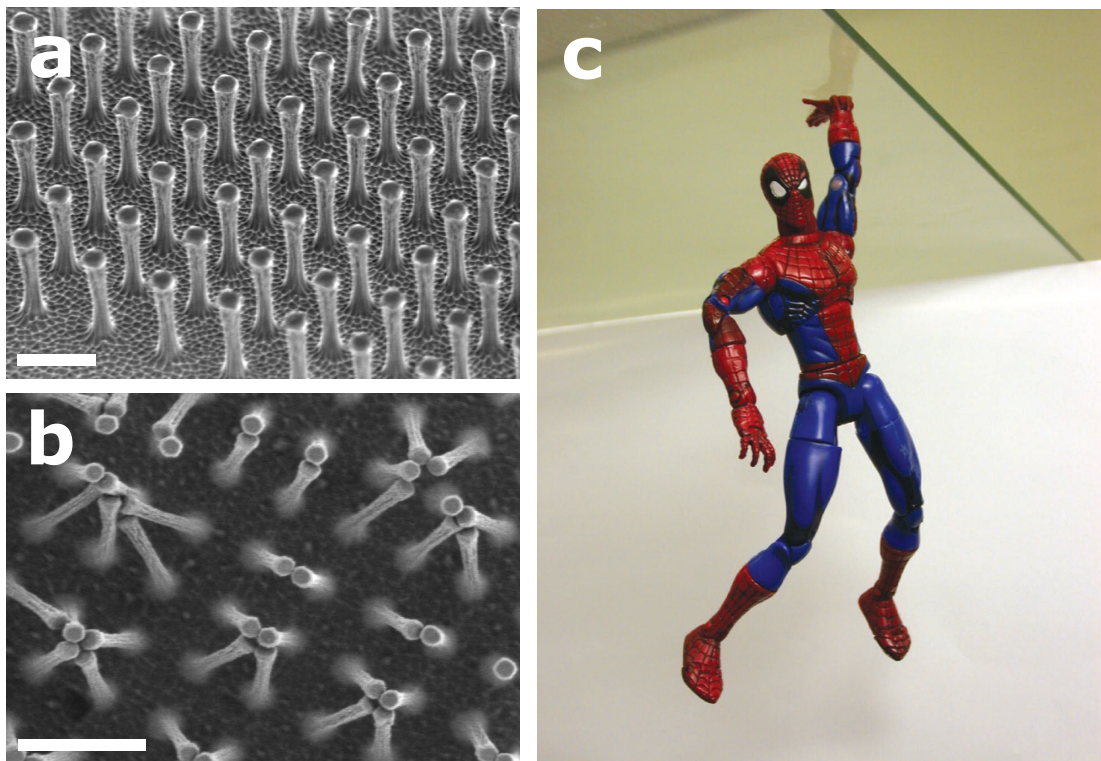


Figure 1.1: (a-b) Scanning electron microscopy micrographs of an area of the fabricated polyimide hairs. (b) Shows the bunching of hairs – this process was found to be responsible for the adhesive force decrease. (c) Photo showing a spider-man toy attached with one of its hands to a horizontal glass plate. The toy is 15 cm in height, weights  $\sim 40$  g and has its hand covered with  $0.5 \text{ cm}^2$  of the gecko tape. Figures taken from [26].

### 1.2.2 Reversible Adhesion

The concept of reversible adhesion was proposed by J. A. Rogers' group at the University of Illinois at Urbana-Champaign who used it to describe the TP technique [20]. Fig. 1.2 depict the protocols of the three proposed TP processes [20], namely: (1) 'Additive Transfer', (2) 'Subtractive Transfer' and (3) 'Deterministic Assembly'. These are described below for the case where a polymeric slab with rectangular  $\mu$ -stamp features is used for the TP processes (see Fig. 1.2). For the 'Additive Transfer' process (left panel in Fig. 1.2), the  $\mu$ -stamps in the polymeric slab are coated (or deposited) with ink; upon the polymeric slab is brought into contact with a receiver substrate, the ink-coated  $\mu$ -stamps, transfer the ink to the receiving substrate. 'Subtractive Transfer', depicted in the middle panel in Fig. 1.2, represents the opposite process to 'Additive Transfer'. Now, the ink is captured by the  $\mu$ -stamps in the polymeric slab, producing as a result patterned structures on a donor substrate. Finally, 'Deterministic Assembly' combines the two aforementioned techniques using a single polymeric slab with  $\mu$ -stamp features. Firstly, the ink is captured from the donor substrate by the  $\mu$ -stamps. Then, the  $\mu$ -stamps are aligned with a receiver substrate; after this, by making a surface contact between the  $\mu$ -stamp and the receiving surface, the ink is transferred at a desired location onto a receiver sample. It must be noted that typically, in the case of 'deterministic transfer', prefabricated features such as  $\mu$ -disk resonators,  $\mu$ -LEDs could be used as ink. Moreover, the devices to be transferred are typically designed with special anchors or pedestals which fracture as the  $\mu$ -stamps make surface contact with the devices, permitting their capture (without affecting device performance). After the 'deterministic transfer' process, the  $\mu$ -stamps could be re-used to print additional devices. In fact, the reported results suggest that the polymeric  $\mu$ -stamps retain their

pick-and-place performance even after  $> 10\,000$  cycles [20, 31, 32]; this was partially confirmed in [26] using the gecko tape, as the authors were able to re-use it several times, although performance decreased due to increasing tearing of the ‘Gecko hair’.

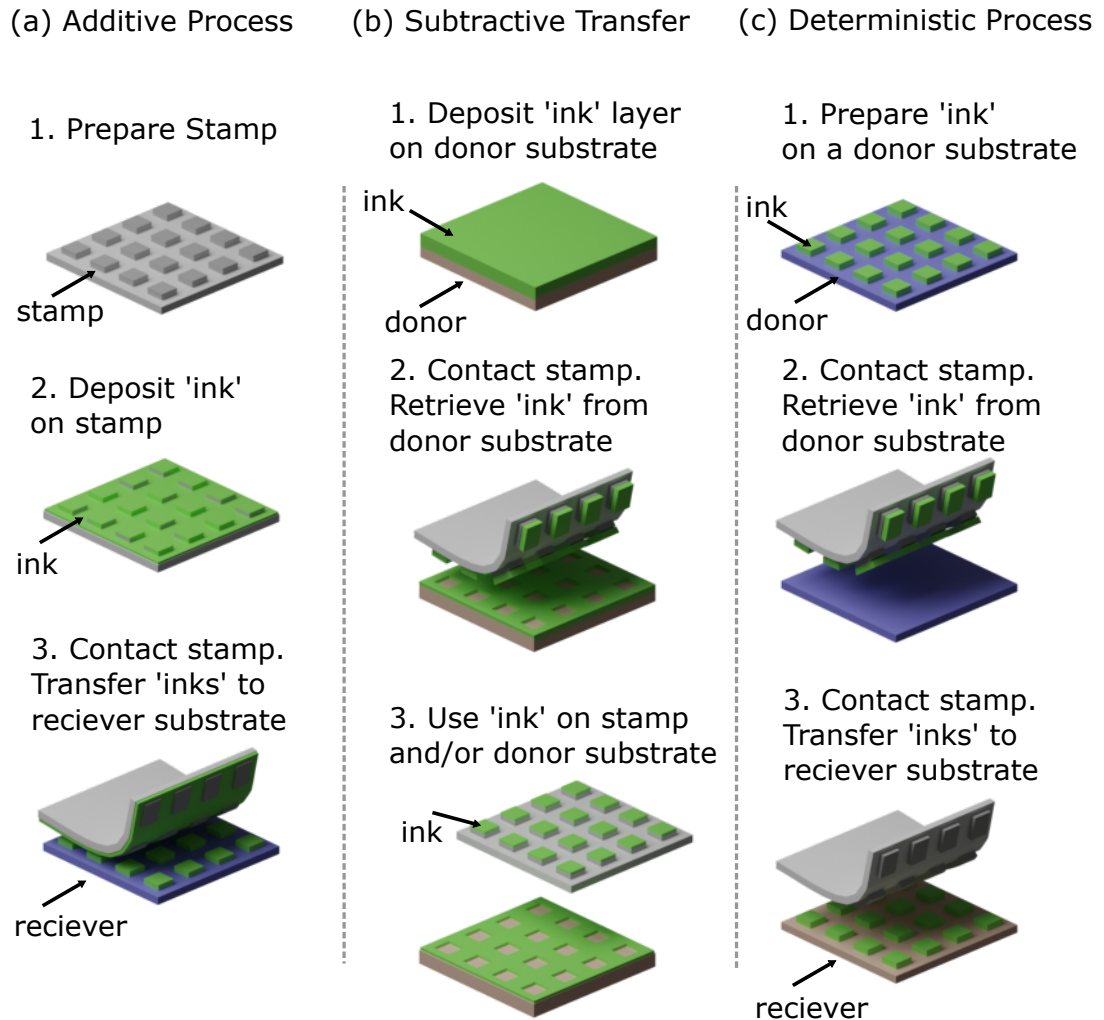


Figure 1.2: Schematic illustrations of three basic modes for transfer-printing:(a) Additive Transfer, (b) Subtractive Transfer, and (c) Deterministic Assembly. Figure adopted from [20].

The mechanisms responsible for adhesion in the TP technique are described by a combination of van der Waals (VdW) forces and capillary interaction [20]. However, for small and nanoscale objects (e.g., semiconductor NWs, QDs, etc.) where no capillary forces are present – the bonding force is purely due to van der Waals forces [33]. VdW

forces are distance dependent interaction between electrically neutral atoms, molecules, and surfaces [34], with surface attraction occurring when these are tens-of-nanometers apart [34]. In 1937, H. C. Hamaker proposed a model for London-VdW interaction between two spherical objects [35]. London-VdW interactions (or London Dispersion force) is an intermolecular force which arises when electrons in two adjacent atoms occupy positions that make the atoms to form temporary dipoles, also described as ‘induced dipole – induced dipole’ interaction [35]. The model proposed in [35] suggested that London-VdW forces generally cause an attraction and estimated it for two cases: sphere-sphere and sphere-flat surface [35]. Moreover, H. C. Hamaker defined a constant (which later became known as Hamaker constant,  $A_{Ham}$ ) describing the strength of the VdW force between two particles in vacuum (see Eq. 1.1):

$$A_{Ham} = \pi^2 \times \lambda_{VdW} \times \rho_1 \times \rho_2 \quad (1.1)$$

Where,  $\lambda_{VdW}$  is London-van der Waals constant that determines the particle-particle pair interactions for two materials and  $\rho_{1,2}$  are number densities (number of atoms per  $\text{cm}^3$ ) of these two materials. The force between the two spherical macromolecules is derived by integrating VdW interaction energy, VdW, as described in [36]:

$$F = -\frac{dW_{VdW}}{dD} \quad (1.2)$$

$$F = -\frac{A_{Ham}}{6D^2} \frac{R_1 R_2}{R_1 + R_2} \quad (1.3)$$

Where,  $D$  is surface separation between the two objects and  $R_1$  and  $R_2$  are radius of these two spheres. Also, due to the distance dependence of VdW interaction Eq. 1.3

should satisfy the condition:  $R_{1,2} \gg D$  [36]. Furthermore, J. N. Israelachvili, in his work [36], derived van der Waals forces for two flat surfaces (per unit area) as:

$$F_{Flat} = -\frac{A_{Ham}}{6\pi D^3} \quad (1.4)$$

It is worth mentioning that negative  $F$  in Eqs. 1.1 - 1.4 implies attraction [36]. From [35, 36], we see that the magnitude of VdW forces is strongly related to the geometry, material, size, and interaction area of the two objects. Therefore, to successfully capture with a polymer stamp a target object ('ink') from its native ('donor') substrate the condition imposed by Eq. 1.4 must be satisfied [36]:

$$\frac{stamp}{G_C^{ink}} > \frac{ink}{G_C^{donor}} \quad (1.5)$$

Where  $G_C$  are interfacial adhesive strengths between the stamp/ink and ink/donor surfaces. From a general form of the steady-state energy release rate [20],  $G = \frac{F}{w}$ , where  $F$  is the force applied to the stamp in the normal direction and  $w$  is the stamp's width. Then, the condition for the release of a target ink, previously captured by a polymeric stamp, onto a receiving surface is described by:

$$\frac{stamp}{G_C^{ink}} < \frac{ink}{G_C^{reciever}} \quad (1.6)$$

From [20], it was shown that the stamp's energy release rate has a strong velocity dependence, hence  $G_C^{stamp/ink}$  can be expressed as  $G_C^{stamp/ink}(v)$ . This relationship is given by [20]:

$$G_C^{stamp/ink}(v) = G_0 \left[ 1 + \left( \frac{v}{v_0} \right)^n \right] \quad (1.7)$$

Where,  $G_0$  is the zero-velocity energy release rate [20],  $v$  is the separation velocity,  $v_0$  is the reference velocity associated with  $G_0$ , and  $n$  is the scaling parameter. From Eq. 1.7 the critical separation velocity can be obtained by rearranging the equation.

$$v_c = v_0 \left[ \frac{\frac{\text{stamp}}{G_C \text{ ink}} - G_0}{G_0} \right]^{\frac{1}{n}} \quad (1.8)$$

This shows that the transfer-printing of target devices with polymeric stamps can be controlled via the release velocity. Fig. 1.3 shows a schematic diagram that marks the transition from a retrieval to printing regime. In simple terms, in order to achieve high-yield device pick-and-place with polymeric stamps during TP, the device release speed must be slower than the pick-up velocity.

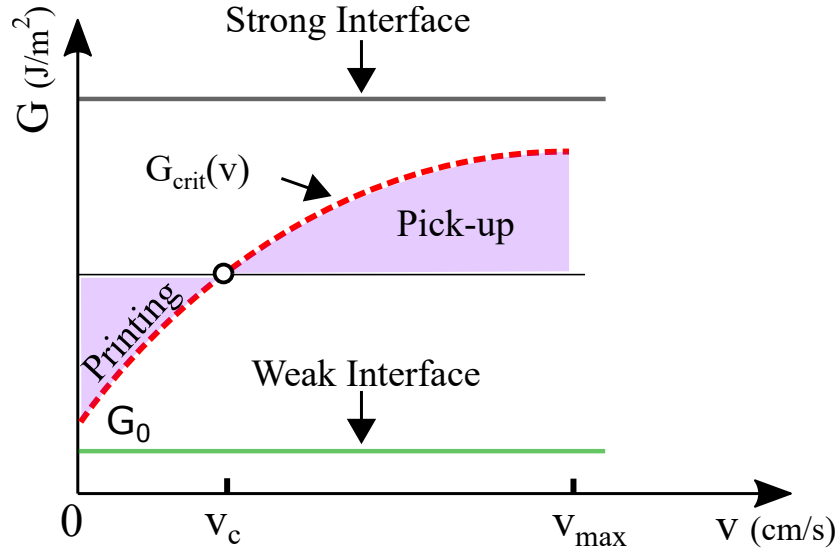


Figure 1.3: “Schematic diagram of critical energy release rates for the stamp/ink and ink/receiver interfaces of a model printing experiment consisting of a stamp, continuous ink film, and receiver substrate” Figure extracted from [20].

In addition to the device capture/release speed control, additional methods of controlling the adhesion force and enhancing the yield of devices for the TP technique have been proposed. These include: laser-assisted integration [37], use of active chemicals

for temporal VdW force increase [38], as well as utilizing different processes to peel the  $\mu$ -stamp during ink release. Moreover, an alternative adhesion force control has been proposed which relies on controlling during the curing process of the stamps the chemical concentration of the PDMS used to fabricate them (see Chapter 2 for a detailed description). This method allows to tailor the elastomeric properties of the stamp material (PDMS); hence permitting the control of the bonding force between ink and a stamp. It is worth mentioning that often this PDMS curing process relies on trial-and-error approach. By fabricating different PDMS stamps with different concentrations, it is possible to generate statistical measurements of device pick-up and release yields. It then becomes possible to determine which specific PDMS composition improves the performance of polymeric  $\mu$ -stamps during the transfer printing of different types of semiconductor NWs or any other type of devices. Furthermore, the full description of the TP technique including the tools, protocols, process for the fabrication of stamps, historical perspective and systems/structures which fabrication has been enabled by TP since its inception are provided in Chapter 2.

### 1.3 Semiconductor Nanowire (NW) Lasers

Semiconductor NWs are small wire structures with diameters in the order of 100s of nm (or smaller) and lengths ranging from 1 to 10s of  $\mu\text{m}$  [39]. NWs have revolutionized the field of (nano-)photonics by enabling the development of novel ultra-small devices impacting a wide range of scientific disciplines, expanding from on-chip communications, quantum-computing, sensing and healthcare [40–42]. Importantly, due to their inherent structure and properties, semiconductor NW devices can exhibit lasing emission [43]. The first semiconductor NW lasers were reported in the early 2000s, see [41]

for review. Since then, in the past two decades, research involving semiconductor NW lasers has gained increasing attention due to its unique properties, versatility, variety and highly reduced footprint of these nanolaser sources [41]. Furthermore, advances in the fabrication of semiconductor NWs has permitted to fabricate novel heterogeneous nanolaser structures with high degree of synthetic control [41]. This section will start providing a brief historical overview of the research developments that led to the demonstration of lasing emission in semiconductor NWs. Then, the growth techniques that have enabled the fabrication of semiconductor NW lasers are discussed along with their capabilities and limitations. It is worth mentioning here, that the devices used in this thesis work, fabricated by our collaborators at Prof. C. Jagadish's group at the Australian National University, are discussed in Chapter 2 in greater detail. Therefore, this section will introduce the background of NW lasers along with the principles of lasing emission, whilst the relevant information about the specific NW laser devices used in this work will be covered in subsequent sections of this thesis.

### **1.3.1 Historical Perspective**

Nanowires are quasi-1D nanostructures with diameters ranging between few and hundreds of nanometers and lengths from hundreds of nanometers to few centimetres [41, 44]. The ability to tailor their morphology makes NW devices interesting to a large variety of applications and fields, including electronics, photovoltaics, nanolasers etc. [45]. The structures which are considered the predecessors of NWs and undoubtedly have paved the way towards their realization are usually referred as whiskers (or nano-whiskers, or nanowires) [41, 46]. Whiskers (nanowires) are crystalline fibre structures with diameters ranging from 100s to 10s of nm (similar to the dimension of NWs). These devices were firstly reported by R. S. Wagner and W. C. Ellis in 1964 at Bell Lab-

oratories [46] using a crystallographic growth concept called vapour-liquid-solid (VLS). In their work [46], Wagner and Ellis presented Silicon (*Si*) whiskers (nanowires) of 1000 Å (100 nm) in diameter and 0.2 mm in length grown on a *Si* substrate. The growth process on which the whisker (wire) growth is based, could be divided into several important stages: (1) The *Au* particle is placed on a {111} *Si* surface and heated to  $\sim 1223$  K (950 C°) forming an *Au-Si* alloy (*Au-Si* eutectic bonding, see [47] for further reading). (2) A precursor mixture of *SiCl<sub>4</sub>* and hydrogen is added for the whisker (nanowire) growth, as referred in [46]: “The liquid alloy acts as a preferred sink for arriving *Si* atoms or, perhaps more likely, as a catalyst for the chemical process involved.” (3) “The *Si* enters the liquid and freezes out, with a very small concentration of *Au* in solid solution, at the interface between solid *Si* and the liquid alloy.” [46]. “The gold-catalyst droplets rise elevator-like from the substrate, riding upon the tips of the growing wires.” [48] resulting in growth of the *Si* crystal (in the  $\langle 111 \rangle$  direction) until the *Au* particle is consumed, or until the growth conditions change.

In the mid-1970s, E. L. Givargizov at the U.S.S.R Academy of Sciences and K. Hiruma at Hitachi’s Central Research Lab reported respectively, methods for the fabrication of whiskers (nanowires) built from compound semiconductors (*InAs* and *GaAs*) [49]. This enabled to investigate novel possibilities of fabricating whiskers (or nanowires) using wider material platforms. However, it was not until decades later, specifically in 2001, when P. Yang and his group at the University of California, Berkeley demonstrated lasing emission in a semiconductor NW [7]. Although, it is worth mentioning that also during that time, works by C. M. Lieber and L. Samuelson were focused on demonstrating photoluminescence in semiconductor NWs [50–52]; P. Yang’s group managed to achieve room temperature UV emission in optically-pumped self-organized

$\langle 0001 \rangle$  oriented  $ZnO$  NWs grown on a sapphire substrate [7].

### 1.3.2 Growth Techniques for the Fabrication of NW Lasers

Growth mechanisms are central for the NW laser fabrication. These shape both their morphological and topological parts, affecting not only their light emission properties, but also their aspect ratio. Importantly, the latter is a critical element to achieve successful TP processes permitting their integration with heterogeneous substrates and systems. There are various methods that enable the fabrication of NW devices, see for example [53] for a review on different techniques. Here, we focus the scope on ‘Bottom-Up’ and ‘Top-Down’ NW fabrication techniques, since these two are directly related to the results presented in this thesis. These two techniques have their own advantages and limitations; and it could also be said that each of these two groups has their own different set of growth methods, based on nuances associated with available materials, tools, machines also importantly applications. Hence, here we focus on the general introduction of both the ‘Bottom-Up’ and ‘Top-Down’ NW fabrication techniques to provide context to the two main growth methods of the NW devices that were used in this PhD project. In general, in the ‘Bottom-Up’ growth technique the NW devices are chemically synthesised by systematically assembling molecules piece-by-piece from the substrate’s surface upwards. This is therefore an additive process that enables a precise control over the fabricated structures [53]; hence offering to produce highly ordered arrays of NW devices. The ‘Bottom-Up’ NW growth technique is depicted in Fig. 1.4(a): small ‘seed’ particles are positioned in the substrate before the NW growth process is started. These ‘seed’ particles have the mission to induce the NW growth at their specific locations. This part of the process is similar to that described for the VLS technique [46]. After the deposition of the ‘seed’ particles, a vapour material

is introduced to start the formation of crystalline structures [46]. As a result of this process, NW devices start to grow upwards (from the substrate’s surface) continuously and controllably. Moreover, the NWs’ shape and orientation can be precisely controlled during growth. Furthermore, the ability to implement several phases during the growth process offers the possibility to fabricate complex multi-layer structures within the NWs [46]. This technique is widely used from NW device growth due to its flexibility and potential for realizing novel designs with nanoscale control.

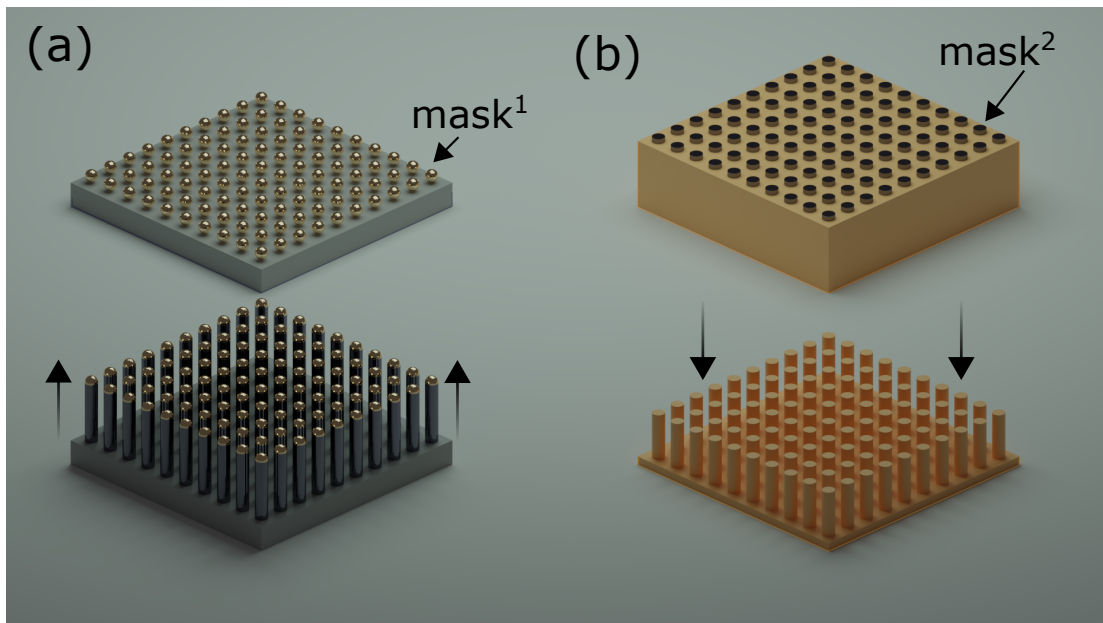


Figure 1.4: Comparison of (a) ‘Bottom-Up’ and (b) ‘Top-Down’ fabrication processes. Mask<sup>1</sup> refers to template particles, Mask<sup>2</sup> is a photoresist mask.

For instance, the Indium Phosphide ( $InP$ ) NWs used in this work, were fabricated using the ‘Bottom-Up’ growth technique, by a process referred as selective-area metal-organic-vapor-phase epitaxy (SA-MOVPE) [54]. This method [54] allowed to grow wurtzite (WZ)  $InP$  NWs with high-quantum efficiency and room-temperature lasing emission. However, a limitation of the ‘Bottom-Up’ technique is the inhomogeneous variations in NW height across a whole sample, which affects the possibility to produce highly ordered NW structures formed by identical devices. As a result of these

inhomogeneous variations in height, the NW devices grown by this method exhibit slight differences in their dimensions, thereby affecting their specific lasing characteristics (e.g. differences in emission wavelength or lasing thresholds between NWs) [54,55]. Nevertheless, importantly in Chapter 5 we describe a novel deterministic technique that permits the selection and binning of NW lasers from a single growth sample with required lasing parameters using pre-screening methods and transfer printing techniques in combination [56]. This novel technique that will be presented in this thesis (see Chapter 5) partially solves difficulties related to device variation within a single growth batch [57].

In contrast, the ‘Top-Down’ growth technique is a subtractive fabrication method based on chemical etching for the development of NW devices. This ‘Top-Down’ NW fabrication technique is typically related to lithography methods. In this technique a layer of semiconductor material (e.g. *InP*, *GaN*, etc.) with user-defined and precise thickness is firstly grown on a substrate. After this initial growth, positive or negative masks (with desired spatial patterns) are used in combination with etching processes to fabricate the individual NW devices from the initial layer of semiconductor material [58]. The etching processes typically offer good vertical control of the fabricated NW devices and may permit the fabrication of structured arrays of devices (defined by the masks design); however, this top-down NW fabrication technique can also cause surface defects and might have reduced resolution [53], as a result of the wavelength used for light-induced lithography. Or, in the case of electron-beam lithography it might require an excessive amount of time for fabrication. It is worth mentioning that in Chapter 2 a similar method was used for the fabrication of the polymer  $\mu$ -stamps that will be used during this Thesis for the heterogeneous integration of NW devices. Hence, this

specific method will be discussed in Chapter 2 in greater detail.

### 1.3.3 Lasing Emission in Semiconductor NWs

#### Carrier Generation and Recombination in Semiconductors

Recombination mechanisms in direct bandgap semiconductors can be divided into two groups: radiative and non-radiative. Radiative recombination occurs when an electron in the conduction band (CB) recombines with a hole in the valence band (VB) resulting in the excess energy emitted in the form of a photon [45]. These radiative transitions processes are: (i) spontaneous and (ii) stimulated emission, shown respectively in Figs. 1.5(a) and 1.5(c). As seen in Fig. 1.5(a), the spontaneous emission process occurs when an atom in an upper level spontaneously decays to the lower energy level as a result emitting a photon with random direction and phase. The energy of the photon is equal to,  $h\nu = E_2 - E_1$ , where  $\nu$  is the photon frequency,  $h$  is Planck's constant and  $E_1$  and  $E_2$  are the energies of the ground and excited states, respectively. The Einstein coefficient  $A_{21}$  describes the rate of spontaneous emission for the transition from  $E_2$  to  $E_1$  and is given by:

$$-\frac{dN_2(t)}{dt} = A_{21}N_2(t) = \frac{dN_2(t)}{\tau_{21}} \quad (1.9)$$

where,  $\tau_{21}$  is the radiative lifetime and  $N_2$  is the number density of atoms in the  $E_2$  state.

Stimulated emission is a process where a photon is emitted with the same energy and momentum as an incident photon [59]. In thermal equilibrium, a direct bandgap semiconductor has few electrons in the CB and few holes in the VB. As shown in Fig. 1.5(b), when a photon of energy ( $h\nu$ ) passes through a semiconductor, the photon

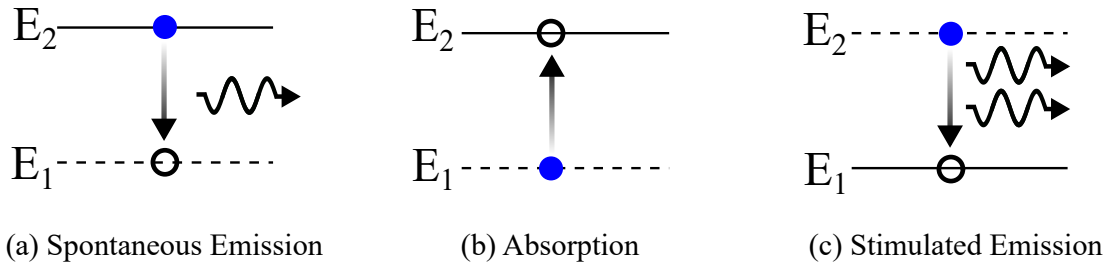


Figure 1.5: Spontaneous emission, Absorption and Stimulated emission processes under photon stimulation, adapted from [59].

has a high probability of being absorbed. As depicted in Fig. 1.5(b), absorption is a process in which an atom absorbs an incoming photon (of energy,  $h\nu$ ) and as a result an electron makes a transition from a lower to a higher energy state. The incoming photon transfers its energy to an electron in the VB, thus moving the electron to the CB. In this situation, a new incoming photon can stimulate the emission of a second identical photon associated with the transition of an electron from the CB back to the VB. As mentioned above, in thermal equilibrium the number of electrons in the CB is relatively small [59], hence the probability of stimulated emission is much lower than that of absorption. However, external excitation can significantly increase the number of electrons in the CB, resulting in the probability of stimulated photon emission becoming higher than that of absorption [59]. This process leads to population inversion and is essential for lasing emission. Therefore, population inversion is a state in a laser system in which a higher energy level is much more populated than the lower level; thus, this cannot occur under conditions of thermal equilibrium [60]. To achieve realistic thermal non-equilibrium state, 3- and 4-level laser systems must be used. For further reading see ref. [60]. It is worth mentioning here, that classically there are two excitation methods used in semiconductor lasers – optical and electrical excitation. In optical excitation, light from an external light source is injected into the gain medium of a target laser to achieve stimulated emission. In electrical excitation, an electrical

current is applied to induce population inversion. For the case of the NW devices utilised in this work, optical excitation was used, as it will be described in subsequent chapters of this thesis. Eq. 1.10 describes the rate at which the stimulated emission process occurs:

$$\frac{dN_2(t)}{dt} = B_{21}N_2(t)S(v) \quad (1.10)$$

where,  $B_{21}$  is Einstein's coefficient for stimulated emission and  $S$  is the spectral density of electromagnetic energy. The non-radiative recombination of an electron-hole pair is defined by the absence of an emitted photon [61]. Fig. 1.6 shows two types of non-radiative processes, namely Shockley-Read-Hall Recombination and Auger Recombination. Shockley-Read-Hall Recombination (also known as Trap-Assisted Recombination) is a process which occurs in defects of the crystal lattice of semiconductors. As it has already been described, the 'Bottom-Up' process often involves a catalyst particle (*Au* particle for example) that induces 1D grow of semiconductor crystals. However, during growth the particle defuses into the structure producing local defects, triggering non-radiative carrier recombination processes in NW devices [61]. As shown in Fig. 1.6(a), Trap-Assisted Recombination creates a new energy state ( $E_t$ ) that affects the local absorption and emission properties of the material. Importantly, the energy is exchanged in the form of lattice vibrations, resulting in an emitted phonon [61]. Auger Recombination has higher probability to occur in non-equilibrium conditions, when carrier density is high [61]. As shown in Fig. 1.6(b) Auger Recombination is a three-carrier process. During the recombination of an electron-hole pair the energy is absorbed by a third carrier, instead of producing a photon [61]. The third carrier then loses energy to thermal vibrations. Typically, this effect is taken into consideration when designing

laser cavities, as it can significantly worsen laser performance [61].

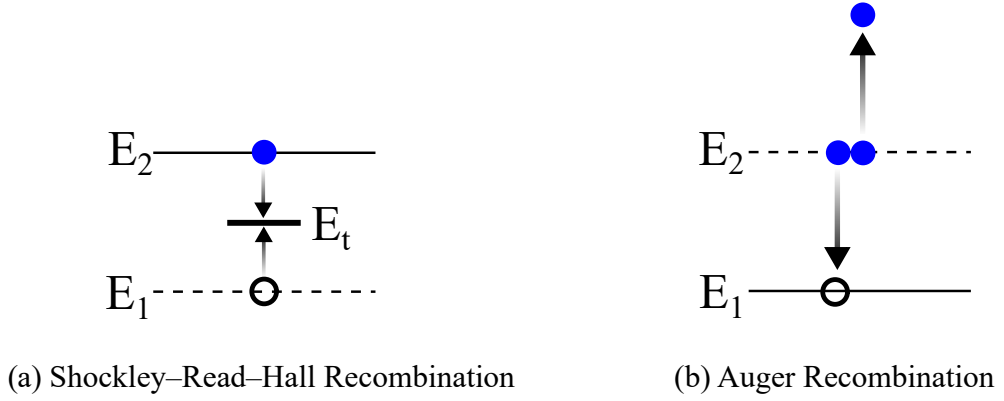


Figure 1.6: Non-Recombination Processes, diagram adapted from [61].

As shown in Fig. 1.7, semiconductors can have two different types of bandgap, referred as direct and indirect bandgap. The bandgap represents the minimal energy difference between the minimal-energy state in the CB and the maximal-energy in the VB. In the case of direct bandgap materials (see Fig. 1.7(a)), the CB and the VB occur at the same value of quasimomentum. Thus, the emission or absorption of a photon occurs without change of  $\kappa$ -vector. As shown in Fig. 1.7(b), for indirect bandgap materials, a photon cannot make a direct transition into the CB minimum and thus must change its wave vector ( $\kappa$ -vector) to absorb or emit photons. Hence, the direct bandgap semiconductors (e.g. *InP*, *ZnO*, *GaAs*) are good candidates for emitting photons. Thus, the reason for the wide development of NW lasers in III-V and II-VI semiconductors.

### 1.3.4 Fabry-Perot (FP) Cavities

This section describes the concept and principle behind Fabry-Perot (FP) cavities and their relevance for the development of laser sources. In fact, NW devices given their specific dimensions and inherent structure, form micron-scale FP cavities along their longitudinal axes [62], hence similar concepts that describe their mode formation, gain-

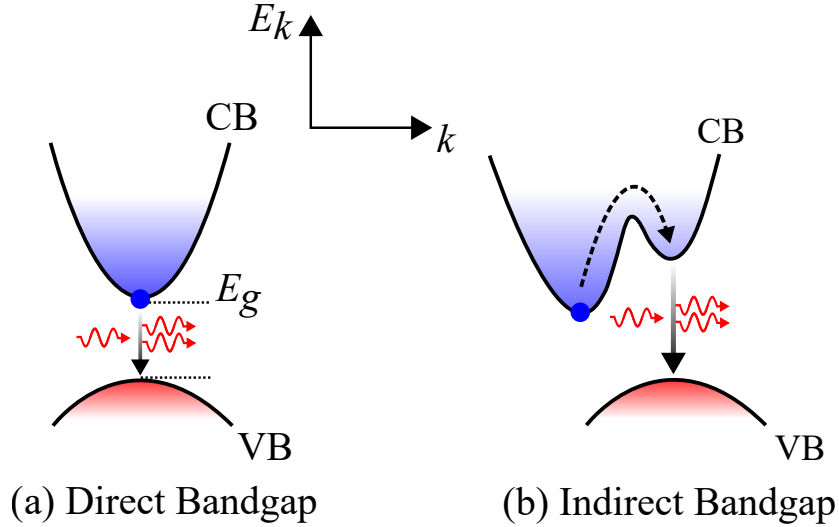


Figure 1.7: E-k diagrams showing the interband transition in (a) Direct Bandgap and (b) Indirect Bandgap semiconductors, adapted from [61].

and-loss parameters and lasing threshold can be used. In their simplest form, FP lasers are the earliest developed general-purpose laser diodes [62]. As shown in Figs. 1.8(a) and 1.9(a), a FP cavity consists of an active layer (typically a semiconductor crystal) that is placed between two highly reflective mirrors forming a resonant cavity. Mirrors provide the required reflectivity feeding back a portion of the emitted photons back to the active medium to stimulate the emission of more photons; hence yielding the amplification process required for lasing emission [62]. Obviously, to construct a FP laser, the reflectivity of the mirrors has to be high enough (but below 100%) to allow part of the emitted light to escape the cavity through the mirrors. The reflectance of the mirrors can be either equal or one of the mirrors can be purposely designed with lower reflectivity to favour higher light emission from one of the sides of the device. Fig. 1.8(b) depicts schematically the structure of a NW laser which can on its own create a FP lasing cavity. Here, the NW end-facets act as partially-reflecting mirrors thanks to the contrast in the refractive indices at the NW-air interface found at the NW's end-facets. For example for an *InP* NW device, the refractive index of InP is  $\sim 3.4$  whilst

the refractive index of air is 1, so from the Fresnel reflection calculation, the reflectivity is  $\sim 0.3$ . The NW is placed on a low refractive index surface (typically  $\sim 1.5$ ) to enable high mode confinement [63]. During excitation (by means of optical pumping) energy is provided to the system to trigger stimulated emission of photons and population inversion. In this situation, the NW's facets act as mirrors as indicated, reflecting light back into the cavity (formed by the semiconductor NW itself) hence permitting the achievement of lasing emission from these nanoscale devices.

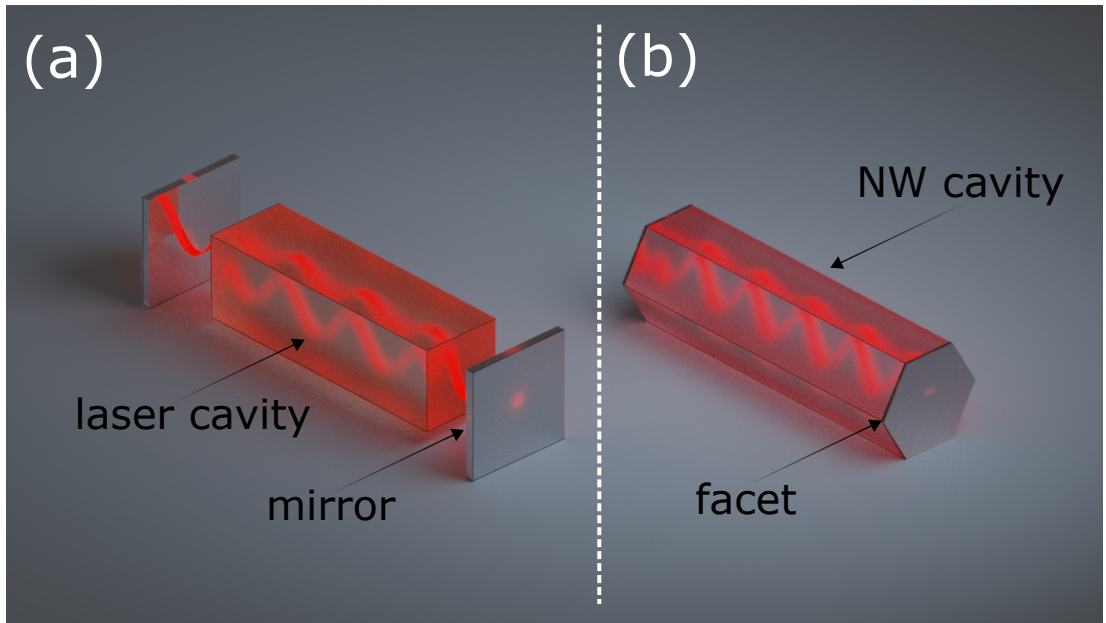


Figure 1.8: Diagrams depicting (a) FP cavity and (b) NW laser cavity.

From FP theory [64], the captured optical waves (inside the cavity) travel back and forth along the length of the laser in the presence of mirrors (forming the cavity). As an optical wave travels along the cavity, it gets scattered and amplified [64]. For lasing operation, the gain (of the laser) must overcome the losses in the cavity. It must therefore satisfy the following condition:  $g_m - a_m > 0$ , where  $g_m$  is the optical gain per unit length and  $a_m$  is the loss per unit length. Both loss and gain in the cavity will vary with wavelength [64]. The condition of an oscillating cavity is described by:

$$r_1 r_2 e^{ikL_c} E_0 = E \quad (1.11)$$

where,  $r_1$  and  $r_2$  are complex end-facet reflectivities (classically,  $r_1 \neq r_2$ ),  $L_c$  is the cavity length,  $\kappa$  is the wave vector and  $E_0$  the incident EM field [64]. The cavity length ( $L_c$ ) is equal to  $\lambda/2q$ ; where,  $\lambda$  is the wavelength and  $q$  is an integer, also known as the mode order [64]. As depicted in the top panel of Fig 1.9(b), FP lasers can produce an infinite number of standing waves. However, the active medium, depending on the specific material it is built from, will only be able to provide gain for a specific range of wavelengths, as shown in the middle plot in Fig 1.9(b). Hence, only some of the resonant wavelengths are supported, as shown in the bottom plot in Fig. 1.9(b). As stated, lasing emission will only occur when the gains exceed all losses in the cavity. The mirror losses are defined as:

$$\alpha_M = \frac{1}{L_C} \frac{1}{\ln(\sqrt{R_1 R_2})} \quad (1.12)$$

However, these are not the only losses present. To account for the total losses, intrinsic losses should be also considered. To satisfy the threshold condition, the round-trip gain must be equal to losses [64]:

$$\Gamma g_{th} = \alpha_i + \alpha_M \quad (1.13)$$

where,  $\Gamma$  is the confinement factor,  $g_{th}$  is the threshold gain,  $\alpha_i$  – internal modal absorption loss,  $\alpha_M$  are mirror losses [64]. The confinement factor is described as the ratio between the power of the optical mode within the gain region and the total power [64]:

$$\Gamma = \frac{\int_0^d E^2 dz}{\int_{-x}^x E^2 dz} \quad (1.14)$$

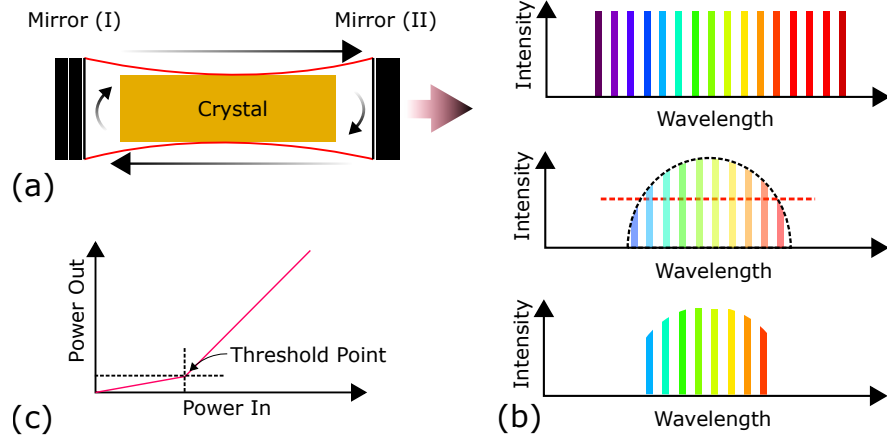


Figure 1.9: (a) FP laser with Mirror (I) being the high-reflectance mirror and Mirror (II) the low-reflectance mirror. (b) Images showing the gain and loss concepts in lasers, where the top figure represents the FP modes with a mode separation of  $c/2nL$ ; the middle figure shows the gain curve (black dashed curve) and loss level (red dashed line) and the bottom figure shows the modes that are supported for lasing emission. (c) L(in)-L(out) curve of a laser.

A longitudinal mode is a standing wave pattern formed by waves confined in the cavity. As defined in [65], “the longitudinal modes correspond to the wavelengths of the wave which are reinforced by constructive interference after many reflections from the cavity’s reflecting surfaces”. Therefore, all other wavelengths are suppressed by destructive interference [64]. The length of a cavity is described by Eq. 1.15 and the wavelength separation is described by Eq. 1.16:

$$L = \frac{\lambda}{2} q \quad (1.15)$$

$$\Delta v = \frac{c}{2nL} \quad (1.16)$$

Where  $L$  is the cavity length,  $\lambda$  is the emission wavelength and  $q$  is an integer,  $\delta v$  is the wavelength separation between two adjacent longitudinal modes,  $n$  is the refractive index of the material and  $c$  the speed of light.

Depending on their specific dimensions, optical cavities can also support transverse modes. A transverse mode is an electromagnetic field pattern of radiation in the plane perpendicular to the propagation of the radiation. The modes in a cavity depend on the parameters of the electromagnetic field – frequency, polarization as well as the cavity dimensions, surface quality and the refractive indices [45]. The low order cylindrical waveguide modes are derived analytically using Maxwell’s equations [66]. Various types of transverse modes exist – transverse electromagnetic (TEM), transverse electric (TE), transverse magnetic (TM) and hybrid modes (HE, EH), see [45] for description. These types of modes differ in the direction of magnetic and electric components in the direction of propagation. Importantly, in spite of their reduced dimensions semiconductor NWs can support light emission in multiple-transverse modes [45]. In particular, the multiplicity of supported lasing modes for the semiconductor NW lasers used in this work have been numerically calculated and also experimentally described in [45]. In Chapter 5 of this thesis we present novel numerical work on the properties of the transverse modes supported by *InP* NW lasers for the case of pairs of evanescently coupled *InP* NW lasers suggesting the used of this novel structures for very high speed ( $> 100$  GHz functionalities).

Finally, there has been significant progress made in the development and fabrication of semiconductor nanowire devices during the past two decades. A growing number of research groups focus on creating high-quality semiconductor NWs by manipulating the growth conditions [67, 68], optimizing the lasing performance of semiconductor

NW lasers [69–71], creating novel photonic systems where NWs are used as building blocks [23, 56, 72–74], realizing embedded complex structures within NWs’ cavities (e.g. disks, quantum-wells, quantum-dots) [75, 76], utilizing novel material groups [77], to name but a few. It is safe to say that the research related to NW devices is becoming increasingly attractive due to the unique properties that these quasi-1D devices offer at the nanoscale.

## 1.4 Thesis Outline

Chapter 1 introduced the motivation for this work and the background on transfer-printing techniques and NW lasers are presented. Chapter 1 also explained why techniques for NW integration techniques are crucial for developing novel ultra-small footprint nano-photonic systems and the challenges these hold. In subsequent Chapters of this Thesis, I will introduce in detail the transfer-printing technique used in this work. Yet, since most of the work for this thesis was carried out using semiconductor NW laser devices, Chapter 1 also included the operation of Semiconductor Lasers and the lasing principles in nano-size cavities. Finally, Chapter 1 provides a historical review of NW devices, explaining the development process that led to the achievement of stimulated light emission in NW lasers, firstly demonstrated in *ZnO* nano-sized wires. At last, Chapter 1 introduced the principles of lasing emission in NW devices, explaining what are the essential parts that should be considered when developing these devices.

In Chapter 2, the deterministic transfer-printing technique for the controllable and accurate pick-and-place of NW devices and their arrangement on target, non-native surfaces is presented. This chapter also discusses the tools, setups and techniques enabling the NW transfer-printing protocols. Moreover, we show how the  $\mu$ -stamps

(that will be used for the NW pick-and-place processes) are fabricated, we discuss their specific and bespoke designs and their importance for the NW TP technique developed throughout this work. In Chapter 2, we also compare the TP technique for the integration of NW devices with alternative methods, and explain in detail the specific advantages our technique gives as well as its drawbacks. The final section of Chapter 2 describes the alignment technique we developed allowing for the highly accurate positioning of NWs. Further, we demonstrate the systematic integration of NW devices achieving positioning accuracies below  $1 \mu\text{m}$ .

In Chapter 3, the methods and tools for the experimental characterization of NW lasers are discussed. These include a  $\mu$ -photoluminescence ( $\mu$ -PL) setup, spectrometers, scanning electron microscopes (SEM) as well as the other tools and techniques that were extensively used throughout the PhD project for the experimental analysis of NW laser systems.

Chapter 4 reports the multiple nano-photonic integrated systems with embedded semiconductor NW devices that were developed during this project. This chapter begins with the demonstration of on-chip NW laser-waveguide coupled systems fabricated by means of TP techniques, showing successful coupling between the NW lasers emission and waveguides. The different types of waveguide designs investigated, along with two different NW-waveguide coupling methods, namely: atop and head-to-tail integration, presented in Chapter 4. Next, we report a technique which enables the fabrication of NW-nanoantennas coupled systems for vertical NW laser systems. Finally, we describe our results on the integration of semiconductor NWs in a 3D network architecture in the form of a double-cross (nano-hashtag) design. This process describes a key-enabling technique for producing a novel type of THz radiation detectors, permitting

the simultaneous recording of two polarization channels; thus allowing to retrieve the full polarization information of incoming THz signals.

Chapter 5 reports our studies on complex hybrid systems with NW lasers. In this chapter we present at first a numerical model permitting to simulate the operation of evanescently-coupled pairs of semiconductor NW lasers. Using this model we report for the first time the achievement of very high frequency oscillations (exceeding 100 GHz) in couple pairs of InP NW lasers. Chapter 5 also reports a novel experimental method for the selection, binning and integration of NW lasers with specific desired configurations and performance. The last section of Chapter 4 provides our results on the integration of semiconductor NW lasers forming compact structures with controllable edge-to-edge separations between devices ranging from below 1  $\mu\text{m}$ . We used that technique to demonstrate dual-colour lasing emission from heterogeneous NW laser systems with extremely reduced footprint and permitting their optical excitation with a single (micrometric) beam spot from a pump laser.

Finally, Chapter 6 reports on our preliminary work on the transfer-printing of inorganic perovskite quantum-dots (QDs) for their integration into non-native polymer (PDMS) and diamond substrates. This is followed by the introduction of a novel technique for the simultaneous printing of multiple NW devices over a large-area in receiving substrates, with which this Thesis concludes.

## Chapter 2

# Transfer-Printing of Semiconductor Nanowires

In this chapter, the technique developed for the nanoscale transfer-printing (TP) of semiconductor nanowires (NWs) is presented. This technique enables the heterogeneous integration of semiconductor NWs with high positioning accuracy into a wide variety of substrates and surfaces. This opens new routes for the use of semiconductor NWs as building blocks for the fabrication of future nano-phonic systems. This chapter begins introducing the concepts and motivation behind the technique used for the deterministic assembly of NW devices. We present the specific features of our technique in comparison to alternative methods for NW transfer or assembly. Furthermore, this chapter describes the concept of reversible adhesion behind the described technique and reviews previous work on TP of larger micro-metric photonic devices onto planar and flexible substrates. Additionally, we outline the fabrication techniques used to develop the different designs of polymeric  $\mu$ -stamps enabling the TP of semiconductor NWs. These include the development of the moulds to fabricate the  $\mu$ -stamps and

the process followed to cast the viscoelastic polymer (polydimethylsiloxane, PDMS) used to fabricate the  $\mu$ -stamps and for  $\mu$ -stamp testing. Finally, this chapter describes the modified dip-pen nano-lithography setup used for the controlled assembly of NW devices by means of TP processes at the nanoscale.

In the second part of Chapter 2, we present the experimental results achieved with the TP technique for the controllable capture-and-release of semiconductor NW lasers for the fabrication of bespoke nanophotonic systems with these devices. These results were obtained using Indium Phosphide (InP) NWs of different dimensions showing all room-temperature lasing emission. The NWs were selectively removed from their growth substrates and placed onto multiple types of non-native surfaces, either as individual devices or forming NW bundles, using our developed TP technique at the nanoscale. After integration, the transfer-printed NW lasers were optically excited to verify that their room-temperature lasing emission was retained. We also report the integration of semiconductor NW lasers onto patterned structures and passive photonic circuitry. Furthermore, we present the ad-hoc alignment technique developed during this work and which enables the lateral integration of NW arrays with a controlled (sub- $\mu\text{m}$ ) separation between target devices. This alignment technique was used to demonstrate the fabrication of semiconductor NW arrays into non-native surfaces with both fine (1 - 3  $\mu\text{m}$ ) and coarse (10 - 40  $\mu\text{m}$ ) separations between individual elements.

## 2.1 Concept and Motivation

The aim of this work is to develop a  $\mu$ -TP system with extended-capabilities permitting the controllable integration of selected semiconductor NWs with highly-precise (sub- $\mu\text{m}$ ) accuracy. Such TP system will hence serve as an enabling tool for the as-

sembly of NW devices (as building blocks) into tailored (nano-)photonic systems and circuitry. As discussed in Chapter 1, the TP technique allows seamless integration of optoelectronic devices onto non-native surfaces. The flexibility of this technique also offers the possibility to pre-select devices prior to their integration or to combine multiple different structures in a single system. During the last two decades, since the concept of TP was initially described numerous advances have been reported for this technique including the method for parallel integration of devices, high-yield printing, multi-stacking (3D-integration), to name a few [20].

Moreover, TP was a technique designed to allow the fabrication of novel photonic devices and structures beyond their growth limits [20]. For instance, early works have reported experimentally on the integration of 2D structures, micro-platelets and disks, as well as on large scale integration of nanorods [20]. Furthermore, the technique became widely used for high yield integration of  $\mu$ -LEDs onto non-native substrates [78]. The micrometric printing precision and parallel integration of hundreds of devices in a single step enabled by TP processes was soon established as a commonly accepted approach for the assembly of photonic devices [79]. Importantly, the TP technique is solution-free and does not require any processing of the target substrate or the devices themselves.

In the case of the heterogeneous integration of NW devices by means of TP, published reports have mostly focused on demonstrating stamping of large-scale NW arrays [20]. Moreover, when applied to NW devices the reported TP processes were similar to the so-called contact-printing method [80], where a NW growth sample is directly dragged against a target surface to achieve controlled release of large number of devices. Importantly, no specific reports demonstrated the use of TP processes for

the controllable integration of individually-selected NW devices into target locations in non-native substrates. For the case of integration of single NW devices, alternative techniques have been reported including the use of micro-probes [81], optical tweezers [82], or fluid-assisted techniques [83,84]. However, those methods typically relied on a NW scatter onto the target area before a fine alignment process. Therefore, these approaches offered a poor control over the characteristics of the integrated NW devices, reduced positioning accuracy and did not allow pre-selecting those prior integration. In our work, we have developed a TP technique at the nanoscale permitting the controllable integration of individually-selected NWs onto diverse surfaces and pre-patterned substrates without damaging the devices or affecting their optical properties whilst allowing high positioning and orientation accuracy. Our technique therefore enables the fabrication of novel nanophotonic systems with NWs at their core (including devices with room-temperature lasing emission). Importantly, the flexibility of our reported technique permits the integration of NW devices atop other structures, therefore opening perspectives for the integration of nano-light emitting structures into 3D photonic systems. During our work, we have particularly focused on the accurate heterogeneous integration of semiconductor NW lasers. These devices offer a revolution in photonics research enabling a wide range of novel nanolaser systems with reduced footprint [16,19,42,85,86] with great prospects to yield crucial impact across scientific disciplines, e.g. on-chip communications [72], security [87], spectroscopy [74,88], etc.

## 2.2 Methods

In this section we demonstrate the methods and the setups developed to successfully achieve controlled transfer-printing of semiconductor NW lasers. Additionally, the

modified dip-pen nanolithography system at the heart of the developed TP technique is described in detail. Moreover, we describe the processes followed to fabricate and test the  $\mu$ -stamps used to capture and release the NW devices for their deterministic integration into target surfaces.

### 2.2.1 Modified Dip-Pen Nanolithography

The TP technique developed during this PhD project is based on a modified dip-pen nanolithography (DPN) system. DPN is a patterning technique developed to transfer collections of molecules in a positive printing mode [89]. Molecules are transferred with atomic force microscope (AFM) tips via capillary transporting [90], as depicted in Fig. 2.1(a). It is worth mentioning here, that AFM systems are typically equipped with high-resolution translational stages permitting them to perform nanoscale measurement and operations. In [90], it was concluded that the deposition rate of molecules is strongly associated with the surrounding environment (e.g. temperature, humidity), writing speed and the chemical nature of the molecules. Thereby, DPN systems are typically implemented with humidity control and piezoelectric translational stages offering high accuracy steps. Fig. 2.1(b) shows a set of fabricated patterns using the DPN technique on a gold substrate. These show arrays, clusters, and grids ranging from nano to micro-scales in size. And were fabricated to demonstrate the capabilities and transfer resolution of the technique.

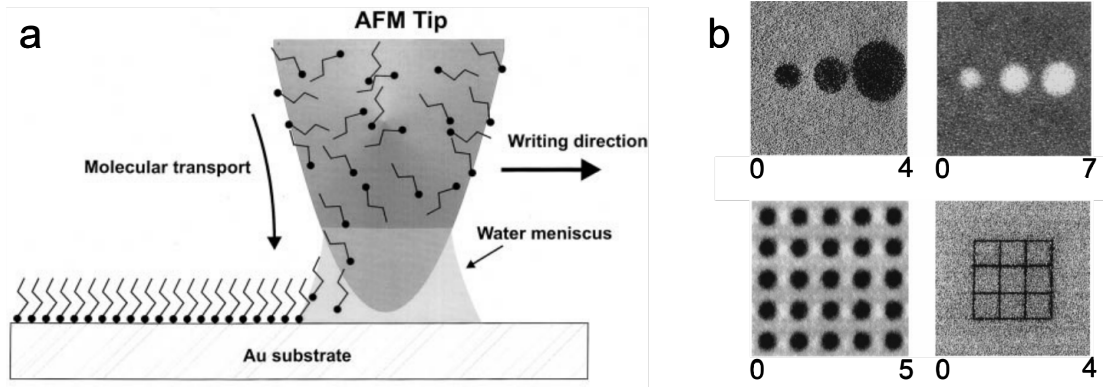


Figure 2.1: (a) Schematic diagram of the DPN technique depicting how water meniscus are formed between the AFM probe, coated with 1-octadecanethiol molecules, and the gold substrate. (b) Micrographs of the fabricated patterns with the DPN system at various transportation and contact rates. The numbers in the figures indicate distance in  $\mu\text{m}$ . Images were taken from [89].

The dip-pen system used during this project is a commercially available Desktop Nano Lithography Platform System (NLP 2000), an instrument with a graphical user interface and capabilities of depositing a wide range of materials with sub- $\mu\text{m}$  accuracy and precision, as described in [91]. As shown in Fig. 2.2(a), this system includes an integrated microscope, translational stage modules, and an assembly area [91]. The integrated microscope module is equipped with interchangeable 10x and 50x optical objectives and an interface connected CCD camera. The translational stage modules include XYZ encoded piezo-driven linear stages, two encoded goniometer tilt stages ( $T_x$ ,  $T_y$ ) and an implemented rotation stage system (R) [92], with an area coverage of a 4 inch wafer.

The dip-pen system was customized to permit its application as a TP system for the heterogeneous integration of (nano-)photonic structures. To that end, the original bespoke cantilevers in the dip-pen system were replaced by polymeric  $\mu$ -stamps mounted in bespoke stamp holders. Fig. 2.2(b) shows an image of the assembly area in the dip-pen system, with the stamp holder (replacing the original cantilever in the module), as well as the donor and receiver samples, and a metallic plate. The polymeric  $\mu$ -stamps

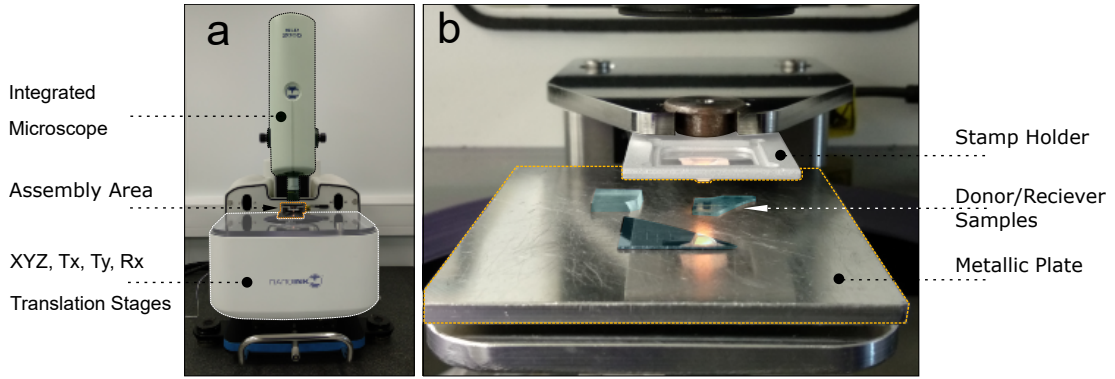


Figure 2.2: Photographs of the modified DPN system used during this PhD project showing different modules.

used for the selective device capture and release are mounted onto the stamp holder, which is in turn inserted into the main system, as shown in Fig. 2.2(b). Donor and receiver samples are wax bonded to the metallic plate to ensure that they stay fixed during the TP process. The metallic plate is placed on the translational stage module. Additionally, since the polymeric  $\mu$ -stamps used for the TP processes are transparent by nature, our system permits to continuously observe the target area using the integrated microscope module in the dip-pen systems connected via the computer interface.

The computer interface also allows controlling the translational stages and the integrated camera module of the setup. Fig. 2.3(a) shows the translational stages control module. This permitted to control the position in precise increments varying from 100 nm to 1 mm in XYZ coordinates. Moreover, absolute coordinates are displayed in consoles and available for a fast recover and recording of coordinates (with a recovery accuracy of the coordinates of  $\pm 25$  nm). The tilts of the stages are controlled using the rotation axis section in the interface, with a range going from 0.01 to 1 degrees. The integrated rotational module consists of an externally mounted closed-loop rotation stage, commercially sourced from SmarAct [92]. The resolution of the stage is  $\sim 4 \mu^\circ$ , as specified in the data-sheet [92]. The camera interface, shown in 2.3(b), allows

recording and varying focal points of the camera by moving the column.

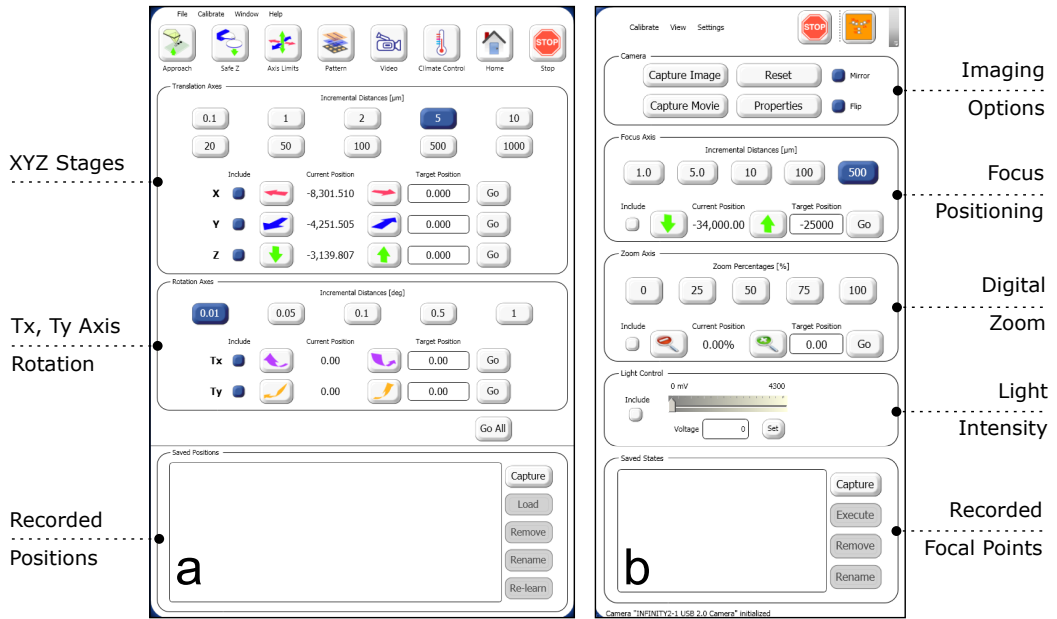


Figure 2.3: User interfaces of the (a) translational stage and (b) camera module of the modified dip-pen system.

## 2.2.2 Previous TP Works with Optoelectronic Structures

As previously outlined, the main focus of the previous works on the use of TP technique has been the implementation of micro-scale photonic circuitry (using for example  $\mu$ -LEDs or membranes). For example, at our institute, several works have reported on the fabrication of  $\mu$ -LEDs arrays achieving close to nanoscale ( $< 100$  nm) printing resolution. Figs. 2.4(a-e) show results on constructing arrays of  $2 \mu\text{m}$ -thick *AlInGaN* LEDs on a polyethylene terephthalate/PDMS substrate with a reduced target separation ranging from  $1 - 0.150 \mu\text{m}$ . The devices in the array were individually transferred and aligned to those previously printed.

Figs. 2.4(f-g) show further work on the integration and arrangement on a single substrate of LEDs operating at various colours for dual-color emission [93]. Here, blue and green pixels were transfer-printed from their growth substrate onto contacts

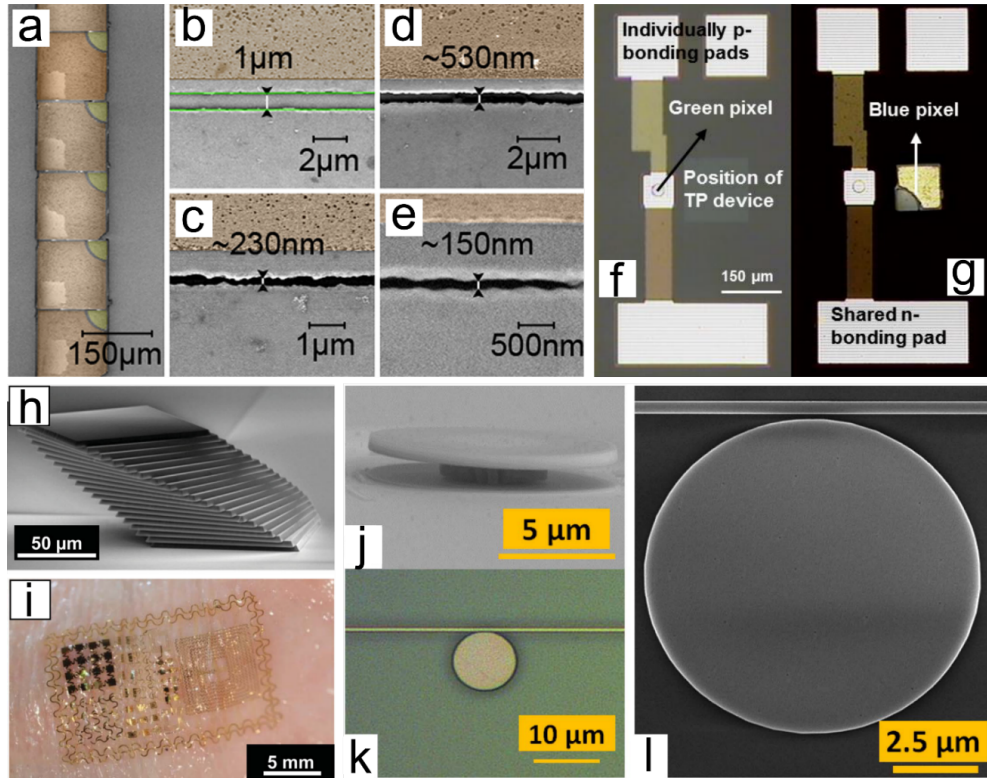


Figure 2.4: (a-e) An array of transfer-printed LEDs on a host substrate, images taken from [78]. (f-g) Micro transfer-printed multi-colour LEDs on bonding pads, figures taken from [93]. (h) Silicon plates stacked in a controlled manner. (i) on-skin flexible electronics with TP chips, extracted from [20]. (j-k) TP micro-ring resonators onto silica substrate, figures taken from [94].

between the n-/p-bonding pads, as shown in Fig. 2.4(f). The fabrication process combined devices of different dimensions: green-emitting InGaN micro-LEDs (disk diameter of  $20 \mu\text{m}$ ) and blue-emitting ultra-thin InGaN  $\mu$ -LED ( $100 \times 100 \mu\text{m}$ ) which were individually transferred onto target locations. Moreover, previous works by Prof J.A. Rogers' group at Illinois included the integration of a multilayer stack of silicon platelets, demonstrating 3-D assembly of photonic structures and fabrication of passive devices in flexible and curvilinear formats [20]. Recently, the TP technique was used to develop hybrid coupled photonic circuitry by printing disk resonators next to the planar silicon waveguides [94]. *AlGaAs* micro-disk resonators were picked from their growth substrate and subsequently integrated with a target separation gap of 100 nm

achieving the measured Q-factor of  $7 \times 10^3$ . These selected works clearly depicted the flexibility and applicability of the TP technique for a systematic and accurate integration of passive and active photonic devices/components into a target area and host substrates.

## 2.3 Polymer $\mu$ -stamps for TP of NW Devices

The capture-and-release mechanisms of optoelectronic structures at the core of the transfer-printing are achieved using polymeric  $\mu$ -stamps, mostly fabricated out of PDMS (polydimethylsiloxane) a polymer belonging to the organosilicon compound group. Over the past years, PDMS has been ubiquitously used in micro fluidics and soft-lithography areas [95]. One of the paramount advantages of this material is its viscoelastic properties which allow producing optically transparent, flexible, and tacky surfaces [27], [28].

### 2.3.1 Procedures for the Capture/Release of NW Lasers

The mechanism of reversible adhesion for heterogeneous integration of optoelectronic structures was proposed by Prof. Rogers' group at the University of Illinois. His group presented the concept [20], described the underlying physics, and worked on the optimization of the properties of elastomeric stamps for work with multiple structures [29]. To illustrate the concept of reversible adhesion, we introduce a case describing the capture/release processes of a silicon membrane using a bespoke polymeric  $\mu$ -stamp, see Figs. 2.5(a(i-ii)). The presented  $\mu$ -stamp has four pointy pyramids at the corners, as shown in the inset of Fig. 2.5(a). When force is applied to the stamp, its roof collapses forming a larger contact area between the  $\mu$ -stamp and the silicon membrane. Due to

the stamp's viscosity, if properly optimized [29], the bonding force is large enough to overcome that between the membrane and the substrate, permitting the membrane's capture by the stamp. Then, once the membrane has been lifted off from the surface, the polymer stamp returns back to its original shape, keeping the membrane captured. The contact area between the stamp and the membrane decreases and is only held by the four pyramids. Thus, when the membrane is slowly released onto the receiver substrate, it's successfully integrated onto the target area, as described in Chapter 1.

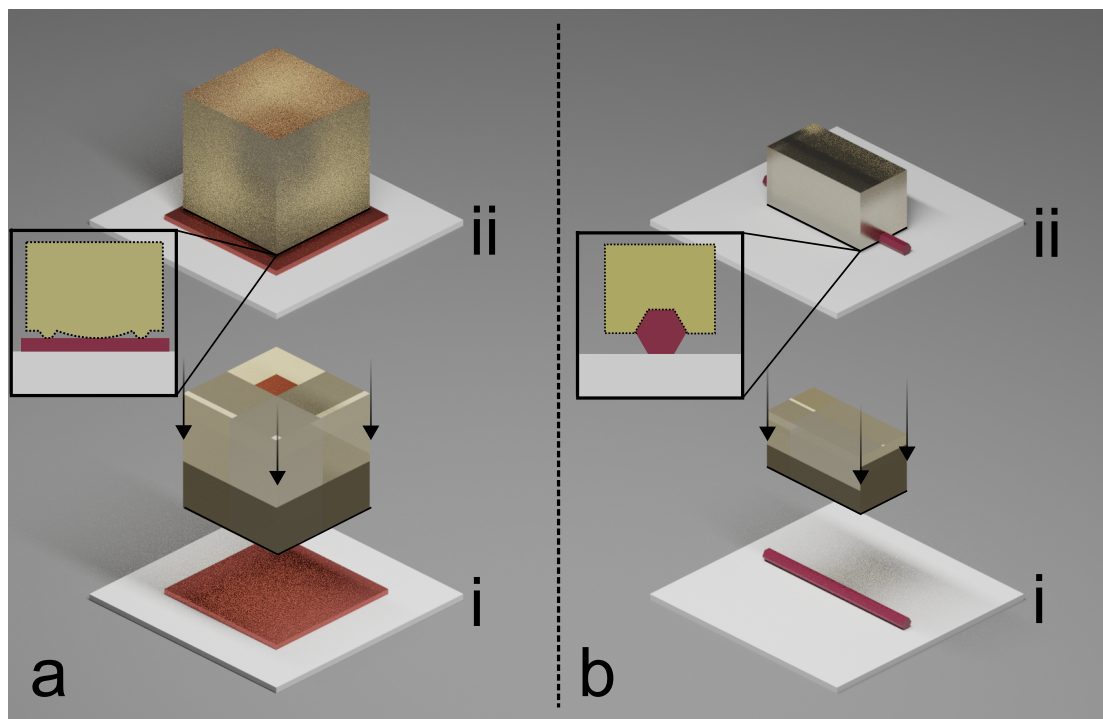


Figure 2.5: Schematic 2D diagram of the capture process for: (a)  $\mu$ -LEDs, (b) NWs. Typical dimensions of  $\mu$ -LED stamp  $\sim 100 \times 100 \mu\text{m}$ , for the NW stamp these are in the order of  $\sim 10 \times 30 \mu\text{m}$ .

Since, semiconductor NWs are orders of magnitude smaller in area than the membranes or  $\mu$ -LEDs of Fig. 2.5, both the technique for their capture/release with polymer  $\mu$ -stamps, and the latter's design and dimensions needed to be consequently altered. To achieve successful capture and release of semiconductor NWs we developed new bespoke  $\mu$ -stamps with a specifically designed  $\mu$ -tip suitable for single NW device. Fig.

2.5(b(ii)) depicts the designed  $\mu$ -stamp's tip making contact with a NW. The inset in Fig. 2.5(b(ii)) shows that when force is applied to the  $\mu$ -stamp, it deforms covering a larger area, than in Fig. 2.5(b(i)). Hence, this allows to increase the adhesion between the  $\mu$ -stamp and the NW making it higher than that between NW and substrate. As a result, we are able to capture controllably selected devices from the substrate. After the NW is detached from the surface, the  $\mu$ -stamp recovers its original shape, therefore decreasing the contact area between  $\mu$ -stamp and NW, whilst still keeping it captured. After this process it is then possible to release the captured NW on a different receiving substrate to complete the TP process.

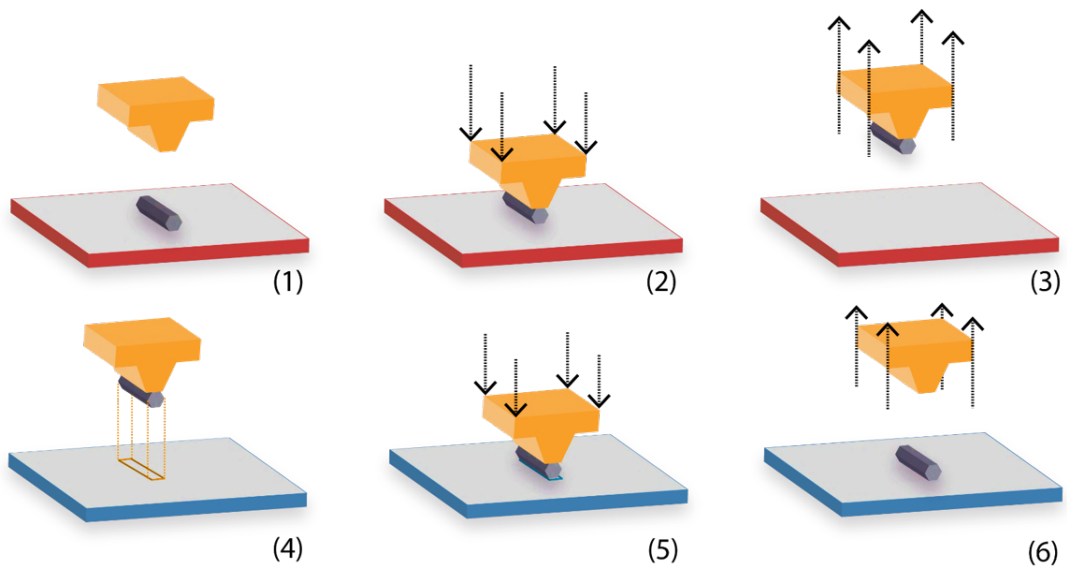


Figure 2.6: Stages of the TP technique at the nanoscale used for the integration of semiconductor NWs: (1) NW lying on donor substrate (red). (2) Polymer  $\mu$ -stamp is aligned with the NW. (3) NW is captured by the  $\mu$ -stamp. (4)  $\mu$ -stamp is aligned on the receiving surface (blue). (5)  $\mu$ -stamp makes surface contact with the receiving substrate. (6) NW is released at the desired location.

The different stages of the TP technique for the heterogeneous integration of NW lasers are shown in Fig. 2.6: (1) The  $\mu$ -stamp is aligned with a desired semiconductor NW on the donor substrate. During this stage, all angular or rotational misalignment and tilts are adjusted between the NW and the stamp's  $\mu$ -tip. (2) Full surface contact

is produced between the  $\mu$ -tip and the selected NW. (3) The stamp deforms conforming to the NW's shape. Then, the resulting enhanced adhesion between NW and  $\mu$ -stamp enables to overcome that between NW and substrate, allowing to capture the NW. (4) The  $\mu$ -stamp returns to its original shape, hence reducing the contact area between the stamp and NW. After this, the  $\mu$ -stamp with the captured NW is aligned with the target location on the receiving substrate. (5) Mechanical pressure is applied to the  $\mu$ -stamp until full surface contact is produced between the NW and the receiving substrate. (6) By slowly lifting the  $\mu$ -stamp, the bonding force between the  $\mu$ -stamp and NW decreases until it becomes insufficient to overcome the bonding between the NW and substrate. Hence, the NW is released at the desired position in the receiving substrate.

### 2.3.2 Design and Fabrication of Polymer $\mu$ -Stamps

The TP procedures for the controllable capture and release of semiconductor NWs required careful tuning of the PDMS  $\mu$ -stamp's composition in order to perform such operation with a high transfer yield. We also outline how the tuning of the composition of the polymeric  $\mu$ -stamps was achieved and describe the fabrication process of the moulds used to produce the  $\mu$ -stamps. In this section we present two bespoke  $\mu$ -stamp designs developed during this project to transfer-print NW devices.

Stamp moulds were designed and fabricated to allow the supple casting of  $\mu$ -stamps. An open-source software K-Layout was used to develop masks which were then used for the development of the  $\mu$ -stamps' shapes. The  $\mu$ -stamp moulds were fabricated on silicon wafers, as depicted in Fig. 2.7(a). At first, a whole Si wafer was solvent cleaned following the standard procedure of Acetone, Methanol and Isopropyl alcohol soaking in an ultrasonic bath. After this process, the wafer was placed on a hot-plate and baked

at 100°C for 10 minutes to ensure all remaining solvents are evaporated.

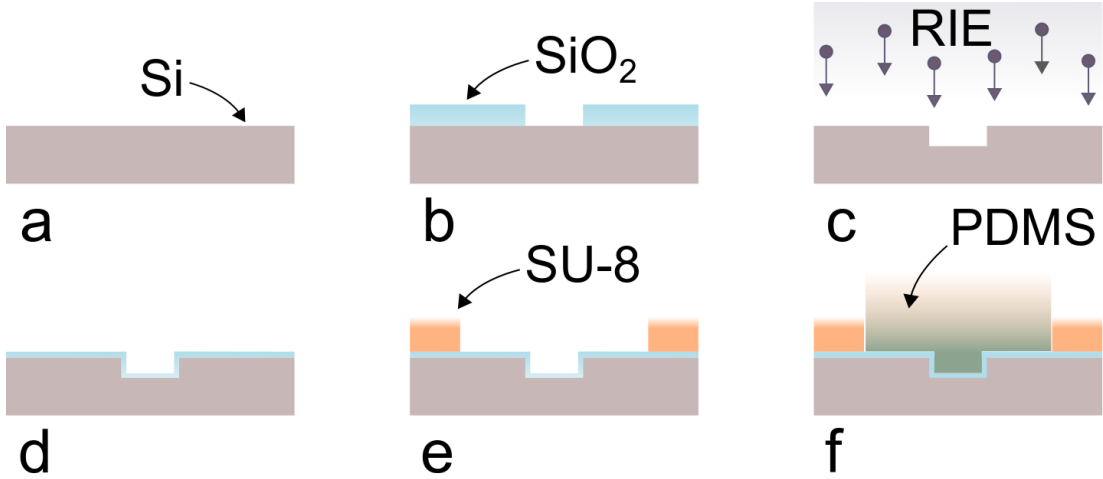


Figure 2.7: Process diagram of the fabrication of the polymeric  $\mu$ -stamps by means of moulding. (a) Si substrate. (b) Selectively patterned silica on silica substrate. (c) Reactive ion etching of the substrate. (d) Silica deposition atop the substrate. (e) Photoresist patterning atop the etched structure. (f) Fabrication of the polymeric  $\mu$ -stamps by casting PDMS inside the fabricated moulds.

The wafer was masked with a thin layer of  $SiO_2$  forming the shape of the  $\mu$ -tip ( $10 \times 30 \mu\text{m}$ ), depicted in Fig. 2.7(b). A reactive ion etching process was used to etch the whole substrate. However, as  $SiO_2$  and Si have different etching rates, as we etched silica, we produced a  $10 \times 30 \mu\text{m}$  and  $6 \mu\text{m}$  in thickness trench inside the substrate, see Fig. 2.7(c). After building a hard mould for the  $\mu$ -tip, the surface was covered with a thin layer of  $SiO_2$  for the next fabrication stage, see Fig. 2.7(d). At this point, we have fabricated a  $6 \mu\text{m}$  thick block inside the silicon substrate. Next, we spin-coat the sample with SU-8 photoresist. It should be noted however, that the thickness of the SU-8 solely depends of the type of photoresist used. Next, the structure is moved to the lithography setup where a selected mask is chosen and applied onto the device. As the lithography tool exposes a certain dosage of UV light, the covered regions are getting cured. We then move the structure onto the developing station, where the sample is dipped into the developing solution. The latter is specifically chosen depending on the

type of the photoresist used. After this procedure, the whole structure is baked at  $140^\circ$  for 5 minutes. After which, the mould for the polymeric  $\mu$ -stamp is produced, as seen in the cross-section shown in Fig. 2.7(e).

PDMS is provided as a two-part liquid compound which cures differently under various temperature conditions [28]. From a chemical point of view, PDMS is made of long siloxane polymer chains. The supplied PDMS (Silicone Solutions) comes as a base (RTV615A) and a curing agent (RTV615B) materials. The flexibility of the produced material is strongly linked to the base/agent weight ratio (the higher the cross-link ratio, the stiffer the stamp becomes) and was recently studied here [28]. To cast the  $\mu$ -stamps, a PDMS mix (base/agent) with a RTV615A/RTV615B weight ratio of 10:1 is poured into the mould. Prior to that the solution is stirred to mix the two compounds. To achieve the required elastomeric properties of the micro-stamps, we leave the mixture at  $100^\circ\text{C}$  for 2 hours. Fig. 2.7(f) depicts the last stage of the  $\mu$ -stamp fabrication process, when the PDMS is fully cured.

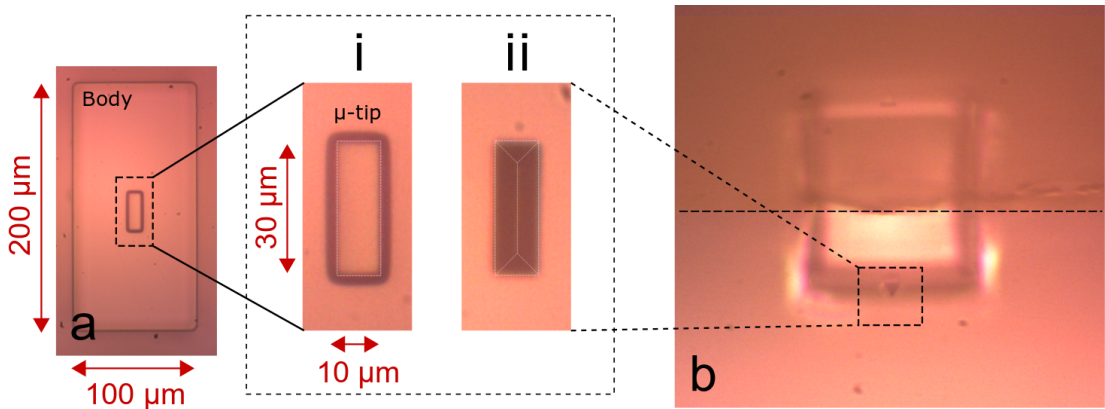


Figure 2.8: Types of polymeric  $\mu$ -stamps developed during this project and their geometries. (a) Top-view of a PDMS flat  $\mu$ -stamp with: (i) flat-tip and (ii) elongated pyramidal-tip designs. (b) Micrograph of a side-view showing a PDMS pyramidal  $\mu$ -stamp.

After the PDMS curing process, the fabricated  $\mu$ -stamps are casted and peeled off their moulds resulting in negative polymeric structures with defined features. Impor-

tantly, PDMS is an elastomeric material acting like a transparent rubber, hence it can be stretched and deformed, returning later to its original shape. We have designed and fabricated two different types of  $\mu$ -stamps, namely flat-tip and elongated pyramidal-tip  $\mu$ -stamps. Images of both are shown in Figs. 2.8(a(i)) and 2.8(a(ii)), respectively. Fig. 2.8(a) shows a micrograph of a top-view outline of a flat-tip polymeric  $\mu$ -stamp. The  $\mu$ -stamp consists of two main sections: body and  $\mu$ -tip, the latter is used to capture and release the NWs. The thickness of the body is an order of magnitude higher than that of the tip to prevent stamp collapse onto the substrate during the NW capture/release processes. During the course of this PhD project, we have investigated the use of these two  $\mu$ -stamp designs for the TP of NW devices, as it will be detailed later in this chapter. Fig. 2.8(a(i)) shows a typical flat stamp which is used to transfer-print NW devices with high accuracy, very high yield and which benefits from its total transparency, permitting to visualise at all moments the TP processes. Fig. 2.8(a(ii)) shows in turn an elongated pyramidal tip  $\mu$ -stamp, which was used to integrate semiconductor NWs on surfaces with weak bonding or reduced contact area (see Chapter 5). Additionally, Fig. 2.8(b) shows a side-view of an elongated pyramidal  $\mu$ -tip to better showcase its structural features.

To optimize the performance of the developed PDMS pyramidal-tip  $\mu$ -stamp for the TP of semiconductor NWs we purposely fabricated  $\mu$ -stamps with 3 different base-to-agent concentrations of 6:1, 8:1, and 10:1, respectively, to determine the most effective compositions. The different fabricated  $\mu$ -stamp samples were tested by measuring their success rate in capturing NWs from a given surface under analogous conditions. Specifically, we used InP NWs (diameter: 435 nm, length:  $\sim 5 \mu\text{m}$ ) NW devices randomly scattered on a  $\text{SiO}_2$  substrate. The NW capture success rate at the first

attempt for the 3 different stamps' composition was equal to 20%, 60%, and 90% for 6:1, 8:1, and 10:1 concentration (tests were carried out with 20 NWs for all cases). Moreover, PDMS curing parameters were also optimized following the recipes in [96].

## 2.4 Heterogeneous Integration of NW Devices

In this section we present results on the systematic and accurate TP of semiconductor NWs of different dimensions into diverse material substrates, patterned structures, and pre-fabricated systems. These results therefore demonstrate that the developed TP technique at the nanoscale provides a novel nanofabrication method opening new routes towards the fabrication of heterogeneous (nano-)photonic systems with embedded NW devices at their core [72, 73, 97, 98].

### 2.4.1 Integration of NW Lasers into Diverse Substrates

In this section, we report results demonstrating the integration of InP NW lasers [55] of various diameters (435, 660, and 920 nm) and length varying from 4 – 7  $\mu\text{m}$  onto heterogeneous surfaces including silicon, silica, gold, diamond, and polymeric substrates [97, 99, 100] by means of the nanoscale TP technique. A CCD camera embedded into the TP rig allows to visually inspect the donor substrate where the InP NW lasers are originally located permitting to cherry-pick selected devices. Fig. 2.9(a) provides a micrograph showing multiple NWs on their original donor substrate next to a flat-tip  $\mu$ -stamp. At this stage, we can visually assess the different NW devices on the donor substrate and select either single NWs or NW bundles for their transfer-printing onto a different substrate by means of TP. Fig. 2.9(b) shows a selected NW that has been captured by the  $\mu$ -stamp from the donor substrate. This is subsequently transferred

onto a receiving PDMS substrate to form an array of NW lasers with a separation of  $\sim 30 \mu\text{m}$  between elements in the array. The latter was formed by both individual NW lasers and clusters (bundles) of NWs bonded together. The versatility of the nanoscale TP technique developed during this project allowed us to mix-and-match different devices into a single platform. Hence, the array of InP NWs shown in Fig. 2.9(c) fabricated by means of TP counted with different types of NWs (435, 660 and 920 nm diameters) in each of its rows.

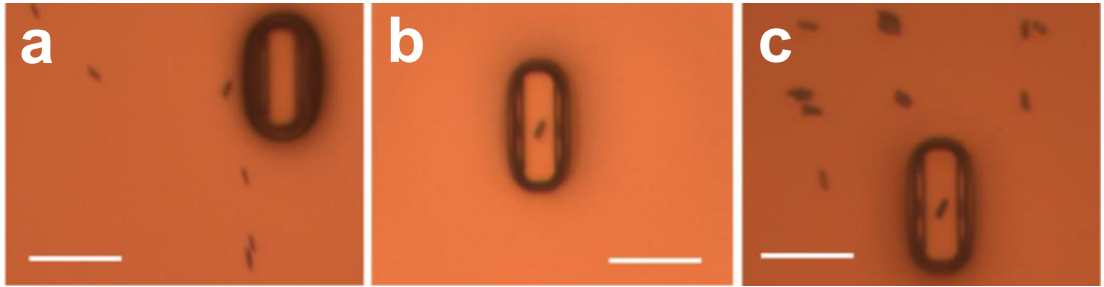


Figure 2.9: Micrographs showing the formation of a NW arrays on PDMS substrates. (a) The target NW is selected from a cluster of scattered devices. (b) The NW is picked with a flat-tip  $\mu$ -stamp. (c) The device is sequentially integrated onto the PDMS substrate. Figures taken from [97]. All scale bars are  $30 \mu\text{m}$ .

A very important property of the TP technique is that the transferred NW devices are not damaged during the integration processes. Since in this work we are mainly dealing with NW lasers, it is of crucial importance that these devices keep their room-temperature lasing emission after transfer. Figure 2.10 shows multiple integrated *InP* NW lasers (diameters ranging between 435 - 920 nm, length  $\sim 6 \mu\text{m}$ ) onto a gold surface by means of TP. The devices were individually and controllably transfer-printed onto a target area in the gold surface at specifically selected locations (to form a 1D array of NW lasers). After integration, the InP NWs were optically excited about their lasing threshold at room temperature (the process of optical excitation is discussed in detail in Chapter 3). Fig. 2.10(a-d) show the obtained characterization measurements for the

NWs (1-4) in Fig. 2.10(e), respectively, as well as bright- and dark-field micrographs of the NWs in plots (i) and (ii), respectively. Lasing emission spectrum in figures (iii) correspond to the dark field micrographs of the lasing devices in (ii).

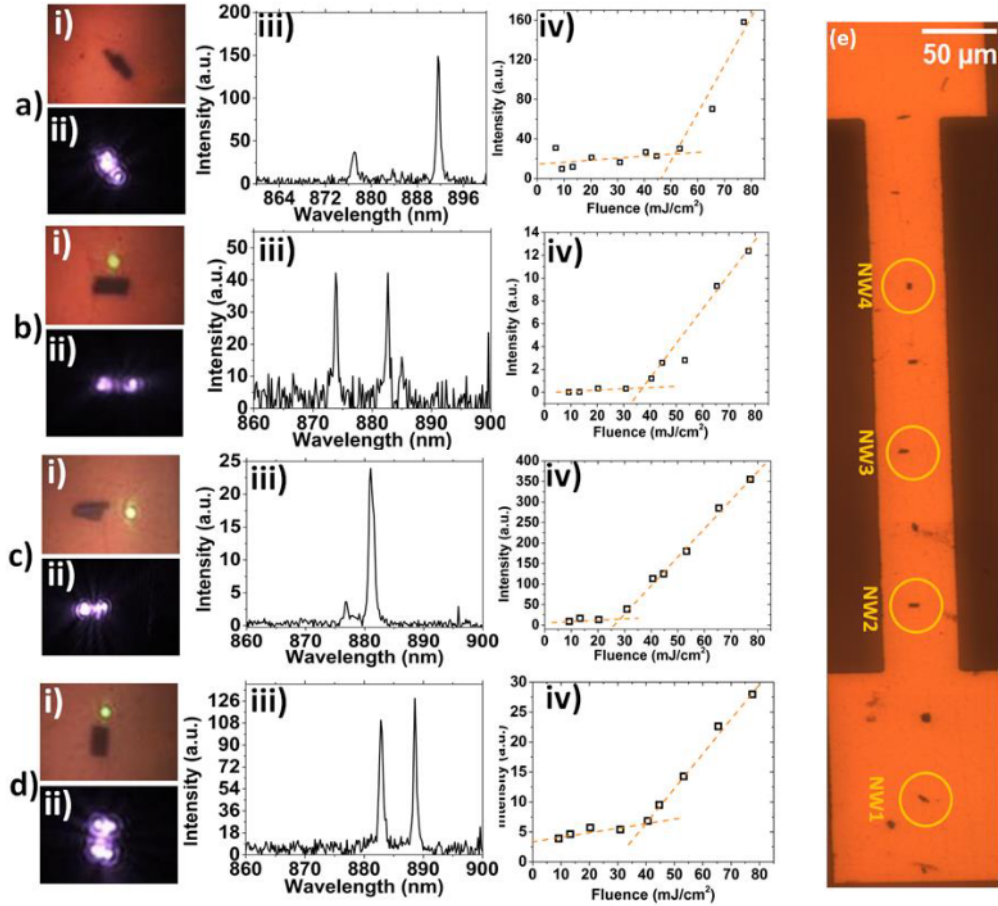


Figure 2.10: (a-d) Bright (i) and dark (ii) field micrographs, lasing spectra (iii) and lasing threshold curves (iv) measured for four selected InP NW bundles forming part of the fabricated 1D array onto the gold surface by means of TP. (e) CCD image of the 1D array marking the four InP NW bundles whose characterization measurements are shown respectively in (a) NW1, (b) NW2, (c) NW3 and (d) NW4. Figure taken from [97].

Moreover, the TP technique can also be fully applicable to the case when semiconductor NW devices need to be integrated onto passive components. As an example, we have also demonstrated the transfer-printing of *InP* NWs onto a 0.5 x 0.5 cm, 10  $\mu\text{m}$  thick diamond membrane bonded onto a silica substrate. However, it is important

to note that thinner membranes could also be used. Figs. 2.11(a-c) show the process to print  $\sim 435$  nm *InP* NW lasers on the diamond membrane sample. The NW lasers were visually pre-selected to enable individual device selection. After a selected NW was transfer-printed on the diamond surface, this was optically excited using a  $\mu$ -PL setup. Fig. 2.11(d) shows a dark field micrograph of one of the integrated *InP* NWs on the diamond membrane showing lasing emission from its end-facets when optically pumped above its room-temperature lasing threshold.

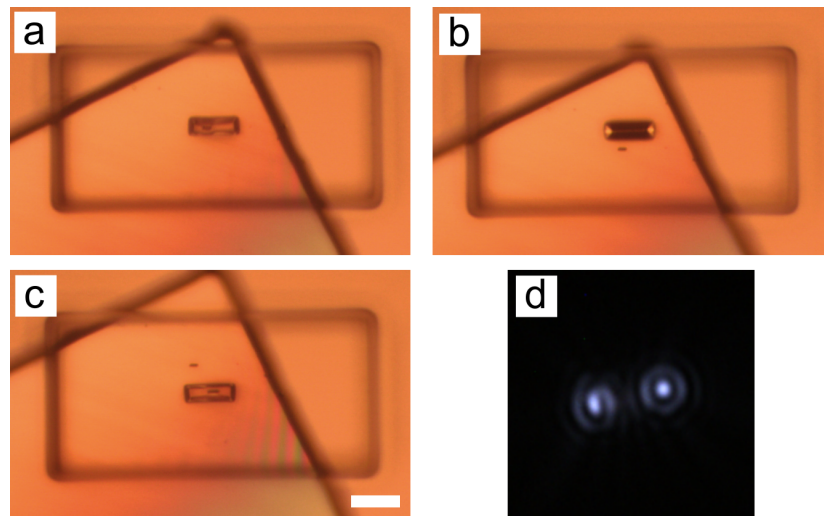


Figure 2.11: (a-c) Figures show various transfer-printing steps of NW lasers on Diamond substrate: (a-b)  $\mu$ -stamp with a NW is printed into Diamond membrane. (c) Second NW device is aligned and printed close to the first device. (d) A darkfield micrograph of a lasing NW device on diamond substrate. Scale bar is  $30 \mu\text{m}$ .

### Integration of NW Lasers onto Diffractive Surfaces

Integrating semiconductor NW lasers into diffractive patterns and surfaces is of interest to the scientific community due to the variety of applications this would offer [73, 101, 102]. Importantly, the combination of NW lasers with diffractive surfaces paves the way to mode selection mechanisms in these NW devices [102], which would be otherwise difficult to control or might require complex fabrication stages [103] or device post-growth processing [104]. As discussed in Chapter 1, more traditional ways of positioning

and aligning NW devices consist on the use of AFM tips or using Langmuir-Blodgett processes [105, 106]. Typically, this will need NW devices to be mechanically scattered across a target substrate by rubbing the NW donor sample in the receiving area, prior to carrying out the final NW positioning procedures. Hence, a more robust, controlled and precise way to perform the NW integration onto target (diffractive) surfaces from their original donor sample is needed. The use of our newly developed TP technique at the nanoscale permits to tackle this challenge allowing to integrate semiconductor NW lasers into diffractive surfaces, such as period gratings [101]. In addition to these results, later in this thesis we also describe the methods for the integration of NW lasers into Cat's Eye antenna structures by means of TP [73].

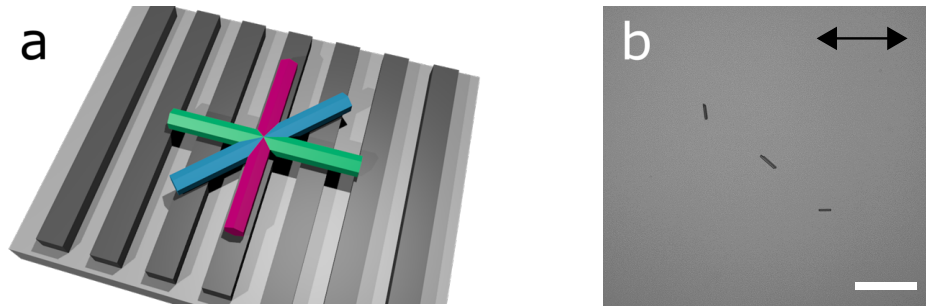


Figure 2.12: (a) Schematic diagram showing NW lasers integrated with different orientations on a diffractive surface. (b) Transfer-printed array of InP NW lasers on a PDMS grating substrate. The arrow indicates the grating orientation. Scale bar is 30  $\mu\text{m}$ .

For the integration of NW lasers onto diffractive periodic structures, we used InP NWs ( $d \sim 435 \text{ nm}$ , length  $\sim 5 \mu\text{m}$ ) with room temperature lasing emission [101]. As the periodic diffractive structure we selected a PDMS grating sample ( $\Lambda = 256 \text{ nm}$ ) and pitch of 50 nm. This was fabricated using a  $\text{SiO}_2$  mould where PDMS was poured and casted. After the PDMS grating fabrication, we controllably integrated by means of TP individually-selected NW lasers in three different axial orientations with respect to the substrate's gratings, as schematically depicted in Fig. 2.12(a). To achieve this result,

we made use of the rotational stage module embedded into the dip-pen nanolithography system. This permitted to rotate the stage holding the grating sample in three steps of 45 degrees. It is worth mentioning here that the grating patterned surface offered a reduced contact area between NW and receiving substrate. Therefore, it was found that the NW release process on the grating surface was very difficult to achieve using the flat-tip  $\mu$ -stamp. This was due to the reduced NW/grating contact area which did not permit to overcome the adhesion between NW and  $\mu$ -stamp. Hence, for this experiment we used the elongated pyramidal tip  $\mu$ -stamp, as its pointy tip use for NW capture permitted to reduce the contact area between NW and stamp, easing in turn the NW release process in the grating surface. At the end of the TP processes carried out with the elongated pyramidal tip  $\mu$ -stamp the transfer-printed NW lasers are successfully integrated atop the polymeric grating, as shown in in Fig. 2.12(b), where the arrow indicated the grating orientation.

#### 2.4.2 Fabrication of Spatial Patterns with NW lasers

Here, we report our results on the fabrication of controllable spatial patterns, such as 2D NW arrays by means of TP. We demonstrate arrays of semiconductor NWs with controlled number of devices, defined spacing between elements and specific device orientations. Fig. 2.13 shows fabricated structures by means of TP where multiple NW devices are systematically and precisely integrated across the metallic electrodes of a pre-fabricated Bow-Tie antenna platform. In the systems of Figs. 2.13(a-c) a controlled number (1, 2 or 3) of *InP* NWs (length  $\sim 10 \mu\text{m}$ , diameter  $\sim 260 \text{ nm}$ ) were systematically integrated in close proximity to successfully form these compact systems. In a similar manner, the TP technique was also used to fabricate arrays of NWs integrated at desired locations across metallic contact terminals and with both

controlled coarse and fine separations between individual integrated elements, as it is shown in Figs. 2.13(d-f). The latter show fabricated systems using individually-selected *GaAs* NWs (length  $\sim 20 \mu\text{m}$  and diameter  $\sim 200 \text{ nm}$ ) which were integrated one-by-one onto a pre-fabricated receiving surface with a controlled separation of these equal to the distance between the existing metallic contacts. Furthermore, our TP technique also allowed to fabricate systems with multiple NWs printed with fine separation across one of the metallic contact pairs, resulting in multiple *GaAs* NW devices being integrated onto a single gate of the device, as shown in Fig. 2.13(e).

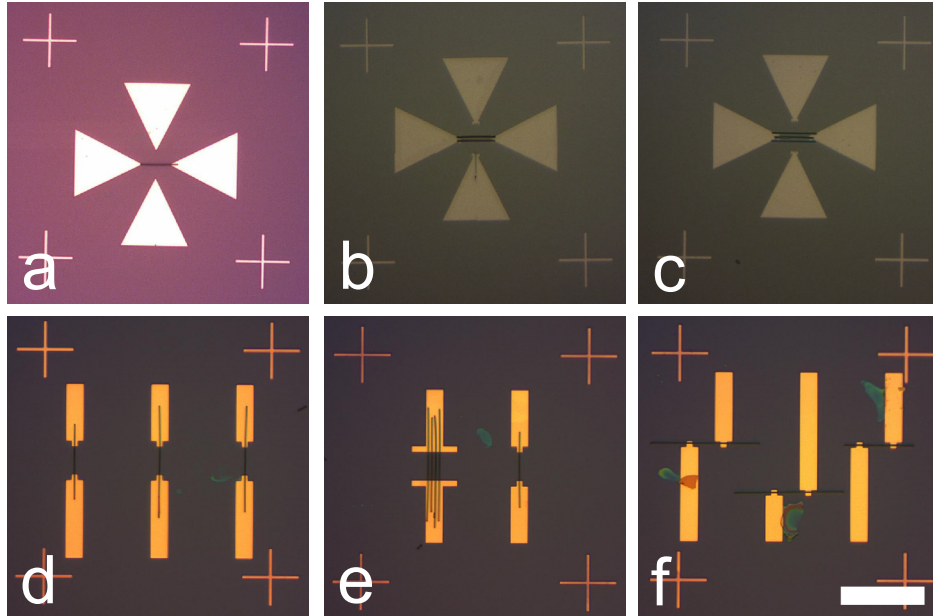


Figure 2.13: (a-c) Micrographs of transfer-printed *InP* NW lasers on 50 nm-thick *Au* Bow-Tie gates. (d-f) micrographs of TP *GaAs/AlGaAs* NW lasers on 50 nm-thick *Au* electrodes. Scale bar =  $20 \mu\text{m}$ .

Finally, we also demonstrate the systematic integration of NW devices by means of our TP technique at the nanoscale onto a single surface forming bespoke spatial patterns, as seen in Fig. 2.14. For example, Figs. 2.14(a-c) depict the process of creating a 1D array of *InP* NWs with controlled micrometric separation between elements and with precise controlled orientation angle of the transfer-printed NWs. The final

fabricated 1D array is shown in Fig. 2.14(d). In the process shown in Figs. 2.14(a-c), the first NW in the array is used as the reference point for the alignment and location of the other NWs. These were integrated with controlled orientation angles, from  $0^\circ$  to  $90^\circ$ , in increasing steps of  $15^\circ$  between consecutively integrated NWs. The NW highlighted with a red square in Fig. 2.14(d) is the NW whose transfer-printing process is shown in Figs. 2.14(b-c). The 1D NW array in Fig. 2.14(d) was fabricated on a silicon substrate. However, the technique described here to fabricate arrays or other spatial patterns with semiconductor NWs with controlled separation between elements and defined orientation angles is fully applicable to other substrates (e.g. silica, diamond, gold, etc.). Additionally, Fig. 2.14(e) shows a 2D array of InP NWs (diameter  $\sim 435$  nm, length  $\sim 7 \mu\text{m}$ ) fabricated on Si substrate with a controlled separation of  $20 \mu\text{m}$  between elements in different rows and columns and with specific selected orientations of (0, 90 and  $45^\circ$ ).

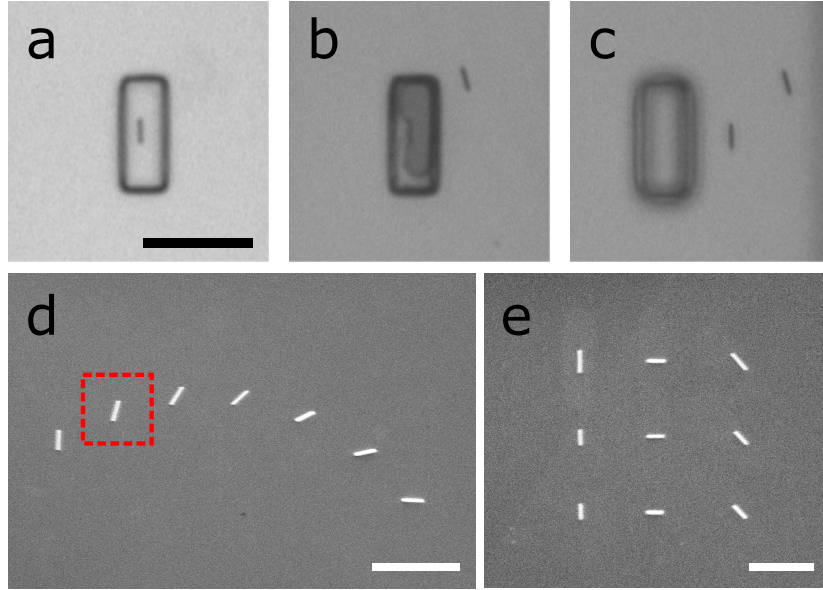


Figure 2.14: (a-c) Images showing the TP stages of an *InP* NW laser: (a) The  $\mu$ -stamp captures an *InP* NW laser from the donor substrate. (b) Surface contact is made between  $\mu$ -stamp and receiving substrate to release the NW. (c) NW is positioned at the desired location on the receiving substrate. Scale bar = 30  $\mu\text{m}$ . (d) SEM image of a 1-D array of NW lasers with individual elements separated by 20  $\mu\text{m}$  and with controlled orientation angles from 0 to 90° (in 15°). Scale bar = 30  $\mu\text{m}$ . (e) SEM image of a 2D array of *InP* NW lasers. The NWs on different columns have been integrated with different angle orientations (0, 45 and 90°). Scale bar = 20  $\mu\text{m}$ . Figure taken from [101].

### 2.4.3 Sub- $\mu\text{m}$ Alignment of NW Devices

In this section, an alignment technique to achieve sub- $\mu\text{m}$  positioning accuracy in the integration of NW devices onto different target surfaces with controlled position and angle orientation is described. This technique is based on image processing techniques to calculate the location of the NW's centroid in real-time. This enables tracking the NW's absolute position on the TP toolset and subsequently record its coordinates. Using this technique it is therefore possible to highly increase the positional accuracy of integrated NW lasers to ensure sub- $\mu\text{m}$  precision. To demonstrate this technique and estimate the printing accuracy of the technique, we fabricated pairs of parallel-aligned NWs with controlled defined separation between individual NWs. The absolute

positioning accuracy was estimated from the positional offsets obtained between the target and finally achieved device separations in the laterally-aligned NW pairs. A high-resolution scanning electron microscope (SEM) system was used to image the fabricated NW pairs and determine the actual device separations for their comparison with the target values.

A first experimental work to demonstrate the repeatability and accuracy of our TP technique at the nanoscale was carried out by sequentially integrating individual InP NWs (435 nm in diameter and  $\sim 5 \mu\text{m}$  in length) in a host Si substrate to form longitudinally-aligned NW pairs in a facet-to-facet configuration whilst still retaining sub- $\mu\text{m}$  alignment resolution [72]. This was achieved by developing an image processing script drawing an artificial line on the dip-pen toolset software interface, in order to align the transfer printed InP NW lasers used in that work. For this activity, a first NW was transfer-printed onto the host Si substrate. In this case, Si was used as it provides good contrast during the SEM image analysis. A second NW was then transfer-printed collinearly with the first device in the indicated facet-to-facet configuration, with the aim to achieve accurate alignment between their longitudinal axes. SEM images of the different fabricated longitudinally-aligned *InP* NW structures are shown in Figs. 2.15(a-d). These revealed an achieved NW facet alignment resolution of  $\sim 50$  nm with a standard deviation of  $\sim 35$  nm for our TP technique.

This simple longitudinal NW-to-NW alignment technique inspired us to develop a computer controlled alignment mechanism based on a real-time image processing. To demonstrate the technique and estimate the actual positioning accuracy it provided we fabricated laterally aligned NW pairs with defined target micrometric separations between devices. The purpose of this activity was two-fold: (1) the development of

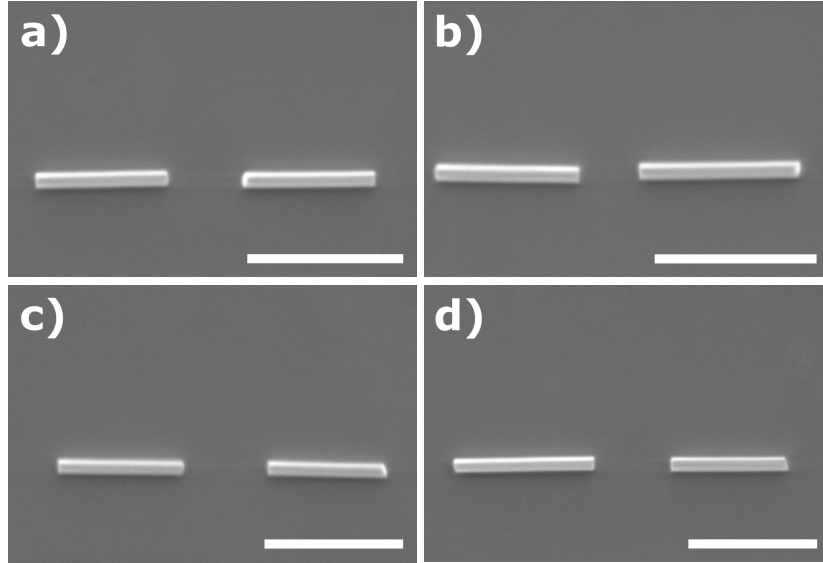


Figure 2.15: SEM images of two longitudinally-aligned InP NWs individually transfer-printed onto a host silicon substrate. Each sub-figure shows a different longitudinally-aligned NW laser pair fabricated by means of TP. Scale bar = 5  $\mu\text{m}$ .

reduced size systems with NW devices in parallel (and also longitudinal) integrated arrangements in its own right is a unique and interesting research area, hence by developing an enabling tool permitting their highly precise and controllable manufacturing that would bring a significant advantage to the field; (2) this configuration permitted use to estimate very efficiently the transfer-printing accuracy of our setup, since all NW dimensions (and the devices' separations after integration) could be easily extracted using SEM imaging.

Fig. 2.16(a) shows a schematic diagram of the technique used for the alignment and positioning of two NW lasers. Before starting the NW alignment process, we pick a set of NWs and release them in bulk onto an intermediate PDMS substrate. There the NWs are visually inspected using the optical microscope module on the TP rig in order to select single NWs for their final integration in the laterally-aligned configuration on a *Si* substrate. A first NW ( $\text{NW}_1$ ) is transfer-printed at a specific location on the target *Si* substrate.  $\text{NW}_1$  is then used as the reference point for the further alignment

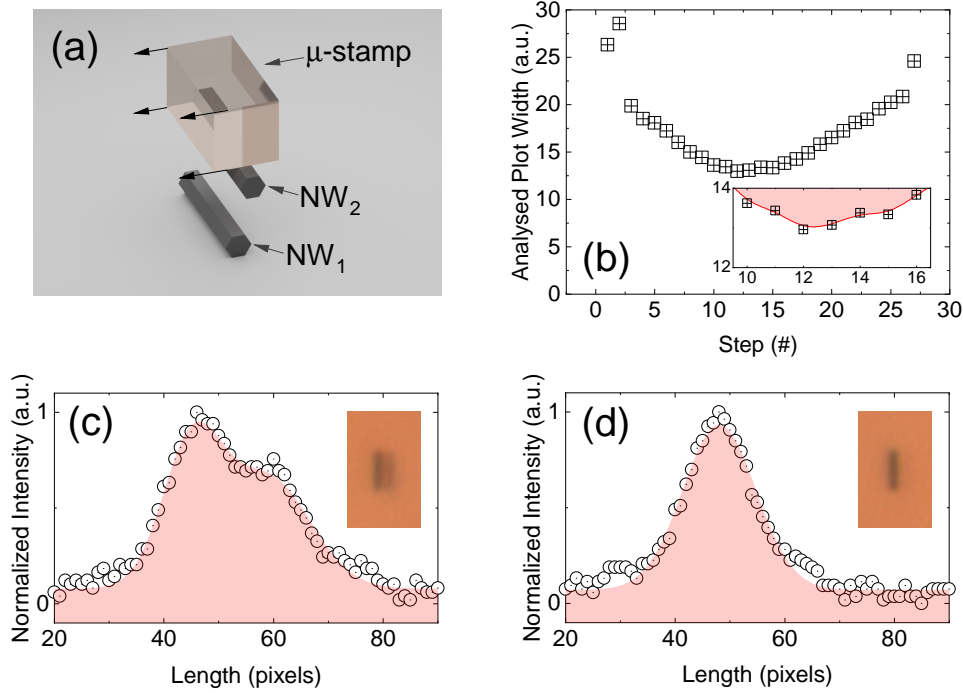


Figure 2.16: (a) Schematic diagram of the process developed to achieve sub-micrometric NW integration by means of TP. A first NW laser (NW<sub>1</sub>) is integrated in the receiving substrate. A second NW laser (NW<sub>2</sub>) is captured by the  $\mu$ -stamp from its original substrate and brought above the location of (NW<sub>1</sub>). NW<sub>2</sub> is moved across NW<sub>1</sub>'s location in steps of 100 nm with images being captured at each step. The images are used to build intensity maps, such as that in (b) to find the position of maximum overlap between the two NWs (zero-offset position). (c and d) Intensity profiles obtained (from the inset images) for the positions of maximum overlap between NWs (c) and a location where the NWs show a large positional offset.

of the second NW (NW<sub>2</sub>). This is picked up with the same orientation as NW<sub>1</sub> using the same polymer  $\mu$ -stamp, as depicted in Fig. 2.16(a). In the next step, the two NWs, NW<sub>1</sub> which is already integrated in the substrate and NW<sub>2</sub>, captured by the polymer  $\mu$ -stamp and located above NW<sub>1</sub> are aligned parallel to each other. At last the TP toolset is controllably moved laterally in steps of 100 nm to sequentially shift the position of NW<sub>2</sub> across the location of NW<sub>1</sub> in the substrate and a micrograph is captured at each of these scanning steps.

The algorithm of the developed alignment technique analyses the micrographs cap-

tured at each step and calculates the overlap width between the NWs. An example of the calculated overlap between the NWs over various scanning steps is shown in Fig. 2.16(b). In the latter, the smaller the calculated value, the higher is the overlap between the two NWs. For instance, Fig. 2.16(c) shows the processed intensity from the micrograph captured at the start of the alignment process (shown in the inset) where the two NWs are misaligned and do not overlap with each other, as a result the plot in Fig. 2.16(c) shows two peaks, one per NW. Fig. 2.16(d), on the other hand, plots the processed intensity from the micrograph captured at a different scanning step (see inset) showing a single peak as the two NWs are perfectly overlapped in this second case. By processing the captured images at the different 100 nm scanning steps we can create a plot showing the overlap distance in pixels, as shown in Fig. 2.16(b). Each point on the plot shows the processed profile at a given scanning step: the lower the analyzed plot width, the larger the overlap between NWs.

For each scanning step the full width at half maximum (FWHM) of the captured micrograph's intensity profile is calculated. The step with the lowest FWHM is then selected as the exact position where two NWs are fully aligned (i.e. arranged at the same lateral position one atop the other). Once the devices are aligned, we define a target separation, which will correspond to the separation between the centroids of both NWs. Next, we move the stage of the TP toolset by a distance equal to the desired separation between the devices and print NW<sub>2</sub> controllably and precisely at that target position. It should be noted that the accuracy of this integration technique depends on the camera's pixel size and the ability to resolve edges of NWs. Since, these define how 'accurately' we can see/record a NW at each scanning step.

To estimate the positioning accuracy of the reported NW alignment and integration

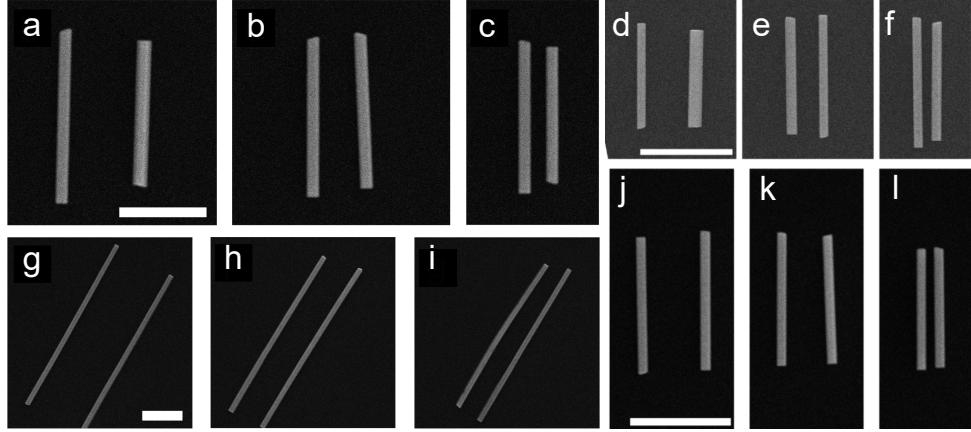


Figure 2.17: (a-l) SEM images of fabricated laterally-aligned InP NW laser pairs on a Si substrate with distinct spacings of 3, 2 and 1  $\mu\text{m}$  between devices. Scale bar in (a) corresponds to images (a-c), scale bar in (d) corresponds to images (d-f), scale bar in (g) corresponds to (g-i), and scale bar in (j) corresponds to images in (j-l), respectively. Scale bars = 5  $\mu\text{m}$  (a-f, j-l) and 2  $\mu\text{m}$  (g,h,i).

technique, we fabricated two different types of NW arrays, with target small and large micro-metric separations between devices. These were fabricated on a Si substrate and built using InP NW lasers of two dimensions ('long' NWs: diameters  $\sim 260$  nm, lengths  $\sim 10$   $\mu\text{m}$ ; 'short' NWs: diameters  $\sim 435$  nm, lengths  $\sim 6$   $\mu\text{m}$ ). The first array consisted of NW pairs integrated with target reduced separations between NW centroids (varying from 1 to 3  $\mu\text{m}$ ). For this first case, the highest optical magnification of the camera on the TP toolset (50%) was used. This resulted in the reduction of the field of view but increased the relative size of the nanowire devices on the captured images. By measuring calibrating structures built by means of e-beam lithography (across the whole field of view) on a test sample, we were able to estimate that the average relative pixel size in these captured images is equal to  $\sim 200$  nm. The second NW laser array was fabricated with larger target separations between the individual NWs growing from 10 and 40  $\mu\text{m}$ . In this second case, a reduced magnification was used in the TP toolset camera for a larger field of view (given the much larger NW separations). As a result, for this second

array type the single pixel size was increased to  $\sim 350$  nm. Once these two types of NW laser arrays were fabricated using the alignment and integration technique previously defined in this section, these were taken to the SEM system for analysis. This was done to calculate the offset between actual achieved and target NW separations (for all integrated devices) in the arrays. This in turn permitted to determine the accuracy of the developed NW alignment and integration technique.

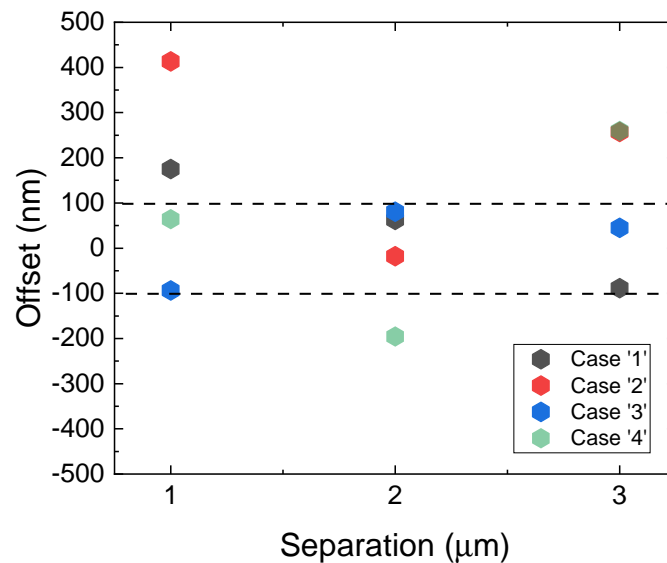


Figure 2.18: Transfer-printing results of 12 NW devices of various dimensions (shown in Fig. 2.17). The accuracy was estimated by comparing measured positional offsets between two NW devices from their target separations of 3, 2 and 1  $\mu\text{m}$ , as shown in Fig. 2.17.

Figs. 2.17 show the fabricated arrays comprised of pairs of *InP* NW lasers (presented above) built with selected separations varying from 1 – 3  $\mu\text{m}$ . The offset between the aimed and achieved NW separations (measured between NW centroids) was used to calculate accuracy of the alignment technique. Fig. 2.18 shows the calculated offsets between target and actual separations between the NWs in the fabricated pairs. From Fig. 2.18 we conclude that the printing accuracy for the developed alignment technique for small NW separations was very high in all cases and systematically below 500 nm.

In Fig. 2.18 Cases ‘1-4’ referred to the different fabricated systems shown in Figs. 2.17. The calculated average offset values for all NW pairs in the 4 fabricated arrays with small separations between devices was calculated to be equal to 80 nm with  $\sigma$  of 165 nm. We have assessed our printing accuracy using two values: average offset and standard deviation ( $\sigma$ ). The average offset is calculated by averaging positional offsets of all printed devices and it shows a systematic shift in direction relative to a target location. The standard deviation ( $\sigma$ ) is calculated using statistical tools and shows the dispersion of a set of positional offsets of the printed devices.

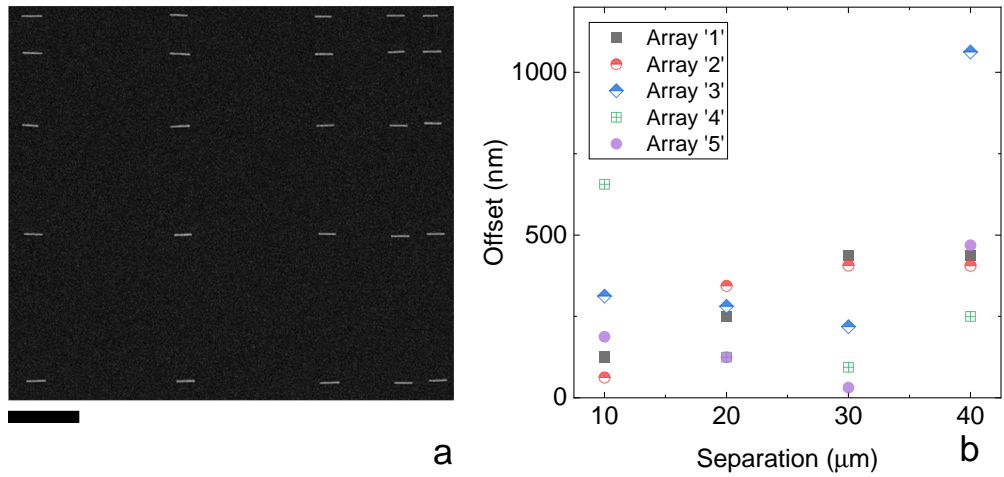


Figure 2.19: (a) Analysis of the positioning accuracy for all NWs in the fabricated 2D NW laser array whose SEM image is shown in (b). Scale bar = 20  $\mu\text{m}$ . The 5x5 array was fabricated on a *Si* substrate using *InP* NW lasers (435 nm diameter and 5  $\mu\text{m}$  long) with larger micrometric spacing between individual NWs growing gradually from 10 to 40  $\mu\text{m}$  in steps of 10  $\mu\text{m}$ .

To demonstrate the versatility of our alignment and integration technique, we have fabricated a second type of NW array with large micrometric separations between the individual elements. Achieving high NW integration precision also for larger spacings between individual NWs is also of great importance. This would be particularly useful for fabrication of hybrid large-scale NW-based systems, where all NWs are placed at precise target locations in pre-selected surface before further device growth processes are

carried out (e.g. metallic contact growth). Fig. 2.19(a) shows an SEM micrograph of a fabricated 2D NW array. In the latter, the individual columns were formed sequentially, integrating selected NWs with growing separations between devices equal to 10, 20, 30 and 40  $\mu\text{m}$ , respectively. As a result, in the array of Fig. 2.19, 25 NWs were integrated onto a Si substrate by means of TP. The top NW of each column was used as the initial reference point to integrate the second NW. After this, the third NW was positioned using the second one as the reference point and so on. Therefore, with this selected array architecture we obtained 20 samples of precisely aligned and integrated NW devices. We must note that, the estimation of the accuracy of the alignment and integration technique for this second array with larger separations between devices was done in the same way as in the previous example. Fig. 2.19(b) shows a graph with the estimated positional offsets between target and achieved NW separations. From the estimated accuracies, it can be concluded that in 19 of the 20 NWs, highly-precise integration with sub- $\mu\text{m}$  positioning resolution was achieved. Moreover, most of the devices were integrated with a positional accuracy below the 500 nm level. The average calculated offset was found to be equal to 94 nm with a  $\sigma$  of  $\sim 370$  nm, with a sample size of 20 NWs. This result outlines a direct relationship with the pixel size that was used in these alignment estimations.

The presented results indicate the achievement of sub- $\mu\text{m}$  positioning accuracy of transfer-printed NW lasers. Our method of aligning the NW devices by calculating the FWHM could be adopted by many systems currently using transfer-printing or any other heterogeneous integration technique counting with an embedded camera system.

To estimate the positioning accuracies of the transfer-printed laterally-aligned NW pairs, we developed a computer-run algorithm to process the SEM images used to

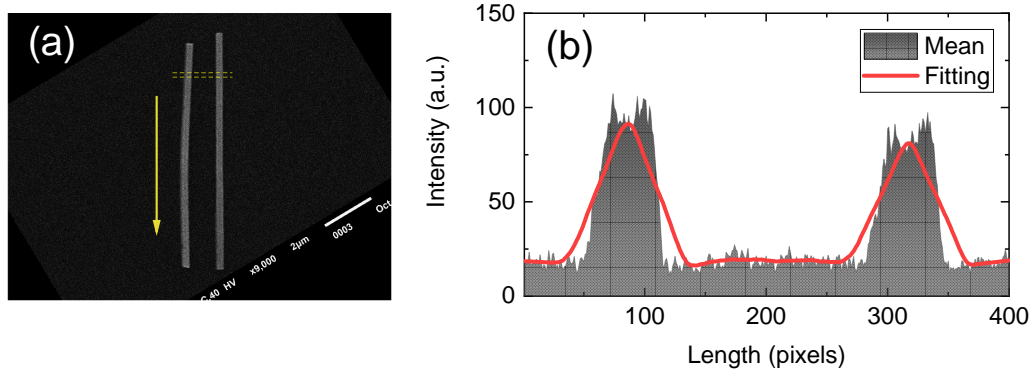


Figure 2.20: (a) SEM image of a fabricated laterally-aligned NW laser pair. *InP* NWs with dimensions of  $10\ \mu\text{m}$  in length and  $260\ \text{nm}$  in diameter were used to fabricate the NW array. (b) Processed image profile obtained at the scanning point indicated by the dashed yellow lines in the NW laser pair shown in (a). It should be noted that the specific pixel size for each of the different SEM images analysed was calculated from known distances within the images.

inspect them. This algorithm was designed to scan the SEM images of the fabricated laterally aligned NW laser pairs (as in Fig. 2.20(a)) to estimate the average distance between the centroids of the two devices forming them. This process was carried out at various scanning steps along the length of a NW laser pair. For each of these steps a processed image profile was generated. As an example, Fig. 2.20(b) shows the image profile obtained for the scanning step carried out at the position in the NW laser pair indicated by a dashed line in Fig. 2.20(a)). Specifically, this process was repeated 20 times along the length of a laterally-aligned NW laser pair following the scanning direction marked by the yellow arrow in Fig. 2.20(a). The generated image profiles were then fitted with a smoothing function (Savitzky-Golay filter) and it was verified that the centre point was located in each instance. These peaks were in turn used as the location of the centroids of the two devices in the NW laser pair. The separation between the two peaks therefore determined the separation distance between the centroids of the two NW for a specific scanning position. The final separation between the two integrated NWs forming a laterally-aligned NW laser pair was calculated averaging the obtained

separation values for the 20 scanning steps considered.

## 2.5 Conclusion

In this chapter we have described and discussed the developed TP technique at the nanoscale for the heterogeneous integration of semiconductor NW devices. We have also introduced the underlying concepts, applications in photonic device assembly and recent advances in the field. Furthermore, other existing techniques for transferring NW devices were discussed and compared to our TP technique. From this comparison, we can conclude that TP offers important advantages that have high potentials for a broad range of applications in nano-/micro-devices integration. These include high-accuracy alignment and rotational control of target devices, an ability to record positions of target devices during the transfer process and flexibility when fabricating patterns and arrays of devices. Furthermore, we have introduced the design and fabrication steps for the development of the polymeric  $\mu$ -stamps used in our TP technique at the nanoscale. Lastly, we have discussed the TP protocols developed for the controllable capture of NWs from their donor substrate for their subsequent release onto receiving surfaces.

In the second part of the chapter, we have demonstrated the ability of our TP technique for the precise integration of semiconductor NWs of different materials and dimension onto a rich variety of receiving surfaces, e.g. polymers, diamond membranes,  $SiO_2$ , gold and  $Si$  substrates, and metals. Importantly, we also show that our nanofabrication technique does not affect the lasing performance of the transfer-printed NW lasers, as these retain their emission properties at room temperature. We also demonstrate that the TP technique enables controllable integration of selected NWs with target orientations and forming spatial patterns (arrays) onto pre-fabricated surfaces

and circuitry (e.g. gratings, Bow-Tie antennas, metallic electrodes). These results open new routes for a variety of potential applications in complex nanophotonic circuitry, where NWs are used as building blocks for future nano-scale optoelectronic systems.

The final section of the chapter discusses a newly developed NW alignment technique incorporated into the TP toolset. Using this technique, we achieved systematic and computer controlled positioning of individually-selected NWs onto a target location with controlled separation between devices whilst retaining sub- $\mu\text{m}$  integration accuracy. Moreover, the technique can be used to form both large arrays and compact systems using semiconductor NWs.

## Chapter 3

# Characterisation of NW Laser Systems

In this chapter the characterisation methods and techniques used to analyse the NW-based systems and devices of this work are described. This section explains the optical excitation technique used to achieve room-temperature lasing emission in semiconductor NWs, and the design of the  $\mu$ -photoluminescence ( $\mu$ -PL) setup used in this work to that end. Additionally, the calibration and alignment techniques used throughout the project are also discussed in this chapter. Finally, the processes used for the characterisation of NW lasers after hybrid integration on heterogeneous surfaces are reviewed.

### 3.1 Micro-Photoluminescence ( $\mu$ -PL) Setup

Micro-photoluminescence is a versatile technique which enables to study light emission from materials and devices by means of optical excitation [81]. The semiconductor NWs of this work were fabricated from direct bandgap materials: InP [54, 55] and GaAs [85]. This, added to the unique structure of the NW devices, forming Fabry-

Perot cavities, permitted the achievement of room-temperature lasing emission from these nanostructures by optically exciting them with photons of energy higher than their bandgap. We therefore designed and built a  $\mu$ -PL setup allowing the efficient and non-destructive characterisation of semiconductor NW lasers at room temperature. Such system is also used to characterise and investigate the performance of the perovskite quantum-dots ( $CsPbX_3$ ) [107] that are described in Chapter 6.

The schematic diagram of the implemented  $\mu$ -PL setup is shown in Fig. 3.1. This included two different pulsed lasers operating respectively at the wavelengths of 532 and 355 nm. The visible light (532 nm) pump laser system is mostly used for the optical excitation of the semiconductor NW lasers used in this work. The laser is a pulsed diode-pumped solid state microchip laser yielding optical pulses with a width of 0.713 ns (Full-Width Half Maximum, FWHM) at a repetition rate of 7.14 kHz. The ultraviolet (355 nm) laser system is a frequency tripled Q-switched Nd:YVO<sub>4</sub> laser yielding 18-ns long pulses (FWHM) with a repetition rate of 28 kHz. The second pump laser system is used for the room-temperature optical excitation of the perovskite quantum dot samples, described in Chapter 6.

Half-waveplates ( $\lambda/2$ ) and polarizing beam splitters (PBS) were included at the output of both pump laser systems, as shown in Fig. 3.1. These components allow to control the polarization and the energy of the optical pulses injected into the main part of the  $\mu$ -PL setup system. Control of the pump light polarization is somewhat essential for NW laser structures; those have been reported to be highly sensitive to pumping light polarisation given their reduced (nanometric) widths [81]. The polarisation of the pumping light was set to be linear at all times during the experiments. Importantly, to reduce operation risks, the additional outputs from the polarization beam splitters

not used in the setup were directed to beam dumps.

A Flipping Mirror (FM) enables to switch between the two pump lasers for their subsequent injection into the main part of the setup. A neutral density filter (NDF) was included to reduce the injected energy from the pump lasers, since the two are emitting at different power rates. Thus, the wave-plates are used to attenuate a portion of the injected light to avoid damaging components in the setup. Lenses  $L_1$  and  $L_2$  are used to focus the pumping light onto the attenuation wheel (AW). By changing the set angle on the attenuation wheel it is possible to control the power injected into the NW lasers or other optically pumped nanophotonic devices. A Beam splitter ( $BS_1$ ) separates the injected light into two different optical paths. This is aligned so that the light from each of the two pump lasers (visible and UV) is separated and directed to two different stages that hold the samples for characterisation. Two different optical objectives ( $OB_1$  and  $OB_2$ ) are used in combination with translational stages (TS) and implemented periscope systems (PS). These allowed to simultaneously pump the investigated NW lasers and collect their emitted light via the same optical path. The optical objective used for the UV excitation part of the setup had a magnification of 60x and a numerical aperture (NA) of 0.85. This allowed for the characterisation of structures with reduced dimensions (measured beam spot of  $\sim 1 \mu\text{m}$ ) structures, as it provides a small beam size and enhanced spatial resolution. The other optical objective ( $OB_2$ ) used for the optical excitation of NW lasers with the green-light (532 nm) laser system, has a magnification of 20x and a NA of 0.5. This enabled the efficient optical excitation of ultra-small NW lasers, as it yielded a measured beam size of  $1.54 \mu\text{m}$  (FWHM), comparable in size to the dimensions of the studied NWs ( $\sim 300 - 900 \text{ nm}$  in diameter and lengths  $2 - 20 \mu\text{m}$ ). The pump laser spot size was measured to be

equal to  $1.54 \mu\text{m}$  using image correlation techniques, as discussed in ref. [97]. This was done by measuring the relative pixel size of an image of the laser pumping spot and comparing it with that of a reference structure of known size.

Optical filters (OF) of different wavelengths depending on the specific pump laser were used to block the excitation light in the detection side of the setup. Thus, only the emitted light from the characterised nano-photonic structures was sent for analysis. A beam splitter ( $\text{BS}_2$ ) is used to separately send the light from the characterised nanostructures into a CCD camera and a fibre-coupled high-resolution spectrometer (SP). Another lens ( $\text{L}_3$ ) is included to focus the collected light into a multimode optical fibre ( $d = 200 \mu\text{m}$ ). The CCD camera is used to collect the emitted light from the characterised structures, enabling the imaging of the lasing emission of the NW lasers of this work, as well as permitting the alignment of the pumping light spot during characterisation. A LED is included in the setup to illuminate the system; hence allowing the capture of brightfield micrographs and the clear visualisation of the area of the sample under analysis: the LED light was injected using a beam splitter ( $\text{BS}_3$ ).

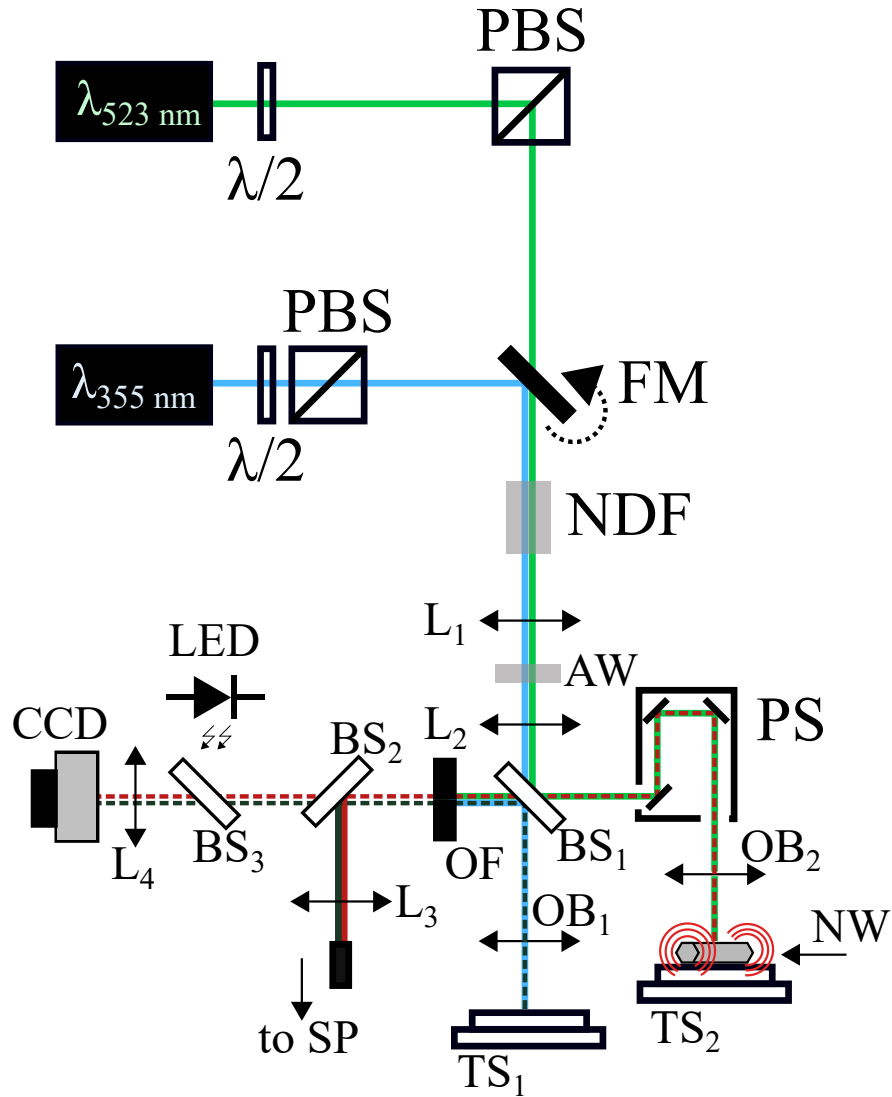


Figure 3.1:  $\mu$ -PL setup used for the characterisation of NW laser systems: PL - Pump Laser,  $\lambda/2$  - Half-Waveplate, PBS - Polarization Beam Splitter, FM - Flipping Mirror, NDF - Neutral Density Filter, L - Lenses, AW - Attenuation Wheel, PS - Periscope, TS - Translational Stage, CCD - Charge-coupled Device Camera, OF - Optical Filter, BS - Beam Splitter, LED - Light Emitting Diode, NW - Nanowire Laser, SP - Spectrometer

An edge detection module (EDM) was built and incorporated into the  $\mu$ -PL setup (Fig. 3.1), as shown in Fig. 3.2. This allows collecting the light emitted directly from the facets of an optically excited NW laser. Here, a NW is optically excited perpendicularly using objective (OB<sub>2</sub>), and the light emission from the NW's facet is collected for analysis using the objective. OB<sub>3</sub> (see Fig. 3.2) was embedded onto a translational stage for alignment purposes. OB<sub>3</sub> has a magnification of 20x, NA of 0.3

and focal length 24.6 mm. A beam splitter ( $BS_4$ ) separated the light collected from the NW's facet into two paths which were sent respectively to a CCD camera and to a fibre-coupled spectrometer (SP). A Lens ( $L_5$ ) was used to focus the collected light into an optical fibre (diameter = 50  $\mu\text{m}$ ) coupled to a spectrometer. The designed system permitted full alignment in all three dimensions (XYZ). The measurements obtained with the setup are discussed in Chapter 4.1.

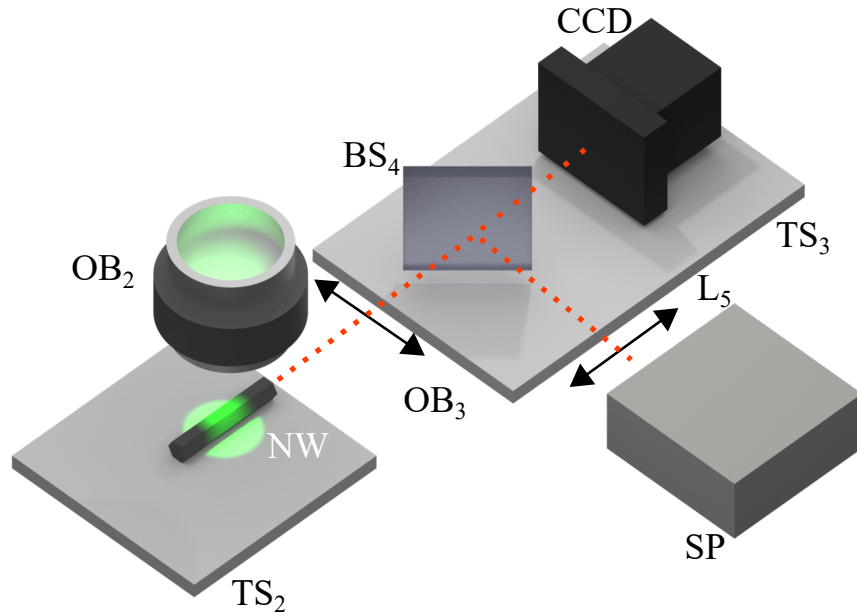


Figure 3.2: Designed Edge-Detection module incorporated into the  $\mu$ -PL setup for the direct detection of the NW lasers' facet emission: TS - Translational Stage, OB - Optical Objective, CCD - CCD Camera, SP - Spectrometer, L - lens, BS - Beam Splitter, NW - Nanowire Laser

### 3.1.1 Optical Excitation of NW Lasers

As previously mentioned, optical excitation is a very efficient and reliable technique to assess the light emission properties and performance of NW lasers and other photonic devices. Using this technique with the  $\mu$ -PL setup described in the previous section we were able to achieve lasing emission at room-temperature from different types of NW lasers without damaging them and analyse their light emission. Our analysis included

the capture of dark-field micrographs and the measurement of the lasing and PL spectra and lasing threshold of the NW lasers. As it had been previously discussed in Chapter 1, to excite NW devices, those had to be detached from their growth substrate and transferred in bulk onto low-index substrates where the NWs laid down horizontally. In such configuration a semiconductor NW forms a FP cavity along its longitudinal axis. Moreover, the large refractive index contrast between the *InP* NW (for example,  $n_{InP} = 3.4$ ) and air ( $n_{air} = 1$ ) yields high reflectivity ( $\sim 0.3$ ). This enables the NW facets to act therefore as highly reflective mirrors and also provides high confinement within the NW's cavity for the supported modes [108]. This results in reduced levels for lasing threshold enabling the achievement of room-temperature coherent light emission with the semiconductor NWs used in this work. Fig. 3.3 shows a schematic diagram of an optically-excited semiconductor NW laser. A pump lasing beam at the wavelength of  $\lambda_p$  is focused onto the centre of the NW cavity. The pumped light is absorbed by the NW, triggering the emission of higher wavelength photons (at  $\lambda_e$ ) which propagate along the longitudinal direction of the NW (forming the cavity) before escaping through the facets. When the optical pumping energy exceeded the lasing threshold of the NW, the latter yielded coherent light emission through the facets at  $\lambda_e$ , as depicted in the diagram of Fig. 3.3.

Following their optical excitation the different NWs of this work provide lasing emission at a wavelength related to their specific material bandgap. This optical excitation technique used here is indeed to date the most commonly used method for NW laser characterisation. The technique is efficient, does not damage the devices and does not require any additional complex fabrication steps. To add, this is discussed in greater detail in Chapter 5.2 of the thesis. Here is worth mentioning that the development of

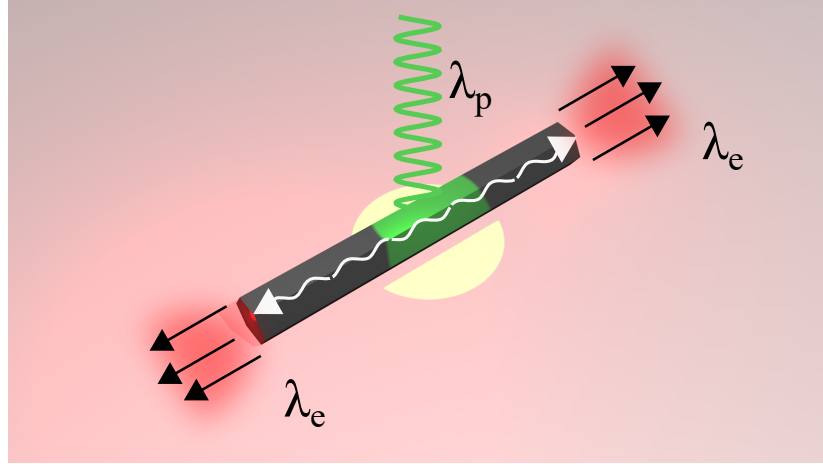


Figure 3.3: Schematic diagram of an optically excited NW laser. The device is subject to optical pumping ( $\lambda_p$ ) and produces lasing emission through its facets at a higher wavelength ( $\lambda_e$ )

functional systems with NW lasers will require the devices to be electrically-injected. We should note that electrical excitation of NW lasers remains to date a fundamental challenge, see ref. [109] for a review. One of the reasons for this is the high cavity losses in NW laser devices and the high complexity in developing high quality electrodes to effectively drive these ultrasmall laser sources. Important research efforts are being currently dedicated to tackle these issues to deliver practical and efficient electrically-injected NW lasers for functional systems reaching the market.

Although the electrical excitation of semiconductor NW devices is highly complex (to the best of our knowledge this was only demonstrated once in the literature ref. [16]) it is still likely that this challenge will be overcome in the future. In our view, the pick-and-place technique investigated in this thesis might play a critical role in the realization of this key objective. The ability to position NW devices vertically on target surfaces can ease or reduce the multi-step fabrication processes. For example, in Chapter 4 we show how to integrate NWs on electrodes. The attractive ability to integrate NWs and other opto-electronic devices at a precise location and between layers during their

multi-stage growth (when necessary) offers a variety of possibilities for the realization of novel devices including future electrically-driven NW laser structures. Hence, given the current limitations in electrically-injected devices and the benefits of optical excitation techniques for our work on heterogeneous integration of semiconductor NWs, it was decided to use exclusively optical pumping techniques for the characterisation of NW lasers during this work. Only a single successful demonstration that author is aware of demonstrating an electrically excited NW laser is reported in the literature so far, see ref [16]. Moreover, for our work the use of pulsed-laser sources, as oppose to continuous wave (CW) lasers to excite our semiconductor NWs was crucial. This ensured that no excessive heat is built inside the NW's cavity which could result in NW overheating and further damage. During our measurements we estimated the optical excitation power using the technique provided in ref. [54]. This was used in turn to calculate the threshold energies required to achieve lasing in these nanoscale devices.

It is worth noting that there are two ways of exciting NW lasers by means of optical pumping. The first one is by injecting light uniformly along the length of the NW laser, see ref. [57, 110] for NW. The second method is achieved by injecting light perpendicularly a specific area of the NW. For this project and for the versatility of the measurements in terms of light collection, we have relied on the second method. In the case of OB<sub>1</sub>, with a reduced size beam spots (less than 1  $\mu\text{m}$ ) it will give a non-uniform gain distribution. This indeed will affect the mode selection during the excitation process. As a result, OB<sub>2</sub> was used as it offers a size of the beam spot at around 1.56  $\mu\text{m}$ . Thus, allowing to get repeatable results, as it would cover a larger area of the NW.

### 3.1.2 Spectral Analysis and Imaging of NW Lasers' Emission

There is a variety of information one can get from the optical excitation of NW lasers. To characterize the lasing properties of these devices, in our work we have focused on the spectral analysis and imaging of their coherent light emission. This allowed us to determine the emission wavelength, characterize the different emission modes, evaluate the lasing threshold characteristics of these nanolasers as well as capture brightfield and darkfield micrographs of their emission. For the characterization processes, the  $\mu$ -PL and NW samples were aligned so that the optical excitation beam would be purposely focused on the middle of a NW. By changing the fixed angle on the attenuation wheel the fluence with which the NWs are optically pumped will increased/decreased. Additionally, a half-waveplate included in the setup permits to control the polarization of the optically-pumped light into the NW lasers under analysis.

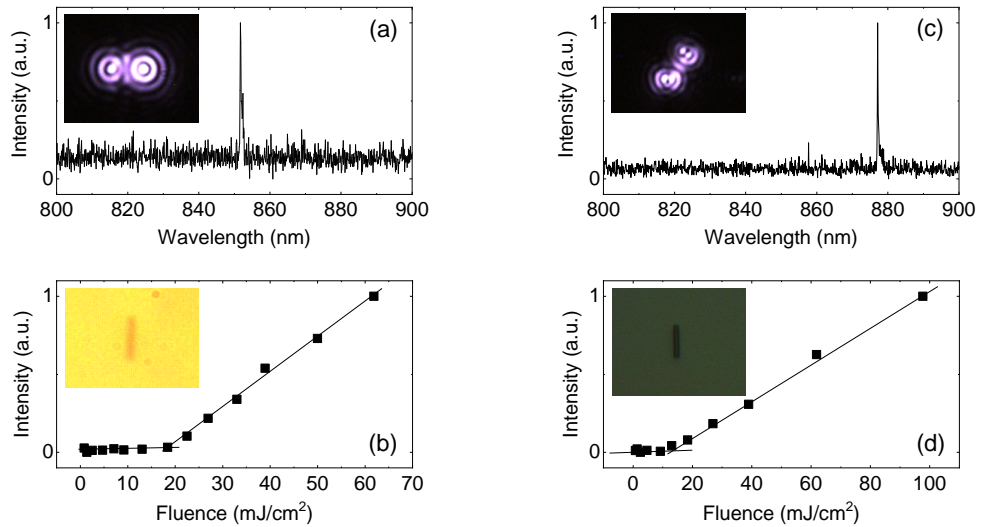


Figure 3.4: Characterisation results of two *InP* NW lasers lying on an aluminum (a,b) and a *SiO<sub>2</sub>* (c,d) substrate obtained with the  $\mu$ -PL setup of Fig. 3.1. (a,c) showing lasing emission spectra and (b,d) threshold curves. Insets in (a,c) and (b,d) are dark- and bright-field micrographs, respectively.

Figs. 3.4 and 3.5 provide examples of typically measured results obtained with

the  $\mu$ -PL setup of Fig. 3.1. Specifically, Fig. 3.4 shows the characterisation results obtained following the optical excitation of individual *InP* NW lasers (dimensions:  $d = 435$  nm, length  $\sim 5$   $\mu$ m) on *SiO*<sub>2</sub> and Al substrates.

Figs. 3.4(a) and 3.4(b) show respectively the measured spectra and threshold curves obtained for a single NW device on Al substrate. Additionally, the insets in Figs. 3.4(a) and 3.4(c) are brightfield micrographs (captured with the CCD camera on the  $\mu$ PL setup) of the corresponding *InP* NW lasers under analysis lying on their specific substrate. In Figs. 3.4(a) and 3.4(c) each point on the plots corresponds to the total integrated emission power from the *InP* NW laser at the different values of excitation fluences. This total emission power is directly calculated measuring spectra for the different excitation fluence values considered and by integrating the emitted light intensity by the NW lasers around their lasing wavelength range.

Using this method, the curves in Figs. 3.4(b) and 3.4(d) were produced allowing to determine the threshold values in optical excitation upon which room temperature lasing onset from the NW lasers was achieved. Specifically, Fig. 3.4(b) reveals that the lasing threshold value at room temperature for the characterised bulk *InP* NW laser on an Al substrate was equal to approx.  $18$  mJ/cm<sup>2</sup>, whereas Fig. 3.4(d) showed a considerably reduced lasing threshold, of approx. to  $10$  mJ/cm<sup>2</sup>, for a bulk *InP* NW laser on a *SiO*<sub>2</sub> substrate.

There are several potential reasons for that: (1) due to the inhomogeneous broadening during the growth process [41], NW lasers, even from the same growth batch, might possess different parameters (e.g. diameter, length, facet quality etc.). Hence, each unique NW device has its own threshold and emission wavelengths [110]. This, is discussed in Chapter 5.2 in more detail along with a technique developed to overcome

this issue; (2) the substrate materials ( $Al$  and  $SiO_2$ ) have different losses. Moreover, even the difference in refractive indices between the two substrate with  $n_{Al} \sim 2.5$  and  $n_{quartz} \sim 1.45$  results in different modes being emitted from the wires [111,112]. Figs. 3.4(a) and 3.4(c) show respectively high resolution spectra for the characterised InP NW lasers on  $Al$  and  $SiO_2$ , measured at the highest excitation fluence values indicated in Figs. 3.4(b) and 3.4(d) respectively. In both cases, single-mode emission with narrow lasing peaks at the wavelengths of 855 nm and 875 nm respectively are obtained from the two characterised InP NWs lasers. Finally, the insets in Figs. 3.4(a) and 3.4(c) depict captured darkfield micrographs for the investigated InP NWs revealing the characteristics of their lasing emission. The latter is obtained from the devices' end-facets and produces typical diffractive patterns revealing the coherence of their emitted light [55].

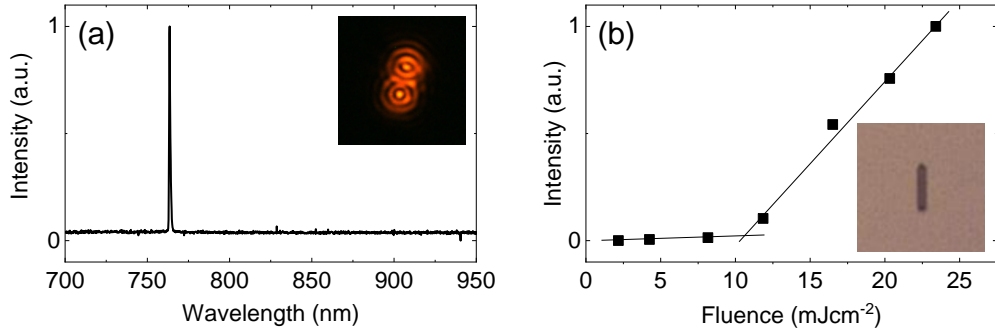


Figure 3.5: Characterisation results of a single MQW GaAs-AlGaAs NW laser lying on  $SiO_2$  substrate. (a) showing lasing emission spectra and (b) threshold curves. Insets in (a,b) are dark- and bright-field micrographs, respectively.

Additionally, Fig. 3.5 collects the characterisation results obtained from a MQW  $GaAs$  NW laser [57, 85] with a diameter of  $d = 450$  nm and a total device length of  $\sim 5$   $\mu m$ . The latter was individually-selected from its original substrate and transfer-printed onto a receiving  $SiO_2$  substrate for analysis. Fig. 3.5(b) shows the measured threshold curve obtained for this device, showing a lasing onset point at an excitation

fluence value of  $\sim 11$  mJ/cm<sup>2</sup>. The inset in Fig. 3.5(a) shows a darkfield micrograph of the MQW *GaAs* NW laser captured when the device was optically excited with a fluence value of 25 mJ/cm<sup>2</sup>. This inset also reveals for the *GaAs* NW under analysis (as it was also the case for the *InP* NW lasers in Fig. 3.4) light emission through the device's end-facets and the observation of the typical diffractive pattern characteristic of lasing emission. Fig. 3.5(a) plots the measured optical spectrum for the MQW *GaAs* NW laser at that same fluence value of 25 mJ/cm<sup>2</sup>. The inset in Fig. 3.5(b) shows a brightfield micrograph of the *GaAs* NW under analysis which is lying down horizontally on the *SiO*<sub>2</sub> substrate.

### 3.1.3 Measurement Techniques

Spectrometers were used to analyse the emission wavelengths and to measure the lasing thresholds of the semiconductor NW devices used during this work. In particular, we have made use of two different spectrometers: Ocean Optics HR4000 and a Jobin Yvon TRIAX 550. We should also point out that during the course of the PhD project, we also used these spectrometer systems to characterise other types of photonic nanostructures (e.g. perovskite quantum dot crystals) and III-V group NW lasers with various emission wavelengths.

The Ocean Optics system has a detection wavelength range going from 300 nm to 1200 nm and provided a spectral resolution of 2.5 nm. Even though, the resolution of this spectrometer is relatively low to allow for the full spectral characterisation of NW laser devices (where FWHM of lasing modes is  $< 1$  nm), this very compact apparatus still enabled to detect the individual emission peaks of NW lasers in a fast and efficient manner for initial rapid characterisation measurements over long wavelength ranges.

The Jobin Yvon TRIAX 550 spectrometer, shown in Fig. 3.6, was very extensively

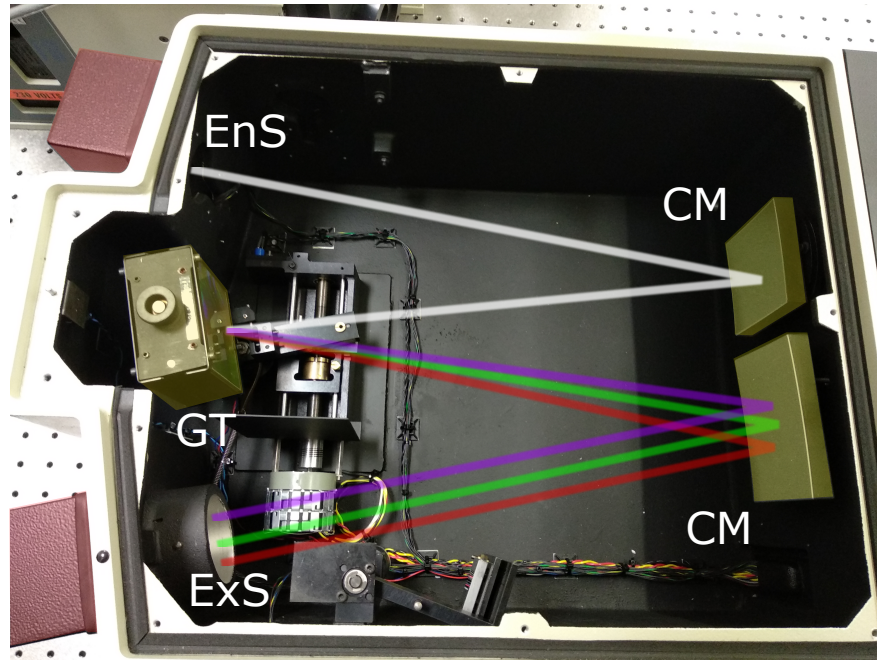


Figure 3.6: Image of the internal structure of the TRIAX 500 spectrometer with a diagram of the optical path for the signal under analysis.

used along our work to characterise the spectral properties of NW lasers (forming the major focus on this work) as well as for the activities with perovskite nanostructures. The TRIAX 500 system is a fully computer-controlled system which consisted of a single entrance slit and 2-output ports (front and side) which could be switched via a computer controlled module. The side exit port was connected to a photomultiplier tube (PMT) detector operating in the wavelength range expanding from 190 nm to 860 nm. The front port was coupled using a in-house built alignment system to a detector module consisting of two sensors: a silicon (*Si*) detector operating from 200 nm to 1100 nm and an *InGaAs* sensor operating in the range going from 950 nm to 1700 nm. This purposely built system consisted of a 3-axis stage enabling the alignment of the exit aperture of the spectrometer with the entrance apertures of the sensors. This detector system was installed onto the TRIAX 500 spectrometer system by matching the focal lengths and apertures externally coupled to the front exit of the spectrometer.

Additionally, the spectrometer was equipped with three grating turrets (3600 g/mm, 1200 g/mm, 300 g/mm) for different resolution and measurement ranges. As a result of all this, the TRIAX 550 spectrometer allowed detection over an extended wavelength range covering from 190 – 1700 nm, providing a maximum spectral resolution of 0.07 nm.

The combination of these two spectrometer systems allowed both the analysis of the light emitted by NW lasers (and other nanostructures) with a higher resolution (TRIAX 550) and in a time efficient manner (OceanOptics) depending on the desired circumstances. Nevertheless, it should be pointed out that both spectrometer systems allowed to distinguish between the individual Fabry-Perot modes of the NW lasers of this work.

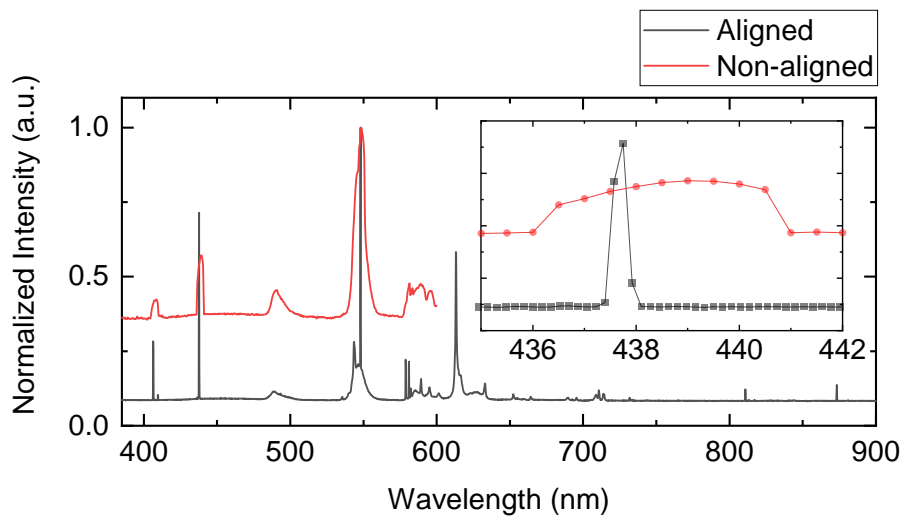


Figure 3.7: Fluorescent lamp spectrum measured from the TRIAX 550 system when the system is aligned (in black) or non-aligned (in red) accurately, affecting the systems resolution.

It is important here to emphasise the relevance of accurate optical alignment to obtain precise spectral measurements with the TRIAX 550 spectrometer. This instrument uses a combination of entrance and exit slits, turret, mirrors and grating for the

analysis of incoming light signals. A small light flux passing through the entrance slit is reflected from the collimating mirror and focused on the grating turret. There, the light is split into individual wavelengths and reflected back onto the second collimating mirror which will send the signal to the Exit Slit towards the detector. Next, only the line that corresponds to the correct position of the turret will have a precise angle to pass through the exit slit. In this way, only light of a certain wavelength will enter the sensors. As a result, the better the beam quality, the more resolved the signal will be, as any divergence in the beam will result in false signal readings. As an example of the latter, Fig. 3.7 shows two measured spectra of light signals with the system properly aligned (black) or non-aligned (red). Specifically, Fig. 3.7 plots measured reference spectra using a fluorescent lamp to generate a light signal with emission at well-known and precise wavelengths [113]. The two spectra in Fig. 3.7 clearly reveal the importance of accurate system alignment for precise readings and high resolution measurements. Moreover, the captured peak (inset of Fig. 3.7) at  $\sim 437.85$  nm corresponds to the  $_{80}Hg$  line at 436.6 nm. The spectrometer was then adjusted and calibrated accordingly to the known wavelengths from the lamp.

## 3.2 Scanning Electron Microscope (SEM)

In our work, various scanning electron microscope systems were used to obtain high-resolution images of the NW lasers investigated during this PhD project. SEM imaging was essential for the parts of our work related to the investigation of the nanometric positioning accuracy provided by our TP technique. Importantly, SEM provides a much better resolution when compared to standard microscopy using visible light to illuminate samples. SEM is based on the injection and scan of an electron beam into

the surface of a sample under analysis. This causes the release of secondary, back-scattered, Auger electrons, as well as, x-rays and energy which is absorbed by the sample. The released secondary electrons are captured by a detector allowing to form a high resolution image of the investigated sample. Since the wavelength of electrons is much more reduced than that of visible light, SEM allows to resolve and image features with increased resolution well below the optical diffraction limit. Hence, using this technique it becomes possible to clearly image the features and specific positions of individual NW lasers as well as to determine the separation between closely integrated devices. In order to obtain a clear and non-saturated image during the SEM imaging procedures, the NW samples were placed on a conductive substrate to avoid a charge build-up on the sample.

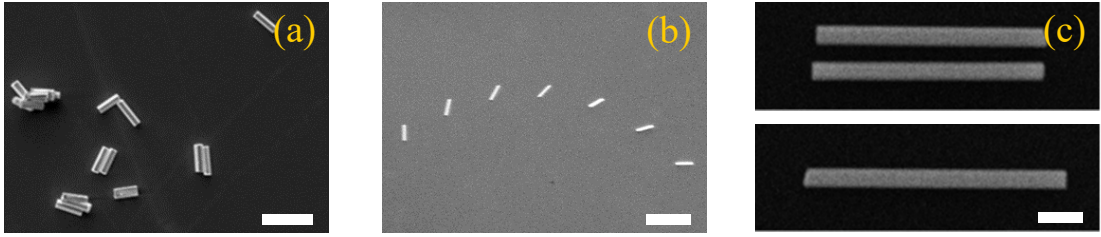


Figure 3.8: (a) NWs mechanically transferred onto a *Si* substrate. (b) *InP* NWs transfer-printed forming a 1D array with selected angle orientations. (c) top: two TP devices in a lateral configuration; bottom: a single *InP* NW laser.

Figs. 3.8 shows examples of SEM images depicting some of the NW laser systems investigated during this PhD project clearly revealing the strengths of the technique allows to resolve features with nanometric resolution. Fig. 3.8(a) shows multiple *InP* NW lasers horizontally disposed and scattered on a *Si* substrate, either individually or forming small clusters of devices, scale bar = 5  $\mu\text{m}$ . Fig. 3.8(b) shows a 1D array of *InP* NW lasers integrated on a *Si* substrate with a separation between NWs of 15  $\mu\text{m}$  and with controlled orientation angles from 0 to 180 degrees in steps of 15 degrees between adjacent devices. Fig. 3.8(c) shows two individual NW lasers integrated on

a *Si* substrate in a laterally-aligned configuration and with a separation between the NWs of  $1\ \mu\text{m}$ . The bottom plot in Fig. 3.8(c) shows an SEM image of a single NW laser on a *Si* surface permitting to clearly resolve its structural features. For this specific PhD project, various types of SEM systems were used: those are specified in different sections of the thesis.

## Chapter 4

# Nanophotonic Integrated Systems with Transfer-Printed Semiconductor Nanowires

In this chapter NW-based nanophotonic integrated devices fabricated using the TP system are demonstrated. Here, semiconductor NWs are used as building blocks in various miniaturized platforms demonstrating enhanced performance and target applications. Chapter 4 is topically divided into three sections, that are focused on presenting: (1) NW-waveguide (WG) coupled systems, (2) vertical lasing emission from coupled NW-Cat's Eye (CE) antenna platforms, and (3) enhanced THz detection using a 3D-cross NW Bow-Tie (BT) antenna system. The results in this chapter show how TP and NW lasers could be used to fabricate a next-generation of integrated NW-embedded systems by means of the deterministic pick and place TP technique of this project.

In the first part of the chapter nanowire-waveguide coupled systems are discussed. These were fabricated by integrating NWs with on-chip WGs following two coupling

methods: lateral and end-to-end facet. The two coupling methods are based on different NW-WG alignment approaches and potentially could be used for different applications and platforms. The versatility of the TP system allowed the practical demonstration of those two different methods, resulting in several NW-WG coupled systems which are presented below. Importantly, these demonstrated wavelength multiplexing, relatively long-propagation lengths, and stable NW-WG coupling under strong sample deformation.

In the second part of the chapter, complex devices demonstrating vertically emitting semiconductor NW lasers are presented. The design of the proposed system has a significantly reduced footprint and lasing threshold, compared to those of the same dimensions on planar substrates.

In the final part of the chapter, a multi-step process for the fabrication of 3D-cross integrated-NW THz detectors is presented. Here, the main emphasis is focused on showing how the pick-and-place TP technique achieved integration of NWs in 3-dimensions and demonstrated that it could be used as a tool for fabricating high-accuracy systems for THz sensing.

## **4.1 Integration of NW Lasers into Waveguide (WG) Systems**

The integration of micro- and nanoscale laser sources with on-chip photonic integrated circuits (PICs) is of great interest for applications from low-power, short haul optical interconnects [114] to point of use biosensor systems [115]. By locating laser sources directly on-chip, the critical alignment of fiber to waveguide couplers can be overcome and sources can be distributed arbitrarily across the chip, reducing packaging costs for

volume manufacture of such devices. In recent years, several reports showing NW-WG coupling were demonstrated [116–118]. These can be grouped into two main methods: direct growth of semiconductor NWs into passive waveguides [118,119] and mechanical transfer of NWs from their growth substrate to target devices [117,120]. Regrowth methods allow high accuracy alignment between physical structures on different material platforms through lithographic processes and have been reported with coupling efficiencies between NW array lasers and silicon waveguides of  $\sim 4\%$  [120]. However, these typically involve complex fabrication growth processes.

In this work, we have used TP to demonstrate the integration of NW lasers into waveguiding platforms showing that it is possible to produce coupled NW-WG systems with the technique. Moreover, the suggested method is much more flexible than the previously reported approaches, allowing to construct bespoke NW-WG systems beyond “single NW-waveguide designs” for different functionalities. For example, using the TP technique we demonstrated Y-junction waveguides and multiplexers with NW lasers.

To demonstrate our technique, *InP* NW lasers operating at near-IR wavelengths ( $\sim 880$  nm) were coupled in this work with pre-fabricated polymeric waveguides using the pick-and-place technique. Next, the printed NW laser devices were optically excited above their lasing thresholds and their guided light emission was investigated to confirm NW-WG coupling and analyze the coupling characteristics. Here, we used *InP* NW lasers with an average length varying between 4 - 6  $\mu\text{m}$  and diameters of  $\sim 435$  nm, with different light emission in the near-infrared region (850 - 900 nm) [55]. These nano-laser devices were selected for several reasons: their lasing properties and mode distribution has been investigated and is well-known [55], due to their dimensions and structure they do not deform during the transfer-printing processes. Moreover, the dimensions

of these InP NWs ensure the achievement of lasing emission at room temperature with reduced threshold energies for lasing [55]. All the aforementioned properties make them excellent candidates for the proof-of-concept demonstration of integrated coupled NW laser WG systems.

The micro-metric polymeric waveguides used during this activity, were fabricated using an in-house built laser-lithography setup [72]. The setup operation is based on a free-space optical system, an ultraviolet laser at the wavelength of 370 nm, and computer controlled positioning stages. The waveguide patterns were direct-written on a silica surface with spin-coated photoresist (SU-8) [72]. Then EC (developer) solvent was used to develop laser-written patterns. Since SU-8 is an epoxy-based photoresist: all parts which were laser-scanned with the lithography system become cross-linked whilst the rest of the surface is washed away during the development process. The waveguide thickness is dependent on the type of photoresist used. Here, the fabricated WGs had a thickness of  $4 \mu\text{m} \pm 0.5 \mu\text{m}$ . Moreover, this technique allows maskless fabrication of waveguides in various lengths and designs: enabling fast and controllable device prototyping.

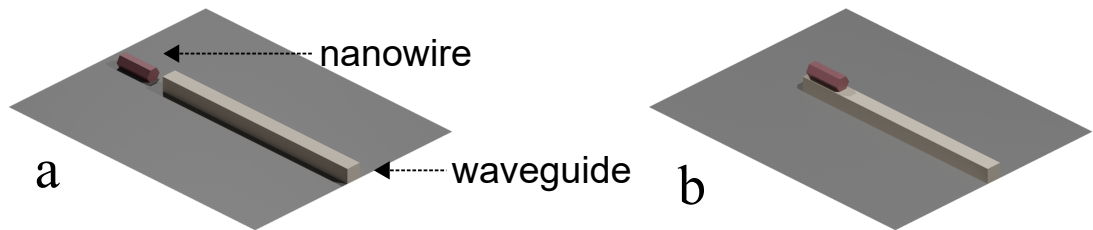


Figure 4.1: Two investigated methods of coupling nanowire lasers into waveguides: (a) end-to-end facet and (b) lateral coupling.

As stated before, two NW laser integration methods were investigated during this

project, namely end-to-end facet (shown in Fig. 4.1(a)) and lateral coupling (shown in Fig. 4.1(b)). The first method is achieved by aligning a NW laser directly to an end facet of the waveguide, as shown in Fig. 4.1(a). By optically exciting the end-to-end coupled NW laser, its lasing emission (from the facet) is injected directly into the aperture of the target waveguide. Next, the lateral coupling technique is achieved by integrating a NW atop the waveguide, as shown in Fig. 4.1(b). In this case, the lasing modes of an excited NW laser overlap with the modes of the polymeric waveguide. Thus, resulting in the coupling of the lasers' emitted light along the length of a waveguide. It should be noted however, that the large refractive index contrast between the two systems ( $n_{InP} = 3.4$  and  $n_{SU8} = 1.5$ ) strongly affected the coupling strength between the two devices [72, 121–123].

Before integrating the selected NW lasers onto the pre-fabricated polymeric waveguides described above, the propagation losses of the latter were characterized. To do this, we used a readily available fibre-optic experimental setup designed to determine system losses in telecommunication platforms and therefore operating at the telecom wavelength of 1550 nm. This wavelength was chosen due to the availability of the loss characterization system, and even if it is different to the wavelength of NW lasers used in this work, it provided nonetheless a good estimation of the losses in the fabricated SU-8 waveguides. A Fast Fourier Transform (FFT) method, described in [124], was used to calculate the propagation loss of the fundamental mode and it was measured to be equal to  $3 \text{ dBcm}^{-1}$ . The emission wavelength of the InP NW lasers of this work was around the 880 nm range [55]. At that wavelength window, and for the dimensions they were fabricated with, the developed polymeric waveguides were estimated to be multi-mode [125]. This was beneficial to the design of our systems for different rea-

sons. Firstly, the NW lasers used in this work are multimode [55]. Secondly, by having multi-mode waveguides we do not compromise on the dimensions, hence these resulted in having higher numerical apertures (waveguide facets) to which it was much easier to align the NWs.

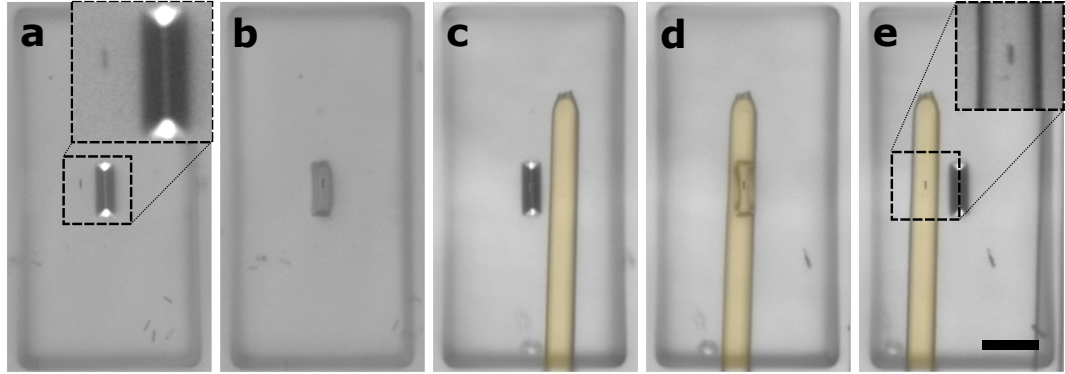


Figure 4.2: (a) The  $\mu$ -stamp is aligned next to the selected NW laser. (b) The NW laser is captured with the micro-tip of the stamp. (c) The  $\mu$ -stamp is aligned with the selected waveguide on the receiving substrate. (d) Surface contact between the NW and polymeric waveguide. (e) The NW laser is released onto the waveguide. For information, the colour of the NW in the micrographs was enhanced for a better contrast. Scale bar: 30  $\mu\text{m}$ .

The NW integration process was achieved by means of TP. In this case the pyramidal-tip  $\mu$ -stamp was used to pick-and-place individually selected *InP* nanowire lasers from their donor substrate and subsequently integrate those onto the polymeric waveguides. Due to the specific design of the stamp, with a narrow ridge at its end, it made easier to control the orientation of the NWs upon their release onto the WGs. Fig. 4.2 show the integration stages of a NW laser onto a SU-8 waveguide. It should be noted here, that the NW had dimensions of diameter  $\sim 435$  nm and length of 5  $\mu\text{m}$ . Fig. 4.2(a) shows a pyramidal shape  $\mu$ -stamp aligned with an *InP* NW laser on the donor substrate. Then, the selected NW is picked up using the stamp's tip, as shown in Fig. 4.2(b). Fig. 4.2(c) shows the alignment process: the NW laser is being transferred onto

the receiving surface, a waveguide in this case. The NW integration stage is depicted in Fig. 4.2(d), where the NW laser is being positioned onto the center of the corresponding waveguide. Next, the NW laser is released controllably onto the waveguide, as shown in Fig. 4.2(e). Prior to the WG integration process, several NWs were printed onto a  $SiO_2$  substrate forming 1D arrays to pre-characterize them, in order to allow selecting comparable devices for a fair comparison. As discussed in Chapters 1 and 5, due to the inhomogeneous broadening during the growth process [69,126], all NWs have slightly different dimensions. Hence, a pre-screening of these NW devices, prior to their integration, is a necessary step that provides, a relative understanding about the lasing properties of the selected devices. After collecting the measured spectra of the lasing emission from these devices using a  $\mu$ -PL setup (see Chapter 3), devices with single-mode emission and comparable lasing threshold were selected for integration. After this, the waveguides were fabricated on a quartz substrate. These WGs were slightly less than 1 cm long after their facets were cleaved and had a thickness of 4  $\mu\text{m}$  and a width of 7  $\mu\text{m}$ . These WGs were tested to characterize their propagation losses and as with NWs, comparable WGs were selected for the transfer-printing process.

#### 4.1.1 Coupling Configuration Between NW Lasers and WGs

The described TP process enables integrating NWs at chosen locations with a minimum of orientation offset (between NW and WG). Herein we show results of the two configurations of NW coupling with SU-8 micro-metric waveguides. Results of the fabricated devices are shown in Figs. 4.3 and 4.4.

In the first case, we have used an individual InP NW ( $d \sim 435$  nm, length  $\sim 5$   $\mu\text{m}$ ) and integrated it onto a 1 cm-long SU-8 waveguide by means of TP, as shown in Fig. 4.3(a). After the printing process, the NW laser was optically excited ( $\lambda_{pump} = 532$

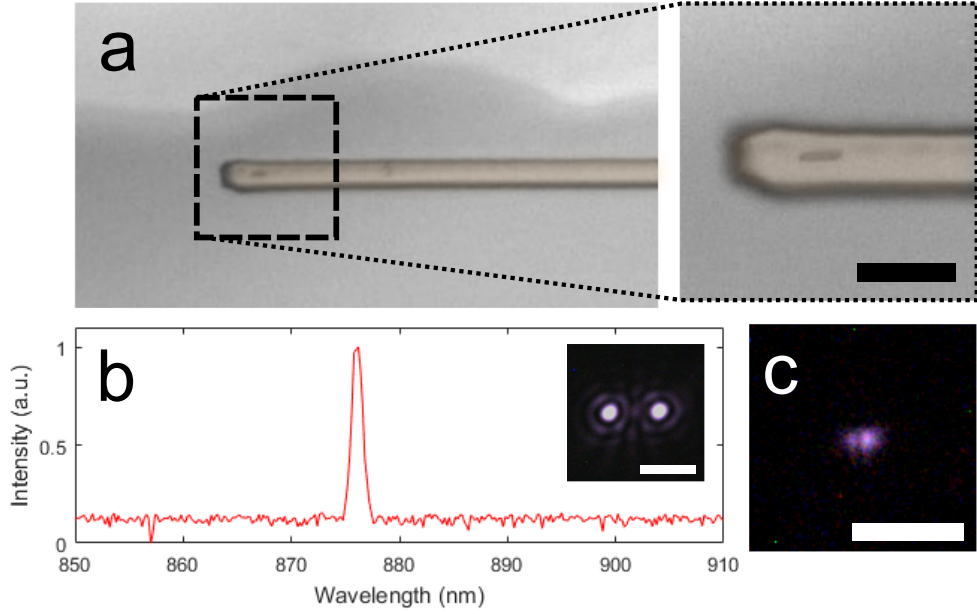


Figure 4.3: (a) False-colour brightfield micrograph of a laterally coupled NW laser atop a WG. The inset shows a boxed area in part (a). Scale bar:  $10\ \mu\text{m}$ . (b) Spectral emission of the laterally coupled NW laser under optical excitation. The inset shows a darkfield micrograph of the lasing emission of the corresponding InP NW laser. Scale bar:  $7\ \mu\text{m}$ . (c) Darkfield micrograph of the light output of the coupled NW-WG laser system. Scale bar:  $15\ \mu\text{m}$ .

nm) at room temperature using the vertical setup (TS<sub>2</sub>) and characterised with the edge-detection module of the  $\mu$ -PL setup (see Chapter 3 for description). Fig. 4.3(b) plots the spectrum of the integrated NW laser measured at an optical excitation of  $38.8\ \text{mJcm}^{-2}$ . This revealed single mode emission at  $\sim 877\ \text{nm}$  as it is shown in Fig. 4.3(b). The inset in Fig. 4.3(b) shows a darkfield micrograph of the lasing emission from the NW laser, showing clearly that the emission comes from the end-facets of the NW. The edge-detection module of the  $\mu$ -PL setup (see Chapter 3) was aligned to capture the light coming out from the far end facet of the waveguide in which we integrated the NW laser ( $\sim 1\ \text{cm}$  away). Fig. 4.3(c) includes a darkfield micrograph showing the collected light from the NW laser at the output facet of the SU-8 WG using the edge-detection system of the  $\mu$ -PL setup. Fig. 4.3(c) therefore demonstrates that the emission from the NW laser indeed couples successfully in part to the waveguide in

which it is integrated and is guided 1 cm on-chip before it is detected at the end-facet of the WG. We must note here that for consistency we used the same camera to capture the images in Figs. 4.3(b-c), controlling in both cases the integration times to avoid low exposure or oversaturation of the signal.

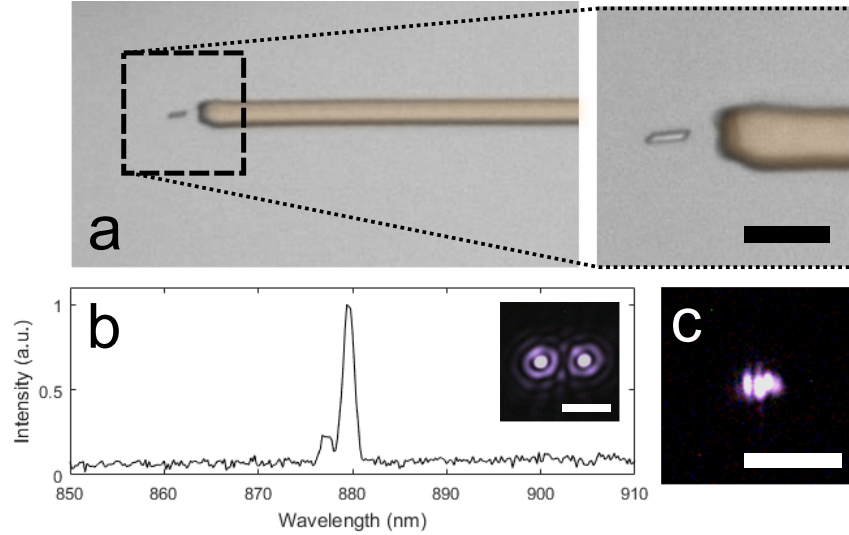


Figure 4.4: (a) False-colour brightfield micrograph of an end-to-end facet coupled NW device. Inset shows boxed area in part (a). Scale bar:  $10 \mu\text{m}$ . (b) Lasing emission spectrum of the corresponding devices under the same excitation as in Fig. 4.3(b). Inset shows darkfield micrograph of the lasing NW laser. Scale bar:  $7 \mu\text{m}$ . (c) Darkfield micrograph obtained at the facet of the NW-coupled waveguide. Scale bar:  $15 \mu\text{m}$ .

The integration process was then repeated, only this time the target NW laser was integrated following the end-to-end coupling design. Fig. 4.4(a) shows a false-colour brightfield micrograph of the integrated NW in an end-to-end facet coupling configuration. Fig. 4.4(b) shows the NW laser's emission spectrum at room temperature when the device is optically-pumped above its lasing threshold. To note, spectra for both devices (shown in Figs. 4.3(b) and 4.4(b)) appear to be broader than a typical lasing emission due to the resolution of the spectrometer. For clarity, we must specify that the devices used are exactly the same as reported in refs. [54, 55]. The inset in Fig. 4.4(b) shows a darkfield micrograph of the light emission of the NW, with the light emitted

at the two end-facets of the device. In this case, we have used the same fluence as in the previous case ( $38.8 \text{ mJcm}^{-2}$ ), for a fair comparison. Fig. 4.4(c) shows the light output at the facet of a the coupled NW laser-WG system for this second configuration. The same integration time in the camera was used as in Fig. 4.3(c). In this case, we see an enhanced (relatively to the previous case) coupling for the end-to-end coupling configuration. Here, the coupling efficiency depends more on the acceptance angle of the waveguide, rather than on the specific distance from the NW to the facet of an uncleaved waveguide [127]. Thus, having a fine facet plays a vital role in achieving higher coupling efficiencies.

After the devices were integrated and coupled with the WGs, we have derived a method to estimate their coupling efficiencies using image processing techniques. The method works by comparing the relationship between the measured average optical power and the detected light intensity in the micrographs collected with the CCD camera. The reason for choosing this method is due to the fact that the light signals from the NW laser WG coupled systems have ultra-low energies which are extremely challenging to measure/detect using our available power-meter systems. At first, the average optical power for the “green” pump laser beam was measured using a Thorlabs S401C power-meter. Next, micrographs were measured for the “green” pump laser, at the same energy and the pixel intensity of the light coupled into the CCD camera was processed. Hence, using this technique we obtain a micrograph of the “green” pump laser beam corresponding to a measured average power of  $56 \text{ nW}$  ( $279 \text{ } \mu\text{Jcm}^{-2}$ ), as it can be seen in Fig. 4.5(a). Then this micrograph was converted into a data file and processed using a developed MatLab script, and the results are shown in Figs. 4.5(b). Next, the background noise present in the micrograph was numerically removed for

a fair comparison and better estimation. The background noise was calculated from a darkfield micrograph with no light turned on at the selected integration time. The processed average value of the pixel then was subtracted from the “green” pump laser data file. Any pixel value below the average noise value was set to 0. In this way, we make sure that the noise is removed from the measurements.

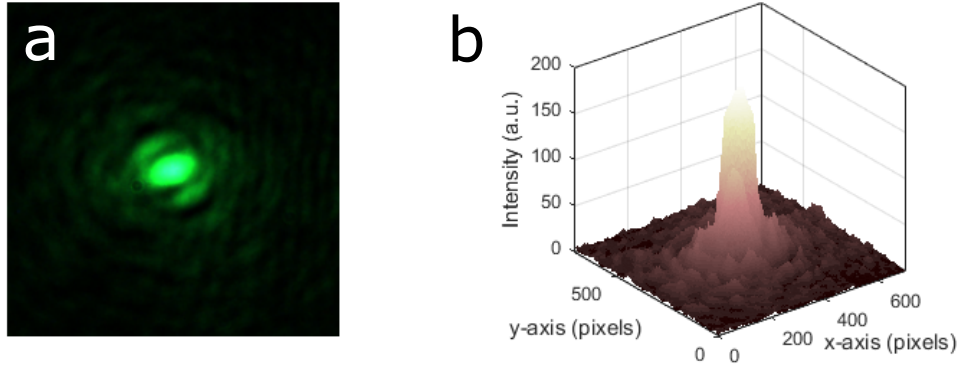


Figure 4.5: (a) Darkfield micrographs of the laser beam at an average power of 56 nW ( $279 \mu\text{Jcm}^{-2}$ ). (b) 3D data graph of the converted darkfield micrograph in (a).

Last, the data file was processed to calculate the total integrated image intensity, this was done by calculating a total value of the individual pixel’s counts. This relationship was used as a reference point to estimate the energy and the coupling efficiencies of the used micrographs. Besides that, the CCD camera was checked to behaving linearly with increasing integration time (i.e. by increasing the integration time of the camera by a factor of 2, the average integrated pixel value will have a 2 fold increase) to enable scaling. Then, we have compared a converted pixel intensity of the “green” pump laser, with the ones collected from the coupled nanowire-waveguide systems for both lateral and end-facet configurations. Fig. 4.6(a) shows a captured darkfield micrograph collected at the end-facet of a waveguide showing the guided NW laser’s emission in the end-to-end configuration. Fig. 4.6(b) shows a 3D graph of the processed image data file with the background noise removed.

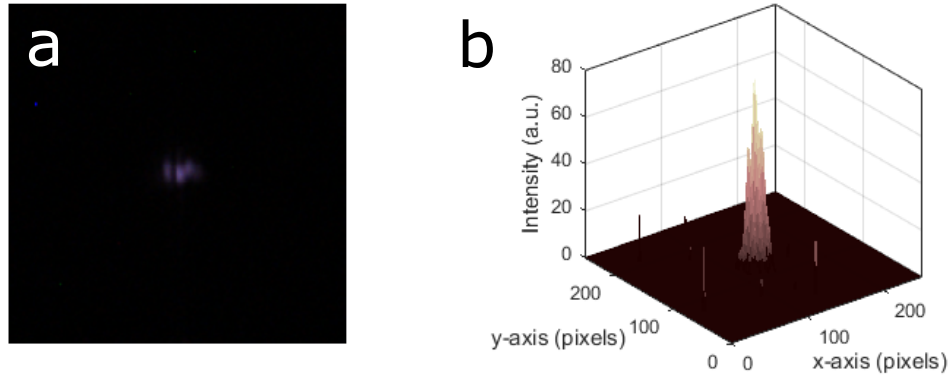


Figure 4.6: (a) Darkfield micrograph of the light coupled at the facet of the waveguide. (b) 3D graph of the converted micrograph in (a) with removed noise.

It is important to note that the spikes outside the localized light area are phantoms that appear due to the long integration times used in the camera settings. However, it should be clear that they do not have a large contribution to the total estimation of the coupled light. All measurements were carried out with the same level of fluence ( $38.8 \text{ mJcm}^{-2}$ ) and the same CCD camera.

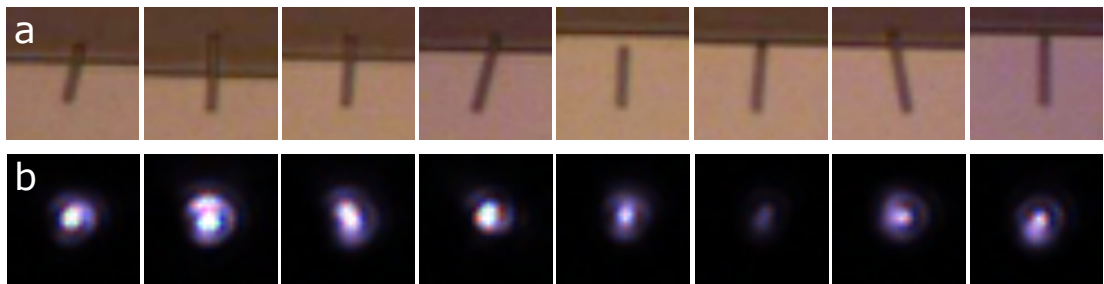


Figure 4.7: (a) Brightfield micrograph at the edge of a cleaved silica substrate. (b) Darkfield micrographs captured with the edge-detection setup (of the  $\mu$ -PL setup) at an optical excitation of  $38.8 \text{ mJcm}^{-2}$ . The micrographs show the direct light emission from the end-facets of the NW lasers.

Next, individual InP NWs (same dimensions as before) were printed at the edge of a cleaved silica substrate. This was done in order to estimate an average power emitted by single laser devices. The printed NW lasers are shown in Fig. 4.7(a). These were individually optically excited with the same optical fluence of  $38.8 \text{ mJcm}^{-2}$  as before and the emitted light from the NW laser's end-facet was collected, as shown in Fig.

4.7(b). Then, we applied the same light relationship method to estimate the average power of the light emission from the end-facet of a nanowire laser. This was found to be equal to 11.2 nW (with a standard deviation of 3.27).

Finally, we have made a direct relationship between the light collected at the end-facet coupled NW laser-WG system (for the two coupling configurations) and those at the edge of a cleaved silica substrate. Then we have accounted for the differences in integration times for the captured micrographs and estimated average power values for the two coupling cases. As a result, average powers of 68 and 189 pW for the lateral and facet nanowire-waveguide coupled configurations, respectively, were obtained. Besides that, since a pulsed laser with a 1.6 ns pulse duration and 10 kHz repetition rates was used to optically excite these semiconductor NW lasers, we could conclude that the NWs will have peak power values of 4.22 and 11.84  $\mu$ W for the lateral and end-facet coupling configurations, respectively. Lastly, these values were used to estimate the coupling efficiencies for the two integration techniques. Hence, using this approach we were able to obtain the coupling to be equal to 1.9 % (or -17.2 dB) and 0.7 % (or -21.5 dB) for the facet and lateral coupling configurations, respectively. We must note that, these are lower bound values as these include the waveguide propagation losses.

#### **4.1.2 Nanophotonic Circuits with Integrated NW Lasers**

As previously discussed, both the laser writing and the TP techniques offer a great degree of freedom in the fabrication of photonic circuitry. Hence, we used these techniques to demonstrate complex waveguide nanophotonic systems with integrated NW lasers on planar surfaces. In particular, we demonstrate Y-junction waveguides for two configurations: 1x2 and 2x1 (input/output) to enable coupling and splitting of light signals from NW lasers. Fig. 4.8(a) shows a false-color brightfield micrograph of a

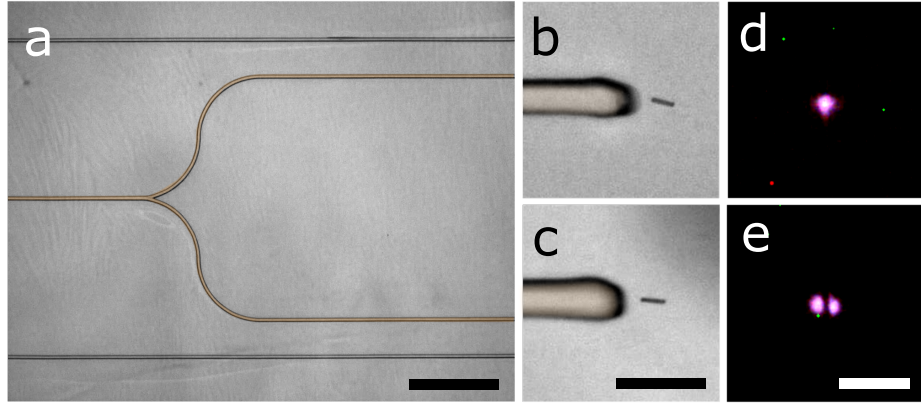


Figure 4.8: (a) False-colour brightfield micrograph of a SU-8 Y-junction WG. Scale bar:  $80\ \mu\text{m}$ . (b and c) Facet-coupled NW lasers into the 2-input of the Y-junction WG. Scale bar:  $10\ \mu\text{m}$ . (d and e) Darkfield micrographs of the light coupled from the NW lasers in (b and c) at the facet of the WG. Scale bar:  $10\ \mu\text{m}$ .

2-to-1 Y-junction waveguide with end-facet integrated NWs as shown in Figs. 4.8(b-c). These NW lasers were individually excited and their light emission was coupled into the Y-junction waveguide, Figs. 4.8(d-e) depict darkfield micrographs of the coupled light from the NW lasers at the facets of the waveguide. Thus, successfully demonstrating light coupling and guiding in these Y-junction WGs. We have estimated a power difference of  $\sim 9\%$  between the top (Fig. 4.8(b)) and bottom (Fig. 4.8(c)) NW lasers. This was done by integrating the intensity measured in both micrographs. The difference in power was not necessarily related to the power split between the two branches of the Y-junction waveguide. Firstly, the NW lasers were optically pumped with the same fluence. However, these might have been at different points in their respective lasing threshold curves, or even emitting in different modes. Regarding the difference in the field distribution, this could be due to the nature of waveguide laser-writing: at first you write one branch of the waveguide, then the second branch is written atop the first one. Thus, even due to some misalignments (even in the order of 10s of nm and other offsets) from the very center of the WG it will affect the optical power transmission

and introduce the differences observed in output modes [72].

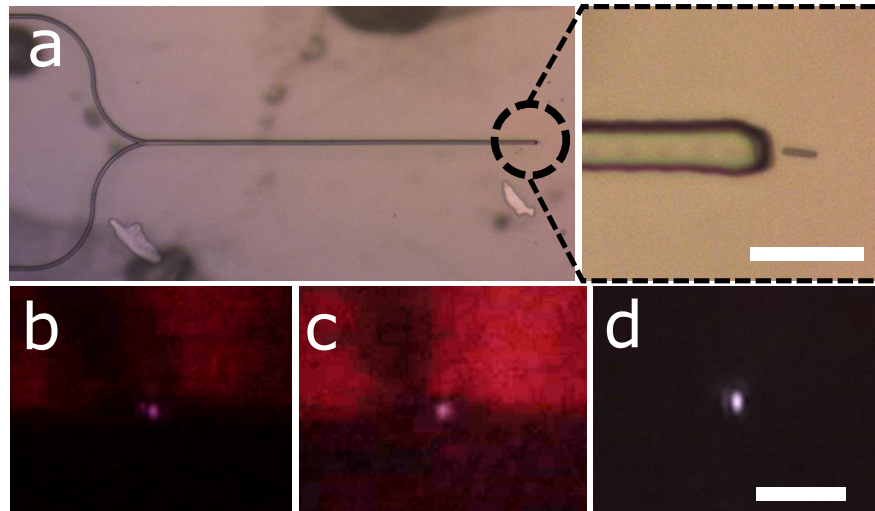


Figure 4.9: (a) Brightfield micrograph of a 1x2 SU-8 Y-junction WG. The inset shows the circled area in (a). Scale bar:  $10 \mu\text{m}$ . (b) and (c) show brightfield micrographs of the coupled light at the facet of the WG. (d) Shows darkfield micrograph of the light scatter from a facet of the NW laser (in (a)). Scale bar (b-d):  $15 \mu\text{m}$ .

Moreover, we demonstrate a similar coupling technique for the other Y-junction WG configuration (1-to-2). Fig. 4.9(a) shows a false-color darkfield micrograph of a 1-to-2 Y-junction WG. This design could be well used to optically split a signal into two paths. Figs. 4.9(b) and 4.9(c) plot the light coupled from the NW laser (in fig. 4.9(a)) into the polymeric SU-8 Y-junction WG. We should note that, these are brightfield micrographs, and as a result the signals appear to be slightly noisy. The coupled light from the NW could be seen in the centre part of the micrographs (Figs. 4.9(b-c)). Fig. 4.9(d) shows an image of the light at the output of the NW laser end-facet.

Additionally to the demonstrated Y-junction designs, we also demonstrate an alternative method of coupling multiple signals from different NW lasers on a single WG. This is achieved by integrating several NW lasers onto a WG using the lateral coupling configuration. For this example we have separately integrated two NW lasers, as shown in Fig. 4.10(a). Figs. 4.10(b) and 4.10(c) show darkfield micrographs of the NW las-

ing devices at room temperature under an optical excitation of  $\sim 40 \text{ mJcm}^{-2}$ . Their coupled light was propagated 1 cm along the waveguide. Figs. 4.10(d-e) show darkfield micrographs captured at the output of the waveguide for the devices depicted in Figs. 4.10(b-c), respectively. Thus, presenting that this could be well used for fabricating small-footprint multiplexing NW laser-WG coupled system. However, even though this technique allows to add multiple NW devices onto a single optical waveguide, it has a drawback. Light propagating along the waveguide will couple into the different NWs, thus providing a non-even power distribution along the waveguide. By looking at the later design, these difficulties were addressed: so we have demonstrated a reduced footprint system with several nanowires lasers (acting as active components). Additionally, this could well be improved by introducing a closely packed nanowire printing capability (described earlier in Chapter 2). Fig. 4.10(f) shows captured spectra at the end-facet of the WG. The NW lasers were individually optically excited, hence Fig. 4.10(f) plots the spectra corresponding to the NW lasers in Figs. 4.10(b-c) when measured separately.

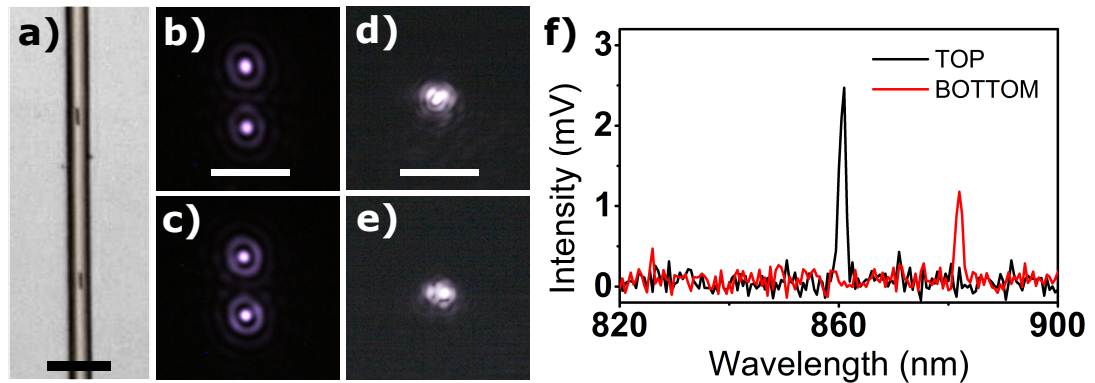


Figure 4.10: A pair of NWs integrated atop a polymeric WG. Scale bar:  $15 \mu\text{m}$ . (b and c) Darkfield micrographs of the NW lasers under optical excitation. Scale bar:  $7 \mu\text{m}$ . (d and e) Darkfield micrographs of the light collected at the waveguide facet. Scale bar:  $15 \mu\text{m}$ . (f) Spectrum captured at the waveguide facet for the two NWs. Figure taken from [72].

### 4.1.3 Mechanically Flexible Systems with Integrated NW Lasers

In the last decade, there has been a significant interest in producing flexible optoelectronic circuitry and devices, see [128–130] for reviews. A stable device performance under severe deformation ensures that these systems have great potential to be exploited in radically novel designs [131–133]. To demonstrate that, a system on a mechanically flexible glass was fabricated and NW lasers were end-facet integrated to WGs [72].

At first, a set of WGs were fabricated using direct laser writing processes on a mechanically flexible substrate (flexible glass), see ref. [134] for the glass sample description. The WGs were fabricated following the same recipe used for planar SiO<sub>2</sub> substrates. NW lasers were then individually transfer-printed in end-facet configuration at the WGs' facets. The flexible NW-WG system was mounted onto the edge-detection setup (see Chapter 3) implemented with a bespoke bending module shown in Figs 4.11(a-b). The bending module consisted of a metallic probe tip mounted on a micrometric translation stage, allowing to be moved along the z-axis (vertically) over a large range of values. The probe tip was used to evaluate the performance of the flexible coupled NW laser WG system by applying linearly pressure to the surface of the sample. Fig 4.11(a) shows an image of the bending module and the flexible glass sample under a stress test. The stage ensures an even increment of the force applied to the sample. As a result, by making surface contact with the sample, the metallic tip bends it vertically (downwards). It should be noted here that the probe tip is wrapped with scotch-tape to avoid local point stresses and secure an even spread of the load to allow for an homogeneous bending angle across the total sample dimensions.

When the sample was mounted into the setup, a selected NW laser coupled into a planar waveguide on a flexible substrate was excited above its lasing threshold. The

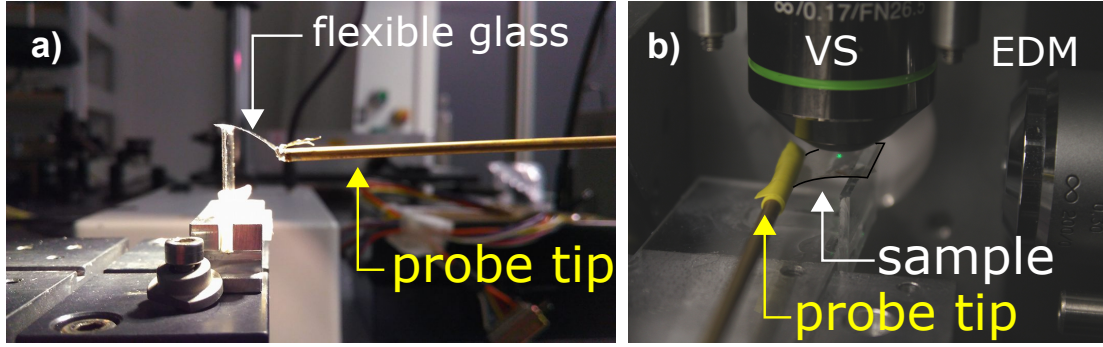


Figure 4.11: (a) Lateral view during the stress test of the flexible glass substrate. (b) A view of the module implemented to the  $\mu$ -PL setup for the characterization of mechanically flexible system. VS - vertical setup, EDM - edge detection module (see Chapter 3 for description). Figure taken from [72].

dimensions of the flexible glass were as follows: area = 1 square inch, thickness = 30  $\mu\text{m}$ . Dimensions of the NW lasers: diameter  $\sim 450$  nm, length  $\sim 5$   $\mu\text{m}$ . Using the edge-detection module, in the  $\mu$ -PL setup, the output of the NW-coupled waveguide system was measured by capturing light at various deformation angles.

Figs 4.12(a) shows the measured spectrum from the NW laser integrated (in end-facet configuration) with a micrometric SU-8 waveguide in-built in a mechanically flexible glass substrate. The left inset shows a brightfield micrograph of the coupled NW laser into the polymeric waveguide on the substrate. The right inset shows a darkfield micrograph of the device under optical excitation at  $\sim 36$   $\text{mJcm}^{-2}$ . In this experiment, two similar CCD cameras were used: (1) to inspect the light emission of the NW laser as captured from its top plane (adjusting the laser focus during the mechanical bending process) and (2) to investigate the light intensity of the coupled emission detected at the output facet of the waveguide at the other end of the substrate (1 cm away). By adjusting the micro-positioning stage we could increase in defined steps the amount of force applied to the substrate to mechanically bend it with a controllable angle. We then collect for each case of analysis the light coming out of the waveguide to investigate the effect of substrate bending angle in the amount of light from the NW laser coupling

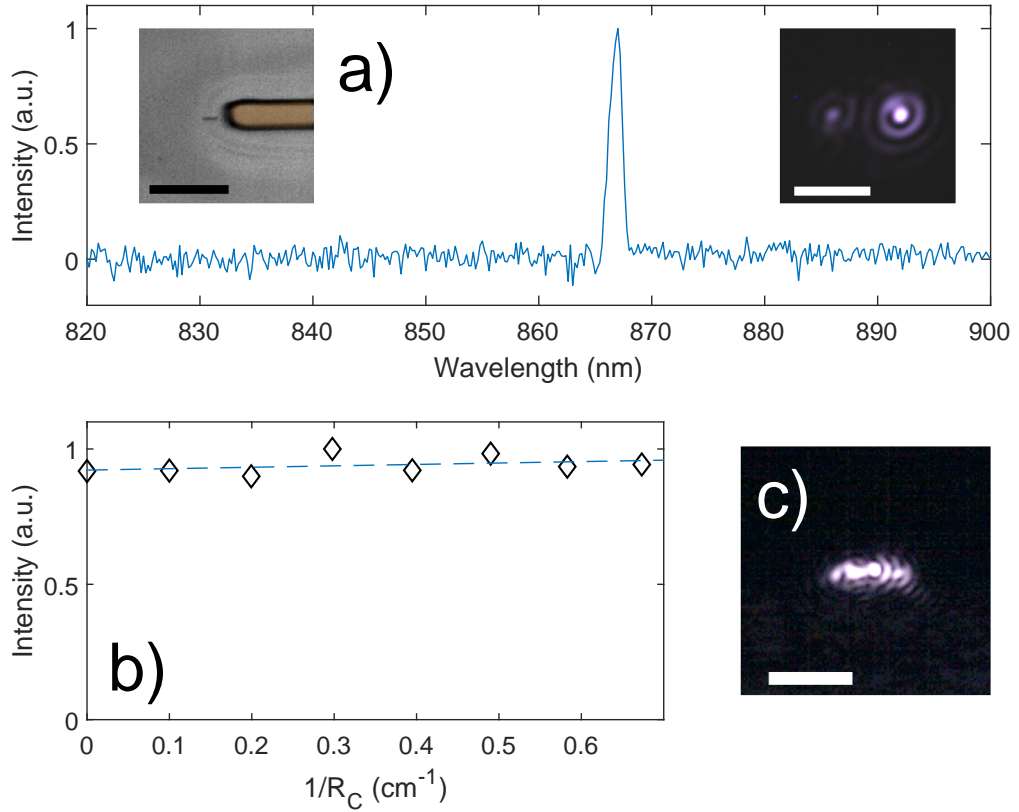


Figure 4.12: (a) Emission spectrum of the NW laser integrated in the WG built in a mechanically flexible substrate. The inset (left) shows a brightfield micrograph of the fabricated structure. Scale bar:  $15 \mu\text{m}$ . The inset (right) shows a darkfield micrograph of the NW laser. Scale bar:  $7 \mu\text{m}$ . (b) Normalised light intensity at the facet of the waveguide as a function of  $1/R_C$ . (c) Darkfield micrograph of the light collected at the facet of the WG. Scale bar:  $15 \mu\text{m}$ .

into the waveguide and reaching the other end of the substrate. Fig. 4.12(b) shows the relationship between the configured substrate bending angle and the detected (normalized) output power of the waveguide. Significantly, the detected light intensity collected from the waveguide's output remains almost constant for all different values of  $1/R_C$  configured. We only detected a slight variation ( $\sim 5\%$ ) in the measured output power for all cases of substrate bending configured. These results therefore demonstrate that for the fabricated system of a NW lasers integrated with a waveguide on a mechanically flexible substrate the coupling efficiency between the NW laser and the waveguide is

practically unaffected, remaining constant from values of radius of curvature all the way from  $1/R_C = 0$  (flat substrate) to very large values of  $1/R_C = 1.6$  cm. Fig. 4.12(c) shows a darkfield micrograph of the light from the NW laser that has coupled into the waveguide after its collection from the far-end facet of the waveguide in the mechanically flexible substrate. Images, like the one shown in Fig. 4.12(c), were processed to obtain a total intensity used in the stability measurement in Fig. 4.12(b).

## 4.2 Integration of Semiconductor NW Lasers with Plasmonic Nanoantennas

In this section we investigate the integration of NW lasers with nano-antennas as a potential route towards improving the light directionality and achieving reduced lasing thresholds in these devices. Moreover, the proposed method allows the achievement of vertical emission in NW lasers as a key feature. Thus, opening new practical functionalities for these devices (e.g. vertically emitting laser arrays and higher coupling rates with optical fibre systems) [73]. The enhanced vertically emitting NW laser systems were developed by integrating *InP* NW lasers into bespoke Cat's Eye *Al* nano-antennas (also known as Split Bull's Eye), for an overview see [135]. Furthermore, full details of this work, including the description of the nano-antennas structure and design, the fabricated NW-CE laser systems and their characterization results can be found in [73].

The structure of the CE nano-antennas used in this work is depicted graphically in the diagrams of Fig. 4.13. The NW-CE systems were designed by our collaborators at Nanjing University (China) and fabricated at the Australian National University (Australia). The nano-antennas were fabricated in *Al* on a quartz substrate. The antennas' design consists of two divided segments separated by an inner central ridge with a total width marked as 'g' in Figs. 4.13(a-b). The design considers the posterior integration of a NW laser right in the middle of this central ridge. With this design the nano-antennas form a metallic resonant cavity with enhanced Q-factor [73]. Periodic circular gratings are formed around the central ridge of the CE antenna as shown in Fig. 4.13. These have been designed with dimensions, 'a', 'b', 'd' and 'h' that optimize the surface plasmon (SP) coupling at the wavelength of 870 nm, precisely the wavelength emission window of the *InP* NW lasers used in this work [73]. Full details on the

CE nanoantennas' design and structure and numerical analyses performed using commercially available software (Lumerical FDTD) were carried out by our collaborators to optimise the NW-CE design and can be found in our joint work [73] (see Supporting Information). There are two different methods to fabricate the NW-nanoantenna laser systems, as reported in [73]. The first method consists on finding a NW and growing the CE nanoantenna around it. This method allows less flexibility, however it enables the fabrication of the NW laser-CE nanoantenna system with ultrasmall NWs at the diffraction limit (diameter  $\sim 290$  nm and length  $\sim 900$  nm) [73]. Moreover, the threshold reduction, due to the high reflectivity of the antenna and coupling of surface plasmons, enables lasing emission at cryogenic temperatures ( $\sim 7$ K) [73]. The second, is based on hybrid fabrication method: a selected NW (diameter  $\sim 435$  nm and lengths  $\sim 5 \mu\text{m}$ ) is integrated in the antenna by means of TP. These results offer higher flexibility and ease of fabrication, as there is no need to find specific NWs on a substrate and building a structure around them.

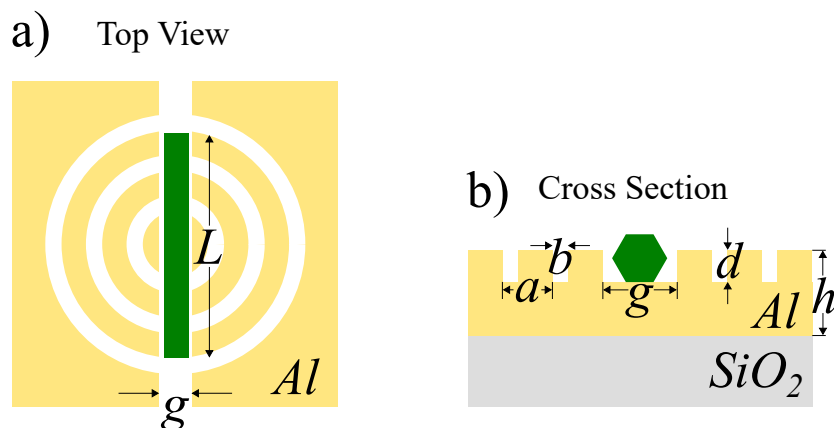


Figure 4.13: (a) Top view schematic diagram and (b) cross section of the Cat's Eye Antenna design.

a	b	d	h	g	L
900 nm	650 nm	200 nm	300 nm	600 nm	$5 \mu\text{m}$

Table 4.1: Table with the corresponding values of Fig. 4.13.

In our work we describe the method used to fabricate NW-CE antenna coupled laser systems using TP processes. To achieve that we have integrated a set of NW lasers and optically excited them above their lasing emission at room temperature. To show how the CE antenna system affects the performance of NW lasers we have compared the NW-CE system with other NW lasers of the same dimensions. For a fair comparison we have fabricated two sets of devices: (1) a NW integrated inside a CE antenna and a bare NW on a  $SiO_2$  substrate; (2) and a NW inside a CE antenna and on a bare NW on an Al substrate. It should be noted that since the CE antennas are made in an Al substrate, this will have higher losses than the  $SiO_2$  substrate due to its metallic nature. Moreover, our TP method enables integrating NW lasers post CE antenna growth, which offers high prospects for the development of practical photonic systems.

#### 4.2.1 TP of InP Nanowires into Cat's Eye (CE) Antenna Cavities

We report here on the demonstration of *InP* NW CE antenna lasers yielding vertical light emission at room temperature at the wavelengths of 850 - 900 nm and with reduced lasing thresholds when compared to bare NWs on bulk un-patterned substrates. The dimensions of the *InP* NW lasers used here were: diameter  $\sim 435$  nm and 4 - 6  $\mu\text{m}$  in length. These NWs were transfer-printed onto Al Cat's Eye antennas fabricated on quartz using standard e-beam evaporation for the metal layer and focused ion beam etching for the patterning of the antennas, as stated in [73].

Here, TP was used to controllably pick-and-place individually selected NW lasers for their integration into the antenna's central ridge. Fig. 4.14 shows essential steps of the fabrication process. At first, NWs were visually pre-selected, as shown in Fig. 4.14(a). Then, the selected devices were captured with an elongated-tip  $\mu$ -stamp (Fig. 4.14(b)). Here it is essential to capture the device with the central part of the  $\mu$ -

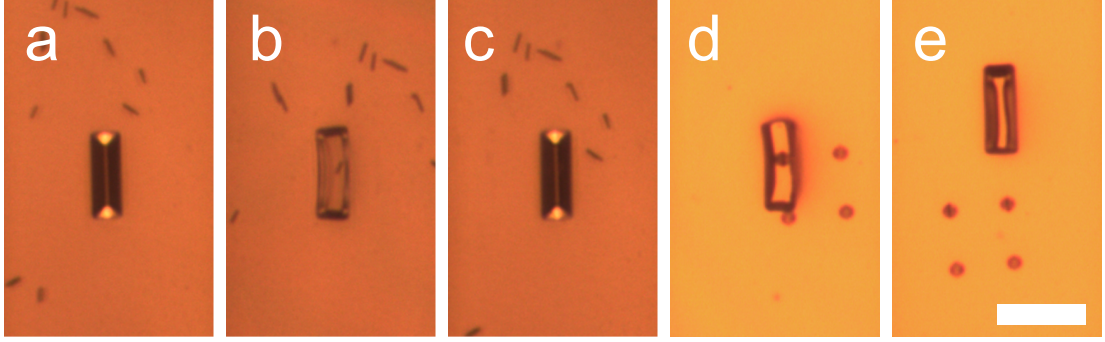


Figure 4.14: Sequential micrographs illustrating the processes for the fabrication of hybrid InP NW CE lasers. (a) The polymer (PDMS)  $\mu$ -stamp is aligned with an individually selected *InP* NW lying down on a donor *Si* substrate. (b) Surface contact between  $\mu$ -stamp and NW is produced to capture the NW. (c) The NW has been captured from the donor substrate by the  $\mu$ -stamp for its transfer to the receiving surface. (d) The  $\mu$ -stamp is aligned with the central gap of the CE antenna, where surface contact is produced for NW release at the desired location. (e) NW is released at the target location into the CE antenna. Scale bar: 30  $\mu\text{m}$ .

stamp (Fig. 4.14(c)), since the tip structure is non-transparent. Then this NW laser is transferred onto the nano-antenna sample, and subsequently printed onto the structure.

This process is shown in Figs. 4.14(d-e).

Moreover, we have fabricated reduced size NW laser-CE antenna using ultra-small NW lasers ( $d = 200 \text{ nm}$  and  $\text{length} = 2 \mu\text{m}$ ). These were subsequently transfer-printed onto the CE antennas. However, in this case due to the optics of the TP system and the small device dimensions we had a poor control over the final positioning of these NW devices. Still, we successfully managed to TP some NW devices inside the antenna's cavity. Fig. 4.15 shows SEM images of our attempts in fabricating structures integrated onto nano-antennas using ultra-small NW devices. The device in Fig. 4.15(d) was then optically pumped using the  $\mu$ -PL setup, however no emission was detected at room temperature. From this case it is possible to see that most of the NWs were integrated near the CE antenna structure. In reality, the final location of the device was strongly related to the release mechanism. Due to their reduced size, these devices exhibit poor release onto metallic surface, see Chapter 2 for discussion. However, a single device

ended up being integrated into the cavity of the CE. The positioning of reduced size nanostructures (those with dimensions barely visible through optical microscopy) will remain a fundamental challenge. However, in this work we showed as a proof-of-concept that the integration itself is possible with the expected reduced control over the printing accuracy. This in turn could create a future work where our  $\mu$ -stamps are fitted into an SEM setup and the printing process is repeated. However, it is unclear if the PDMS material will retain its performance and properties under the SEM environment.

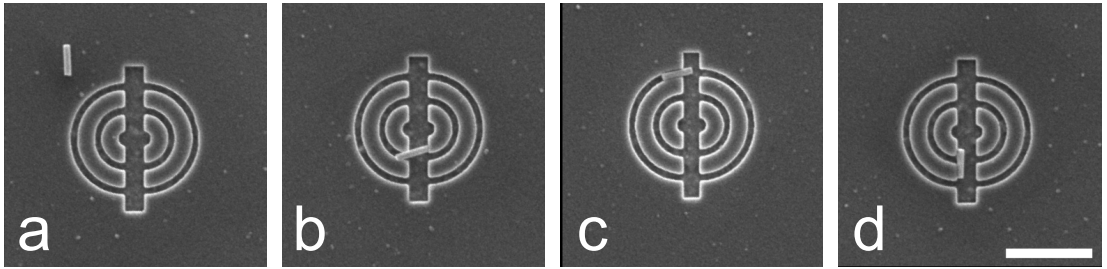


Figure 4.15: SEM micrographs of the integrated reduced size (ultrasmall) NWs into CE antennas. Scale bar:  $3 \mu\text{m}$ .

## 4.2.2 Reduced Lasing Threshold and Vertical Emission in NW-CE Antenna Lasers

We have assessed the performance of the hybrid NW-CE antenna laser systems fabricated by means of TP. We have done so by optically exciting the fabricated coupled nanostructures and comparing their performance against that of bare NW lasers transferred on both un-patterned bulk *Al* and *SiO<sub>2</sub>* substrates. For a fair comparison we have selected NW devices with comparable lengths and excited these with the same optical excitation conditions. Fig. 4.16 plots together for comparison purposes the results for the case of a NW-CE laser with those of NW lasers on bulk substrates. Figs. 4.16(a) and 4.16(b) show lasing emission spectra of the two transfer-printed devices: one on the CE antenna and another on an *Al* substrate, respectively. Both devices have

single mode emission under optical excitation above their lasing threshold. The insets in Fig. 4.16 plot the lasing emission from the NW laser coupled to the CE antenna (Fig. 4.16(a)) and the bare NW laser when optically pumped above their threshold. From the results in Figs. 4.16(c) and 4.16(d) we have recorded a significant threshold reduction. In Fig. 4.16(c) the lasing threshold point is around  $8 \text{ mJ/cm}^2$  for an integrated device into the antenna structure. A SEM image of the fabricated device is shown in the inset of Fig. 4.16(c), with an estimated length of  $4.3 \mu\text{m}$ . For comparison, a NW laser of similar length had a measured threshold point at  $18 \text{ mJ/cm}^2$ . The inset in Fig. 4.16(d) shows a SEM micrograph of the NW laser ( $L=4.2 \mu\text{m}$ ).

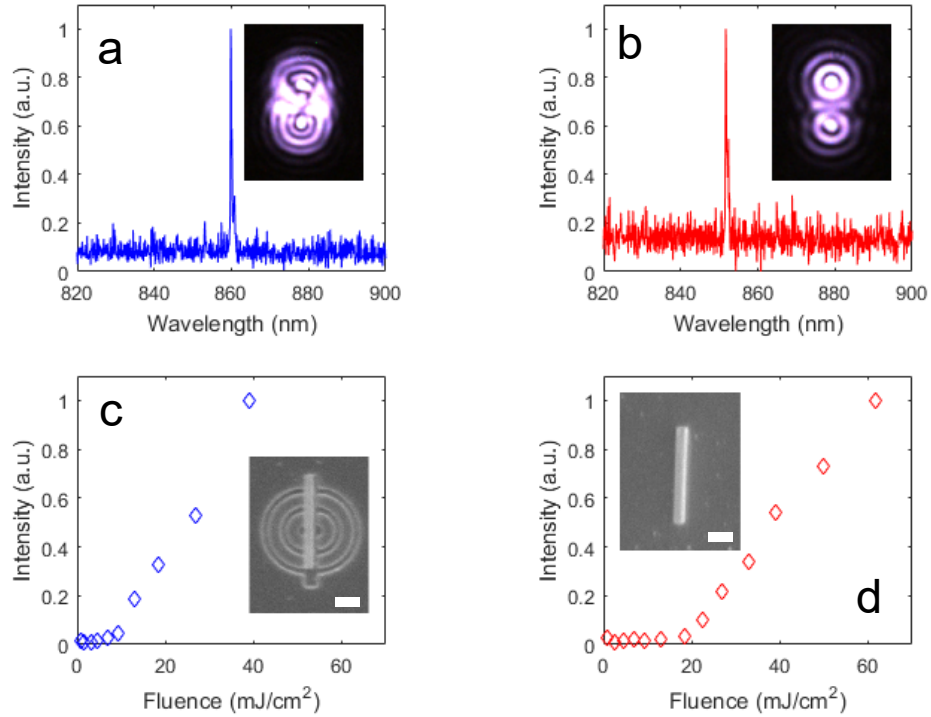


Figure 4.16: (a) *InP* NW laser inside an *Al* CE antenna. The inset shows a darkfield micrograph of the device's lasing emission. The length of both NW lasers was found to be equal to  $\sim 4.2 - 4.3 \mu\text{m}$ . Scale bar:  $1 \mu\text{m}$ .

Moreover, to show the contribution of the CE antenna we made a comparison between a coupled NW-CE antenna system and a single device on a silica substrate. The results are shown in Fig. 4.17. Here, for a fair comparison we have selected in

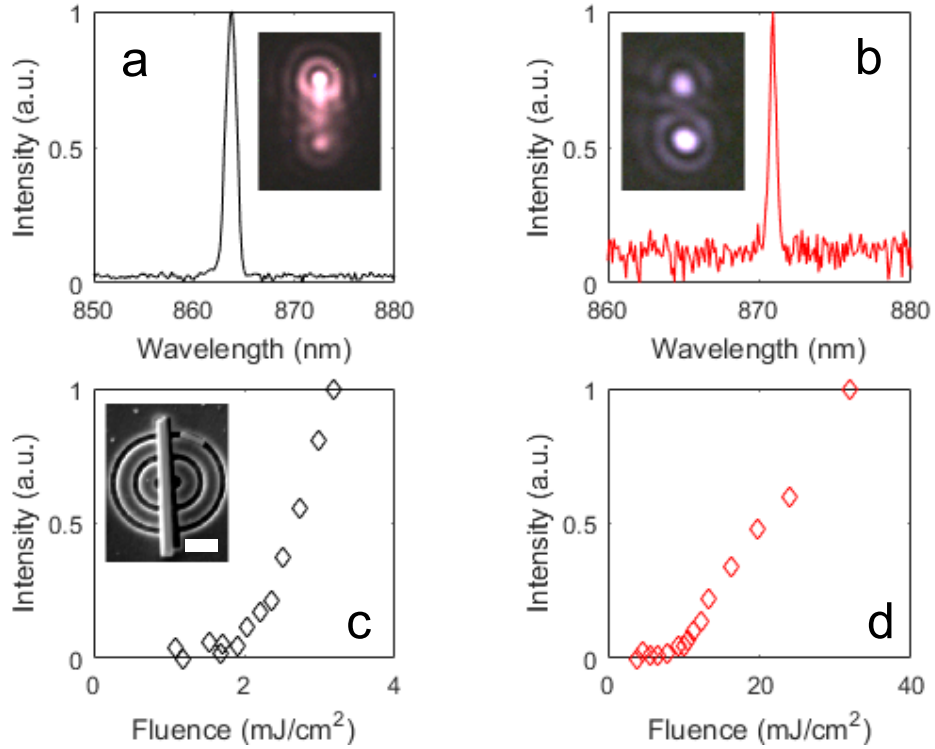


Figure 4.17: (a) Spectrum of an *InP* NW laser integrated onto a CE Antenna. The inset shows a darkfield micrograph of the lasing emission from the NW. (b) Spectrum of a NW laser under optical excitation above threshold. The inset shows a darkfield micrograph of the NW. (c) Lasing threshold plot of the NW in (a). The inset shows a SEM image of the fabricated device. (d) Threshold curve of the corresponding device in (b). Scale bar: 1  $\mu\text{m}$ .

both cases single mode devices. Figs. 4.17(a) and 4.17(b) show single mode emission under optical excitation at room temperature for both NW lasers. The insets in Figs. 4.17(a) and 4.17(b) are darkfield micrographs of the corresponding NW laser devices. Figs. 4.17(c) shows the threshold curve of the fabricated NW laser system with the CE antenna device. In this case, the threshold point was calculated to be equal to  $\sim 2 \text{ mJ/cm}^2$ . The inset shows a SEM image of the fabricated device. For comparison, the lasing threshold curve in Fig. 4.17(d) corresponds to that of a single NW laser on a bulk silica substrate. It should be noted here that the pump laser used for optical excitation was changed between the two sets of results, shown in Figs. 4.16 and 4.17. Therefore, that might have affected the direct comparison between the two sets of

devices. However, it still gives strong proof of the reduction of the pumping power required to achieve lasing emission [73].

### 4.3 3D Integration of NWs onto Bow-Tie Antennas for THz Sensing

Terahertz (THz) sensing has blossomed in the past decade due to the development of novel devices which generate stable, directional and high intensity THz radiation (typically cited as the frequency range between 0.1 - 10 THz, or 3 mm - 30  $\mu\text{m}$  [136, 137]). Since then, a great deal of research has been done towards characterizing and studying devices, materials and systems using THz signals [136]. In general, THz spectroscopy measurements offer “detecting carrier lifetimes, mobilities, dopant concentration and surface recombination velocities with high-accuracy, high-throughput in a contact-free fashion” [136]. This, on its own, provides an excellent set of tools for understanding and measuring physical phenomena occurring at the nanoscale [136]. Due to their unique properties, NWs were proven to be good candidates for realizing photoconductive THz detectors, see [74, 136, 138]. Furthermore, due to the NWs’ quasi-1D structure, NW-based detectors will be ultra-compact and high-sensitive, when compared to conventional bulk designs [74].

To put this in the context of this work, TP is a useful technique for integrating NW lasers with controlled orientation and onto target locations with high-precision. This gives great flexibility in realizing systems where the positioning accuracy of NWs is key. The work described in this section was a collaboration between our group at The Institute of Photonics and the group lead by Michael. B. Johnston at the University of Oxford. The purpose of this work was to design and fabricate a 3-dimensional NW-based THz detector that could be capable of measuring a full THz state (both polarizations at the same time), something that has never been achieved before using conventional detectors.

In this section, a method of fabricating novel NW-based devices for THz sensing is presented. The device consists of a 3D-cross NW network integrated into a dual Bow-Tie (BT) antenna structure. As discussed in our work [139], this opens capabilities of recovering a full terahertz state: electric field vector of light through three dimensions (time and two spatial dimensions). This offers a significant improvement over conventional detectors, since these typically are only capable of measuring intensity of light or count photons. This results in the loss of the light’s phase or full polarization information [139]. Nanowires of certain dimensions and materials have strongly polarization-dependent transmission of THz pulses [138]. Furthermore, since the passing THz pulses are strongly dependent on the angle between the direction of the THz pulse and the NW orientation [140], it becomes possible to measure those with high precision. For a detailed description of relevant works on the topic, see [74,136,138,141]. In this section, we present the state-of-the-art integration of NW lasers on a multi-level structure with reduced contact area between the target devices and the BT antenna.

#### 4.3.1 Multi-stage Fabrication of a 3D-cross NW Network

To achieve controlled NW integration onto the BT antenna contacts (channels) a ”weak bonding” technique was used, as previously described in Chapter 2. This technique enables the integration of target NWs onto surfaces and structures when there is a reduced contact area between those. To achieve this, InP NWs were scattered across a “low adhesion” PDMS substrate which was cured at 6:1 (agent-to-base ratio). Then individual NW devices were controllably captured with a  $\mu$ -stamp (cured at 6:1 ratio). In this way, the 6:1 PDMS is less “tacky” than the 8:1 stamp, resulting in almost 100 % NW pick-up yield. Hence, upon the device release onto the substrate, there is enough bonding force between NW/substrate to overcome that of NW/ $\mu$ -stamp. In Fig. 4.18

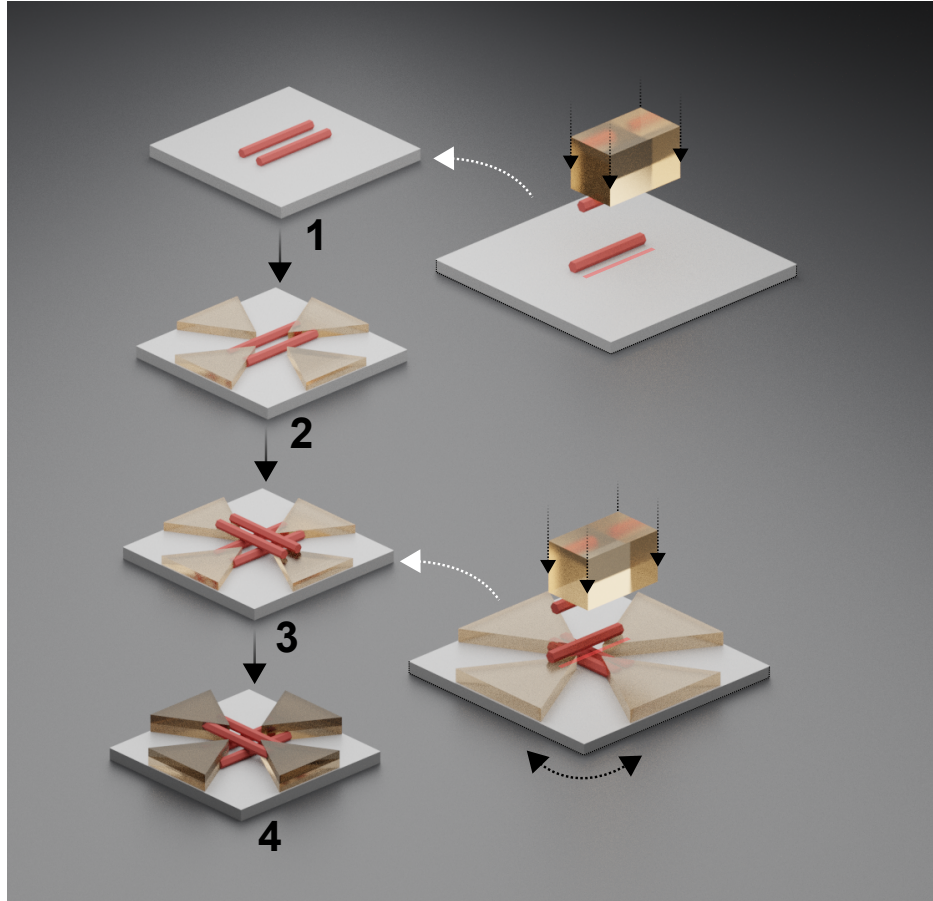


Figure 4.18: Schematic diagram showing the fabrication stages of a polarization-sensitive cross-nanowire THz detector: (1-2) process flow of the nanowires in the initially ‘bare’ z-cut quartz substrate and (3-4) across the bow-tie electrodes of the THz detector. Figure taken from [139].

a schematic illustration of the proposed fabrication stages to produce these devices is shown: (1) a pair of InP NW lasers (diameter  $\leq 260$  nm, length  $\sim 15$   $\mu\text{m}$ ) are transfer-printed onto a quartz x-cut disk in a target area specified by alignment markers on the substrate. (2) The BT antenna structure (height  $\sim 350$  nm) is grown in gold via electron-beam lithography (EBL) [139] with a gap separation between the “electrodes” of  $\leq 5$   $\mu\text{m}$ . The separation ensures that there will be enough contact area to place a second pair of NWs. The BT thickness was designed to avoid the two NW pairs to enter in direct contact with each other after the printing process. (3) the second “orthogonal” NW pair is formed by printing the NWs one by one between the contacts,

as shown in Fig. 4.18. During this step, the rotational stage of the TP system was used to control the orientation of the NW devices and to ensure that they are parallel to each other. (4) A second layer of gold contacts (channels) is grown on the BT antenna structure.

Fig. 4.19 shows SEM micrographs of the fabricated NW-BT antenna detector. Fig. 4.19(a) shows a low magnification image of the BT antennas: each opposite antenna pair corresponds to an individual channel. In Figs. 4.19(b-c) it is possible to see the two-crossed pairs of NW, integrated across the channels forming a characteristic “hash-tag” structure. From the micrographs in Fig. 4.19 it’s possible to see a highly accurate control over the NWs’ orientations. This proved to be extremely important for the subsequent THz signal detection due to the polarization sensitivity of the system [139].

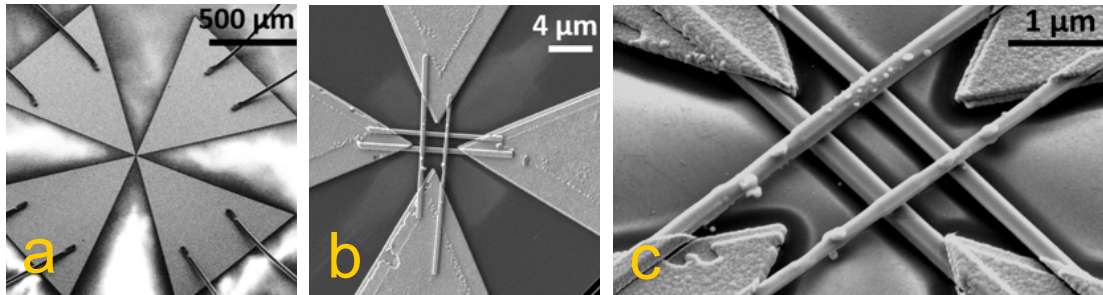


Figure 4.19: (a)-(c) SEM images of the fabricated detector under different magnifications.

After fabrication, the NW detector was placed into a custom-built THz-TDS (Time-domain spectroscopy) system for characterization, see [139]. The characterization measurements were carried out by our collaborators and are included here to show the performance of the fabricated device. The detector was tested for different channel responses using a THz emitter in the setup. By rotating the THz emitter the polarization in the setup was controlled [23]. Fig. 4.20 presents results on the detector characterization. The data shows time-domain THz responses on the individual chan-

nels obtained simultaneously, blue and red lines correspond to vertical and horizontal channels, respectively. The results reveal that the two channels detect simultaneously, hence the detector is able to retrieve the polarisation information.

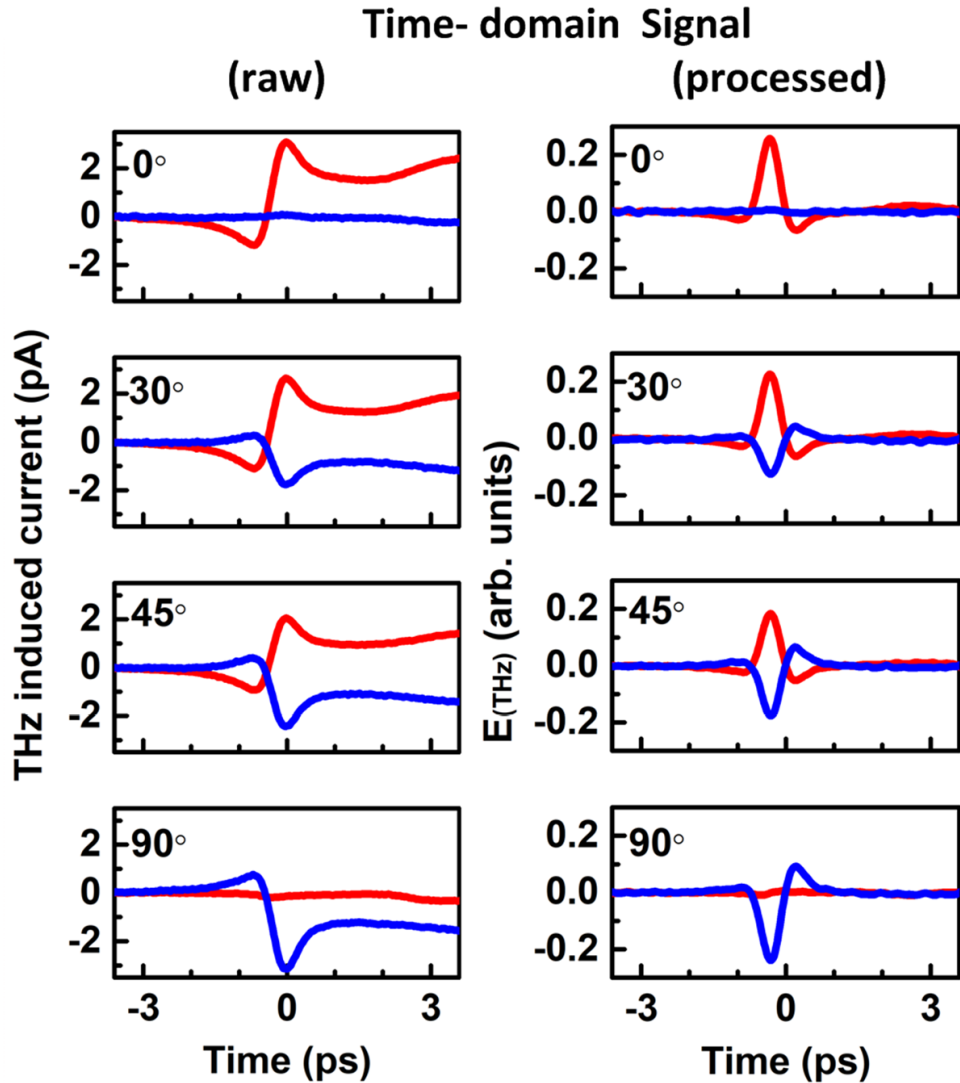


Figure 4.20: Responses of the NW detector relative to the incident THz polarization (left: raw and processed time-domain THz electric field; middle: amplitude and phase spectrum of the THz electric field; right: simulated THz electric field distribution at 1 THz). 0 , 30 , 60 and 90 degrees are the angles that the incident THz pulse is polarized at. Red solid line: response from the horizontal detection channel. Blue solid line: response from the vertical detection channel. Figure taken from [139].

## 4.4 Conclusion and Summary

To summarize, in this chapter we have successfully demonstrated different methods to fabricate NW-based photonic systems by means of TP. The deterministic NW integration allows fabricating devices that could be very useful in a wide variety of fields and scientific disciplines. Here we demonstrate that individual NWs could not only be aligned to a specific target location (e.g. waveguide or nano-antenna's cavity), but be as well integrated vertically forming 3-dimensional nanophotonic systems. It is worth mentioning that no alignment techniques were used in the works described in this chapter and all alignment procedures were achieved by assessing the NWs' position and orientation with the integrated camera module of the TP setup. This, in my view, strongly demonstrates the versatility of the built setup and its boundless capabilities when it comes to NW integration.

In the first work, we have investigated two coupling schemes which allow NW lasers to be precisely and controllably integrated with WGs on-chip. We were able to achieve long propagation distances (relative to the lengths of the NWs devices) in the NW-WG coupled configurations. Furthermore, the flexibility of the used laser-writing system allowed us to fabricate Y-junction waveguides and WGs on mechanically flexible substrates with embedded NW lasers.

In the second section, we have showed vertically emitting NW laser systems with reduced lasing threshold. Here, the lasing threshold of a NW laser system was reduced to  $\sim 2 \text{ mJcm}^{-2}$ . Thus, the lasing threshold was reduced approximately by 1 order of magnitude using this approach.

In the final section, it was shown that our TP system is capable of integrating NW devices forming reduced systems. Specifically, we demonstrated the fabrication of a

3D NW network with a characteristic 'nano-hashtag' pattern to develop a new class of THz detector system. Importantly, these retain their positions after the multi-layer structures are grown atop the TP NWs. This proves that the formed bonding is strong enough to hold them together.

## Chapter 5

# Complex Hybrid Systems with NW Lasers

In this chapter we report on complex nanophotonic systems fabricated using NW lasers as building blocks and enabled by the hybrid TP technique. Systems with embedded NW lasers are of great interest given the unique properties and nanoscale dimensions of these devices [16]. The ability to fabricate such systems will allow for the development of new nanolaser platforms offering not only highly-reduced footprint and ultra-low energy devices (as low as  $43 \mu\text{Jcm}^{-2}$  [57] for lasing threshold), but also exploring material physical properties at the nanoscale [88]. As it has been discussed in this thesis, TP is a great enabling tool for the fabrication of functional and bespoke NW laser systems, as it allows the integration of NW devices onto non-native surfaces beyond their growth substrate. This offers great prospects to drastically increase the potential applications of NW laser-based platforms and their future implementation into next-generation photonic technologies [20]. In this chapter we focus on addressing fabrication challenges and showing means of developing a next generation of nanophotonic devices

with embedded NW lasers.

The structure of this chapter is as follows: in Section 5.1, a numerical model describing an evanescently coupled NW laser system for high-speed functionalities is provided. Here we analyze the dynamics and conditions for stability for such a system in terms of the separation between individual devices, their pumping rates, and their resonant frequencies under conditions of weak coupling. We show that regions of stability were found to be small and located close to zero wavelength offset between the coupled NW laser pairs. Additionally, we have determined that ultra-fast periodic oscillations exceeding the 100 GHz benchmark, could be obtained for realistic laser separations and pumping conditions. These results pave the way towards ultra-small footprint integrated laser modules for future on-chip ultra-high frequency nanophotonic systems.

In Section 5.2, we demonstrate an automated method for the mass-characterisation and classification of NW lasers providing key information and allowing to select specific devices with defined properties, and which is greatly needed for the fabrication of hybrid bespoke nanolaser systems. We present experimental results describing how the lasing emission properties of both transfer-printed and non-transferred NW lasers change over a period of 6 months.

In Section 5.3, we report a wavelength multiplexing (WM) nanowire laser system fabricated combining NW laser structures from different materials in the same platform. These include bulk *InP* [54] and MQW *GaAs/AlGaAs* [57] NW devices. Using the alignment techniques discussed in Chapter 2, we demonstrate the systematic integration of pairs of NW lasers in parallel-aligned architectures, achieving very small controlled edge-to-edge separations between devices at around  $\sim 1 \mu\text{m}$ . This practical and simple arrangement allows both devices to be simultaneously operated by optically

exciting them with a single (diameter of  $1.6 \mu\text{m}$ ) laser spot. Using this architecture, we demonstrate WM NW laser systems operating at different wavelength bands and with both fine and coarse separations between wavelength channels.

## 5.1 Numerical Study of Coupled NW Laser Systems

We start by presenting a numerical work on evanescently coupled NW laser systems. We reveal the high potentials of coupled semiconductor NWs for future nanophotonic integrated systems for ultra-high frequency technologies and high-speed data modulation for applications in future ultrasmall footprint and low energy on-chip optical communication systems [98, 142]. The numerical study in this section results from the combination of two different models, and was carried out in collaboration with colleagues at the University of Essex (Prof. Michael Adams' group). Specifically, we arrive at the results reported here by merging a rate-equation model (developed by our collaborators at Essex, see ref. [143] for the model description) describing coupled slab waveguides, with our developed model of coupled NW laser pairs using a commercially available finite difference eigenmode (FDE) solver [144]. Those two models were combined together to accurately describe the properties of weakly-coupled and parallel-aligned NW laser pairs and study their stability properties and nonlinear dynamics.

Recently, coupled NW lasers systems have started to receive an attention by the scientific community due to their ultra-small footprints and unique properties that these offer, see [98, 145–147] and references therein. For example, a recent work shows butt-coupled NW laser systems for multi-wavelength emission and mode output control [145]. The aforementioned system however, was fabricated using complex techniques [145] where single NW devices are cut into two forming butt-coupled cavities. Hence, in

practice this becomes challenging to realise on a large scale and at target locations in selected substrates. Hence, the TP technique becomes a good candidate for enabling the fabrication of coupled NW laser systems, since it allows integrating NW laser pairs with controlled sub- $\mu\text{m}$  separations (see Chapter 2) at desired locations in a wide range of targeted surfaces (e.g. *Si*, *SiO<sub>2</sub>*, polymers, metals etc. [97]). To create a “first step” towards the future development of coupled NW laser devices using TP techniques, we have focused on investigating numerically such systems for realistic device separations that could potentially be achieved with our nanoscale transfer-printing system [97].

### 5.1.1 Design and Implementation of Coupled NW Lasers Systems

We begin the section, describing the rate-equation model used for the simulation of coupled NW laser pairs. This coupled slab waveguide model describes two identical laser waveguides, ‘A’ and ‘B’, with widths of  $2a$  and edge-to-edge separations equal to  $2d$  (for further details see ref. [143]). The model outlined is schematically depicted in Fig. 5.1(a), with both guides (‘A’ and ‘B’) having the same refractive index ( $n_{core}$ ), dielectric permittivity ( $\epsilon_{core}$ ), and gain per unit length ( $g_{core}$ ). Outside these regions, values for the refractive index and dielectric permittivity are  $n_{clad}$  and  $\epsilon_{clad}$ , respectively.

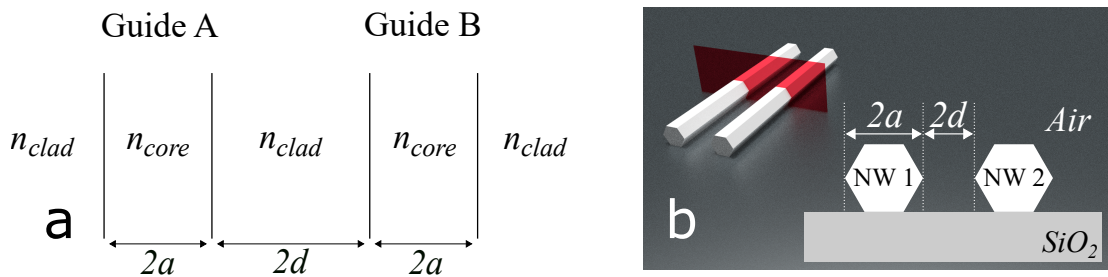


Figure 5.1: (a) Diagram of two coupled slab waveguides, adapted from [98]. (b) Schematic diagram of a coupled nanowire pair on a  $\text{SiO}_2$  substrate.

This model, initially developed for coupled slab waveguide systems, was adapted to simulate the parallel-aligned semiconductor NW laser system schematically depicted

in the 3D diagram (left) and cross-section views included in Fig. 5.1(b). We have simulated the operation of coupled NW laser pairs formed by *InP* NWs with hexagonal structure, with a total length of 5  $\mu\text{m}$ , equal NW diameters of 260 nm and a real refractive index for *InP* equal to 3.4. These devices are placed on a silica substrate and surrounded by air, as shown in Fig. 5.1(b). The refractive index of silica was set equal to 1.5 in the simulations. For simplicity, the imaginary parts of the refractive index in silica and *InP* were both set equal to zero and thus not considered in the modelling. The described configuration of coupled *InP* NW laser pairs on a *SiO<sub>2</sub>* substrate provides a high-contrast ratio between the refractive indices of the NWs and the substrate. This allows for low losses and high reflectivity permitting a simple NW laser excitation as well as allowing easy routes for device fabrication, as outlined in Chapters 1 and 2. Additionally, the NW lasers' diameter (260 nm) was optimised to guarantee emission in the devices' fundamental mode at a realistic device lasing threshold [55].

### 5.1.2 Rate Equation Model

Rate-equation models are widely used tools permitting the study of laser systems by solving differential equations. These models are frequently used to investigate nonlinear dynamics in laser systems in a highly flexible way, whilst also providing accurate and reliable results to help device design or to assess future performance. Eqs. 5.1-5.4 are normalised rate equations used to describe two coupled-slab WGs ('A' and 'B') in ref. [143]. These were used to model the NW lasers, 'NW1' and 'NW2', in Fig. 5.1(b) [98, 143].

$$\frac{dY_A}{dt} = \frac{1}{2\tau_p}(M_A - 1)Y_A - |\kappa|Y_B \sin(\theta + \phi) \quad (5.1)$$

$$\frac{dY_B}{dt} = \frac{1}{2\tau_p}(M_B - 1)Y_B - |\kappa| Y_A \sin(\theta - \phi) \quad (5.2)$$

$$\frac{d\phi}{dt} = \frac{\alpha_H}{2\tau_p}(M_A - M_B) - \Delta\Omega + |\kappa| \left[ \frac{Y_A}{Y_B} \cos(\theta - \phi) - \frac{Y_B}{Y_A} \cos(\theta + \phi) \right] \quad (5.3)$$

$$\frac{dY_{M_{A,B}}}{dt} = \frac{1}{\tau_N} [Q_{A,B} - M_{A,B}(1 + Y_{A,B}^2)] \quad (5.4)$$

Where  $Y_A$  and  $Y_B$  are the normalized field amplitudes and  $M_A$ ,  $M_B$  are the normalized carrier densities in the waveguides ‘A’ and ‘B’, respectively . The phase difference between the fields and detuning between the cavity resonances in ‘A’ and ‘B’ are described by  $\phi$  and  $\Delta\Omega$ , respectively.  $Q_A$  and  $Q_B$  are the normalized pumping rates in guides ‘A’ and ‘B’. The carrier lifetime is  $\tau_N$ ,  $\tau_p$  is the photon lifetime,  $\alpha_H$  is the linewidth enhancement factor,  $|\kappa|$  and  $\theta$  are the amplitude and phase of the coupling coefficient, respectively. It should be noted that the amplitude coupling coefficient  $|\kappa|$  is described in terms of real and imaginary parts:  $|\kappa| = |\kappa_r + i\kappa_i|$ . Where the imaginary part was set to zero. Resulting in  $|\kappa| = |\kappa_r|$ . For full details on the model see [143].

### 5.1.3 Finite Difference Eigenmode Model

Finite Difference Eigenmode (FDE) is an electromagnetic modelling technique enabling the calculation of propagating electromagnetic modes inside a structure [148]. This is done by solving the Maxwell’s equations in a cross-sectional mesh of the defined structure [144, 149]. This is a standard technique used in the modelling of waveguides (and other structures), as it allows to study the properties and performance limits

of such systems by calculating the waveguides' losses, number of propagating modes, refractive indices and confinement factors. The calculations are done within a software defined mesh structure called "Yee Mesh" [150]. In our analysis we have started by calculating the propagating modes (and their characteristics) of *InP* NW lasers (of varying diameters) using a 2D approach, hence obtaining calculated results for a cross section of the NW. The software allows to select different parameters such as: mesh size, simulation area, and drawing structures. For example, a perfect hexagon shape was used to describe the cross section of the *InP* NW lasers under analysis.

Fig. 5.2(a) shows an example of a 2D Yee Mesh, which is used to discretize Maxwell's equations in space; it consists of a grid (matrix) where different electromagnetic (EM) field components are stored (e.g.,  $\mathbf{E}$  and  $\mathbf{H}$ ) [151]. By adjusting the size of the Yee mesh, the accuracy of the simulation can be controlled, as more calculations will describe the simulated object's shape and thus its behaviour. The mesh is used to describe a simulated object shape (hexagonal in our case) and consists of small square boxes, similar to those shown in Fig. 5.2(a). By changing the mesh size, it becomes possible to produce more accurate results, as more "elements" will describe the simulated object's shape. This becomes essential, particularly when studying structures with non-rectangular shapes. By selecting small size grids, we are able to define angles in our simulation. We have found that a mesh size of 5 nm allows to obtain accurate results avoiding large simulation times. Fig. 5.2(b) shows typical computed results using the FDE software. These show the calculated electric field intensity profiles of the first 8 propagating modes in an hexagonal *InP* nanowire (with a diameter of 660 nm and a refractive index of 3.4) suspended in air ( $n_{air} = 1$ ).

These results help identifying the different types of propagating modes as well as

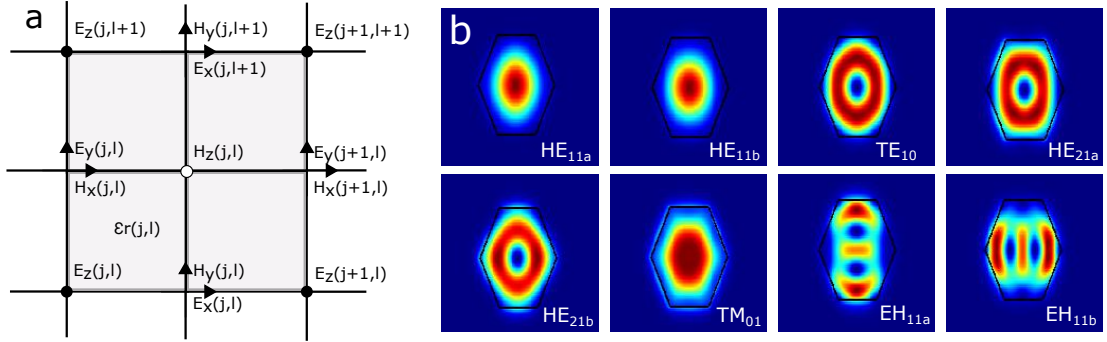


Figure 5.2: (a) Example of a 2D Yee Mesh. (b) First eight transverse modes of an *InP* 660 nm diameter hexagonal NW suspended in air computed with Lumerical Mode Solutions.

calculate their losses and effective indices. Regarding the latter, we have used the method described in ref. [55], to calculate the effective indices of the propagating modes of *InP* NW laser on a silica substrate. This allowed us to choose specific NW dimensions with selected propagating modes for the subsequent analyses of coupled NW laser structures. Fig. 5.3 shows results computed for the case described above. Here we have calculated the first 8 propagating modes in an *InP* NW laser on silica substrate, whose diameter is varied from 200 to 1000 nm.

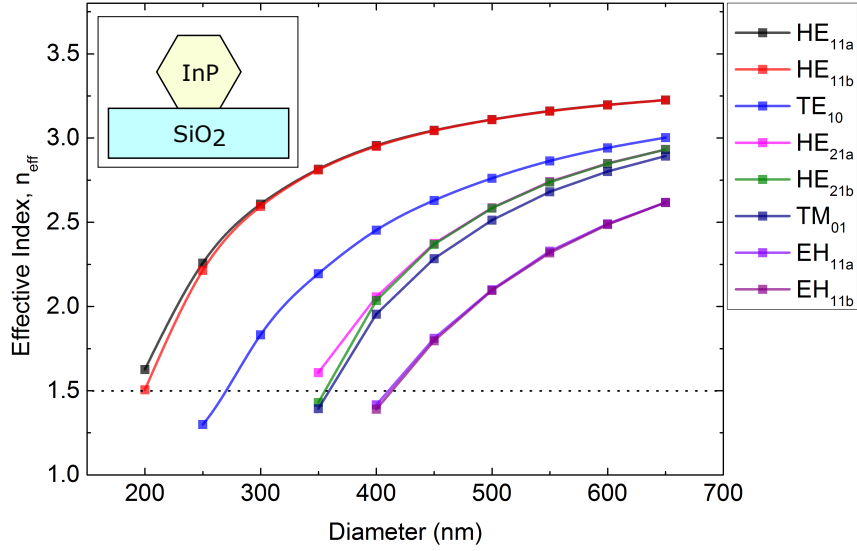


Figure 5.3: Effective indices of propagating modes inside an *InP* NW laser on a silica substrate (measured at the wavelength of 880 nm).

From the results in Fig. 5.3, we can estimate that *InP* NW lasers with a diameter of 260 nm will be optimal for investigation with our model. This parameter choice is based on the fact that for that specific diameter the only possible lasing modes will be the  $HE_{11a}$  and  $HE_{11b}$ . This is not only supported by our calculations but from previous numerical and experimental reports in the literature [55]. Moreover, from ref. [55] we can retrieve the values for the threshold gains for the  $HE_{11a}$  and  $HE_{11b}$  modes for a 260 nm diameter *InP* NW to be equal to  $1870 \text{ cm}^{-1}$  and  $1600 \text{ cm}^{-1}$ , respectively.

#### 5.1.4 Simulation of Evanescently Coupled NW Laser Pairs

Here the process of combining the rate-equation and the FDE models for the analysis of coupled NW laser systems is discussed. The calculated refractive indices from the FDE model were included into the rate-equation model to find regions of stability for an evanescently coupled NW laser pair [98]. Simple but accurate approximations for

the bifurcations separating regions of stable and unstable dynamics have been derived in [98] using a rate-equation based model of evanescently coupled lasers. A schematic for that modelled system is included in Fig. 5.1(a). In our case, when investigating a system formed by evanescently-coupled *InP* NW laser pairs (with equal diameters of 260 nm), we needed to calculate the coupling rate  $\kappa$ . In order to do so, we needed to obtain the values for the propagation constants of the symmetric and anti-symmetric normal modes, referred as  $\beta_1$  and  $\beta_2$  respectively. Using a commercial Lumerical FDE software package, it is possible to calculate two sets of data for the two supported lasing modes in this system,  $HE_{11a}$  and  $HE_{11b}$ , showing symmetric and anti-symmetric modes. That information will be subsequently fed into the rate-equation model derived by Adams et al. [143] to be able to investigate the dynamical operation of the coupled NW laser system under analysis.

To get to that stage, a set of steps needed to be followed. Firstly, we calculated the coupling rate,  $\kappa$ , by finding the index difference between the two supported coupled modes in the system. The index difference ( $\Delta n$ ), between the symmetric and asymmetric modes, is obtained directly by subtracting the effective indices of the symmetric ( $n_1$ ) and anti-symmetric ( $n_2$ ) modes:  $\Delta n = (n_1 - n_2)/2$ . The coupling coefficient per unit length,  $\kappa$ , is related to the normal mode indices by the expression  $\kappa = k\Delta n$ , where  $k$  is the free-space wave number. We then calculate the group indices of the two supported modes  $HE_{11a}$  and  $HE_{11b}$  as a function of wavelength using FDE simulations, as shown graphically in Fig. 5.4, and applying the following expression (Eq. 5.5), where  $n_g$  is the group index and  $n_e(\lambda)$  is the effective index at a given wavelength  $\lambda$ .

$$n_g = n_e(\lambda) - \frac{dn_e(\lambda)}{d\lambda} \lambda \quad (5.5)$$

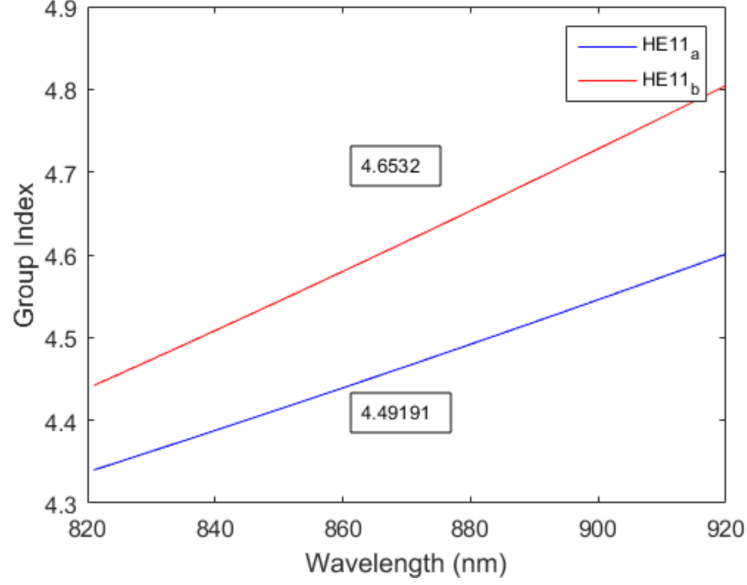


Figure 5.4: Group index values as a function of wavelength for the HE<sub>11a</sub> and HE<sub>11b</sub> modes in an evanescently coupled NW laser system formed by two equal 260 nm diameter *InP* NWs. Values in boxes correspond to group indices at the wavelength of 880 nm.

Next, we calculate the photon lifetime using the expression  $\tau_p = (v_g \Gamma g_{th})^{-1}$ , where  $v_g$  is the group velocity,  $\Gamma$  is the confinement factor and  $g_{th}$  is the threshold gain. The group velocity is defined by  $v_g = c/n_g$ , where  $c$  and  $n_g$  are the speed of light and the group index, respectively. After obtaining this information we can then calculate the coefficient  $\kappa$ , for this system, using the expression, Eq. 5.6, reported in [98, 143]:

$$\kappa = C_k e^{-2wd/a} \quad (5.6)$$

Where  $w = \frac{2\pi a}{\lambda} \sqrt{n_e^2 - n_{clad}^2}$ , being  $2a$  the NWs' diameter,  $\lambda$  is the propagated/simulated wavelength, and  $n_e$  and  $n_{clad}$  are the effective index of the propagated mode and the refractive index of the cladding. In this case, for the evanescently-coupled *InP* NW laser system the values in this expression are equal to:  $\lambda = 880$  nm,  $2a = 260$  nm,  $n_c = 3.4$ ,  $n_{clad} = 1$ . The effective index,  $n_e$  for each guided mode in the coupled

Mode	$w$	$C_k$ ( $ps^{-1}$ )	$\tau_p$ ( $ps$ )
HE <sub>11a</sub>	1.9733	45	0.0656
HE <sub>11b</sub>	1.9321	23	0.0757

Table 5.1: Numerical values of parameters.

*InP* NWs on an SiO<sub>2</sub> substrate are found from the FDE simulations carried out with Lumerical. The value of the constant  $C_k$  is found from fitting the curve depicting the relationship between calculated coupling rate  $\kappa$  versus NW lasers' separation,  $2d$ . The calculated values for  $w$  and  $C_k$  for the two supported modes, HE<sub>11a</sub> and HE<sub>11b</sub>, are shown in Table 5.1. Table 5.1 also shows the photon lifetime values for each of the two modes. Parameter values for both  $\Gamma$  and  $g_{th}$  are extracted from the results provided in [55] for *InP* NW lasers of length equal to 5  $\mu\text{m}$ .

The relationship between the coupling rate-photon lifetime product ( $k\tau_p$ ) versus NW lasers' separation ( $2d$ ) is calculated applying the values included in Table 5.1 into Eq. 5.6. These are compared with the results obtained from FDE simulations. Fig. 5 plots together the results obtained for both supported modes, HE<sub>11a</sub> and HE<sub>11b</sub> using the analytical equations reported in [98] (dashed lines) with those obtained with the FDE simulations (solid dots). The insets in Fig. 5.5 also show the intensity profiles for the two modes, HE<sub>11a</sub> and HE<sub>11b</sub> in the coupled NW laser pair system. Fig. 5.5 shows very good agreement between both approaches for both HE<sub>11a</sub> and HE<sub>11b</sub> modes.

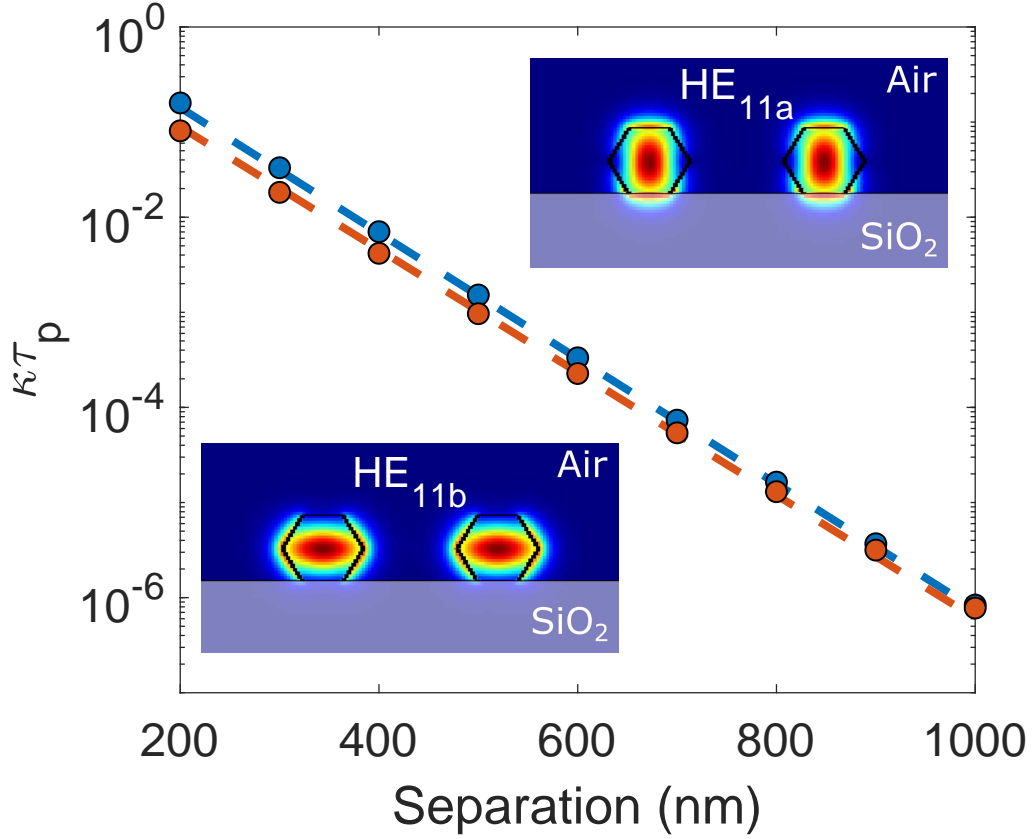


Figure 5.5: Relationship between  $k\tau_p$  and the separation between NWs for the  $HE_{11a}$  (in blue) and  $HE_{11b}$  modes. Comparison of the results obtained from FDE simulations (in circles) with those from Eq. 5.6 (dashed lines). The inset shows the intensity profiles of the two modes supported by the NW structures. Figure taken from [98].

From Fig. 5.5 it is possible to conclude that a large parameter region in terms of separation between the two NW lasers,  $2d > 300$  nm, satisfies this condition for both supported modes in the system. After verifying the very good degree of agreement between the results obtained with FDE simulations and the analytical expressions derived in [98] for a coupled NW laser system, it is now possible to use the model in [143] to determine the stability conditions for our system using the following expressions:

$$\Delta f < \frac{\alpha_H \kappa}{\pi} \quad (5.7)$$

$$\Delta f > \frac{1}{2\pi} \sqrt{(2\alpha_H \kappa)^2 - \left(\frac{Q}{\tau_p}\right)^2} \quad (5.8)$$

Where  $\Delta f$  is the frequency offset between the two lasers in our system. Eqs. 5.7 and 5.8 provide the stability regions of the system limited respectively by saddle-node and Hopf bifurcations. Fig. 5.6 shows the obtained results, for both supported modes  $HE_{11a}$  and  $HE_{11b}$ , from the stability analysis of the system using Eqs. 5.7 and 5.8 with parameter values equal to  $\alpha_H = 3$ ,  $\tau_N = 1$  ns and  $Q = 2$ . In Fig. 5.6, blue and red curves indicate the location of saddle-node and Hopf bifurcations in the  $\Delta f$  vs  $2d$  plane. Regions of stability where the two 260 nm-diameter *InP* NW lasers are phase-locked in the anti-phase normal mode lie between these bifurcations. Outside these regions various forms of instability including periodic oscillation, chaos, and complex dynamics will be found in system [143].

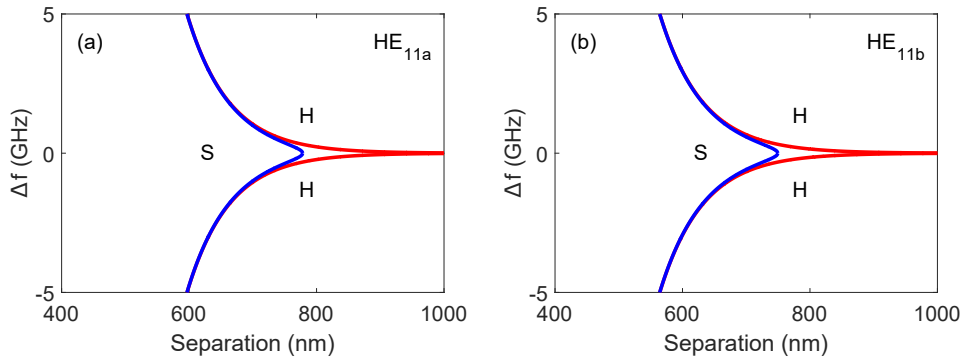


Figure 5.6: Saddle-node(S) and Hopf(H) bifurcations calculated using Eqs. 5.7 and 5.8 for the modes  $HE_{11a}$  (a) and  $HE_{11b}$  (b) in an evanescently coupled *InP* NW laser system. The parameter values used were respectively equal to  $\alpha_H = 3$ ,  $\tau_N = 1$  ns and  $Q = 2$ . Figure taken from [98].

From Fig. 5.6, we can see that the regions of stable phase-locked behavior for the coupled NW laser pair system are very small and located close to zero frequency offset between the two NW lasers. In practice this would imply the selection of devices with very similar resonant frequencies which will be very challenging indeed. We must

note here that an offset in resonant frequency between the two NW lasers ( $\Delta f$ ) will be unavoidable in practice due to differences in the NWs' cavity lengths arising during device growth. For example, a 0.1 nm difference will result in a frequency offset between devices of 5 GHz. This will imply that in practice non-linear operation rather than phase-locked behavior is to be expected from a system of two evanescently-coupled (260 nm diameter) *InP* NW lasers. Using Eq. 5.8 the minimum separation for stable phase-locked operation for the case of zero frequency offset ( $\Delta f = 0$ ) between the two NW lasers is given by:

$$Q = 2\tau_N\alpha_H\kappa \quad (5.9)$$

Fig. 5.7 shows the calculated relationship between the normalised pumping rate  $Q$  and the NWs' separation  $2d$  for both modes,  $HE_{11a}$  and  $HE_{11b}$ , obtained from Eq. 5.9 using the same parameter values as in the results of Fig. 5.6. The region of stable anti-phase normal mode operation lies to the right of the line obtained in Fig. 5.7 for each of the two modes. The normalised pumping  $Q$  is related to the actual pumping rate  $P$  by:

$$Q = C_Q \left( \frac{P}{P_{th}} - 1 \right) + \frac{P}{P_{th}} \quad (5.10)$$

Where  $P_{th}$  is the threshold pumping value of  $P$  and  $C_Q$  is given by:

$$C_Q = \frac{a_{diff}}{g_{th}} N_0 \quad (5.11)$$

Where  $a_{diff}$  is the differential gain and  $N_0$  is the transparency carrier concentration. These latter parameters are difficult to estimate for the case of *InP* NW lasers. For

simplicity, in our calculations we have used widely accepted parameters values for conventional *GaAs* lasers:  $a_{diff} = 5 \times 10^{-16} \text{cm}^2$  and  $N_0 = 1 \times 10^{18} \text{cm}^{-3}$  [143]. Finally, threshold gain values,  $g_{th}$ , of 1870 and 1600  $\text{cm}^{-1}$  for the  $\text{HE}_{11a}$  and  $\text{HE}_{11b}$  modes, respectively, were extracted from [55].

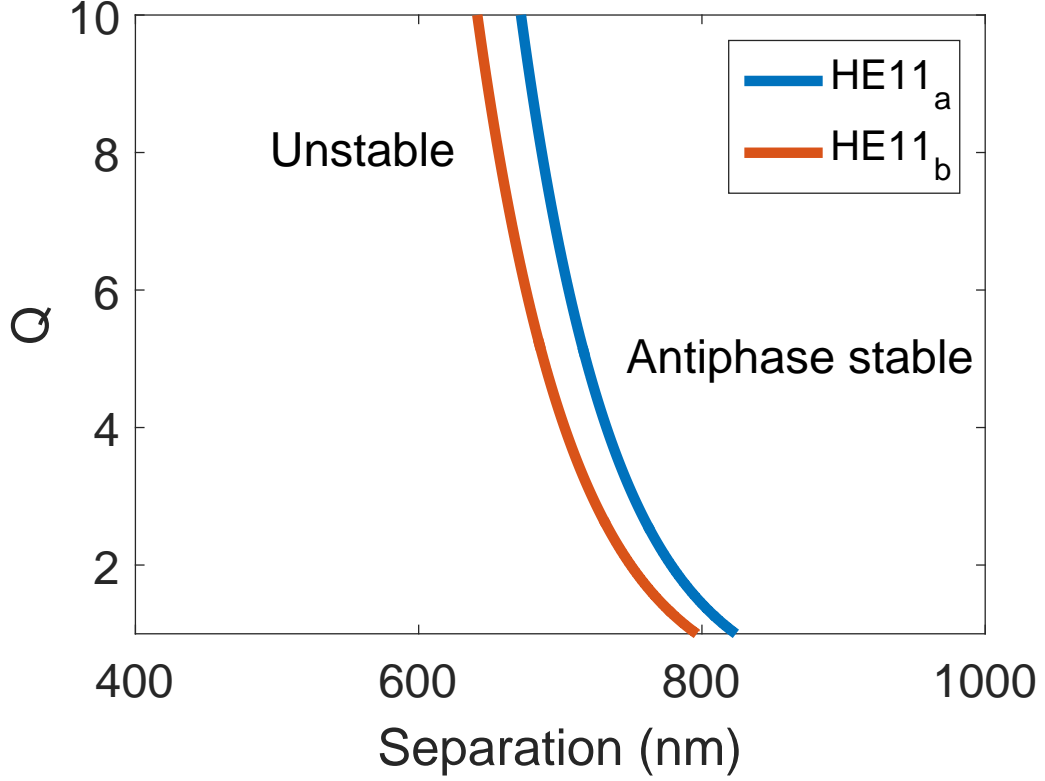


Figure 5.7: Stability boundaries for the  $\text{HE}_{11a}$  and  $\text{HE}_{11b}$  modes of the coupled *InP* NW laser system investigated in this work at zero frequency offset. Figure taken from [98].

It should be noted here that values of these device parameters are subject to some uncertainty for the case of nanowire lasers. The differential gain and transparency carrier concentration both influence the coefficient  $C_Q$  which affects the conversion from normalised pumping to the ratio of pump to threshold. Also, whilst the linewidth enhancement factor,  $\alpha_H$ , is not expected to differ greatly from values found in other semiconductor lasers, the situation for the carrier and photon lifetimes is less clear. In the case of  $\tau_N$  the effect of side-wall roughness and non-uniformity in NWs might intro-

duce non-radiative processes that shorten carrier lifetime. However, provided the pitch to hole diameter ratio is not too large during NW growth, as-grown *InP* nanowires are hexagonal with smooth side walls and a planar top facet, we might not expect major reductions. Nonetheless, for different types of NWs and different growth batches these parameter values might differ. As regards  $\tau_p$ , the values used here are derived, as detailed above, from calculated values of mode confinement factor, and threshold gain. These short lifetimes are, therefore, the result of a relatively low facet reflectivity combined with a length of 5  $\mu\text{m}$ . Further discussions of the result accuracy and sensitivity are given below. As outlined above, outside the regions of stability diverse nonlinear dynamical regimes could be obtained, including sustained periodic oscillations. For the case of zero frequency offset between the two NW lasers, a first-order approximation for the frequency,  $f$ , of periodic oscillations is given by:

$$f = \frac{1}{2\pi} \sqrt{4\kappa^2 + \frac{Q-1}{\tau_N\tau_p}} \quad (5.12)$$

The first term in the square root in Eq. 5.12 refers to the frequency of energy exchange (beating) between the two NW lasers, whilst, the second term corresponds to the relaxation oscillation frequency. Fig. 5.8 plots the oscillation frequency,  $f$ , versus the separation between NWs,  $2d$ , and the normalised pumping,  $Q$ . Fig. 5.8 plots results obtained for the  $\text{HE}_{11a}$  mode and using the same parameter values as before. Remarkably, Fig. 5.8 shows that for low but realistic device separations very high oscillation frequencies exceeding 100 GHz are predicted for a system of two coupled NW lasers.

From the results shown in Fig. 5.8, it is possible to conclude on the perspectives of coupled NW lasers for ultra-high frequency modulation systems. In the case when

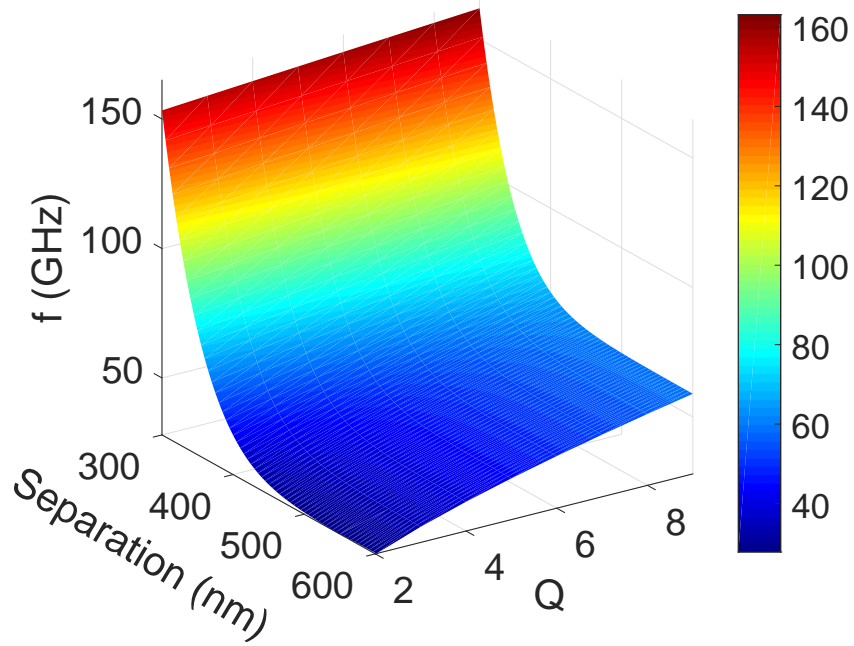


Figure 5.8: Frequency of periodic oscillations at zero frequency offset for the  $HE_{11a}$  mode. Figure taken from [98].

out-of-phase modulation is used, the modulation resonance frequency of evanescently-coupled lasers is given by  $\kappa/\pi$ . Thus, the results of Fig. 5.8 for lower separations indicate a good guide to potential modulation speeds. Recent results obtained with different systems also provide additional basis to support the great prospects of coupled NW laser systems for ultra-high frequency modulation. Specifically, a reported two-element array of photonic crystal VCSELs already demonstrated modulation rates up to 37 GHz [143]. Moreover, the modelling results showed a strong influence on the modulation bandwidth by the phase between NW devices (equivalent to the frequency offset used here) and the injection ratio (equivalent to the coupling rate). To conclude, even though the work is specifically focused on evanescently-coupled  $InP$  NW lasers with emission at 880 nm and diameters of 260 nm, the results, presented here, are extendable to other types of NW lasers (different material systems, dimensions and geometries). It is worth mentioning that recent reports (see refs. [152–154]) show the

possibility of NWs to operate in telecom windows (1310 and 1550 nm). This makes the presented model attractive for further research and when designing evanescently-coupled nanophotonic systems.

## 5.2 Binning of NW Lasers and ‘Champions’ Selection

As it was outlined before, semiconductor NW lasers are a promising technology for the realization of coherent optical sources with ultra-small footprint. However, to fully realize their potential in on-chip photonic systems, scalable methods are required for dealing with large populations of inhomogeneous devices that are typically randomly distributed on their host substrates [69]. In this section, we present work combining two complementary, high-throughput techniques: (1) the characterization of NW laser populations using automated optical microscopy (AOM) [57,70,71,110], and (2) a high-accuracy TP process with automatic device spatial registration and transfer [21,56,97]. It is worth mentioning that this was a collaboration project with Dr. Patrick Parkinson’s group at the University of Manchester. His group developed an automated characterization setup that scans substrates with randomly distributed NWs, maps those and characterizes one by one creating large datasets. By combining both techniques it becomes possible to select ‘champion’ NW lasers with specific laser properties (such as threshold, lasing wavelength, number of lasing modes) and integrate these onto target surfaces.

To experimentally demonstrate our approach, we show how a population of NW lasers was characterized, binned by threshold energy density, and subsequently printed into arrays onto a secondary substrate. Moreover, we provide a statistical analysis of the transferred and control devices showing that the transfer process does not incur in measurable NW laser damage, and the selected threshold binning can be maintained. Moreover, the analysis on the lasing threshold and mode spectra of the device populations proves the potential for using NW lasers for integrated systems’ fabrication.

### 5.2.1 Characterisation, Binning and TP of NW Lasers

In this work, *GaAs-AlGaAs* core-shell NW lasers were used, these were grown on a *GaAs* substrate using a bottom-up approach, as reported in [85]. These NW devices support multiple transverse modes and have a diameter of  $\sim 450$  nm and a length of  $\sim 4$   $\mu\text{m}$ , see [69, 85] for the description of the devices. In Fig. 5.9, a schematic flow diagram of the main stages of NW laser processing, measurement (using AOM) and transfer from the growth substrate onto the host samples is shown: (i)-(ii) vertically grown NWs are released and coarsely distributed on a quartz substrate with random orientation. It is worth mentioning here, that in Chapter 6 we look closely at how to controllably distribute a large-scale number of NW devices with controlled orientation. In this case however, to achieve a successful mapping of the NW lasers, the devices' distribution across the substrate should be relatively small. This ensures that individual devices are characterized and these are not grouped into bundles or small clusters. (iii) The transfer-printed devices are then optically measured and spatially mapped to allow device binning by a specific parameter: threshold or lasing wavelength (in this case). This is done using AOM by our collaborators at Manchester. (iv)-(v) Devices from the population are selected for transfer to a second substrate. An automatically spatially aligned transfer printing process is used to transfer these devices into regular arrays on a second receiver substrate. (vi) Finally, the devices are re-measured using the same setup as in (iii).

For the large-scale integration of NW devices, these were captured from their growth substrate using a  $\sim 2$   $\text{mm}^2$  flat polydimethylsiloxane (PDMS) stamp, as depicted in Figs. 5.10(a-c). The PDMS sample was fabricated following the standard recipe and then cut using a scalpel knife forming a square ( $\sim 2$   $\text{mm}^2$ ) piece. After, the stamp was

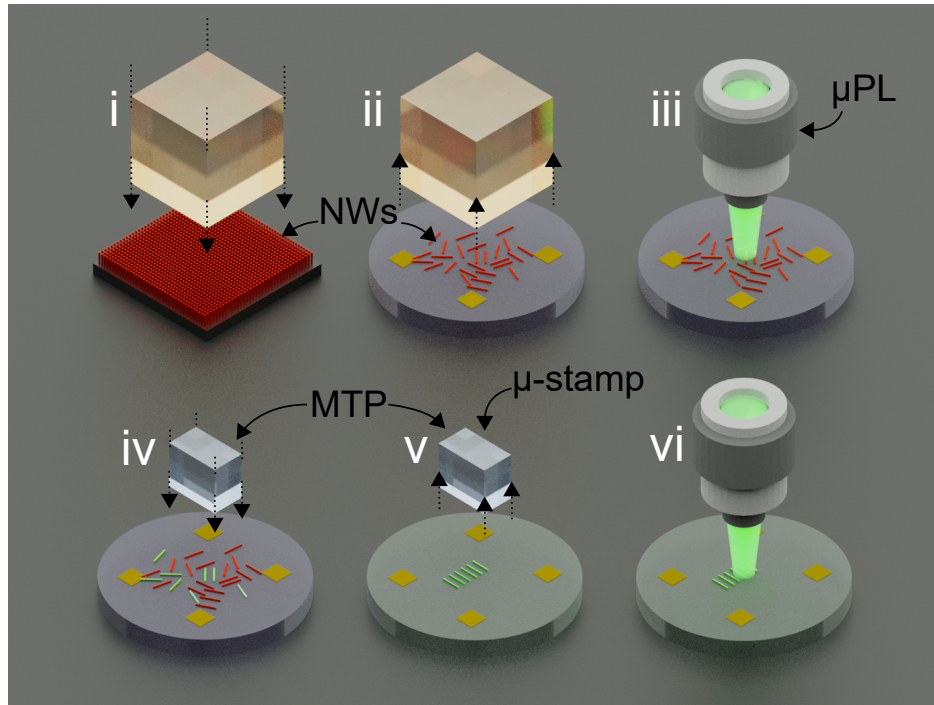


Figure 5.9: Schematic of the process: (i) NW lasers on their growth substrate are released using a large PDMS block and (ii) transferred onto a target quartz disk and randomly distributed on the surface. (iii) Device populations are characterised using an automated scanning microscopy system and binned by threshold. (iv) Selected NW devices are individually picked using a PDMS  $\mu$ -stamp and (v) printed onto a second substrate in regular arrays. (vi) Target devices are re-characterised with the system. Figure taken from [56].

mounted into the TP setup and aligned with the *GaAs-AlGaAs* NW growth sample, as shown in Fig. 5.10(a). The NW capture process was done in two stages, as depicted in Fig. 5.10(b): (1) the stamp was controllably pressed onto the NW sample. (2) the stamp was dragged perpendicularly to the NW growth axis for 20  $\mu\text{m}$  which resulted in the breaking/fracturing and capturing of the NWs by the viscous stamp surface. The stamp with captured NWs was then aligned with the target host sample and pressed into the selected area. Following the developed NW capture/release procedure, after raising the stamp from the sample, NW devices with enough surface bonding will be left on the host sample, as graphically shown in Fig. 5.10(d). In the last stage we found that the transfer yield was of the order of 50 %, resulting in a low density distribution

of wires. However, in this very case the relatively low yield was expected as no stamp optimization was carried out at this stage and the captured NWs had formed multi-layer surfaces on the stamp. Next, a z-cut quartz disk, coated with  $\sim 4 \mu\text{m}$  thick photopolymer [155] layer was used as the receiver. The photopolymer provided an adhesive surface to improve capture of the NWs, and the quartz and photo-polymer are transparent in the visible spectral range, allowing for measurement of the devices in a transmission microscopy arrangement. The NWs were transferred from the large area PDMS stamp to the quartz sample producing a randomly distributed population of devices on the sample. The spatial density of these devices was coarsely controlled through the initial release and subsequent printing process parameters.

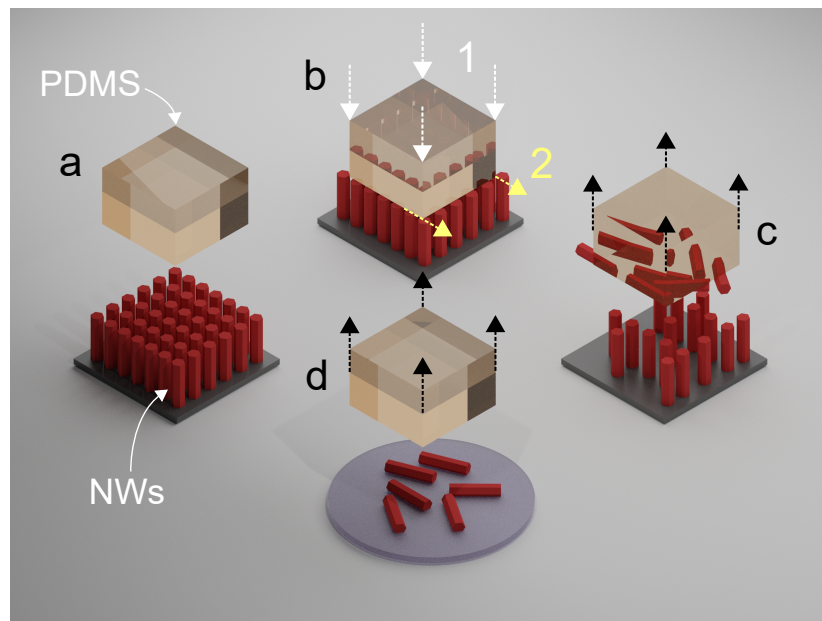


Figure 5.10: Transfer-printing process of as-grown NW lasers from their growth substrate onto a quartz disk sample: (a) a PDMS slab is aligned with the NW growth sample. (b) (1) PDMS stamp is pressed into the growth sample, (2) the stage underneath the sample is moved, NWs are captured by the PDMS. (c) captured devices are attached to the surface of PDMS. (d) captured NWs are transferred onto a target disk sample. Figure was taken from [56].

A relatively sparse population was targeted to ensure the automatic characterisation method addressed single, easily distinguishable devices. Fig. 5.11(a) shows an

optical microscope image of a random distribution of NWs on the quartz substrate with low spatial density. Furthermore, both the initial and final quartz receiver samples were patterned with lithographic markers to allow spatial mapping of the NWs to a predefined grid.

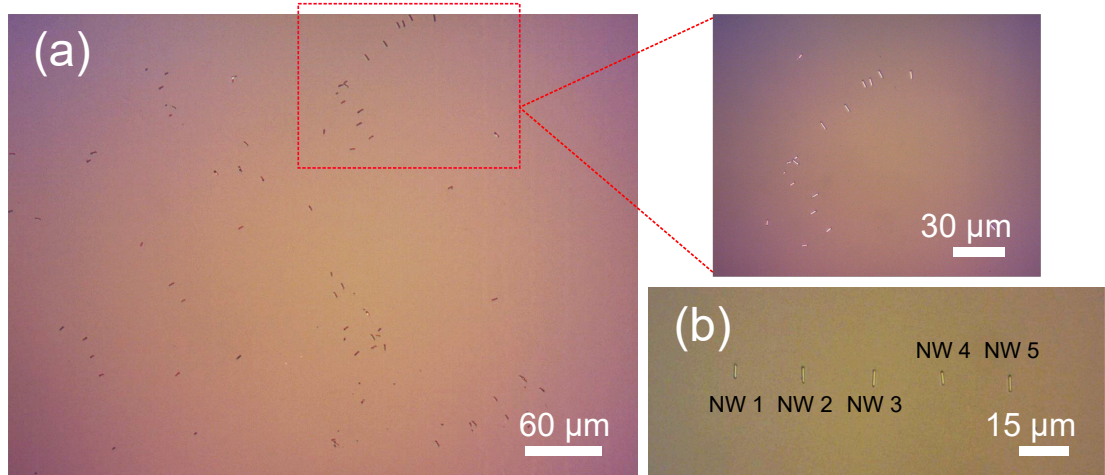


Figure 5.11: Quartz substrates with printed NW laser devices. (a) Randomly distributed 1st transfer and (b) 5 device array of binned and deterministically placed devices. Figure taken from [56].

The randomly deposited NW lasers were measured using the AOM setup at room temperature as previously described in ref. [69,71]. The automated scanning measurement technique allows the direct mapping of NW spatial position to be associated with the optical measurements. The measurements taken include below and above threshold emission spectra, pump energy vs emission power and both dark and bright-field micrographs of the device obtained with a CCD camera. Fig. 5.12(a-f) show an example of typical characterisation information for a NW device. A plot in Fig. 5.12(a) shows the device (red dot) location on the disk substrate relatively to the alignment markers (black grids). Processed bright-field images, like that in Fig. 5.12(b), were used to estimate the NWs' lengths and their relative orientation to that of the markers. The 'orientation parameter' became crucial when verifying if a specific device was correctly

identified, prior to its further integration onto the host disk substrate. Fig. 5.12(c) plots a dark-field micrograph of the lasing emission of the NW when optically pumped above threshold. Figs. 5.12(d-e) depict collected emission spectra of the NW laser at various excitation powers and the processed the light-in-light-out curve, respectively. The later was used to calculate the device lasing threshold level. Fig. 5.12(f) shows the measured PL spectrum of the device below its lasing emission threshold. By using the processed data, the NWs were pre-binned and selected for their further transfer printing onto the host substrate.

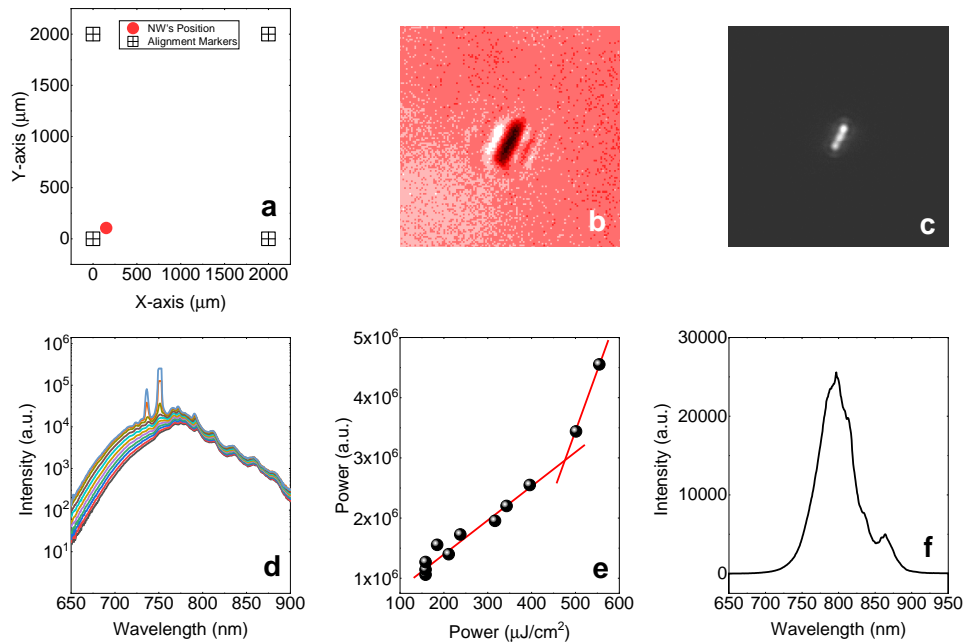


Figure 5.12: (a) Spatial map showing the location of a NW device. Dark grids indicate alignment markers on the substrate. (b) Image processed bright-field micrograph of the NW laser. (c) Darkfield micrograph of an excited NW laser above its lasing emission. (d) Spectra showing emission wavelength at various excitation energies. (e) A threshold plot showing LILO curve. (f) PL spectra of the NW laser taken at sub-threshold level. Figure was taken from [56].

### 5.2.2 Analysis of Target NW Devices

Due to the multi-mode nature of these NW devices, we have selected the threshold energy as the binning parameter. Furthermore, we believe this will be an important metric parameter in the fabrication of future integrated NW laser systems. For example, allowing to utilize designs of large-array (nano-)systems operating with similar performance (lasing threshold) across a chip. The initial transfer step created a population of 221 NW devices, out of which 180 of them showed lasing emission, on the first quartz substrate. Fig. 5.13(a) shows spatial mapping scatter plot of NW lasers across the disk substrate: red dots are coordinates of the NW devices and dark grids depict the alignment markers on the substrate. Fig. 5.13(b) shows a histogram of the initially measured threshold energy densities of the NW laser population. From this population, five bins of lasing threshold energy were selected as shown in Fig. 5.13(c), varying between 500 - 2500  $\mu\text{J}/\text{cm}^2$ , with mean values separated by  $\sim 500 \mu\text{J}/\text{cm}^2$ , to produce distinguishable sets. Five devices were selected per bin, and subsequently printed onto the second quartz sample. The selected devices were distributed throughout the population with randomly distributed orientation of their long axes. The printing process was semi-automated, taking as inputs the position of the NW relative to the registration marker at (0,0) and the orientation taken from the bright field microscopy image of the NW. The NW target position was defined as a set of coordinates on the target sample, relative to a registration marker on that substrate and all devices were rotated to have their long axes co-linear. The translation and rotation of the NWs during the printing process was computer controlled based on the measured registration marker and NW device positions. Fig. 5.13(d) shows the measured coordinates of the printed arrays as measured by the characterization system. Printed devices were separated by

$\sim 20 \mu\text{m}$  to allow individual optical injection and measurement.

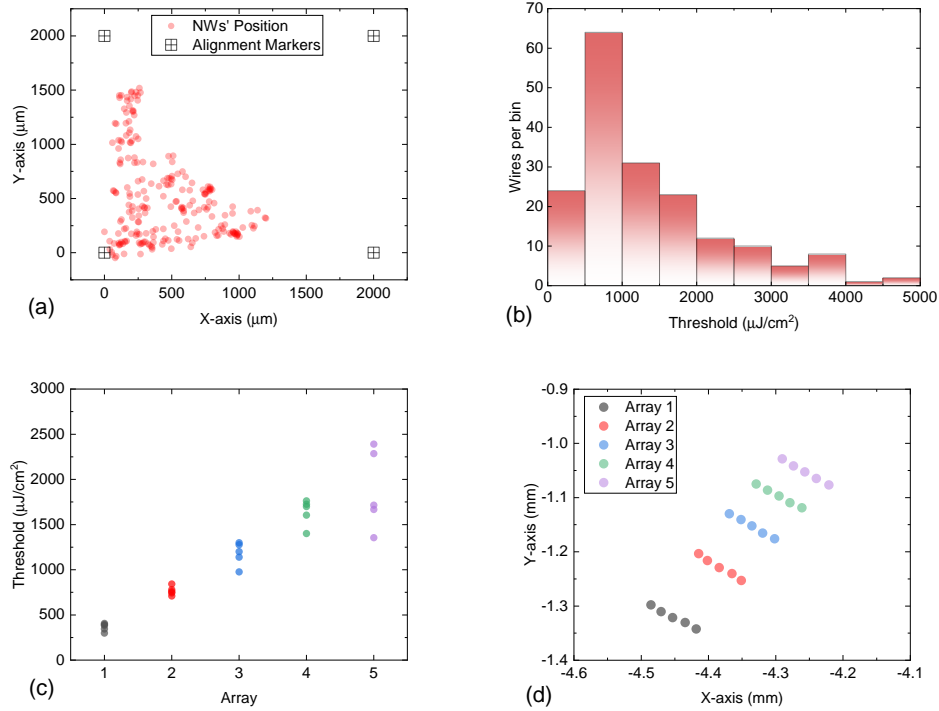


Figure 5.13: (a) Spatial map of 221 NWs (red circles) on quartz substrate identified by the characterization setup. Dark grids indicate alignment markers on the substrate, with a marker at (0,0) being the reference point. (b) Histogram of measured NW thresholds before the selection and transfer processes. (c) Binning of selected NW lasers by lasing threshold energy. (d) Absolute coordinates of the transfer-printed arrays on the second quartz disk. Figure taken from [56].

The post-processing round of measurements was performed on both printed and un-printed samples after a period of six months, during which time both sets of samples were stored together in a desiccator cabinet in a temperature controlled lab. By using the un-printed sample as a reference, we were able to control for variation in experimental conditions (and device aging) between these two measurements. In particular, our comparison allows compensation for changes made to the laser characterization tool during this period, that may introduce some absolute variation between first and second measurement rounds, but should not affect relative changes between printed and un-printed device sets. Fig. 5.14 shows the extracted threshold energy densities of the

printed (in color) and un-printed (black grids) devices before and after the transfer process, a dashed line is included as a visual aid corresponding to ideal correlation. In the printed device group, 24 out of 25 NW devices retained their lasing emission properties at room temperature, one device did not exhibit lasing. In the case of the un-printed devices, 74 out of the remaining 155 devices exhibited lasing during the second round of measurements. The reason for the significant decrease in lasing population in the un-printed devices is not clear at this stage, but may be due to thermal effects on the polymer layer at the laser surface during repeated measurements.

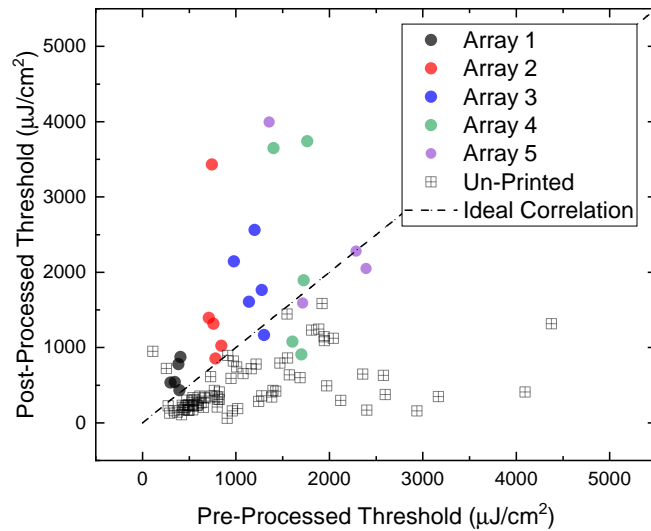


Figure 5.14: Correlation of laser threshold values between two measurements for printed and un-printed NW lasers. Dashed line represents ideal correlation ( $\rho = 1$ ). Figure taken from [56].

Individually, both populations of devices show correlation of their lasing threshold energy density from the first to second measurements, though there are clear differences. The linear correlation coefficient of threshold for the printed devices is moderate and significant, at 0.462 with  $p$ -value of .023, showing that the binned devices retain the global trend of threshold ranges, although a clear increase in absolute threshold levels is

observed. Similarly, the un-printed devices exhibit a moderate and significant correlation coefficient of 0.435. In this case the second measurement round exhibits a decrease in absolute threshold levels. The threshold energy densities for both populations show systematic variation in absolute values, but retain their global relative trends. Therefore, the low threshold binned devices can be selected for, even though absolute values are not stable for either printed or un-printed populations, due to changes in the laser excitation system described above. From Fig. 5.16, a comparable scatter around ideal correlation line ( $\rho=1$ ) could be seen for both printed and un-printed devices indicating that there was no systematic wavelength shifts in the two batches.

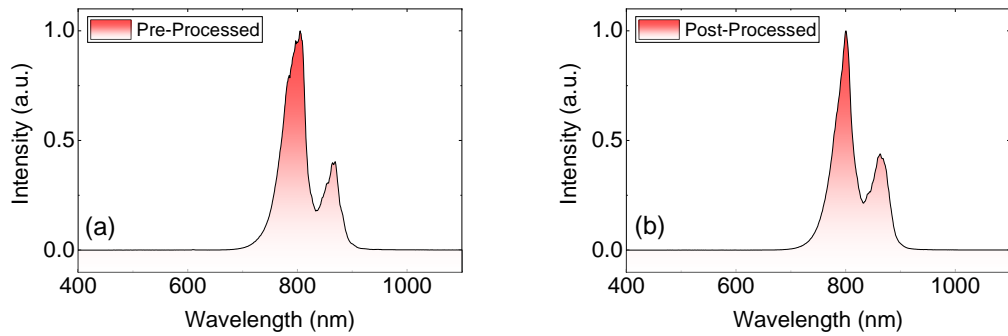


Figure 5.15: (a) Pre- and (b) post-processed PL spectra of a randomly selected NWs laser. Figure taken from [56].

As noted earlier, the NW lasers in this work support multiple modes and therefore any changes in the lasing threshold may be due to a change in dominant lasing mode between first and second measurement rounds. Before considering the lasing spectra, the sub-threshold photo-luminescence of the NWs was measured. As previously shown in ref. [69], the photoluminescence spectral form of these devices consisted of two distinct peaks, at  $\sim 810$  and  $870$  nm, which correspond to the emission from the core and MQW regions of the devices. The shape of emission is unique from wire-to-wire due to

the growth inhomogeneity. To verify that the TP techniques do not affect the printed devices both pre- and post-processing spectra were compared, an example of the plots is shown in Fig. 5.15. As no significant variations in the PL spectra were apparent, the peak lasing wavelength for both populations of devices was measured, as shown in Fig. 5.16, where red circles represent printed devices and black grids represent un-printed devices.

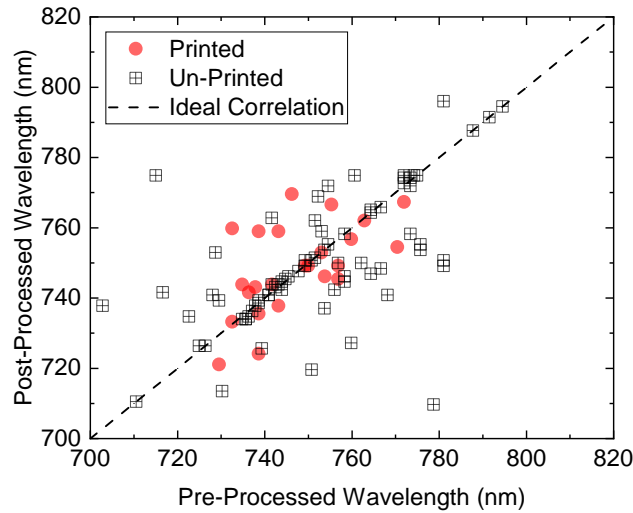


Figure 5.16: Correlation of peak lasing wavelength between two measurements for printed (red circles) and un-printed (black grids) devices. Dashed line represents ideal correlation. Figure taken from [56].

### 5.2.3 Comparison between Printed and Non-Printed Devices

Both populations of devices exhibit a similar scatter around the ideal correlation curve, suggesting that the printing process is not the dominant cause explaining the variations in peak lasing wavelength. The latter can be in fact significant, extending beyond 10nm in some cases, given the multimode nature of these devices. The peak wavelength measurement does not give a full account of the laser modal structure of the devices and therefore a further qualitative measure of the spectra can be defined to help ascertain

if the NWs have been physically altered between measurements. The modal structure of the NW lasers is directly related to their physical geometry and it can be used to provide a useful probe of any damage induced in the NWs. Three possible cases are presented in Fig. 5.17 that show how the modal structure of the laser may change between measurements.

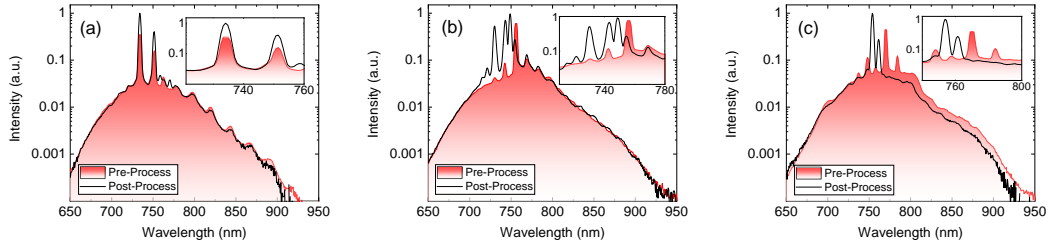


Figure 5.17: Three representative cases of printed and un-printed devices showing the optical spectra pre- and post-processing: (a) reconstructed, (b) partially reconstructed, (c) non-reconstructed spectrum. Figure taken from [56].

In the first case ‘A’, shown in Fig. 5.17(a), the Fabry-Perot (FP) modes of the specific device under analysis in both measurements fully overlap, i.e. the modes overlap in wavelength and exhibit similar distribution of optical power. For the particular device presented, the lasing threshold changed from 734 to 356  $\mu\text{J}/\text{cm}^2$ , but the modal structure shows very little variation. This suggests that the device losses, gain or absorption properties may be affected but its geometry and hence FP mode structure is consistent. The second common case ‘B’, Fig. 5.17(b), exhibits a spectrum where the FP modes of the device overlap between measurements, but the distribution of optical power has changed significantly. Again, in this case it would suggest that the geometry of the device is unaffected but the internal laser properties, or pumping conditions have changed enough to favour lasing of an alternative mode. Finally, in case ‘C’, in Fig. 5.17(c) the two modal spectra do not appear to overlap well, suggesting that the device has been physically affected, inducing a change in the FP mode structure.

Fig. 5.18 shows the correlation between measured laser threshold values between first and second measurement rounds. The form of each data point marker (black, red and blue) indicates whether the lasing spectral overlap between measurement ‘A’ and ‘B’ resembles case ‘A’, ‘B’ or ‘C’ most closely.

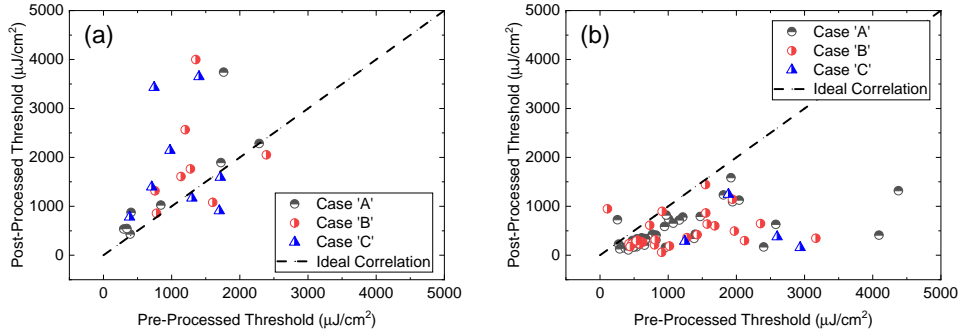


Figure 5.18: A scatter plot showing modal cases relative to the threshold change in the NW devices: (a) printed and (b) un-printed devices. Figure taken from [56].

Table 5.2 presents the correlation coefficients and p-values for each of three spectral overlap cases and the full printed and un-printed device populations. In both the printed and un-printed devices, case ‘A’ (full mode overlap) shows good correlation between first and second measurements. Cases ‘B’ and ‘C’ exhibit no significant correlation values for both populations. This suggests that where the device lasing conditions are consistent between first and second measurements, the printing process does not introduce significant detrimental effects to the devices and lasing thresholds are consistent. Nevertheless, the multi-modal nature of the NW lasers studied here allows for variation in lasing mode between measurements and therefore a shift in lasing threshold. In order to maintain tight control over device characteristics single transverse-mode NW lasers could be used.

Mode Spectrum Case [un-printed   printed]	Un-printed		Printed	
	$\rho$ -value	$p$ -value	$\rho$ -value	$p$ -value
All devices [74   24]	0.435	< .001	0.462	.023
Case A [45   8]	0.584	< .001	0.841	.009
Case B [25   8]	0.265	.200	0.239	.568
Case C [4   8]	-0.294	.706	0.006	.989

Table 5.2: Threshold fluence correlations for devices grouped by modal spectrum correlations.

### 5.3 Towards Fabricating Coupled-NW Laser Systems

For functional NW laser systems to become a reality, it is key to deliver flexible, reliable and reproducible nanofabrication techniques going beyond the current state-of-the-art to yield nanoscale integration accuracy of individual NW lasers. Such nanofabrication processes should also enable the integration of different types of NW lasers (emitting at diverse wavelengths) onto multiple surfaces, and their integration over large distances using simple protocols for operation. Such capability, would pave the way towards new key-enabling on-chip NW laser systems (e.g. NW laser arrays, coupled NW laser systems, multi-wavelength NW laser modules, etc.) with ultrafast speed operations, low energy requirements and ultrasmall footprints [98] for transformative developments in nanolaser-based ultra-frequency technology for on-chip data communications and multi-wavelength systems for sensing and spectroscopy [56, 72].

In this section, we demonstrate Wavelength Multiplexed Nanowire (WM-NW) laser systems enabled by TP techniques, permitting the positioning of individually-selected NWs into target locations with sub- $\mu\text{m}$  precision in different selected substrates, as described in Chapter 2. The WM-NW lasers were produced with controlled coarse ( $> 100$  nm) and fine ( $< 10$  nm) spacing between wavelength channels and with light emission in different infrared windows. These are fabricated using different types of semiconductor NWs (bulk *InP* [54] and core-shell *GaAs/AlGaAs* [85] NWs) with lasing emission at

room temperature integrated in laterally-aligned architectures yielding highly reduced footprints ( $> 10 \mu\text{m}^2$ ); hence allowing their simultaneous optical excitation using a single pumping laser spot (diameter  $\sim 1.6 \mu\text{m}$ ).

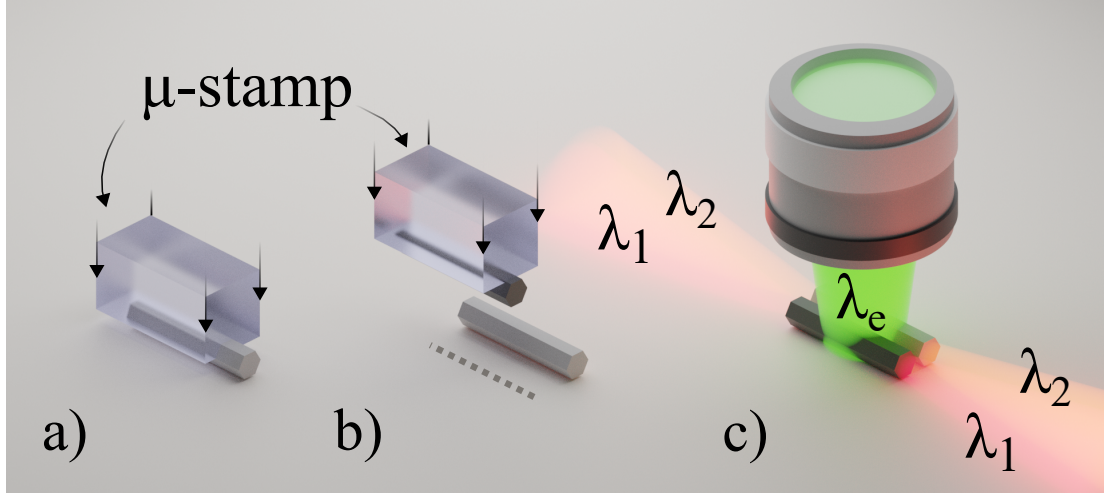


Figure 5.19: (a and b) Schematic diagrams illustrating the process to fabricate a laterally-aligned NW laser pair by means of TP. (c) Sketch of the WM-NW laser systems proposed in this work. Figure taken from [56].

Fig. 5.19 illustrates the geometry of the WM-NW laser systems of this work, where two NW lasers with light emission at distinct selected wavelengths ( $\lambda_1, \lambda_2$ ) are controllably integrated in a parallel-aligned arrangement (with facet-to-facet separation between NWs down to  $< 1 \mu\text{m}$ ). Figs. 5.19(a) and 5.19(b) depict the TP processes followed to fabricate the laterally-aligned WM-NW lasers systems: a first NW laser is captured using a polymer  $\mu$ -stamp from its original substrate and transfer-printed into a desired location in the receiving surface (Fig. 5.19(a)); subsequently, using the NW-to-NW alignment method (described in Chapter 2) a second NW laser is transfer-printed next to the first NW (with a desired separation) keeping the same device orientation (Fig. 5.19(b)). The diagram in Fig. 5.19(c) shows that the reduced separation between the two NWs in the formed WM-NW laser system permits their simultaneous optical excitation with a single pumping spot (at  $\lambda_e$ ) to yield dual-wavelength emission (at  $\lambda_1$

and  $\lambda_2$ ).

### 5.3.1 Wavelength Division Multiplexing (WDM) using NW Lasers

In this work we used two different types of NWs, namely bulk *InP* NW lasers [54] and core-shell *GaAs/AlGaAs* NWs [85], showing both room-temperature lasing emission in the wavelength ranges 840 - 900 nm and 750 - 800 nm, respectively. These NWs had all hexagonal cross-sections but different dimensions. Specifically, we used *InP* NW lasers of two different sizes, with average lengths of 5 and 10  $\mu\text{m}$  and average diameters of 435 and 260 nm, respectively. Concerning the core-shell *GaAs/AlGaAs* NW lasers we used devices with average diameters and lengths of 450 nm and 4  $\mu\text{m}$ , respectively. The variety of NW lasers used in this work allowed for a wide selection of their wavelength emission; hence enabling the fabrication of WM-NW laser systems with user-engineered wavelength operation.

Nevertheless, to develop the nanolaser systems of Fig. 5.19, counting with an alignment technique permitting sub- $\mu\text{m}$  positioning accuracy is key. Our developed NW alignment procedure is capable of achieving high positioning accuracy of  $\sim 200$  nm (see Chapter 2). The alignment NW-to-NW method is exactly the same as described in Chapter 2. This developed process, added to key capabilities of the TP platform, such as the full visualisation and imaging in real-time of the nanofabrication processes, and the highly-precise, software-controlled translational stages it possesses, ensures the achievement of sub- $\mu\text{m}$  NW placement accuracies in different receiving surfaces. This crucial result opens the door to new transformative developments in coupled NW laser systems and multi-wavelength NW laser modules. To showcase the potentials of the highly-precise nanofabrication technique of this work, we focused on demonstrating new WM-NW laser systems with ultra-small footprints based upon this approach. Impor-

tantly, the versatility of the TP technique allows such systems to be fabricated using NWs from different materials; hence emitting at different wavelength windows. This remarkable feature is used to develop WM-NW laser systems with different wavelength spacings between multiplexed channels and operating at different infra-red spectral windows. Nevertheless, it should be highlighted that TP is technology agnostic and could therefore enable the accurate fabrication of radically new, complex (nano-)photonic circuitry and coupled-cavity systems using optoelectronic nanostructures (such as NWs amongst other components) with user-engineered properties as building blocks.

Figs. 5.20 and 5.21 provide experimental proof-of-concept demonstration of novel WM-NW lasers with both coarse ( $> 100$  nm) and fine ( $< 10$  nm) spacing between channels. The ultra-small dimensions of the developed WM-NW lasers permit their optical excitation with a single micrometric pumping spot from a green 532 nm-pulsed pump laser (spot size =  $1.6 \mu\text{m}$ ) to achieve room-temperature dual-colour nanolaser systems. It is worth mentioning here, that the  $\mu\text{PL}$  setup, used in this work, is that described in Chapter 3.

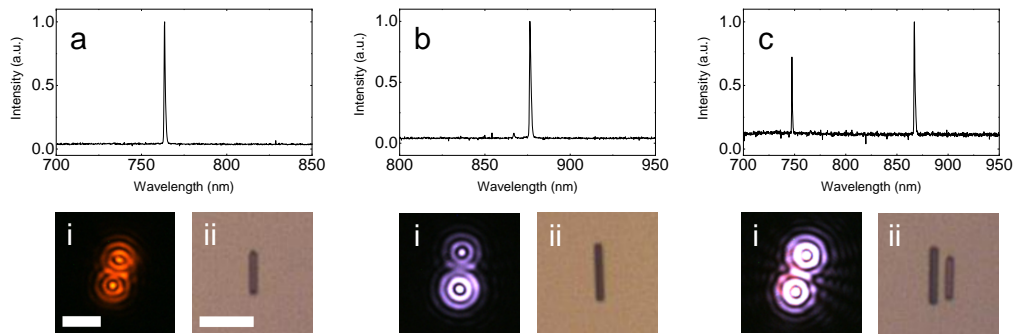


Figure 5.20: Room-temperature lasing spectra of the individual (a) core-shell  $GaAs-AlGaAs$  and (b) an  $InP$  NW lasers in a  $SiO_2$  substrate. The insets in (a and b) plot dark- (i) and bright-field (ii) micrographs of the NW lasers showing the devices' structure and their lasing emission from the NWs end-facets. (c) Room-temperature lasing spectra from the fabricated coarse wavelength spacing ( $> 100$  nm) WM-NW laser system. The images in the insets in (c) show the fabricated WM-NW laser system with closely separated ( $1 \mu\text{m}$  side-to-side) laterally-aligned NW lasers and its emission under optical excitation with a single pumping spot. Scale bars in (a)-(c):  $5 \mu\text{m}$

Specifically, Fig. 5.20 plots results for a coarse channel spacing ( $> 100$  nm) WM-NW laser system fabricated on a  $SiO_2$  substrate. This was built using two heterogeneous NW lasers, namely a core-shell  $GaAs/AlGaAs$  NW laser (450 nm-diameter; 4  $\mu\text{m}$ -long) and a bulk  $InP$  NW laser (435 nm-diameter; 5  $\mu\text{m}$ -long). Figs. 5.20(a) and 5.20(b) plot the room-temperature lasing spectra of the core-shell  $GaAs/AlGaAs$  and bulk  $InP$  NW lasers, when individually excited above their lasing threshold (at  $\sim 50$   $\text{mJcm}^{-2}$ ) and showing emission at the wavelengths of  $\sim 760$  nm and  $\sim 880$  nm, respectively. Insets (i) in Figs. 5.20(a) and 5.20(b) show images of the  $GaAs/AlGaAs$  and  $InP$  NW lasers on a  $SiO_2$  substrate. Additionally, insets (ii) in Figs. 5.20(a) and 5.20(b) plot dark-field micrographs of the  $GaAs/AlGaAs$  and  $InP$  NW lasers under optical excitation (above threshold) showing their characteristic lasing emission from their two end-facets. After these two heterogeneous NWs are individually characterized, they are integrated together in a laterally-aligned NW laser pair arrangement to form the WM-NW laser system, reported in Fig. 5.20(c). The latter was fabricated in a  $SiO_2$  substrate with a target separation between NW centroids of just 1.4  $\mu\text{m}$  (for an effective separation between the sides of both NWs of 1  $\mu\text{m}$ ). A CCD image of the fabricated WM-NW laser is included in inset (ii) in Fig. 5.20(c). Fig. 5.20(c) plots the measured room-temperature lasing spectrum of the formed WM-NW laser under optical excitation (above threshold) with a single lasing spot (spot size of 1.6  $\mu\text{m}$ ). This shows dual-wavelength emission with coarse wavelength spacing ( $> 100$  nm) between two multiplexed channels at different infrared windows ( $\sim 760$  and  $\sim 880$  nm). Additionally, inset (i) in Fig. 5.20(c) includes a dark-field micrograph of the WM-NW laser showing its characteristic lasing emission from the end-facets of the two heterogeneous NWs forming it.

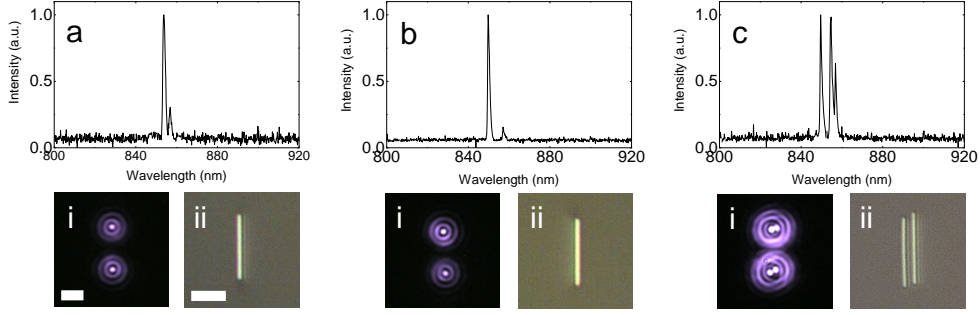


Figure 5.21: (a and b) Room-temperature lasing spectra measured from two individually-operated *InP* NW lasers (diameter: 260 nm; length 10  $\mu\text{m}$ ) in a  $\text{SiO}_2$  substrate. The insets in (a and b) plot dark- (i) and bright-field (ii) micrographs of the two *InP* NW lasers showing the achievement of lasing from the NWs' end-facets. (c) Room-temperature lasing spectra from the fabricated laterally-aligned WM-NW laser system (in a  $\text{SiO}_2$  substrate) with fine wavelength spacing ( $< 10\text{nm}$ ) between multiplexed channels. The insets in (c) show the fabricated WM-NW laser system with closely spaced (1  $\mu\text{m}$  side-to-side) laterally-aligned NW lasers and its emission under optical excitation with a single pumping spot. Scale bars in (a)-(c): 5  $\mu\text{m}$

Furthermore, we have also fabricated laterally-aligned WM-NW lasers using homogeneous devices (bulk *InP* NWs) and thus with similar properties. This will enable the demonstration of WM-NW lasers with fine spacing between multiplexed wavelength channels and with operation in a single spectral window in the infrared ( $\sim 850\text{ nm}$ ). These WM-NW lasers were built using two *InP* NWs with average lengths of 10  $\mu\text{m}$  and diameters of 260 nm. Fig. 5.21 provides spectral characterization and imaging data, obtained from the two individual *InP* NW lasers (Figs. 5.21(a) and 5.21(b)) and the finally fabricated WM-NW laser systems (Fig. 5.21(c)). All devices in fig. 5 have been transfer-printed on a  $\text{SiO}_2$  substrate for operation. The spectra in Figs. 5.21(a) and 5.21(b) showed that the individual *InP* NWs exhibited lasing emission in two different modes, at the wavelengths of 854 and 857 nm for the NW in fig. 7(a)), and at 850 and 857 nm for the NW in Fig. 5.21(b). Given the reduced diameter (260 nm) of these *InP* NWs, they would only support lasing on two transverse modes, namely  $\text{HE}_{11a}$  and  $\text{HE}_{11b}$ , with similar wavelengths [98]. The two lasing peaks in the spectra

of the individually-operated devices of Figs. 5.21(a) and 5.21(b), therefore correspond to those modes. Besides, the images in the insets in Figs. 5.21(a) and 5.21(b) show the separate *InP* NW lasers on the *SiO<sub>2</sub>* substrate (see inset (ii)) and their characteristic lasing emission through their end-facets (see inset (i)). After the *InP* NW lasers are individually characterized, these are integrated together to form the laterally-aligned WM-NW laser system of Fig. 5.21(c). The latter was built by means of TP with a target distance between NWs centroids of 1.26  $\mu\text{m}$ ; hence yielding an effective separation between the lateral sides of the NWs of 1  $\mu\text{m}$ . Fig. 5.21(c) shows that the measured room temperature spectrum from the combined WM-NW laser system (when optically excited above lasing threshold at  $\sim 40 \text{ mJcm}^{-2}$ ), exhibited emission in two main peaks at  $\sim 850 \text{ nm}$  and  $\sim 854 \text{ nm}$ , with an additional lower intensity emission peak at  $\sim 857 \text{ nm}$ . The spectrum in Fig. 5.21(c) therefore shows multi-wavelength lasing emission from the developed WM-NW laser system at the wavelengths of the individual *InP* NW lasers (850, 854 and 857 nm) and within the same spectral window in the infrared. The results in Fig. 5.21 therefore demonstrate also the achievement of WM-NW laser systems with fine wavelength spacing ( $< 10\text{nm}$ ) between channels and ultra-small footprints ( $< 10 \mu\text{m}^2$ ) and allowing simultaneous optical excitation with a single micrometric laser pumping spot. In summary, this work demonstrates highly accurate integration of individually-selected NW lasers with nanometric positioning accuracies into multiple substrates by means of TP techniques. Our approach permits successful operation with NW devices built from diverse material systems (e.g. bulk *InP* and core-shell *GaAs/AlGaAs*) and therefore showing lasing emission at diverse wavelength ranges ( $\sim 880 \text{ nm}$  and  $\sim 750 \text{ nm}$ , respectively). The developed nanofabrication technique has been used to develop new laterally-aligned NW laser systems with

very high NW integration accuracies, offering ultrasmall footprints ( $> 10 \mu\text{m}^2$ ) and allowing their simultaneous pumping with a single optical excitation spot (spot size  $1.6 \mu\text{m}$ ). We also demonstrate WM-NW laser systems built with laterally-aligned NW lasers from similar (bulk *InP*) or different (bulk *InP* and core-shell *GaAs/AlGaAs*) material systems yielding respectively fine ( $< 10 \text{ nm}$ ) and coarse ( $> 100 \text{ nm}$ ) spacing between wavelength channels. These results pave the way for new tailored wavelength-multiplexed nanolaser modules with operation at user-defined wavelengths, with controlled number of multiplexed channels and selected wavelength spacings whilst also yielding ultrasmall footprints and permitting optical excitation with a single micrometric pump laser spot. These results therefore offer exciting prospects for novel on-chip integrated nanophotonic platforms with in-built nanolaser systems for on-chip data communications, spectroscopy and sensing functionalities.

## 5.4 Conclusion and Summary

In conclusion, in this chapter we have shown and discussed the main concepts behind the design and production of complex hybrid systems with NW lasers. In the first part of the chapter, we analyse the dynamics and conditions for stability in an array of two laterally-coupled NW lasers in terms of their separation, difference in resonant frequencies and pumping rate under conditions of weak coupling. We find that the regions of stability are very small and are found close to zero frequency offset between the NW lasers. Outside these regions various forms of instability including periodic oscillation, chaos and complex dynamics are predicted to occur. Importantly, the analysis of the frequency of periodic oscillations for realistic laser separations and pumping conditions yields values of order 100 GHz thus underlining the significant potential of nanowire laser arrays for ultra-high frequency on-chip systems with very low foot-print and energy requirements.

In the second part of the chapter, we have demonstrated that large populations of NW lasers with random spatial distribution can be rapidly characterized and sorted using their measured lasing parameters. These populations can then be transferred to separate substrates using a semi-automated pick and place technique that uses the same spatial registration markers as the characterization measurements. NW lasers can be binned by lasing threshold and spatially arranged into regular arrays on a secondary substrate. Repeated measurements on both un-printed and printed device populations show that the multi-mode nature of the devices allows for variations in measured laser characteristics in both cases. Nevertheless, in cases where the laser modal spectrum is similar in both measurements, the lasing threshold energy densities are strongly correlated, showing that effective binning and device assembly can be achieved. These

results suggest that the printing process does not induce any particular detrimental effects in the transferred devices and could be a route to scalable systems assembly from large inhomogeneous distributions of NW devices. Furthermore, by targeting single-mode devices, some of this variability may be mitigated.

In the final section, we have showed how the TP technique combined with the accurate alignment processes developed was used to enable the capability to fabricate laterally-aligned NW laser systems with ultra-small separations between devices ( $\sim 1 \mu\text{m}$ ) and built using different types of NW devices. Such systems form the basis of the Wavelength Multiplexed NW laser systems demonstrated in this work. The latter provided controlled emission wavelengths in different infrared bands ( $\sim 760 \text{ nm}$  and  $\sim 850 \text{ nm}$ ) and were designed with both coarse ( $> 100 \text{ nm}$ ) and fine ( $< 10 \text{ nm}$ ) wavelength spacing between multiplexed channels. Importantly, such WM-NW lasers yield ultra-small footprints ( $> 10 \mu\text{m}^2$ ) allowing their optical excitation with a single pump laser spot ( $\sim 1.6 \mu\text{m}$  spot size).

## Chapter 6

# Conclusion and Future Work

This chapter brings the thesis to a conclusion. Here, a summary of the key points of this project are presented along with suggested lines for future work. The latter are illustrated with additional preliminary results, not included in the main framework of the thesis. The structure of this chapter is as follows: in the first section, the main research outcomes are summarized describing how these align with the main goals set at the beginning of the PhD project and reviewing the main achievements of our contributions and the new ideas these have triggered. We also provide a detailed summary of the main experimental and numerical results provided in Chapters 2 - 5.

In the second section, we discuss ideas for future research work providing early preliminary results for those new directions. These include: (1) large-area transfer-printing of NW devices with controlled orientation and high-printing coverage. This new approach with our transfer-printing technique enables producing large arrays of NWs on a target substrate, where printed devices have the same orientation; (2) We also present our new work on the transfer-printing of other types of nanostructures, namely Perovskite quantum-dot clusters, onto non-native substrates forming spatially controlled patterns. We also provide preliminary evidence that after the printing pro-

cess, the transferred Perovskite QD clusters retained their light emission properties, which could prove a significant result towards the fabrication of novel photonic systems with embedded QDs.

## 6.1 Conclusion

The main aim of this PhD project was to develop a novel system permitting the heterogeneous and controllable integration of semiconductor nanowire devices for the manufacturing of a new generation of nanophotonic circuitry. We have successfully achieved this ambitious goal set at the beginning of this PhD, with main research outcomes including:

- (1) The deterministic pick-and-place of target semiconductor nanowire devices from their growth substrate for their integration onto non-native surfaces. To achieve this we designed and fabricated bespoke polymeric  $\mu$ -stamps permitting the transfer-printing of semiconductor nanowires by allowing the control of the bonding forces (between nanowire and substrate) during the capture and release processes. This technique made possible not only to controllably capture different types of NWs (in terms of geometry, length, diameter, material), but also to release those at desired locations on non-native surfaces.

- (2) The assembly of arrays and other spatial patterns of NW lasers onto heterogeneous surfaces. Such systems were fabricated with target number of devices and controlled separations between them. Furthermore, an alignment technique was developed during this PhD project, enabling to position selected NW devices onto target locations with sub- $\mu\text{m}$  positional accuracy. This, combined with the NW pre-screening technique also presented in this work allowed us to create arrays of devices on tar-

get locations with control of key NWs' parameters (e.g. lasing threshold, emission wavelength).

(3) The integration of semiconductor NW devices, including NW lasers into pre-patterned nanophotonic systems (e.g. waveguides, nano-antennas) with absolute sub- $\mu\text{m}$  transfer-printing accuracy. Importantly, we have showed that the transfer-printed NW lasers retained their room-temperature lasing properties. This offers significant potential for a next generation of nanophotonic and optoelectronic systems with key-enabling NW devices at their core.

(4) The development of a numerical framework for the design and simulation of ultra-small footprint ( $< 5 \mu\text{m}^2$ ) high frequency (100 GHz) on-chip coupled NW laser systems. The model was designed for realistic NW separations, dimensions and pumping conditions, making it possible to be used for the design of bespoke coupled NW laser systems for their future assembly with the developed TP technique of this work.

I now summarize the main works presented in this thesis. I also give detailed comments on the future perspectives and directions that these might have. The works are summarized in the same order as they are presented in this thesis.

Chapter 2 describes the newly developed NW transfer-printing system, states its underlying operating principle and compares it with other alternative techniques. We show that the highly-precise NW positioning system of this PhD project using transfer-printing protocols has important advantages in terms of flexibility, repeatability and ease of use. Moreover, the ability to have several 'donor' and 'receiver' samples on a single TP system opens great perspectives for new routes towards advanced nanophotonic devices assembly into a single chip. Thanks to the developed TP technique at the nanoscale we can assemble nanophotonic systems built with different nanostruc-

tures and integrate those with sub- $\mu\text{m}$  accuracy. In Chapter 2 we also described the proposed new polymeric (PDMS)  $\mu$ -stamp designs for NW integration and show how and which of these should be used in different cases. Additionally, we state the optimal  $\mu$ -stamp composition (in terms of PDMS agent-to-base ratio) for successful NW integration with high printing yield. To demonstrate the NW transfer-printing technique, *InP* NWs with room temperature lasing emission were used with diameters and lengths ranging from 450 – 900 nm and 4 – 8  $\mu\text{m}$ , respectively. These were subsequently integrated from a ‘donor’ substrate onto target ‘receiver’ surfaces to demonstrate heterogeneous NW integration. Different receiver substrates were used including polymers, metals, gold-plated surfaces and diamond membranes. Importantly, our technique did not damage the NWs after the integration processes and these retained their lasing properties at room temperature. This was verified using  $\mu$ -PL characterization of the TP devices, before and after integration. Finally, we demonstrated a NW alignment technique using the ‘microscopy module’ integrated on the TP system and based on a real-time image processing algorithm combined with SEM imaging processes. This technique enabled us to achieve NW integration with sub- $\mu\text{m}$  positioning resolution. Importantly, the alignment technique is flexible permitting different potential routes towards its implementation for the fabrication of systems with even higher resolution. For example, by integrating the  $\mu$ -stamp (used for NW capture and release) directly into an SEM imaging system and implementing the developed algorithm, in principle it could be possible to achieve significant improvement in terms of positioning accuracy (sub-10 nm printing resolution) thanks to the greatly improved resolution provided by SEM techniques.

We also used the developed TP technique to fabricate diverse NW-based hybrid

photonic systems, as described in Chapter 4. At first, we demonstrated the integration of semiconductor NW lasers with waveguide (WG) systems on chip using two NW-WG coupling schemes: ‘lateral’ and ‘end-to-facet’ coupling. The results showed successful NW coupling to on-chip micrometric polymer waveguides with estimated coupling values of up to 1.9%. This value, however, is more governed by the refractive index mismatch between NW and WG, than the coupling scheme itself. Moreover, we showed that by employing mask-free laser-writing tools in combination with our TP technique it is possible to fabricate on-chip NW-WG coupled systems with various complex configurations (e.g. Y-junction architectures) on regular or mechanically-flexible substrates. Furthermore, the TP technique was used also to demonstrate vertically emitting nanowire laser systems with reduced lasing threshold. These were fabricated by means of TP integrating semiconductor NWs with Cat’s Eye (CE) nano-antennas. These showed low threshold room temperature lasing emission at  $\sim 2 \text{ mJcm}^{-2}$ , which is significantly lower compared to the lasing threshold measured on silica or aluminium substrates for comparable devices. Finally, we showed the capabilities of our TP technique for the integration of NW devices in 3-D architectures on prefabricated platforms and onto surfaces with reduced contact area. Importantly, the individual devices in the developed 3-D NW architectures retained their integrated positions after the multi-layer structures were processed. In particular we were able to successfully fabricate a 3D NW network forming a characteristic ‘hash-tag’ pattern onto bow-tie electrodes with a reduced contact area.

We also introduced complex hybrid systems with integrated NW lasers and the proposed methods to building those by means of TP, as described in Chapter 5. Essentially, this work could pave ways towards realizing novel ultra-compact NW systems providing

high-frequency complex dynamical regimes and multi-wavelength operation directly on-chip. We report a numerical model investigating the operation of evanescently-coupled *InP* NW laser pairs. Using this model we analyzed their dynamics and conditions for stability in terms of the separation between the NWs, their difference in resonant frequencies and pumping rate (under conditions of weak coupling). Our results show that the regions of stability were very small and found close to the zero frequency offset between the NW lasers. Furthermore, it is predicted that outside these regions various forms of instability including periodic oscillation, chaos and complex dynamics will occur. Moreover, high-frequency responses, exceeding 100 GHz were obtained. Hence, these results show the potential of NW laser arrays for ultra-high frequency on-chip systems with very low footprint and energy requirements for operation. Additionally, we also show that large populations of NW lasers with random spatial distributions can be rapidly characterized and sorted using their measured lasing parameters. We have binned by lasing threshold the characterised NW devices and transferred those using our TP technique to a host receiving substrate with spatial registration markers. We then spatially arranged the transfer-printed devices into regular NW arrays on a secondary (host) substrate. The repeated characterisation measurements of these devices showed that the multi-mode nature of the devices allows for variations in measured laser characteristics. This implies that in cases where the laser modal spectrum is similar in both measurements, the lasing threshold energy densities are strongly correlated, showing that effective binning and device assembly can be achieved. At last, we also used the TP technique combined with a developed algorithm for accurate alignment to fabricate laterally-aligned NW laser systems with reduced separations between devices (edge to edge separation of  $\sim 1 \mu\text{m}$ ), built using different types of semiconductor NWs.

Such devices form the basis of the wavelength multiplexed (WM) NW laser systems with controlled emission wavelengths reported in Chapter 5 of this thesis. For these systems, we used NW lasers emitting in two distinct infrared bands ( $\sim 760$  nm and  $\sim 850$  nm) and designed systems with both coarse ( $> 100$  nm) and fine ( $> 10$  nm) wavelength spacing between multiplexed channels. Importantly, such WM-NW lasers yield ultra-small footprints ( $< 5 \mu\text{m}^2$ ).

## 6.2 Future Work

### 6.2.1 Towards Large-Area and Parallel NW Printing

A line for future research would be the integration of NW devices in a large-scale with controlled orientations using the transfer-printing technique. We have started preliminary work in this research direction towards the fabrication of a next-generation of switchable THz polarization modulators built with NW devices at their core (see [141] for a description of these type of devices). To successfully fabricate such systems, it is strictly necessary to integrate a uniform layer of semiconductor NWs aligned in the same orientation. An alternative method to fabricate these devices relies in the use of a direct-printing technique (when a growth sample is dragged across the target surface). However, this method is not fully controllable and there is a difficulty associated with implementing an alignment mechanism or targeting a specific area in a given substrate where the device is to be fabricated. Using our developed TP technique, properly modified to be able to also perform large-scale device integration could help overcome these challenges. Hence, we have modified our TP apparatus and developed a larger square-shaped  $\mu$ -stamp  $500 \times 500 \mu\text{m}$  in dimensions to provide a first-proof-of-concept demonstration of large-scale aligned NW integration.

The large-scale NW capture process is very similar to that used to pick-up small bundles of NWs (from their growth substrate), for their integration onto a ‘donor’ sample. Such NW bundle integration was carried out prior to starting the transfer-printing processes used to integrated individual NW devices in diverse platforms, as presented during this thesis. However, in this case the stamp has a much larger area ( $500 \times 500 \mu\text{m}$ ). As a result, this approach allows not only to capture more NW devices at once, but also upon detaching these from the growth substrate, the devices

are forced to align into a single direction. This process is depicted in Figs. 6.1(a-b), where a square  $\mu$ -stamp is positioned atop an ‘as-grown’ NW array (Fig. 6.1(a)) before it is pressed-and-dragged against it (Fig. 6.1(b)). After this process is completed the ‘target’ NWs within the range of the larger area  $\mu$ -stamp are captured. The process used for the large-scale NW release is analogous to that used when transfer-printing a single NW, however here we have found that typically a 50% printing yield was achieved. We believe this is mainly due to the multiple layers of overlapping NWs captured at one go. In principle, when decreasing a NW array density, we should achieve a comparable to single NW devices printing yields.

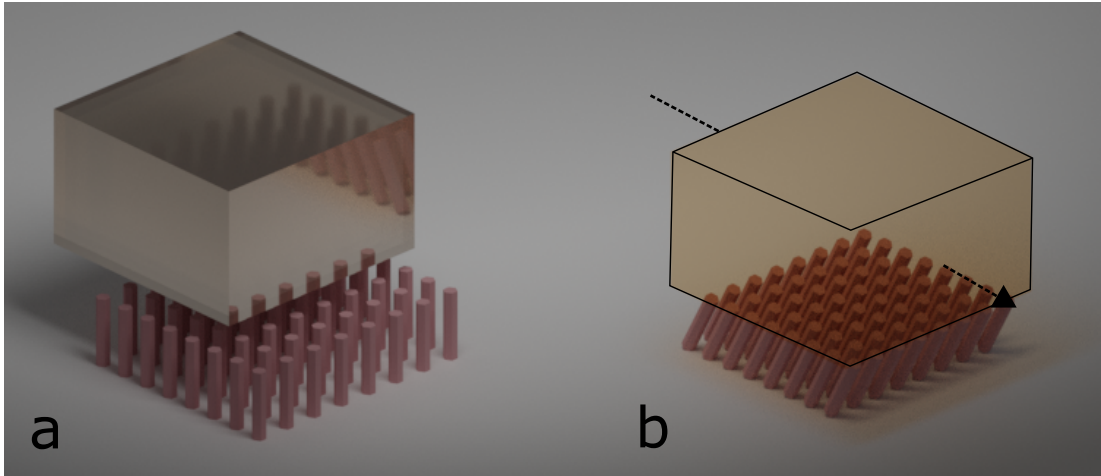


Figure 6.1: (a) Micro-stamp is aligned with as-grown NWs on a substrate. (b) Micro-stamp is dragged across NWs’ array and devices are captured with the  $\mu$ -stamp.

Fig. 6.2 show our first preliminary results on the large-area NW device printing. For this first demonstration *InP* NWs (length  $\sim 10 \mu\text{m}$  and diameter  $\sim 260 \text{ nm}$ ) were used. These were transfer-printed onto a quartz disk substrate targeting a defined (vertical) orientation, as shown in Fig. 6.2. Since this was a first trial, we have not yet achieved full uniform device spread. Additionally, since multiple layers of NWs are simultaneously captured, these detached from the growth substrate at different points, resulting in a certain variation in the dimensions of the released NWs in the receiver

substrate, as seen in Fig. 6.2. However, these early results clearly show the potentials of using our developed TP for this large-scale integration task. There is also significant room for improvement for our approach going forward, both in terms of stamp design and in the density of integration of ‘as-grown’ NWs. Moreover, a clear advantage of our technique over direct printing alternatives is the ability to fully visualize the whole process through the transparent  $\mu$ -stamp used in our approach to carry out the NW printing mechanisms. As a result, it becomes possible to locally print NW devices at target areas within a substrate, by selecting a specific geometry for the  $\mu$ -stamp used for outlining the region of interest with positional markers.



Figure 6.2: Optical micrograph of the fabricated large-scale area on a quartz disk substrate. Arrows indicate the target orientation of the  $\sim 10 \mu\text{m}$  NW devices. Scale bar:  $100 \mu\text{m}$ .

The further improvements to the large-scale technique can offer parallel and scalable integration of NW devices onto heterogeneous surfaces and into systems. This will allow integrating 100s or even 1000s of devices in a single transfer step (in a similar

way it's done using  $\mu$ -LEDs [78]). Prior to that, however, certain challenges must be solved: (1) high-capture yield, (2) common orientation of the captured devices, and (3) equispaced device separation. To achieve better capture yield, stamp's parameters should be properly tuned/optimized (its base/agent ratio) during the curing process. Or even other stamp designs should be investigated. In principle, this will ensure more devices are successfully picked during a single capture step. Which in turn will result in more NWs being aligned in the same orientation. The later difficulty can be solved by adjusting the as-grown NW sample: by making larger separations between adjacent NWs (50 - 100  $\mu\text{m}$ , for example). After, a stamp that complies with the outline can be fabricated. It will have an array of stamp heads on the stamp's base to enable parallel integration (individual elements of the array will be separated by the same distance as as-grown NWs). To illustrate the idea, Fig. 6.3 depicts the proposed stamp design, where an array of stamp heads is located on the stamp's base. Finally, if the same sub- $\mu\text{m}$  printing accuracy is maintained during the TP process, this will enable a significant step forward in realizing NW devices for industrial purposes and would open a large-scale manufacturing capabilities.

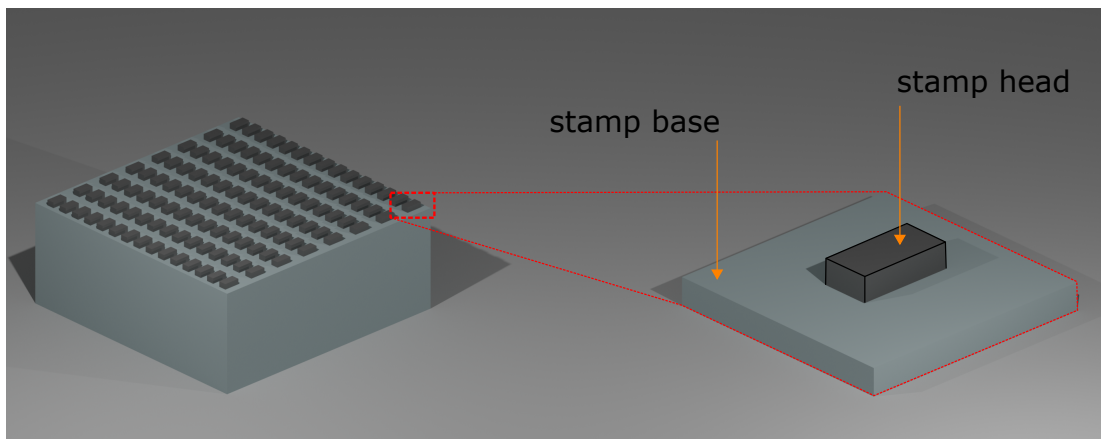


Figure 6.3: Sketch of a large-scale NW stamp for parallel and scalable integration.

## 6.2.2 Transfer-Printing of Perovskite Quantum-Dots (QDs) onto Non-Native Surfaces

In the past several years, Perovskite quantum dots (QD) have received considerable attention by the scientific community due to their unique properties at the nanoscale [156–158]. For example, due to their reduced lattice defect properties these nanostructures perform well even under non-ideal growth conditions. These nanostructures have become building blocks for a large number of QD-embedded photonic systems, including resonators such as whispering gallery mode and Fabri-Perot resonators [159, 160]. Recent studies have also shown that the devices offer great prospects for the development of ultra-small laser sources with emission [161] at room temperature. Hence, using TP processes to controllably transfer Perovskite QDs into target locations on selected surfaces or pre-fabricated substrates, will open new exciting routes towards the development of novel hybrid (nano-)photonic integrated systems using these unique nanostructures as main elements.

We have started preliminary work in this research direction using in-house synthesized Perovskite QDs [162] and transfer-printed them onto heterogeneous surfaces. Specifically we have used  $\text{CsPbX}_3$  QDs [162] which due to their band-gap structure exhibited photoluminescence emission at the wavelength range around 530 nm. Hence, for their characterization we optically pumped these nanostructures with a 355 nm UV pump laser using the setup described in Chapter 3.

Here we present our preliminary results on the transfer-printing of uncoated Perovskites QD crystals onto both polymer (PDMS) and diamond substrates. We show first our results using PDMS as the target receiving substrate. Due to the strong adhesive properties of PDMS, it becomes possible to release Perovskite QD crystals onto

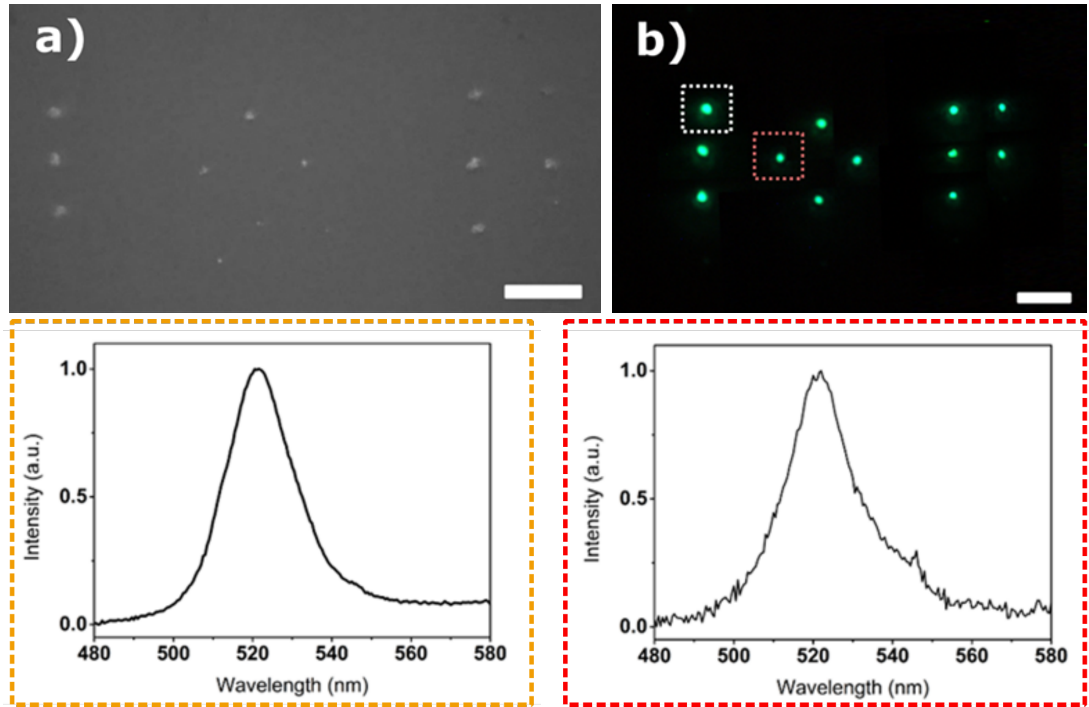


Figure 6.4: (a) bright-field micrograph of a TP array of uncoated-perovskite QD crystals. (b) collage of separate dark-field micrographs of an optically excited QD crystals. Spectrum plots below are measurements of the optically excited quantum-dot clusters in dotted-lines of dark-field micrograph in (b).

its surface when these are captured with a PDMS  $\mu$ -stamp with a lower base-to-agent ratio. A similar method was used for the transfer-printing of NW devices (see Chapter 2). As a result, we have managed to sequentially-print Perovskite QD clusters to build an array forming the pattern ‘IOP’, initials of the Strathclyde’s Institute of Photonics, onto a PDMS substrate. Before the transfer-printing processes, a preparation process had to be followed. At first, the Perovskite QDs were diluted in isopropanol were drop-coated onto a thin-glass slide. After the isopropanol evaporated, the thin glass slide was covered with randomly distributed Perovskite QD clusters. After this, the glass-slide was mounted onto the TP setup where a flat-tip  $\mu$ -stamp (analogous to that used to transfer-print NW devices) was used to capture individually-selected Perovskite QD clusters. Next, the stamp (with the captured QD cluster) was brought over to a desired location in the receiving substrate (PDMS in this case) where the Perovskite QD cluster

was finally released. Fig. 6.4(a) shows a bright-field micrograph of the transfer-printed array of Perovskite QD crystals forming the “IOP” acronym on a PDMS surface. Fig. 6.4(b) shows in turn a dark-field micrograph of the formed array when the transferred QD clusters are optically excited with the UV pump laser revealing their light emission (after integration). Fig. 6.4 shows emission spectra for the QD clusters marked with yellow and red dotted squares. The central PL wavelength of both QD clusters is comparable in both cases and centered at around 522 nm. These results show that Perovskite QD clusters can be transfer-printed onto a non-native surface whilst keeping their emission properties at room temperature. This opens a variety of possibilities of integrating those into photonic circuitry (for example, WGs and antennas), which in turn, will enable creating ultra-compact novel devices.

## List of Publications

- (1) B. Guilhabert, A. Hurtado, **D. Jevtics**, Q. Gao, H. H. Tan, C. Jagadish, and M. D. Dawson, "Transfer Printing of Semiconductor Nanowires with Lasing Emission for Controllable Nanophotonic Device Fabrication," *ACS Nano* 10(4), 3951–3958 (2016).
- (2) **D. Jevtics**, A. Hurtado, B. Guilhabert, J. McPhillimy, G. Cantarella, Q. Gao, H. H. Tan, C. Jagadish, M. J. Strain, and M. D. Dawson, "Integration of Semiconductor Nanowire Lasers with Polymeric Waveguide Devices on a Mechanically Flexible Substrate," *Nano Letters* 17(10), 5990–5994 (2017).
- (3) W.-Z. Xu, F.-F. Ren, **D. Jevtics**, A. Hurtado, L. Li, Q. Gao, J. Ye, F. Wang, B. Guilhabert, L. Fu, H. Lu, R. Zhang, H. H. Tan, M. D. Dawson, and C. Jagadish, "Vertically Emitting Indium Phosphide Nanowire Lasers," *Nano Letters* 18(6), 3414–3420 (2018).
- (4) A. Hurtado, **D. Jevtics**, B. Guilhabert, Q. Gao, H. H. Tan, C. Jagadish, and M. D. Dawson, "Transfer printing of semiconductor nanowire lasers," *IET Optoelectronics* 12(1), 30–35 (2018).
- (5) M. J. Adams, **D. Jevtics**, M. J. Strain, I. D. Henning, and A. Hurtado, "High-frequency dynamics of evanescently-coupled nanowire lasers," *Scientific Reports* 9(1), (2019).
- (6) K. Peng, **D. Jevtics**, F. Zhang, S. Sterzl, D. A. Damry, M. U. Rothmann, B. Guilhabert, M. J. Strain, H. H. Tan, L. M. Herz, L. Fu, M. D. Dawson, A. Hurtado, C. Jagadish, and M. B. Johnston, "Three-dimensional cross-nanowire networks recover full terahertz state," *Science* 368(6490), 510–513 (2020).
- (7) **D. Jevtics**, J. McPhillimy, B. Guilhabert, J. A. Alanis, H. H. Tan, C. Jagadish, M. D. Dawson, A. Hurtado, P. Parkinson, and M. J. Strain, "Characterization, Selection, and Microassembly of Nanowire Laser Systems," *Nano Letters* 20(3), 1862–1868 (2020).
- (8) J. McPhillimy, **D. Jevtics**, B. J. E. Guilhabert, C. Klitis, A. Hurtado, M. Sorel, M. D. Dawson, and M. J. Strain, "Automated Nanoscale Absolute Accuracy Alignment System for Transfer Printing," *ACS Applied Nano Materials* 3(10), 10326–10332 (2020).
- (9) L. W. Smith, J. O. Batey, J. A. Alexander-Webber, Y. Fan, Y.-C. Hsieh, S.-J. Fung, **D.**

**Jevtics**, J. Robertson, B. J. E. Guilhabert, M. J. Strain, M. D. Dawson, A. Hurtado, J. P. Griffiths, H. E. Beere, C. Jagadish, O. J. Burton, S. Hofmann, T.-M. Chen, D. A. Ritchie, M. Kelly, H. J. Joyce, and C. G. Smith, "High-Throughput Electrical Characterization of Nanomaterials from Room to Cryogenic Temperatures," *ACS Nano* 14(11), 15293–15305 (2020).

## List of Conference Presentations and Publications

(1) **D. Jevtics**, B. Guilhabert, A. Hurtado, Q. Gao, H. H. Tan, C. Jagadish, and M. D. Dawson, "Transfer printing of semiconductor nanowires," in 2016 IEEE Photonics Conference (IPC) (IEEE, 2016).

(2) A. Hurtado, **D. Jevtics**, B. Guilhabert, Q. Gao, H. H. Tan, C. Jagadish, and M. D. Dawson, "Novel nanoscale transfer printing technique for precise positioning of nanowire lasers," *SPIE Newsroom* (2017).

(3) **D. Jevtics**, A. Hurtado, B. Guilhabert, M. Jankauskas, N. Laurand, Q. Gao, H. H. Tan, C. Jagadish, and M. D. Dawson, "Precise Positioning and Orientation of Nanowire Lasers in Regular and Patterned Surfaces," in 2018 IEEE 18th International Conference on Nanotechnology (IEEE-NANO) (IEEE, 2018).

(4) A. Hurtado, **D. Jevtics**, M. D. Dawson, M. J. Adams, and I. D. Henning, "Laterally Coupled Nanowire Lasers: Bifurcations, Dynamics and High-Speed Potential," in 2018 IEEE Photonics Conference (IPC) (IEEE, 2018).

(5) A. Hurtado, **D. Jevtics**, B. Guilhabert, J. Robertson, J. McPhillimy, M. Strain, F.-F. Ren, H. Tan, C. Jagadish, and M. Dawson, "Transfer printing of semiconductor nanowire lasers for nanophotonic device fabrication (Conference Presentation)," in *Smart Photonic and Optoelectronic Integrated Circuits XXI*, (SPIE, 2019).

(6) **D. Jevtics**, M. Hejda, K. Peng, B. Guilhabert, J. Robertson, J. McPhillimy, H. Tan, C. Jagadish, M. B. Johnston, M. Strain, M. Dawson, and A. Hurtado, "Heterogeneous integration of semiconductor nanowires in 2D and 3D nanophotonic systems," in *Physics and Simulation of Optoelectronic Devices XXIX*, (SPIE, 2021).

# Bibliography

- [1] M. J. Klein, “Thermodynamics and quanta in planck's work,” *Physics Today*, vol. 19, no. 11, pp. 23–32, Nov. 1966.
- [2] D. Kleppner, “Rereading einstein on radiation,” *Physics Today*, vol. 58, no. 2, pp. 30–33, Feb. 2005.
- [3] J. P. Gordon, H. J. Zeiger, and C. H. Townes, “The maser—new type of microwave amplifier, frequency standard, and spectrometer,” *Physical Review*, vol. 99, no. 4, pp. 1264–1274, Aug. 1955.
- [4] M. A. Shampo, R. A. Kyle, and D. P. Steensma, “Nikolay basov—nobel prize for lasers and masers,” *Mayo Clinic Proceedings*, vol. 87, no. 1, p. e3, Jan. 2012.
- [5] T. H. MAIMAN, “Stimulated optical radiation in ruby,” *Nature*, vol. 187, no. 4736, pp. 493–494, Aug. 1960.
- [6] R. N. Hall, G. E. Fenner, J. D. Kingsley, T. J. Soltys, and R. O. Carlson, “Coherent light emission from GaAs junctions,” *Physical Review Letters*, vol. 9, no. 9, pp. 366–368, Nov. 1962.
- [7] M. H. Huang, “Room-temperature ultraviolet nanowire nanolasers,” *Science*, vol. 292, no. 5523, pp. 1897–1899, Jun. 2001.
- [8] F. S. Ujager, S. M. H. Zaidi, and U. Younis, “A review of semiconductor lasers for optical communications,” in *7th International Symposium on High-capacity Optical Networks and Enabling Technologies*. IEEE, Dec. 2010.

- [9] E. Tournié and A. N. Baranov, “Mid-infrared semiconductor lasers,” in *Advances in Semiconductor Lasers*. Elsevier, 2012, pp. 183–226.
- [10] I. D. W. Samuel and G. A. Turnbull, “Organic semiconductor lasers,” *Chemical Reviews*, vol. 107, no. 4, pp. 1272–1295, Apr. 2007.
- [11] J. M. Dudley, “Light, lasers, and the nobel prize,” *Advanced Photonics*, vol. 2, no. 05, Oct. 2020.
- [12] S. Karki, D. Tuyenbayev, S. Kandhasamy, B. P. Abbott, T. D. Abbott, E. H. Anders, J. Berliner, J. Betzwieser, C. Cahillane, L. Canete, C. Conley, H. P. Daveloza, N. D. Lillo, J. R. Gleason, E. Goetz, K. Izumi, J. S. Kissel, G. Mendell, V. Quetschke, M. Rodruck, S. Sachdev, T. Sadecki, P. B. Schwinberg, A. Sottile, M. Wade, A. J. Weinstein, M. West, and R. L. Savage, “The advanced LIGO photon calibrators,” *Review of Scientific Instruments*, vol. 87, no. 11, p. 114503, Nov. 2016.
- [13] A. Tartakovskii, Ed., *Quantum Dots*. Cambridge University Press, 2009.
- [14] A. Ruyter, *Quantum wells : theory, fabrication and applications*. New York: Nova Science Publishers, Inc, 2009.
- [15] *Optics and Photonics*. National Academies Press, Feb. 2013.
- [16] X. Duan, Y. Huang, R. Agarwal, and C. M. Lieber, “Single-nanowire electrically driven lasers,” *Nature*, vol. 421, no. 6920, pp. 241–245, Jan. 2003.
- [17] Y. Zhang, D. Saxena, M. Aagesen, and H. Liu, “Toward electrically driven semiconductor nanowire lasers,” *Nanotechnology*, vol. 30, no. 19, p. 192002, mar 2019.
- [18] D. Vanmaekelbergh and L. K. van Vugt, “ZnO nanowire lasers,” *Nanoscale*, vol. 3, no. 7, p. 2783, 2011.
- [19] S. W. Eaton, A. Fu, A. B. Wong, C.-Z. Ning, and P. Yang, “Semiconductor nanowire lasers,” *Nature Reviews Materials*, vol. 1, no. 6, may 2016.

- [20] A. Carlson, A. M. Bowen, Y. Huang, R. G. Nuzzo, and J. A. Rogers, “Transfer printing techniques for materials assembly and micro/nanodevice fabrication,” *Advanced Materials*, vol. 24, no. 39, pp. 5284–5318, aug 2012.
- [21] J. McPhillimy, B. Guilhabert, C. Klitis, M. D. Dawson, M. Sorel, and M. J. Strain, “High accuracy transfer printing of single-mode membrane silicon photonic devices,” *Optics Express*, vol. 26, no. 13, p. 16679, jun 2018.
- [22] J. McPhillimy, D. Jevtics, B. J. E. Guilhabert, C. Klitis, A. Hurtado, M. Sorel, M. D. Dawson, and M. J. Strain, “Automated nanoscale absolute accuracy alignment system for transfer printing,” *ACS Applied Nano Materials*, vol. 3, no. 10, pp. 10 326–10 332, Sep. 2020.
- [23] K. Peng, D. Jevtics, F. Zhang, S. Sterzl, D. A. Damry, M. U. Rothmann, B. Guilhabert, M. J. Strain, H. H. Tan, L. M. Herz, L. Fu, M. D. Dawson, A. Hurtado, C. Jagadish, and M. B. Johnston, “Three-dimensional cross-nanowire networks recover full terahertz state,” *Science*, vol. 368, no. 6490, pp. 510–513, Apr. 2020.
- [24] A. Mata, A. J. Fleischman, and S. Roy, “Characterization of polydimethylsiloxane (PDMS) properties for biomedical micro/nanosystems,” *Biomedical Microdevices*, vol. 7, no. 4, pp. 281–293, Dec. 2005.
- [25] E. Kroner, R. Maboudian, and E. Arzt, “Adhesion characteristics of PDMS surfaces during repeated pull-off force measurements,” *Advanced Engineering Materials*, vol. 12, no. 5, pp. 398–404, May 2010.
- [26] A. K. Geim, S. V. Dubonos, I. V. Grigorieva, K. S. Novoselov, A. A. Zhukov, and S. Y. Shapoval, “Microfabricated adhesive mimicking gecko foot-hair,” *Nature Materials*, vol. 2, no. 7, pp. 461–463, Jun. 2003.
- [27] Y. Xia and G. M. Whitesides, “Soft lithography,” *Angewandte Chemie International Edition*, vol. 37, no. 5, pp. 550–575, Mar. 1998.

- [28] O. Sahin, M. Ashokkumar, and P. M. Ajayan, “Micro- and nanopatterning of biomaterial surfaces,” in *Fundamental Biomaterials: Metals*. Elsevier, 2018, pp. 67–78.
- [29] D. Lipomi, R. Martinez, L. Cademartiri, and G. Whitesides, “Soft lithographic approaches to nanofabrication,” in *Polymer Science: A Comprehensive Reference*. Elsevier, 2012, pp. 211–231.
- [30] X. Jiang, S. Takayama, R. G. Chapman, R. S. Kane, and G. M. Whitesides, “Micro-scale patterning of cells and their environment,” in *Principles of Tissue Engineering*. Elsevier, 2007, pp. 265–278.
- [31] J. B. Park, W. S. Choi, T. H. Chung, S. H. Lee, M. K. Kwak, J. S. Ha, and T. Jeong, “Transfer printing of vertical-type microscale light-emitting diode array onto flexible substrate using biomimetic stamp,” *Optics Express*, vol. 27, no. 5, p. 6832, Feb. 2019.
- [32] D. Gomez, K. Ghosal, M. A. Meitl, S. Bonafede, C. Prevatte, T. Moore, B. Raymond, D. Kneeburg, A. Fecioru, A. J. Trindade, and C. A. Bower, “Process capability and elastomer stamp lifetime in micro transfer printing,” in *2016 IEEE 66th Electronic Components and Technology Conference (ECTC)*. IEEE, May 2016.
- [33] V. A. Parsegian, *Van der Waals Forces*. Cambridge University Press, Nov. 2005.
- [34] Y. Luo, R. Zhao, and J. B. Pendry, “van der waals interactions at the nanoscale: The effects of nonlocality,” *Proceedings of the National Academy of Sciences*, vol. 111, no. 52, pp. 18 422–18 427, Dec. 2014.
- [35] H. Hamaker, “The london—van der waals attraction between spherical particles,” *Physica*, vol. 4, no. 10, pp. 1058–1072, Oct. 1937.
- [36] *Intermolecular and Surface Forces*. Elsevier, 2011.
- [37] J. Bian, L. Zhou, X. Wan, C. Zhu, B. Yang, and Y. Huang, “Laser transfer, printing, and assembly techniques for flexible electronics,” *Advanced Electronic Materials*, vol. 5, no. 7, p. 1800900, May 2019.

- [38] C. Linghu, S. Zhang, C. Wang, and J. Song, “Transfer printing techniques for flexible and stretchable inorganic electronics,” *npj Flexible Electronics*, vol. 2, no. 1, Oct. 2018.
- [39] *Semiconductor Nanowires*. Elsevier, 2015.
- [40] E. Garnett, L. Mai, and P. Yang, “Introduction: 1d nanomaterials/nanowires,” *Chemical Reviews*, vol. 119, no. 15, pp. 8955–8957, Aug. 2019.
- [41] L. Güniat, P. Caroff, and A. F. i Morral, “Vapor phase growth of semiconductor nanowires: Key developments and open questions,” *Chemical Reviews*, vol. 119, no. 15, pp. 8958–8971, Apr. 2019.
- [42] L. N. Quan, J. Kang, C.-Z. Ning, and P. Yang, “Nanowires for photonics,” *Chemical Reviews*, vol. 119, no. 15, pp. 9153–9169, jul 2019.
- [43] S. W. Eaton, A. Fu, A. B. Wong, C.-Z. Ning, and P. Yang, “Semiconductor nanowire lasers,” *Nature Reviews Materials*, vol. 1, no. 6, May 2016.
- [44] E. Barrigón, M. Heurlin, Z. Bi, B. Monemar, and L. Samuelson, “Synthesis and applications of III–v nanowires,” *Chemical Reviews*, vol. 119, no. 15, pp. 9170–9220, Aug. 2019.
- [45] C. Couteau, A. Larrue, C. Wilhelm, and C. Soci, “Nanowire lasers,” *Nanophotonics*, vol. 4, no. 1, pp. 90–107, May 2015.
- [46] R. S. Wagner and W. C. Ellis, “VAPOR-LIQUID-SOLID MECHANISM OF SINGLE CRYSTAL GROWTH,” *Applied Physics Letters*, vol. 4, no. 5, pp. 89–90, Mar. 1964.
- [47] A. L. Pinaridi, S. J. Leake, R. Felici, and I. K. Robinson, “Formation of an au-si eutectic on a clean silicon surface,” *Physical Review B*, vol. 79, no. 4, Jan. 2009. [Online]. Available: <https://doi.org/10.1103/physrevb.79.045416>
- [48] W. E. Buhro, “In the flow: a finely controlled approach to catalyzed nanowire growth,” *NPG Asia Materials*, vol. 6, no. 2, pp. e83–e83, Feb. 2014. [Online]. Available: <https://doi.org/10.1038/am.2013.77>

- [49] E. Givargizov, “Fundamental aspects of VLS growth,” *Journal of Crystal Growth*, vol. 31, pp. 20–30, Dec. 1975.
- [50] N. Sköld, L. S. Karlsson, M. W. Larsson, M.-E. Pistol, W. Seifert, J. Trägårdh, and L. Samuelson, “Growth and optical properties of strained GaAs-GaxIn1-xP core-shell nanowires,” *Nano Letters*, vol. 5, no. 10, pp. 1943–1947, Oct. 2005.
- [51] T. Mårtensson, C. P. T. Svensson, B. A. Wacaser, M. W. Larsson, W. Seifert, K. Deppert, A. Gustafsson, L. R. Wallenberg, and L. Samuelson, “Epitaxial III-v nanowires on silicon,” *Nano Letters*, vol. 4, no. 10, pp. 1987–1990, Sep. 2004.
- [52] C. M. Lieber and Z. L. Wang, “Functional nanowires,” *MRS Bulletin*, vol. 32, no. 2, pp. 99–108, Feb. 2007.
- [53] R. G. Hobbs, N. Petkov, and J. D. Holmes, “Semiconductor nanowire fabrication by bottom-up and top-down paradigms,” *Chemistry of Materials*, vol. 24, no. 11, pp. 1975–1991, May 2012.
- [54] Q. Gao, D. Saxena, F. Wang, L. Fu, S. Mokkalpati, Y. Guo, L. Li, J. Wong-Leung, P. Caroff, H. H. Tan, and C. Jagadish, “Selective-area epitaxy of pure wurtzite InP nanowires: High quantum efficiency and room-temperature lasing,” *Nano Letters*, vol. 14, no. 9, pp. 5206–5211, Aug. 2014.
- [55] D. Saxena, F. Wang, Q. Gao, S. Mokkalpati, H. H. Tan, and C. Jagadish, “Mode profiling of semiconductor nanowire lasers,” *Nano Letters*, vol. 15, no. 8, pp. 5342–5348, Jul. 2015.
- [56] D. Jevtics, J. McPhillimy, B. Guilhabert, J. A. Alanis, H. H. Tan, C. Jagadish, M. D. Dawson, A. Hurtado, P. Parkinson, and M. J. Strain, “Characterization, selection, and microassembly of nanowire laser systems,” *Nano Letters*, feb 2020.
- [57] J. A. Alanis, D. Saxena, S. Mokkalpati, N. Jiang, K. Peng, X. Tang, L. Fu, H. H. Tan, C. Jagadish, and P. Parkinson, “Large-scale statistics for threshold optimization of optically pumped nanowire lasers,” *Nano Letters*, vol. 17, no. 8, pp. 4860–4865, Jul. 2017.

- [58] M. N. M. N, U. Hashim, M. K. M. Arshad, A. R. Ruslinda, S. F. A. Rahman, M. F. M. Fathil, and M. H. Ismail, “Top-down nanofabrication and characterization of 20 nm silicon nanowires for biosensing applications,” *PLOS ONE*, vol. 11, no. 3, p. e0152318, Mar. 2016.
- [59] M. Grundmann, *The Physics of Semiconductors*. Springer Berlin Heidelberg, 2010.
- [60] P. W. Milonni and J. H. Eberly, *Laser Physics*. Nashville, TN: John Wiley & Sons, Apr. 2010.
- [61] D. Neamen, *Semiconductor physics and devices : basic principles*. New York, NY: McGraw-Hill, 2012.
- [62] *Physics of Semiconductor Lasers*. Elsevier, 1991.
- [63] Z. Gu, Q. Song, and S. Xiao, “Nanowire waveguides and lasers: Advances and opportunities in photonic circuits,” *Frontiers in Chemistry*, vol. 8, Jan. 2021.
- [64] N. Hodgson and H. Weber, “The fabry perot resonator,” in *Optical Resonators*. Springer London, 1997, pp. 137–162.
- [65] Wikipedia, “Longitudinal mode — Wikipedia, the free encyclopedia,” <http://en.wikipedia.org/w/index.php?title=Longitudinal%20mode&oldid=889368634>, 2021, [Online; accessed 16-May-2021].
- [66] R. Boyd, *Nonlinear optics*. Amsterdam Boston: Academic Press, 2008.
- [67] Y. Zhang, A. M. Sanchez, M. Aagesen, H. A. Fonseka, S. Huo, and H. Liu, “Droplet manipulation and horizontal growth of high-quality self-catalysed GaAsP nanowires,” *Nano Today*, vol. 34, p. 100921, Oct. 2020.
- [68] J. Wu, A. Ramsay, A. Sanchez, Y. Zhang, D. Kim, F. Brossard, X. Hu, M. Benamara, M. E. Ware, Y. I. Mazur, G. J. Salamo, M. Aagesen, Z. Wang, and H. Liu, “Defect-free self-catalyzed GaAs/GaAsP nanowire quantum dots grown on silicon substrate,” *Nano Letters*, vol. 16, no. 1, pp. 504–511, Dec. 2015.

- [69] J. A. Alanis, D. Saxena, S. Mokkalpati, N. Jiang, K. Peng, X. Tang, L. Fu, H. H. Tan, C. Jagadish, and P. Parkinson, “Large-scale statistics for threshold optimization of optically pumped nanowire lasers,” *Nano Letters*, vol. 17, no. 8, pp. 4860–4865, jul 2017.
- [70] J. A. Alanis, M. Lysevych, T. Burgess, D. Saxena, S. Mokkalpati, S. Skalsky, X. Tang, P. Mitchell, A. S. Walton, H. H. Tan, C. Jagadish, and P. Parkinson, “Optical study of p-doping in GaAs nanowires for low-threshold and high-yield lasing,” *Nano Letters*, vol. 19, no. 1, pp. 362–368, dec 2018.
- [71] J. A. Alanis, Q. Chen, M. Lysevych, T. Burgess, L. Li, Z. Liu, H. H. Tan, C. Jagadish, and P. Parkinson, “Threshold reduction and yield improvement of semiconductor nanowire lasers via processing-related end-facet optimization,” *Nanoscale Advances*, vol. 1, no. 11, pp. 4393–4397, 2019.
- [72] D. Jevtics, A. Hurtado, B. Guilhabert, J. McPhillimy, G. Cantarella, Q. Gao, H. H. Tan, C. Jagadish, M. J. Strain, and M. D. Dawson, “Integration of semiconductor nanowire lasers with polymeric waveguide devices on a mechanically flexible substrate,” *Nano Letters*, vol. 17, no. 10, pp. 5990–5994, sep 2017.
- [73] W.-Z. Xu, F.-F. Ren, D. Jevtics, A. Hurtado, L. Li, Q. Gao, J. Ye, F. Wang, B. Guilhabert, L. Fu, H. Lu, R. Zhang, H. H. Tan, M. D. Dawson, and C. Jagadish, “Vertically emitting indium phosphide nanowire lasers,” *Nano Letters*, vol. 18, no. 6, pp. 3414–3420, may 2018.
- [74] K. Peng, P. Parkinson, L. Fu, Q. Gao, N. Jiang, Y.-N. Guo, F. Wang, H. J. Joyce, J. L. Boland, H. H. Tan, C. Jagadish, and M. B. Johnston, “Single nanowire photoconductive terahertz detectors,” *Nano Letters*, vol. 15, no. 1, pp. 206–210, dec 2014.
- [75] Y. Park, S. Jahangir, Y. Park, P. Bhattacharya, and J. Heo, “InGaN/GaN nanowires grown on SiO<sub>2</sub> and light emitting diodes with low turn on voltages,” *Optics Express*, vol. 23, no. 11, p. A650, May 2015.

- [76] J. Tatebayashi, Y. Ota, S. Ishida, M. Nishioka, S. Iwamoto, and Y. Arakawa, “Nanowire–quantum-dot lasers on flexible membranes,” *Applied Physics Express*, vol. 11, no. 6, p. 065002, May 2018.
- [77] M. Royo, M. D. Luca, R. Rurali, and I. Zardo, “A review on III–v core–multishell nanowires: growth, properties, and applications,” *Journal of Physics D: Applied Physics*, vol. 50, no. 14, p. 143001, Mar. 2017.
- [78] A. J. Trindade, B. Guilhabert, D. Massoubre, D. Zhu, N. Laurand, E. Gu, I. M. Watson, C. J. Humphreys, and M. D. Dawson, “Nanoscale-accuracy transfer printing of ultra-thin AlInGaN light-emitting diodes onto mechanically flexible substrates,” *Applied Physics Letters*, vol. 103, no. 25, p. 253302, dec 2013.
- [79] D. Gomez, K. Ghosal, T. Moore, M. A. Meitl, S. Bonafede, C. Prevatte, E. Radauscher, A. J. Trindade, and C. A. Bower, “Scalability and yield in elastomer stamp micro-transfer-printing,” in *2017 IEEE 67th Electronic Components and Technology Conference (ECTC)*. IEEE, may 2017.
- [80] C. G. Núñez, F. Liu, W. T. Navaraj, A. Christou, D. Shakthivel, and R. Dahiya, “Heterogeneous integration of contact-printed semiconductor nanowires for high-performance devices on large areas,” *Microsystems & Nanoengineering*, vol. 4, no. 1, aug 2018.
- [81] H. Xu, A. Hurtado, J. B. Wright, C. Li, S. Liu, J. J. Figiel, T.-S. Luk, S. R. J. Brueck, I. Brener, G. Balakrishnan, Q. Li, and G. T. Wang, “Polarization control in GaN nanowire lasers,” *Optics Express*, vol. 22, no. 16, p. 19198, Jul. 2014.
- [82] P. J. Pauzauskie, A. Radenovic, E. Trepagnier, H. Shroff, P. Yang, and J. Liphardt, “Optical trapping and integration of semiconductor nanowire assemblies in water,” *Nature Materials*, vol. 5, no. 2, pp. 97–101, jan 2006.
- [83] Y. Huang, “Directed assembly of one-dimensional nanostructures into functional networks,” *Science*, vol. 291, no. 5504, pp. 630–633, jan 2001.

- [84] S. Jin, D. Whang, M. C. McAlpine, R. S. Friedman, Y. Wu, and C. M. Lieber, “Scalable interconnection and integration of nanowire devices without registration,” *Nano Letters*, vol. 4, no. 5, pp. 915–919, may 2004.
- [85] D. Saxena, S. Mokkalapati, P. Parkinson, N. Jiang, Q. Gao, H. H. Tan, and C. Jagadish, “Optically pumped room-temperature GaAs nanowire lasers,” *Nature Photonics*, vol. 7, no. 12, pp. 963–968, Nov. 2013.
- [86] D. Saxena, S. Mokkalapati, and C. Jagadish, “Semiconductor nanolasers,” *IEEE Photonics Journal*, vol. 4, no. 2, pp. 582–585, apr 2012.
- [87] J. Tatebayashi, S. Kako, J. Ho, Y. Ota, S. Iwamoto, and Y. Arakawa, “Room-temperature lasing in a single nanowire with quantum dots,” *Nature Photonics*, vol. 9, no. 8, pp. 501–505, jun 2015.
- [88] Z. Yang, T. Albrow-Owen, H. Cui, J. Alexander-Webber, F. Gu, X. Wang, T.-C. Wu, M. Zhuge, C. Williams, P. Wang, A. V. Zayats, W. Cai, L. Dai, S. Hofmann, M. Overend, L. Tong, Q. Yang, Z. Sun, and T. Hasan, “Single-nanowire spectrometers,” *Science*, vol. 365, no. 6457, pp. 1017–1020, Sep. 2019.
- [89] R. D. Piner, J. Zhu, F. Xu, S. Hong, and C. A. Mirkin, ““dip-pen” nanolithography,” *Science*, vol. 283, no. 5402, pp. 661–663, Jan 1999.
- [90] S. Rozhok, R. Piner, and C. A. Mirkin, “Dip-pen nanolithography: what controls ink transport?” *The Journal of Physical Chemistry B*, vol. 107, no. 3, pp. 751–757, jan 2003.
- [91] A. J. Trindade, “Transfer printing of nitride based light emitting diodes,” Ph.D. dissertation, University of Strathclyde, 5 2015.
- [92] SmarAct, “Sr-2013 datasheet, p. 26135,” Tech. Rep., 2019.
- [93] K. Rae, E. Y. Xie, A. J. Trindade, B. Guilhabert, R. Ferreira, J. J. D. McKendry, D. Zhu, N. Laurand, E. Gu, I. M. Watson, C. J. Humphreys, D. J. Wallis, and M. D. Dawson, “Integrated dual-color InGaN light-emitting diode array through transfer printing,” in *2015 IEEE Photonics Conference (IPC)*. IEEE, oct 2015.

- [94] B. Guilhabert, J. McPhillimy, S. May, C. Klitis, M. D. Dawson, M. Sorel, and M. J. Strain, “Hybrid integration of an evanescently coupled AlGaAs microdisk resonator with a silicon waveguide by nanoscale-accuracy transfer printing,” *Optics Letters*, vol. 43, no. 20, p. 4883, oct 2018.
- [95] M. Agostini, G. Greco, and M. Cecchini, “Polydimethylsiloxane (PDMS) irreversible bonding to untreated plastics and metals for microfluidics applications,” *APL Materials*, vol. 7, no. 8, p. 081108, aug 2019.
- [96] F. Prabowo, A. L. Wing-Keung, and H. H. Shen, “Effect of curing temperature and cross-linker to pre-polymer ratio on the viscoelastic properties of a PDMS elastomer,” *Advanced Materials Research*, vol. 1112, pp. 410–413, Jul. 2015.
- [97] B. Guilhabert, A. Hurtado, D. Jevtics, Q. Gao, H. H. Tan, C. Jagadish, and M. D. Dawson, “Transfer printing of semiconductor nanowires with lasing emission for controllable nanophotonic device fabrication,” *ACS Nano*, vol. 10, no. 4, pp. 3951–3958, Mar. 2016.
- [98] M. J. Adams, D. Jevtics, M. J. Strain, I. D. Henning, and A. Hurtado, “High-frequency dynamics of evanescently-coupled nanowire lasers,” *Scientific Reports*, vol. 9, no. 1, apr 2019.
- [99] A. Hurtado, D. Jevtics, B. Guilhabert, Q. Gao, H. H. Tan, C. Jagadish, and M. D. Dawson, “Transfer printing of semiconductor nanowire lasers,” *IET Optoelectronics*, vol. 12, no. 1, pp. 30–35, feb 2018.
- [100] D. Jevtics, B. Guilhabert, A. Hurtado, Q. Gao, H. H. Tan, C. Jagadish, and M. D. Dawson, “Transfer printing of semiconductor nanowires,” in *2016 IEEE Photonics Conference (IPC)*. IEEE, oct 2016.
- [101] D. Jevtics, A. Hurtado, B. Guilhabert, M. Jankauskas, N. Laurand, Q. Gao, H. H. Tan, C. Jagadish, and M. D. Dawson, “Precise positioning and orientation of nanowire lasers in regular and patterned surfaces,” in *2018 IEEE 18th International Conference on Nanotechnology (IEEE-NANO)*. IEEE, jul 2018.

- [102] J. B. Wright, S. Campione, S. Liu, J. A. Martinez, H. Xu, T. S. Luk, Q. Li, G. T. Wang, B. S. Swartzentruber, L. F. Lester, and I. Brener, “Distributed feedback gallium nitride nanowire lasers,” *Applied Physics Letters*, vol. 104, no. 4, p. 041107, jan 2014.
- [103] J. Arbiol, M. de la Mata, M. Eickhoff, and A. F. i Morral, “Bandgap engineering in a nanowire: self-assembled 0, 1 and 2d quantum structures,” *Materials Today*, vol. 16, no. 6, pp. 213–219, jun 2013.
- [104] X. Li, R.-L. Su, Z.-K. Zhou, Y. Yu, and A. D. Falco, “Photonic trimming of quantum emitters via direct fabrication of metallic nanostructures,” *APL Photonics*, vol. 3, no. 7, p. 071301, jul 2018.
- [105] H. Xu, J. B. Wright, A. Hurtado, Q. Li, T.-S. Luk, J. J. Figiel, K. Cross, G. Balakrishnan, L. F. Lester, I. Brener, and G. T. Wang, “Gold substrate-induced single-mode lasing of GaN nanowires,” *Applied Physics Letters*, vol. 101, no. 22, p. 221114, nov 2012.
- [106] G. T. Wang, H. Xu, J. B. Wright, A. Hurtado, T.-S. Luk, J. J. Figiel, I. Brener, and Q. Li, “Mode and polarization control in gallium nitride nanowire lasers,” in *2014 IEEE Photonics Society Summer Topical Meeting Series*. IEEE, jul 2014.
- [107] Y. Kim, E. Yassitepe, O. Voznyy, R. Comin, G. Walters, X. Gong, P. Kanjanaboos, A. F. Nogueira, and E. H. Sargent, “Efficient luminescence from perovskite quantum dot solids,” *ACS Applied Materials & Interfaces*, vol. 7, no. 45, pp. 25 007–25 013, Nov. 2015.
- [108] A. B. Greytak, C. J. Barrelet, Y. Li, and C. M. Lieber, “Semiconductor nanowire laser and nanowire waveguide electro-optic modulators,” *Applied Physics Letters*, vol. 87, no. 15, p. 151103, Oct. 2005.
- [109] Y. Zhang, D. Saxena, M. Aagesen, and H. Liu, “Toward electrically driven semiconductor nanowire lasers,” *Nanotechnology*, vol. 30, no. 19, p. 192002, Mar. 2019.
- [110] P. Parkinson, J. A. Alanis, K. Peng, D. Saxena, S. Mokkaapati, N. Jiang, L. Fu, H. H. Tan, and C. Jagadish, “Modal refractive index measurement in nanowire lasers—a correlative approach,” *Nano Futures*, vol. 2, no. 3, p. 035004, Jul. 2018.

- [111] Q. Li, J. B. Wright, W. W. Chow, T. S. Luk, I. Brener, L. F. Lester, and G. T. Wang, “Single-mode gan nanowire lasers,” *Opt. Express*, vol. 20, no. 16, pp. 17 873–17 879, Jul 2012.
- [112] Y. Ma, X. Guo, X. Wu, L. Dai, and L. Tong, “Semiconductor nanowire lasers,” *Advances in Optics and Photonics*, vol. 5, no. 3, p. 216, Jul. 2013.
- [113] C. J. Sansonetti, M. L. Salit, and J. Reader, “Wavelengths of spectral lines in mercury pencil lamps,” *Applied Optics*, vol. 35, no. 1, p. 74, jan 1996.
- [114] D. A. B. Miller, “Attojoule optoelectronics for low-energy information processing and communications,” *Journal of Lightwave Technology*, vol. 35, no. 3, pp. 346–396, feb 2017.
- [115] R. Yan, J.-H. Park, Y. Choi, C.-J. Heo, S.-M. Yang, L. P. Lee, and P. Yang, “Nanowire-based single-cell endoscopy,” *Nature Nanotechnology*, vol. 7, no. 3, pp. 191–196, dec 2011.
- [116] X. Wu, Y. Xiao, C. Meng, X. Zhang, S. Yu, Y. Wang, C. Yang, X. Guo, C. Z. Ning, and L. Tong, “Hybrid photon-plasmon nanowire lasers,” *Nano Letters*, vol. 13, no. 11, pp. 5654–5659, 2013, pMID: 24144390.
- [117] B. Chen, H. Wu, C. Xin, D. Dai, and L. Tong, “Flexible integration of free-standing nanowires into silicon photonics,” *Nature Communications*, vol. 8, no. 1, jun 2017.
- [118] H. Kim, W.-J. Lee, A. C. Farrell, J. S. D. Morales, P. Senanayake, S. V. Prikhodko, T. J. Ochalski, and D. L. Huffaker, “Monolithic InGaAs nanowire array lasers on silicon-on-insulator operating at room temperature,” *Nano Letters*, vol. 17, no. 6, pp. 3465–3470, may 2017.
- [119] G. N. Malheiros-Silveira, F. Lu, I. Bhattacharya, T.-T. D. Tran, H. Sun, and C. J. Chang-Hasnain, “III–v compound semiconductor nanopillars monolithically integrated to silicon photonics,” *ACS Photonics*, vol. 4, no. 5, pp. 1021–1025, apr 2017.
- [120] S. Sergent, M. Takiguchi, T. Tsuchizawa, A. Yokoo, H. Taniyama, E. Kuramochi, and M. Notomi, “Nanomanipulating and tuning ultraviolet ZnO-nanowire-induced photonic crystal nanocavities,” *ACS Photonics*, vol. 4, no. 5, pp. 1040–1047, may 2017.

- [121] J. Bissinger, D. Ruhstorfer, T. Stettner, G. Koblmüller, and J. J. Finley, “Optimized waveguide coupling of an integrated III-v nanowire laser on silicon,” *Journal of Applied Physics*, vol. 125, no. 24, p. 243102, jun 2019.
- [122] E. Bermúdez-Ureña, G. Tutuncuoglu, J. Cuerda, C. L. C. Smith, J. Bravo-Abad, S. I. Bozhevolnyi, A. F. i Morral, F. J. García-Vidal, and R. Quidant, “Plasmonic waveguide-integrated nanowire laser,” *Nano Letters*, vol. 17, no. 2, pp. 747–754, Jan. 2017.
- [123] J. Lee, I. Karnadi, J. T. Kim, Y.-H. Lee, and M.-K. Kim, “Printed nanolaser on silicon,” *ACS Photonics*, vol. 4, no. 9, pp. 2117–2123, Aug. 2017.
- [124] D. Hofstetter and R. L. Thornton, “Theory of loss measurements of fabry–perot resonators by fourier analysis of the transmission spectra,” *Optics Letters*, vol. 22, no. 24, p. 1831, dec 1997.
- [125] B. E. A. Saleh and M. C. Teich, *Fundamentals of Photonics*. John Wiley & Sons, Inc., Aug. 1991.
- [126] P. Parkinson, J. A. Alanis, K. Peng, D. Saxena, S. Mokkaapati, N. Jiang, L. Fu, H. H. Tan, and C. Jagadish, “Modal refractive index measurement in nanowire lasers—a correlative approach,” *Nano Futures*, vol. 2, no. 3, p. 035004, jul 2018.
- [127] G. Son, S. Han, J. Park, K. Kwon, and K. Yu, “High-efficiency broadband light coupling between optical fibers and photonic integrated circuits,” *Nanophotonics*, vol. 7, no. 12, pp. 1845–1864, oct 2018.
- [128] D.-H. Kim, R. Ghaffari, N. Lu, and J. A. Rogers, “Flexible and stretchable electronics for biointegrated devices,” *Annual Review of Biomedical Engineering*, vol. 14, no. 1, pp. 113–128, aug 2012.
- [129] J. Tatebayashi, Y. Ota, S. Ishida, M. Nishioka, S. Iwamoto, and Y. Arakawa, “Nanowire–quantum-dot lasers on flexible membranes,” *Applied Physics Express*, vol. 11, no. 6, p. 065002, may 2018.

- [130] M. Hossain, G. S. Kumar, S. N. B. Prabhava, E. D. Sheerin, D. McCloskey, S. Acharya, K. D. M. Rao, and J. J. Boland, “Transparent, flexible silicon nanostructured wire networks with seamless junctions for high-performance photodetector applications,” *ACS Nano*, vol. 12, no. 5, pp. 4727–4735, may 2018.
- [131] C. Linghu, S. Zhang, C. Wang, and J. Song, “Transfer printing techniques for flexible and stretchable inorganic electronics,” *npj Flexible Electronics*, vol. 2, no. 1, oct 2018.
- [132] S. Khan, L. Lorenzelli, and R. Dahiya, “Flexible MISFET devices from transfer printed si microwires and spray coating,” *IEEE Journal of the Electron Devices Society*, vol. 4, no. 4, pp. 189–196, jul 2016.
- [133] H. Zhou, W. Qin, Q. Yu, H. Cheng, X. Yu, and H. Wu, “Transfer printing and its applications in flexible electronic devices,” *Nanomaterials*, vol. 9, no. 2, p. 283, feb 2019.
- [134] “Af 32 environmentally friendly thin glass: Schott advanced optics: Schott ag.” [Online]. Available: [https://www.schott.com/advanced\\_optics/english/products/optical-materials/thin-glass/thin-glass-af-32-eco/index.html](https://www.schott.com/advanced_optics/english/products/optical-materials/thin-glass/thin-glass-af-32-eco/index.html)
- [135] F.-F. Ren, K.-W. Ang, J. Ye, M. Yu, G.-Q. Lo, and D.-L. Kwong, “Split bull’s eye shaped aluminum antenna for plasmon-enhanced nanometer scale germanium photodetector,” *Nano Letters*, vol. 11, no. 3, pp. 1289–1293, Mar. 2011.
- [136] H. J. Joyce, J. L. Boland, C. L. Davies, S. A. Baig, and M. B. Johnston, “A review of the electrical properties of semiconductor nanowires: insights gained from terahertz conductivity spectroscopy,” *Semiconductor Science and Technology*, vol. 31, no. 10, p. 103003, sep 2016.
- [137] H. Pahlevaninezhad, B. Heshmat, and T. E. Darcie, “Advances in terahertz waveguides and sources,” *IEEE Photonics Journal*, vol. 3, no. 2, pp. 307–310, apr 2011.
- [138] H. J. Joyce, S. A. Baig, P. Parkinson, C. L. Davies, J. L. Boland, H. H. Tan, C. Jagadish, L. M. Herz, and M. B. Johnston, “The influence of surfaces on the transient terahertz

- conductivity and electron mobility of GaAs nanowires,” *Journal of Physics D: Applied Physics*, vol. 50, no. 22, p. 224001, may 2017.
- [139] K. Peng, D. Jevtics, F. Zhang, S. Sterzl, D. A. Damry, M. U. Rothmann, B. Guilhabert, M. J. Strain, H. H. Tan, L. M. Herz, L. Fu, M. D. Dawson, A. Hurtado, C. Jagadish, and M. B. Johnston, “Three-dimensional cross-nanowire networks recover full terahertz state,” *Science*, vol. 368, no. 6490, pp. 510–513, Apr. 2020.
- [140] G. Lee, I. Maeng, C. Kang, M.-K. Oh, and C.-S. Kee, “Strong polarization-dependent terahertz modulation of aligned ag nanowires on si substrate,” *Optics Express*, vol. 26, no. 10, p. 13677, may 2018.
- [141] S. A. Baig, J. L. Boland, D. A. Damry, H. H. Tan, C. Jagadish, H. J. Joyce, and M. B. Johnston, “An ultrafast switchable terahertz polarization modulator based on III–v semiconductor nanowires,” *Nano Letters*, vol. 17, no. 4, pp. 2603–2610, mar 2017.
- [142] A. Hurtado, D. Jevtics, M. D. Dawson, M. J. Adams, and I. D. Henning, “Laterally coupled nanowire lasers: Bifurcations, dynamics and high-speed potential,” in *2018 IEEE Photonics Conference (IPC)*. IEEE, Sep. 2018.
- [143] M. J. Adams, N. Li, B. R. Cemlyn, H. Susanto, and I. D. Henning, “Effects of detuning, gain-guiding, and index antiguiding on the dynamics of two laterally coupled semiconductor lasers,” *Physical Review A*, vol. 95, no. 5, may 2017.
- [144] “Lumerical mode solutions.” [Online]. Available: <https://www.lumerical.com/products/mode/>
- [145] H. Gao, A. Fu, S. C. Andrews, and P. Yang, “Cleaved-coupled nanowire lasers,” *Proceedings of the National Academy of Sciences*, vol. 110, no. 3, pp. 865–869, jan 2013.
- [146] C. Zhang, C.-L. Zou, H. Dong, Y. Yan, J. Yao, and Y. S. Zhao, “Dual-color single-mode lasing in axially coupled organic nanowire resonators,” *Science Advances*, vol. 3, no. 7, p. e1700225, jun 2017.

- [147] R. Ditcovski and T. Ellenbogen, “Spectral shaping of lasing in vertically aligned coupled nanowire lasers,” *Optics Express*, vol. 25, no. 24, p. 30115, nov 2017.
- [148] M. Adams, “Optical waveguide theory,” *Optica Acta: International Journal of Optics*, vol. 31, no. 5, pp. 497–497, may 1984.
- [149] A. W. Snyder and J. D. Love, *Optical Waveguide Theory*. Springer US, 1984.
- [150] C.-P. Yu and H.-C. Chang, “Yee-mesh-based finite difference eigenmode solver with PML absorbing boundary conditions for optical waveguides and photonic crystal fibers,” *Optics Express*, vol. 12, no. 25, p. 6165, 2004.
- [151] Wikipedia, “Finite-difference time-domain method — Wikipedia, the free encyclopedia,” <http://en.wikipedia.org/w/index.php?title=Finite-difference%20time-domain%20method&oldid=1070031893>, 2022, [Online; accessed 11-May-2022].
- [152] D. Ren, L. Ahtapodov, J. S. Nilsen, J. Yang, A. Gustafsson, J. Huh, G. J. Conibeer, A. T. van Helvoort, B.-O. Fimland, and H. Weman, “Single-mode near-infrared lasing in a GaAsSb-based nanowire superlattice at room temperature,” *Nano Letters*, vol. 18, no. 4, pp. 2304–2310, mar 2018.
- [153] T. Stettner, A. Thurn, M. Döblinger, M. O. Hill, J. Bissinger, P. Schmiedeke, S. Matich, T. Kostenbader, D. Ruhstorfer, H. Riedl, M. Kaniber, L. J. Lauhon, J. J. Finley, and G. Koblmüller, “Tuning lasing emission toward long wavelengths in GaAs-(in,al)GaAs core-multishell nanowires,” *Nano Letters*, vol. 18, no. 10, pp. 6292–6300, sep 2018.
- [154] Y. Han, Z. Yan, W. K. Ng, Y. Xue, K. S. Wong, and K. M. Lau, “Bufferless 15  $\mu\text{m}$  III-v lasers grown on si-photonics 220 nm silicon-on-insulator platforms,” *Optica*, vol. 7, no. 2, p. 148, feb 2020.
- [155] <https://www.norlandprod.com/literature/65tds.pdf>.
- [156] G. Rainò, M. A. Becker, M. I. Bodnarchuk, R. F. Mahrt, M. V. Kovalenko, and T. Stöferle, “Superfluorescence from lead halide perovskite quantum dot superlattices,” *Nature*, vol. 563, no. 7733, pp. 671–675, Nov. 2018.

- [157] H. Zheng, S. Hou, C. Xin, Q. Wu, F. Jiang, Z. Tan, X. Zhou, L. Lin, W. He, Q. Li, J. Zheng, L. Zhang, J. Liu, Y. Yang, J. Shi, X. Zhang, Y. Zhao, Y. Li, C. Lambert, and W. Hong, “Room-temperature quantum interference in single perovskite quantum dot junctions,” *Nature Communications*, vol. 10, no. 1, Nov. 2019.
- [158] H. Utzat, W. Sun, A. E. K. Kaplan, F. Krieg, M. Ginterseder, B. Spokoyny, N. D. Klein, K. E. Shulenberger, C. F. Perkinson, M. V. Kovalenko, and M. G. Bawendi, “Coherent single-photon emission from colloidal lead halide perovskite quantum dots,” *Science*, vol. 363, no. 6431, pp. 1068–1072, Feb. 2019.
- [159] D. Yan, T. Shi, Z. Zang, S. Zhao, J. Du, and Y. Leng, “Stable and low-threshold whispering-gallery-mode lasing from modified CsPbBr<sub>3</sub> perovskite quantum dots@SiO<sub>2</sub> sphere,” *Chemical Engineering Journal*, vol. 401, p. 126066, Dec. 2020.
- [160] H. Zhu, Y. Fu, F. Meng, X. Wu, Z. Gong, Q. Ding, M. V. Gustafsson, M. T. Trinh, S. Jin, and X.-Y. Zhu, “Lead halide perovskite nanowire lasers with low lasing thresholds and high quality factors,” *Nature Materials*, vol. 14, no. 6, pp. 636–642, Apr. 2015.
- [161] J. Chen, W. Du, J. Shi, M. Li, Y. Wang, Q. Zhang, and X. Liu, “Perovskite quantum dot lasers,” *InfoMat*, vol. 2, no. 1, pp. 170–183, Nov. 2019.
- [162] X. Li, Y. Wu, S. Zhang, B. Cai, Y. Gu, J. Song, and H. Zeng, “CsPbX<sub>3</sub> quantum dots for lighting and displays: Room-temperature synthesis, photoluminescence superiorities, underlying origins and white light-emitting diodes,” *Advanced Functional Materials*, vol. 26, no. 15, pp. 2435–2445, Feb. 2016.